Durham E-Theses

The simulation of transient cross-wind gusts and their aerodynamic influence on passenger cars.

Ryan, Anthony G.

How to cite:

Ryan, Anthony G. (2000) *The simulation of transient cross-wind gusts and their aerodynamic influence on passenger cars.*, Durham theses, Durham University. Available at Durham E-Theses Online: http://etheses.dur.ac.uk/1203/

Use policy

The full-text may be used and/or reproduced, and given to third parties in any format or medium, without prior permission or charge, for personal research or study, educational, or not-for-profit purposes provided that:

- a full bibliographic reference is made to the original source
- a link is made to the metadata record in Durham E-Theses
- the full-text is not changed in any way

The full-text must not be sold in any format or medium without the formal permission of the copyright holders.

Please consult the full Durham E-Theses policy for further details.

Academic Support Office, The Palatine Centre, Durham University, Stockton Road, Durham, DH1 3LE
e-mail: e-theses.admin@durham.ac.uk Tel: +44 0191 334 6107
http://etheses.dur.ac.uk

The Simulation of Transient Cross-Wind Gusts and Their Aerodynamic Influence on Passenger Cars

by

Anthony Ryan

The copyright of this thesis rests with the author. No quotation from it should be published in any form, including Electronic and the Internet, without the author's prior written consent. All information derived from this thesis must be acknowledged appropriately.

A Thesis submitted for the degree of

Doctor of Philosophy

School of Engineering

University of Durham

2000

13 JUL 2001

The copyright of this thesis rests with the author. No quotation from it should be published without the author's prior written consent, and information derived from it should be acknowledged.

Copyright © 2000, Anthony Ryan.

Declaration

The work contained in this thesis has not been submitted elsewhere for any other degree or qualification, and unless otherwise acknowledged, it is the author's own work.

Acknowledgements

I am most grateful for the guidance and encouragement provided by my supervisor, Dr. Robert Dominy, throughout the completion of this work.

Appreciation is extended to Mr. Brian Blackburn and Mr. Ian Glassford of the mechanical workshop, and Mr. Ian Hutchinson and Mr. Ian Garret of the Electrical workshop, who between them provided me with the experimental facilities to complete this work. Guidance and assistance was also received from many other members of the Engineering Department, both academic and technical, who are too many to name, but this has not been forgotten.

I also wish to express appreciation to my fellow researchers, David Sims-Williams, Sue Crossland and Alistair Elfick, to name a few, with whom much time has been spent, and discussion had, both engineering and otherwise.

Finally, I would like to thank my family, without whose continued support none of this would have happened.

The Simulation of Transient Cross-Wind Gusts and Their Aerodynamic Influence on Passenger Cars

Anthony Ryan

Abstract

The unique University of Durham transient cross-wind facility has been developed such that sharp edged, finite length, cross-wind gusts with a relative yaw angle of 22° can be developed at the rate of 1000/hr. This cross-wind facility uses the transient interaction of two wind tunnel jets to create these gusts, with the fully automated, rapid, repeatable gust production process allowing ensemble averaging to significantly improve data quality.

The cross-wind gust characteristic, as observed for the empty working section, has some inherent problems. A yaw angle undershoot, and more importantly, an overshoot occur at the leading edge of the gust. A transient total pressure overshoot is also observed at the leading edge of the gust. Computational fluid dynamics (CFD) simulations of the empty working section have replicated these anomalies, and suggestions are proposed for their elimination.

Two aerodynamic models were tested in this facility, each being subjected to transient cross-wind gusts of 10 model lengths. Both models exhibited significant transient force and moment overshoots. These overshoots were found to be a consequence of delayed pressure development in regions of separated flow, with full flow development requiring up to seven model lengths of cross-wind gust.

These results, which cannot be replicated by any steady testing procedure, confirm the requirement for transient testing, if transient forces and moments are required.

Table of Contents

1 Introduction

2 A Review of Vehicle Aerodynamics

3 The Static-Dynamic Jet Interaction Technique

4 Instrumentation and Aerodynamic Models

5 Experimental and Computational Investigations

6 Results

7 Discussion

8 Conclusions

9 Recommendations for Further Work

List of Figures

List of Tables

Nomenclature

A	Vehicle frontal area at zero yaw
Cmx	Rolling moment coefficient
Cmy	Pitching moment coefficient
Cmz	Yawing moment coefficient
Cp	Pitch angle coefficient (five hole probe calibration)
Cp_{dyn}	Dynamic pressure coefficient
Cp_o	Total pressure coefficient
Cp_s	Static pressure coefficient
Cs	Static pressure coefficient (five hole probe calibration)
Ct	Total Pressure Coefficient (five hole probe calibration)
Cv_i	General velocity coefficient
Cx	Drag coefficient
Cy	Side force coefficient / Yaw angle coefficient (five hole probe calibration)
Cz	Lift coefficient
Czu	Upper surface lift coefficient
d	Diameter
dA	Element of area
f_c	Filter cut-of frequency
f	Characteristic frequency
f_{red}	Reduced frequency
f_s	Filter stop frequency
F_a	Force in body axial direction (when body at yaw)
F_p	Force in body perpendicular direction (when body at yaw)
F_x	Force in axial (x) direction
F_y	Force in y direction
h	Model height
l	Model length

m_d	Microdrag
m_s	Microside
n-ens	Number of ensemble averages
p_{1-5}	Individual hole pressures (five hole probe calibration)
p_{av}	Average pressure of holes 2-5 (five hole probe calibration)
p_{dyn}	Dynamic Pressure
p_{dyn_ref}	Reference dynamic pressure
p_o	Total pressure
p_{o_ref}	Reference total pressure
p_s	Static Pressure
p_{s_ref}	Reference static pressure
r	Corner radius
Re_d	Reynolds number based on diameter
Re_l	Reynolds number based on length
s	Distance around a model perimeter
S	Half perimeter of the Docton geometry
t	Time
Tu	Turbulence intensity
u	Axial (x) direction velocity
u_r	Resultant velocity
u_{ref}	Reference axial (x) velocity
v	Cross-stream (y) velocity
v_{ref}	Reference cross-stream (y) velocity
w	Vertical (z) velocity / Model width
w_{ref}	Reference vertical (z) velocity
x	Axial (streamwise) direction
y	Cross-stream direction
z	Vertical direction

Greek Symbols

β	Backlight angle (figure 2.1)
μ	Air dynamic viscosity
π	Pi
ρ	Air density
σ	Standard deviation
ξ	Vorticity
ψ	Yaw angle

Subscripts and Superscripts

x'	Fluctuating component of x
$\overline{x}$	Mean of x
x_{min}	Minimum of x

Aerodynamic Load Sign Convention

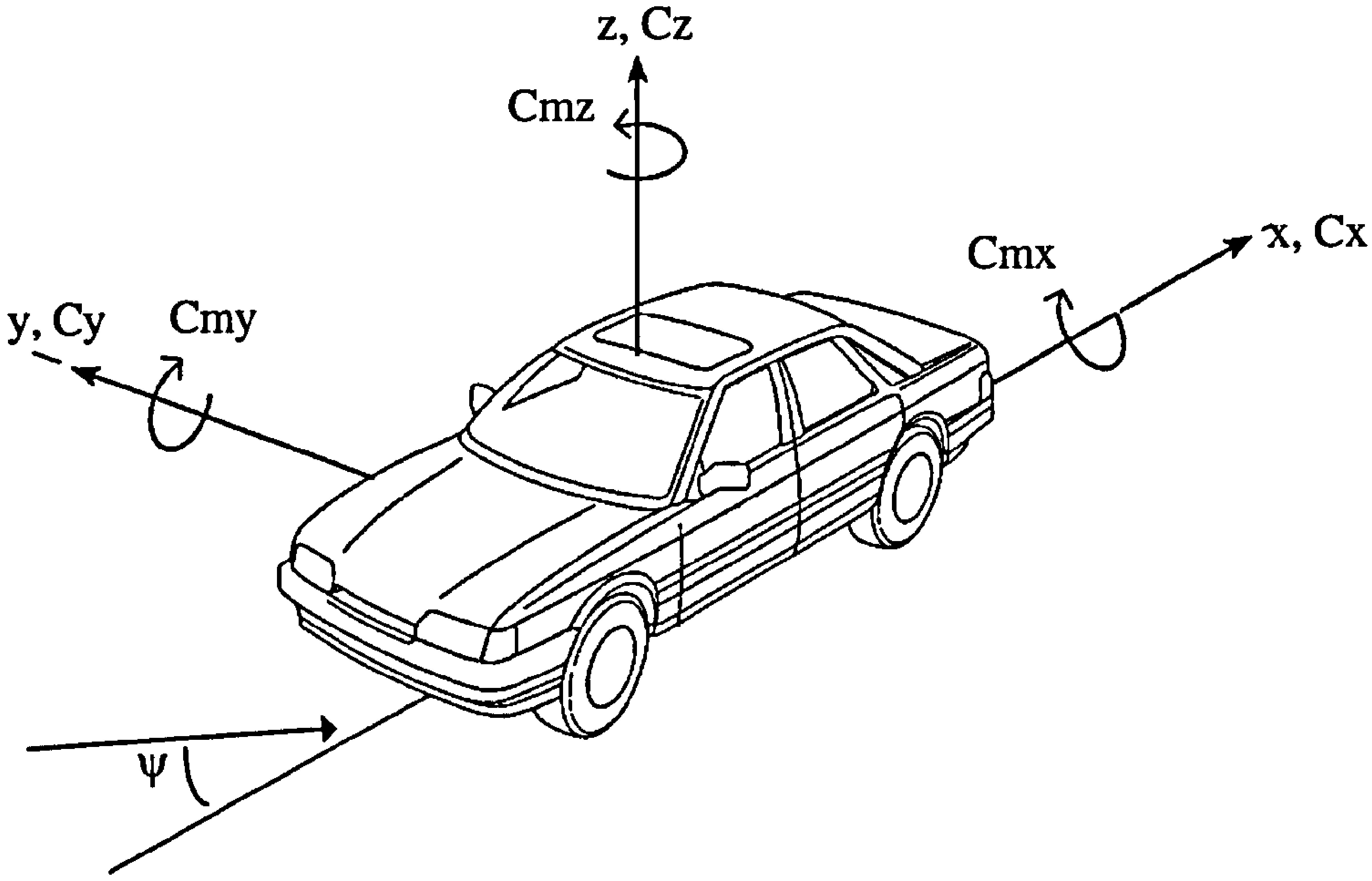

(from Barnard [1])

Chapter One

Introduction

1.1 Vehicle Aerodynamics

Vehicle aerodynamics can be broadly split into three areas; external aerodynamics, component cooling and passenger comfort.

Even the simplified vehicle shapes used for fundamental investigations, for example the Ahmed geometry [2], produce complex three dimensional flowfields. The external flowfield of a true vehicle, be it either in a wind tunnel or the road environment, is further complicated by wheels, surface detail, underbody roughness and the interaction of peripheral objects such as wing mirrors and windshield wipers. As is true for flow over any bluff body, at some point the boundary layer separates from the surface. Automotive shapes are usually characterised by a number of regions of separated flow. The contribution to drag and the other components of force from these separated regions is much greater than that of the viscous forces on the surface and hence much research has been undertaken to further understanding of the flow mechanisms present in these regions, for example see [3, 4, 5].

The underbonnet layout of a vehicle must not only provide air for the combustion demands of the engine, but must also provide adequate cooling for many components. For example, a modern vehicle will require cooling air for the engine water, engine oil, brake components, potentially turbocharger and intercooler and engine electronics. An engine cooling system must be designed such that it can not only cope with these demands under the most arduous conditions, but must do this whilst giving as small a decrease in overall vehicle performance as possible. Cooling drag may be split into three constituent components. Pressure drag will result directly from pressure loss across cooling systems, for example the pressure loss across a radiator. The turbulent outflowing cooling air is also likely to have a detrimental effect on the external aerodynamics, although this is not always the case. Finally, elements such as radiators have a significant 'wetted area' and therefore although the through velocity is low, a significant contribution from skin friction drag can be expected.

Hucho [6] reports a typical increase in drag coefficient, Cx, as result of cooling airflow of $\Delta Cx = 0.03$. This is a significant percentage of what may be considered as a typical overall passenger car drag coefficient of $Cx = 0.35$. More recently Freymann *et al* [7] quote $\Delta Cx = 0.013$ for a BMW 8 series. This much lower value was a consequence of a concerted effort by BMW to reduce the overall drag of their vehicles and within this framework was the minimising of cooling airflow drag. It was achieved by optimisation of the intake and outflow geometry, the shape of the air ducts and the arrangement of the radiators. Further improvements were realised through minimisation of flow restrictions and the use of active elements for flow control.

From an aerodynamic viewpoint, passenger comfort is concerned with the ventilation, heating, air conditioning and noise experienced in the passenger compartment of a vehicle. With an increasingly competitive car market, these factors are becoming much more important in selling a vehicle. Advances in technology are not only leading to quieter engines, but better suppression of engine and other forms of noise (e.g. road noise) is leading to aerodynamic noise becoming increasingly important. The major contributions to aerodynamic noise come from flow around the wing mirrors and the unsteady nature of flow in the A- and C-pillar regions [8] (key vehicle geometrical features are illustrated in figure 1.1). Current research topics not only include methods of reducing noise, but also prediction of the sound transmission properties of closed windows [9].

Passenger compartment ventilation is generally provided by air intake ducts at the bottom of the windscreen. This location is ideal in that it is situated in a region of high pressure, thus providing good intake flow rates. Carr [10] quotes $Cp_s = 0.5$ as typical in this region for a vehicle with a 45° windshield. This location is also remote enough to the ground that exhaust fumes are not ingested. Prior to flowing into the passenger compartment conditioning of this air is likely, such that its temperature or humidity is altered.

1.2 Cross-Wind Aerodynamics

Outlined above are some of the important features of vehicle aerodynamics. When designing a vehicle, it must be considered that the majority of driving conditions encountered will not be ideal. Thus, as the design process becomes more advanced and car sales more competitive, it is possible and necessary to design for a much wider range of driving conditions. Cross-winds are one of these driving conditions, not only are they unnerving for drivers, but have been an integral part of a significant number of road accidents [11, 12]. In efforts to meet future emissions regulations it is probable that motor manufacturers will need to produce lighter vehicles. The reduced inertia of these vehicles is likely to make them more sensitive to cross-winds, although undoubtedly advances in suspension technologies will partially offset this.

Essentially there are three possible types of cross-wind condition. These are steady cross-winds, unsteady cross-winds and so called transient cross-winds. Steady cross-winds are a result of a steady atmospheric wind condition, but in reality are rare. The inherently gusty nature of atmospheric winds makes unsteady conditions much more likely. Transient cross-winds are caused by the combination of one of the above conditions and the relative motion of a vehicle. For example, a vehicle may exit from a tunnel into a transverse wind condition, either steady or unsteady, at which point it will be subjected to a cross-wind transient. Many similar situations exist where a vehicle can appear from a sheltered position into a region of cross-wind. For example, emergence from a bridge abutment, or the passing of a gap in a hedge, or between buildings. A similar condition may be experienced when overtaking a large vehicle in a cross-wind and in this situation the effects may be exaggerated by buffeting from the unsteady wake of the large vehicle.

Figure 1.2 illustrates the transient cross-wind condition that results from a vehicle being suddenly exposed to a transverse wind. Initially the vehicle is travelling through nominally stationary air and hence is subjected to axial flow, as depicted by the left hand velocity triangle. It subsequently rapidly passes through a shear layer into a region of yawed flow, where the resultant velocity vector, u_r, comprises of the vehicles relative forward velocity, u, and the cross-wind velocity, v. Thus the vehicle is subjected to an increased resultant velocity at a yaw angle of ψ (central velocity triangle). A short time later the vehicle passes through a second shear layer and is returned to the original axial flow condition. The transition from axial to yawed flow is potentially very rapid, with the rapidly changing forces and moments the vehicle is subjected to requiring fast, corrective, driver reaction. In many situations this leads to over-reaction. Similarly fast reaction is required on exit from the gust. If the region of cross-wind is of short duration, these two driver reactions are required within a short time and hence from a driver reaction perspective, sharp edged, finite length cross-wind gusts are considered to be a worst case scenario.

Only in the most extreme conditions will a wind induced accident involve the overturning of a passenger car, although this is a serious problem for high sided vehicles. It is much more common for cross-wind conditions to produce excessive and dangerous vehicle deviation, either through direct forces and moments or through driver over-reaction. The aerodynamic moment of most interest for directional stability is yawing moment, as this determines the steering angle input required to maintain a straight vehicle path. In addition to yawing moment, for transient conditions yaw rate is of extreme importance, as this determines the time available for a driver to take corrective action. A low yaw rate is desirable, as clearly this provides a driver with more time to make a correction, hence reducing the risk of over-correction. Of secondary importance are side force and lift, with low values for both being desirable. The side force determines the tyre slip angle required to maintain a straight path, with a small side force requiring a small slip angle, and hence there is less of a discrepancy between the angle of the vehicle and the direction of forward travel. Reducing the lift, or even producing a downforce, has been shown by researchers such as Buchheim *et al* [13] and Howell [14] to increase stability.

1.3 Objectives of the Work

The aim of the work detailed in this thesis was to further the investigations of Docton [61] into the transient flow effects observed around a vehicle on entry to a sharp edged region of cross-wind. A facility for conducting the required tests existed, however the cross-wind gust generation process was labour intensive and relatively slow. Thus a priority was the development of this facility to allow fully automated generation of rapid and repeatable cross-wind gusts. The aim was then to use the developed facility to further understanding of the underlying flow physics and mechanisms responsible for the observed transient effects. This was to be achieved through the investigation of surface pressures, aerodynamic forces and wakes of two vehicle like bodies under the transient cross-wind conditions.

1.4 Thesis Structure

A brief introduction into vehicle aerodynamics including cross-wind aerodynamics has been given in this Chapter.

Chapter Two reviews literature relevant to this thesis, focusing on cross-wind aerodynamics of passenger vehicles and also reviews some of the more pertinent aspects of general wind tunnel testing techniques.

A review of the unique University of Durham transient cross-wind facility is given in Chapter Three. This covers historical aspects of the facility, it theoretical operation and the developments made by the current author.

The aerodynamic models and instrumentation used for data acquisition are covered in Chapter Four. This gives a brief discussion of the geometry of the two aerodynamic models and their instrumentation with pressure tappings. The five hole pressure probe and two component force balance are also reviewed, with estimations made as to the accuracy of the measurements. Also discussed is the dynamic correction technique used to accurately replicate the amplitude and phase of the unsteady pressure data.

Chapter Five discusses the experimental technique and outlines the experiments performed. Also discussed is the computation fluid dynamics (CFD) investigation of the empty working section.

The results, both experimental and computational, are presented in Chapter Six. These are subsequently discussed in Chapter Seven. Conclusions are drawn in Chapter Eight, and recommendations for further work outlined in Chapter Nine.

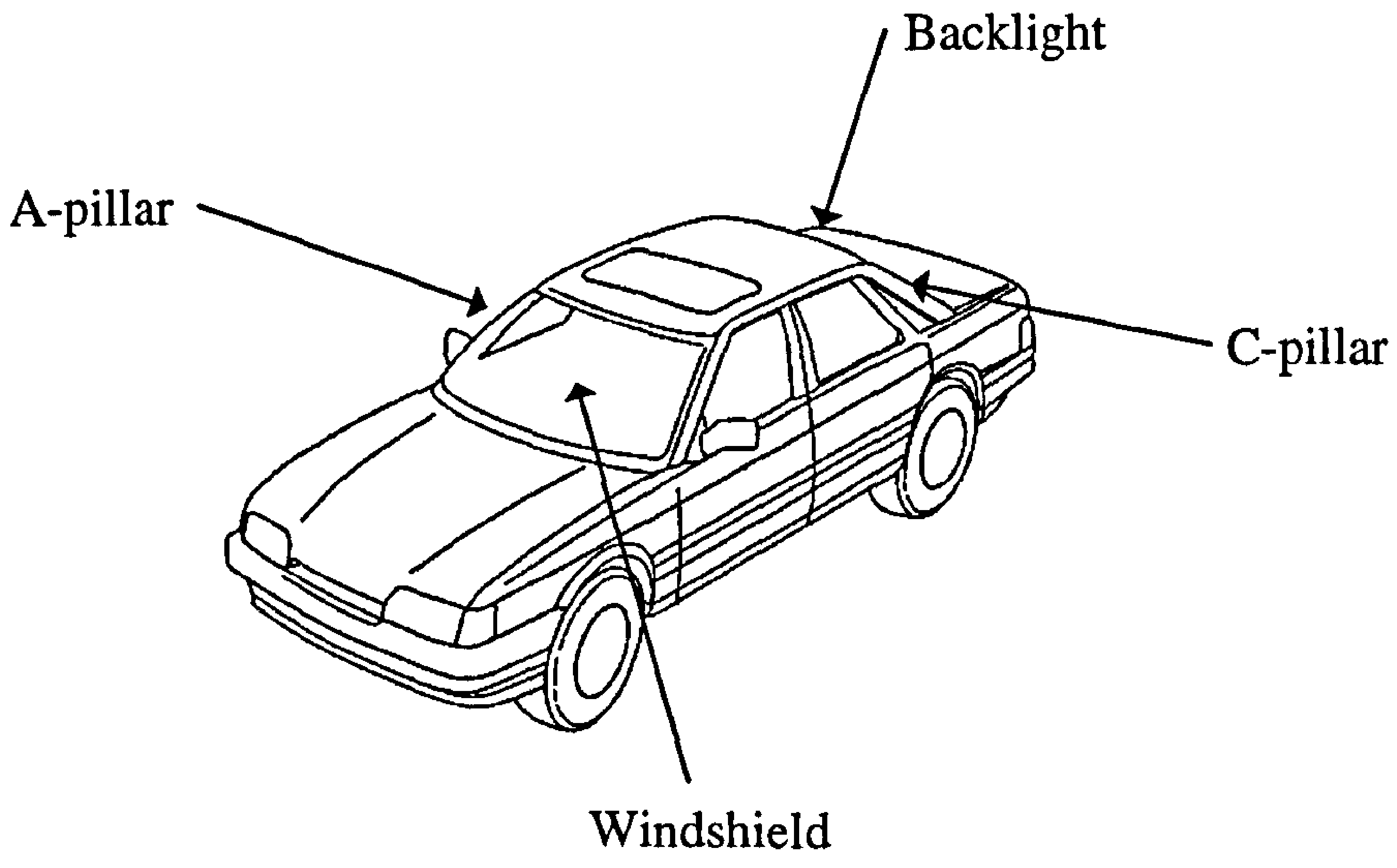

Figure 1.1 Key Features of a Vehicle Geometry (from Barnard [1])

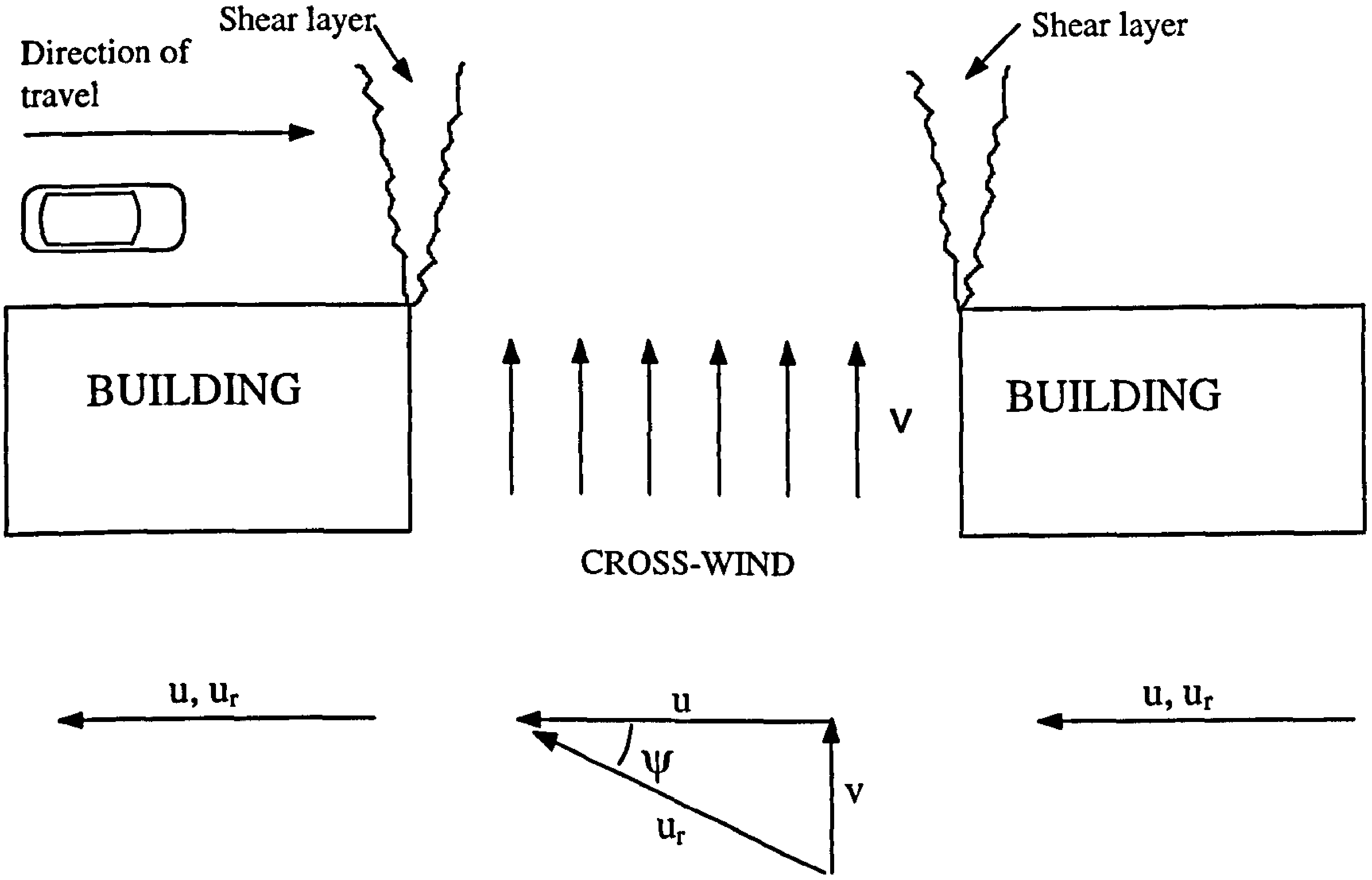

Figure 1.2 A Transient Cross-Wind from a Steady Atmospheric Wind

Chapter Two

A Review of Vehicle Aerodynamics

2.1 Aerodynamic Design

The aerodynamic design of passenger vehicles is driven by the requirements of fuel efficiency, low noise and stability. Often these requirements conflict with those of the stylist, who needs to design a body shape that is aesthetically pleasing and will therefore sell. Much research is undertaken by vehicle aerodynamicists in an attempt to achieve their goals.

2.2 Current Vehicle Aerodynamics Research

2.2.1 Generic Bodies and Vehicle Shapes

Vehicle external aerodynamics research may be split into two domains depending on the geometry being investigated. Flow fundamentals are much easier to isolate on simple generic bodies that do not include much of the detail of a real vehicle. This however is of little interest to motor manufacturers, who are primarily interested in the flow around real vehicle shapes.

Barlow *et al* [15] investigated the wake structure of three dimensional rectangular bodies with rounded front and sharp rear corners. They were interested in the effects of changing the aspect ratio on drag. Their results highlighted one of the drawbacks of using simple bodies; they found that for smooth surfaced bodies drag increased with increasing aspect ratio, but for bodies with a rough underbody (as most vehicles have), drag decreased with increasing aspect ratio. Ahmed [16] encountered a similar problem after adding surface detail to the underbody of a 1/4 scale squareback car. The addition of this detail changed the lift coefficient from Cz = -0.148 to Cz = 0.129. Lajos [17] investigated the drag reduction possibilities for a bluff body by the introduction of various flow disturbing features on the front face. He found a 60% reduction in drag could be achieved by the introduction of a backward facing step on the front face, this is something that has little relevance as for reasons of aesthetics it would never be adopted by a motor manufacturer.

Williams *et al* [18] highlighted the true potential of fundamental investigations by successfully using simple radiused rectangular boxes to aid explanation of the decrease in drag coefficient they observed for increasing aspect ratio on several potential van shapes. Thus, these fundamental investigations had a true commercial application. Other investigations are solely interested in the performance of real vehicles, for example see Howell and LeGood [19] and LeGood *et al* [20].

2.2.2 Vehicle Wakes

The wake of a vehicle forms an important part of its flowfield, being a consequence of the drag inducing flow structures around a vehicle. Although a wake is very dependent on the flow around the rear, it is also affected by the flow structures that have developed as a result of the upstream geometrical features.

The flow structure of a fastback type vehicle (figure 2.1 illustrates the three passenger car rear end shapes) is of most interest as it can take one of two fundamentally different forms. It will either fully separate at the roof/backlight intersection, forming a large region of recirculating flow, or it will remain attached. The attached structure may involve separation at the roof/backlight intersection and subsequent reattachment further down the backlight. The attached flow structure is characterised by a much smaller region of recirculating flow in the near wake and two strong contra-rotating trailing vortices. The flow structure, either attached or separated, observed for a particular vehicle is dependant on the 'history' of the airflow upstream and specific geometry of the vehicle. Indeed, both flow regimes may be observed for the same geometry, with some external factor such as the presence of a splitter plate in the wake determining the current flow structure [21].

Some of the earliest observations of this phenomena were made by Morel [22]. His geometry consisted of a circular cylinder of aspect ratio 9:1, with an aerodynamically shaped nose and the rear of the cylinder truncated to form a backlight (figure 2.2). He investigated the effect of changing the backlight angle on the flow structure and found that transition between the two flow regimes was very sudden, but that either flow pattern was stable once it had been established.

Morel [22] subsequently investigated this phenomenon on a vehicle like geometry in ground proximity. The model, as seen in figure 2.3, was a cuboid of aspect ratio 3.33:1.5:1.0 (l:w:h) with well rounded front corners to minimise the upstream effect on the wake structure and a slanted interchangeable backlight region, such that the backlight angle was variable. Again, he observed a similar bi-stable flow regime, with a critical backlight angle of $\beta = 30^\circ$. Production road vehicles are unlikely to experience a bi-stable flow structure, however the significant variations in drag coefficient with backlight angle observed are of importance.

Ahmed *et al* [2] used results obtained from flow visualisation and surface pressure measurements to describe in detail the wake structure of the Ahmed geometry for both attached and separated flow. This geometry has the same well rounded front corners and backlight as the Morel geometry, but a different aspect ratio of 3.36:1.37:1 (l:w:h). Figure 2.4 shows the wake structure for the attached flow regime. Flow separation occurs at the roof/backlight intersection, but with subsequent reattachment on the backlight. This forms a closed recirculation bubble (E), with two triangular regions of attached flow (F). Strong trailing vortices are formed as the shear layers from the sides of the model roll onto the low pressure backlight. The cores of these vortices are further fed with low energy fluid from the recirculation bubble (E). Two areas of opposite sense recirculating flow exist behind the rear vertical face (A and B). Further increasing the backlight angle causes the recirculating regions A and E to merge, such that the flow no longer reattaches to the backlight and the separated flow regime is formed. The separated flow regime is characterised by the absence of strong trailing vortices and consequently usually exhibits a lower drag.

Figure 2.5 shows the variation of drag coefficient with backlight angle for the Ahmed geometry. Here it can be seen that for the attached flow case ($0^\circ \leq \beta \leq 30^\circ$), the drag coefficient exhibits a minima at 10°, from where there is a rise to the maximum at 30°. If the backlight angle is further increased the flow regime changes to the separated case and a sudden decrease in drag is observed. Sedney [23] later highlighted that the variation in drag observed for the attached flow regime is much greater that that of the separated flow regime. This is presumably a result of the significant change in strength of the trailing vortices with backlight angle for the attached flow regime.

A squareback geometry can be considered as a fastback with a very steep backlight angle. Hence flow separation occurs at the roof/backlight intersection, with no subsequent reattachment. The flow also separates from the sides and underbody, forming a large region of recirculation region in the near wake. Ahmed and Baumert [24] found the contra rotating vortices in the wake of a 1/4 scale squareback model were opposite in sense to those found for a comparable fastback. From this they concluded that somewhere between these configurations would be a configuration that would not exhibit C-pillar trailing vortices and hence would not suffer from trailing vortex drag. However, as indicated by Bearman [25], it is possible that the trailing vortices they observed were formed by flow around the A-pillars and weaker C-pillar vortices were formed that were not visible on the relatively coarse vector plots of their results. Also, the formation of A-pillar vortices, which is common to all car configurations, would make it impossible to entirely eliminate vortex drag.

The near flowfield of a notch back type vehicle contains a complex arrangement of separated regions and trailing vortices. The relatively steep backlight angles found on notchback vehicles promotes flow separation at the roof/backlight intersection. The formation of weak C-pillar vortices causes a downwash in the wake, with this aiding reattachment on the boot lid, however this may not occur for all geometries. Nouzawa *et al* [26] found the critical geometry defining whether the flow reattached or not could be defined by the angle θrt, this being the angle formed when a straight line is drawn from the roof/backlight intersection to the top of the rear of the boot lid. They found a drag maxima at $\theta rt = 25^\circ$, indicating this was the critical angle.

2.2.3 Wake Surveys and Integrals

Wake surveys have been used as a powerful tool to investigate the structure of vehicle wakes. For example Cogotti [27] used a fourteen hole probe to investigate the steady (time-averaged) wake of several squareback configurations. The probe design and large number of holes permitted flow angles of 70° to 250° to be measured in pitch, with the yaw range being ±90°. This large range allowed measurements in regions of near reversed flow, allowing him to build up a complete picture of the vehicle wake. He concluded that for all the configurations tested trailing vortices did exist. The sense of these vortices depended on the specific geometry. No significant changes in drag coefficient were observed for the different wake structures, suggesting the separation points, base pressure and contribution to drag coefficient from the trailing vortices remained relatively constant.

A detailed steady wake survey can also be integrated to yield the drag of a vehicle. This has been done by many authors, for example Onorato *et al* [28], Cogotti [29], Hackett and Sugavanam [30], and Hackett *et al* [31]. The advantage of using a wake survey to calculate drag is that the energy transferred into to the trailing vortices (so called vortex drag) can be isolated, such that the direct effect of geometrical configuration changes to reduce the strength of these vortices (and hence hopefully drag) can be assessed. The local contribution to total drag (microdrag) can also be assessed, allowing the aerodynamicist to concentrate refinements on certain areas of a vehicle.

Two slightly different approaches have been adopted by the various authors; Onorato *et al* [28] and Cogotti [29] used the basic momentum equation, as seen in Appendix B, whereas Hackett and Sugavanam [30] and Hackett *et al* [31] applied a development of a the basic momentum equation, as first used by Maskell [32]. By modelling the wake of the body, and its reflections in the wind tunnel walls, as a potential flowfield, Maskell [32] demonstrated that the terms in the basic momentum equation could be adjusted such that the area from which data is required to perform a wake integral can be reduced to just the wake of the body. Thus, his final equations require data from a relatively small traverse area. The major limitation of the first method is that for correct prediction of aerodynamic coefficients, the wake survey has to be completed over the entire area of flow that is affected by the presence of the body. This can not only be impractical, but is very time consuming, and hence the development of the Maskell [32] method. Wake surveys conducted by both methods are very sensitive to grid density. Davis [33] integrated wake surveys using the Maskell [32] method for a 1/10th scale generic vehicle shape in ground proximity. He found that decreasing the spatial resolution in area by a factor of four (10mm grid to a 20mm grid) introduced errors of over 50% in the value of drag force.

The practical difficulties in meeting the traverse area requirements of the first technique make it somewhat less rigorous, with the chosen limits of the traverse potentially having a significant effect on the aerodynamic coefficients. This to a certain extent allows fortuitous results to be obtained. That said, this method has produced results that are equally good in their agreement with the force balance results. Onorato *et al* [28] quoted drag figures for a 20% scale simplified vehicle shape at 0° yaw from a 20mm grid that are within 1.3% of the force balance results. In comparison, Hackett and Sugavanam [30] quoted drag figures obtained from a 12.5mm grid for a 15% scale vehicle shape, of similar design, that are in agreement with force balance results to within 3.5%.

2.3 Cross-Wind Vehicle Aerodynamics Research

2.3.1 Introduction

The majority of cross-wind vehicle aerodynamics research is carried out under steady cross-wind conditions. This is primarily due to the simplicity of the technique, with many current wind tunnels, for example the MIRA wind tunnel, as used by Docton [34], able to rotate a vehicle in the working section, allowing it to be subjected to steady yawed flow. Aerodynamic coefficients obtained under these conditions are pertinent to steady atmospheric winds, and probably hold true for the majority of unsteady atmospheric winds. The technique used for steady cross-wind testing of vehicles has been referred to as the 'static-static' technique by Macklin *et al* [35], with results obtained from this technique reviewed in section 2.3.2.

The aerodynamic coefficients recorded for a vehicle on entry to, and exit of, a region of cross-wind will be significantly different to their comparable steady yawed coefficients and hence the interest in these transient cross-wind conditions. Consider a quasi-steady process, where the vehicle is incremented into a region of cross-wind flow in a series of stationary positions. Initially, only the front of the vehicle is subjected to cross-wind flow. Thus the side force will be lower than that of steady yawed flow, however as no restoring moment is provided by yawed flow around the rear of the vehicle, the yawing moment will be larger than that of steady yawed flow. As the vehicle increments further into the cross-wind, both side force and yawing moment will tend to their steady yawed values. The maximum yawing moment is recorded when the entire vehicle ahead of the centre of pressure is in the cross-wind gust, with the peak magnitude depending on the exposed side area. Neglecting end effects, both coefficients should equal their steady yawed values after 1 model length of cross-wind flow.

If this process is turned into a continuous one, whereby the vehicle is driven into the region of cross-wind, albeit at a slow velocity, flow hysterisis may make a contribution. This will cause the peak yawing moment, and the steady yawed side force and yawing moment coefficients, to be reached after an increased number of vehicle lengths of cross-wind flow. The time-dependent coefficients will however still be characterised by the side force coefficient rising asymptotically to the steady yawed value, with no overshoot, and the yawing moment coefficient exhibiting an overshoot before falling to the steady yawed value.

A third situation may also be considered, whereby a rapid change in flowfield around a vehicle as it enters a cross-wind region results in significant transient flow effects. These are the situations of most interest, where transient overshoots of both side force and yawing moment are likely to occur, as the forces and moments generated cannot be replicated by any steady testing technique. It is probable that these effects will only occur for a limited number of situations, where the velocity into the cross-wind is relatively high, the yaw angle is significant, and the vehicle geometry is appropriate.

A variety of techniques have been used to obtain data for transient cross-wind conditions. Macklin *et al* [35] classify these techniques as either 'dynamic-static' or 'static-dynamic'. Dynamic-static techniques keep the gust source constant and move the vehicle. This has been applied at both full scale, for example MacAdam [36] and Kobayshi and Yamada [37], and in a wind tunnel facility, for example Kramer *et al* [38] and Yoshida *et al* [39]. In contrast 'static-dynamic' techniques, as used by Ryan and Dominy [40, 41] and Dominy and Ryan [42] for example, keep the model stationary and simulate the cross-wind by either varying the gust profile, or by the introduction of a second gust. Results obtained from the dynamic-static technique are reviewed in section 2.3.3, with those from the static-dynamic technique reviewed in section 2.3.4.

In addition to experimental investigations, several empirical and theoretical methods have been developed that attempt to model cross-wind conditions, both steady and transient. These are reviewed in section 2.3.5.

2.3.2 The Static-Static Technique

As for general vehicle aerodynamic research, the bodies investigated under cross-wind conditions range from simple box like shapes, for example Cooper [43], to scale vehicles, for example Davis [44] who investigated a 1/4 scale two seater performance car. Two relatively exhaustive parameter studies have been completed by Gilhaus and Renn [45] and Howell [46]. Gilhaus and Renn [45] tested a 3/8th scale model vehicle with interchangeable body parts at a speed of 210km/h (this corresponds to 80km/h full scale, $Re_l = 5.5 \times 10^6$). The model had a smooth underbody, with no cooling airflow simulation. Data was taken at a constant yaw angle of $\psi = 20°$; their data suggested a linear increase in yawing moment up to 20°, and hence data taken at this yaw angle could be used to imply forces and moments at lower yaw angles. Howell [46] used a combination of two generic vehicle models that permitted geometry alterations and some data from full scale vehicle tests. The generic models were 1/4 scale and were tested at a nominal test speed of $27ms^{-1}$ ($Re_l = 1.85 \times 10^6$). Data was taken at a range of yaw angles for $0° \leq \psi \leq 40°$. The models had a smooth underbody and no wheels. A similar, although more restricted, parameter study was conducted by Kohri and Kataoka

[47] who tested a 1/5th scale notchback. The effects on yawing moment of some of the geometrical changes undertaken by these authors are presented in table 2.1. As can be seen from table 2.1, there is a certain amount of conflicting evidence, highlighting the sensitivity of some of these geometrical changes to the exact model shape, and hence caution should be exercised before applying the results universally. In addition to these data, both Howell [46] and Buchheim *et al* [13] found that for notchback vehicles moving the canopy rearwards decreases the yawing moment; this is a consequence of decreased front side area and increased rear side area. In general both Gilhaus and Renn [45] and Kohri and Kataoka [47] agree that aerodynamic optimisation for drag causes greater conflict with yawing moment for geometrical changes adopted at the rear rather than at the front of a vehicle.

Wake surveys and integrals have also been conducted for generic models at yaw, for example Bearman [25] and Bearman *et al* [48]. These yield both side force and drag coefficients. Davis [33] reports on the wake behind a family of generic models at a range of yaw angles for $\psi \leq 10^{\circ}$. Comparison of the wake integral obtained side force for several of the models indicated that the leeward side A-pillar vortex, which was the dominant feature of the yawed wakes, was responsible for a considerable percentage of the increase in side force observed at yaw.

Howell [49] similarly investigated the wake of a saloon car under yawed flow conditions, concluding that as yaw angle increased the wake became increasingly dominated by two distinct vortices of equal rotation, as opposed to the contra rotating vortices generally observed under axial flow conditions.

	Gilhaus & Renn [45]	Howell [46]	Kohri & Kataoka [47]
Lowering of front spoiler	• Decreased yawing moment	• Decreased yawing moment	
Increased front wing vertical edge curvature	• Increased yawing moment	• Increased yawing moment - also decreased drag	
Increasing front wing side edge curvature	• Decreased yawing moment	• Decreased yawing moment	
Increasing A-pillar curvature	• Decreased yawing moment	• Decreased yawing moment	
Increasing C/D-pillar curvature	• Increased yawing moment - also decreased drag	• Increased yawing moment	• Increased yawing moment
Increased bonnet front edge curvature	• Increased yawing moment	• Increased yawing moment - also decreased drag	
Increased planform curvature - (boat-tailing)	• Increased yawing moment - also decreased drag	• Decreased yawing moment	• Increased yawing moment - also decreased drag
Change from notchback to hatchback	• Decreased yawing moment	• Increased yawing moment	• Increased yawing moment
Increased rear overhang (notchback only)	• Increased yawing moment - also decreased drag	• Increased yawing moment	
Increased boot deck height (notchback only)		• Decreased yawing moment	• Decreased yawing moment - also decreased drag

Table 2.1 Effect of Geometrical Changes on Yawing Moment Characteristic

Baker [50], whose interests mainly lie with high sides lorries and trains where overturning is a potential problem, considered the quantities that will affect the values of force, moment and pressure coefficient acting on a vehicle under steady cross-wind conditions. Included in these quantities were the properties that would be considered to constitute an atmospheric turbulence simulation, namely mean velocity profile, turbulence profile, turbulence length scale profile and reference values for these properties at a particular height.

Dimensional analysis was used to demonstrate that if wind tunnel simulations are to yield correct values for the steady coefficients, it is necessary to use a dynamic-static testing technique with an atmospheric boundary layer simulation. He further commented that in reality it is difficult to produce the correct turbulence length scale for an atmospheric boundary layer simulation, as the wind tunnels available are too small to do this at realistic model scales.

Baker [51] subsequently investigated the effects of the unsteady wind component on the force and moment coefficients. He defined an aerodynamic admittance (in the frequency domain) that related the force fluctuations experienced by a vehicle to the wind velocity fluctuations. This admittance combined with the available wind spectrum for a particular site can then be used, via an extreme value coefficient, to calculate the required combination of wind speed and wind direction to overturn a vehicle, or as shown in Baker [52], a train.

Humphreys and Baker [53] fully applied Baker's conclusions that both atmospheric boundary layer simulation and a dynamic-static testing technique are required. They investigated the mean force and moment coefficients generated by a 1/50th scale sharp edged lorry, comparing those calculated from dynamic-static track tests to those from static-static tests. The dynamic-static forces were taken to be the mean force measured over the central part of a run, thus not including the overshoots that occur on entry to, or exit of, a region of cross-wind. Although an atmospheric boundary layer simulation was used, the turbulent length scale produced was 1/2 that required. The results indicated that only the mean side force coefficient was in good agreement between dynamic-static and static-static tests. The remaining four measured mean coefficients (yawing, rolling and pitching moment and lift force) all showed significant discrepancies. The mean static coefficients were also compared to some obtained in a low turbulence simulation, again side force showed good similarity, with the other components showing significant discrepancies. Although some doubt was expressed over the lift coefficient, and hence pitching moment coefficient, the results would tend to indicate that an atmospheric boundary layer simulation and a dynamic-static test technique are significant factors in determining the mean coefficients.

2.3.3 The Dynamic-Static Technique

The most common form of dynamic-static testing is the track technique. This involves propelling a vehicle along a straight track, such that it passes through a wind tunnel jet that has its axial direction perpendicular to the direction of travel of the vehicle.

This has been applied at full scale by Kobayshi and Yamada [37] who drove a one-box type van through a sharp edged region of cross-wind at a relative yaw angle of 30^0. In general, two types of full scale test may be conducted, one where the steering input is fixed and the vehicle deviation over a fixed length of cross-wind is measured - termed ‘closed loop’. The second type is where a driver attempts to drive along a fixed path, this involves corrective driver input which is very hard to quantify - termed ‘open loop’. Figure 2.6 shows the transient yawing moment (Cym) and side force (Cs) coefficients obtained by Kobayshi and Yamada [37] by integration of the transient pressures from 120 tappings located on the surface of their vehicle. On entry to the cross-wind region the yawing moment exhibits a significant transient overshoot, corresponding to approximately 100% of the final value, with the peak overshoot occurring at $x/l = 1.3$, where x represents the distance the vehicle is into the cross-wind and l the length of the vehicle. The yawing moment overshoot subsequently decays to a steady value over a period of about seven vehicle lengths. A smaller overshoot of about 30% of the final value occurred for the transient side force coefficient. Thus, the flow around this vehicle under these conditions is subject to transient effects that could not be replicated by any steady testing procedure. Although this technique accurately replicates the real finite length, sharp edged condition, full scale testing has to be conducted at a late stage in the design process, from where it is costly and time consuming to make any changes, should they be necessary. It is also difficult to directly measure the aerodynamic forces and moments the vehicle is subjected to. If serious aerodynamic investigations are to be conducted into the forces and moments and the underlying flow physics, tests need to be conducted under controlled and repeatable conditions. Wind tunnel testing of scale models is arguably the best way to achieve this.

Some of the first wind tunnel investigations were conducted by Beauvais [54]. He constructed a 9.5m track along which a 1/10th scale model passenger car was propelled. The cross-wind tunnel was of low turbulence with $0.01\% \leq Tu \leq 0.02\%$, depending on tunnel speed, and created cross-wind gusts of approximately five model lengths. Rubber shock chord was used to accelerate the model to a maximum speed of $15.2ms^{-1}$. The notchback type model was constructed in a space frame style from balsawood, keeping the weight below 0.170kg. The model contained an internally mounted two component balance (side force and yawing moment), this being isolated from track vibration by means of rubber isolators. The model and balance were mounted on a carriage above the track, such that the model would not be considered to be in ground proximity. Force and moment coefficients were compared for static and moving model tests for a yaw angle range of $0^{\circ} \leq \psi \leq 90^{\circ}$, with the yaw angle for the moving model tests controlled by adjusting both the model and tunnel speeds. The test Reynolds number was dependent on speed, and hence varied with yaw angle, however the minimum was $Re_l = 1.6 \times 10^5$, based on model forward speed and length. His results (figure 2.7) showed the transient side force increasing from zero to the value found for a comparable steady yawed condition over a distance equivalent to three model lengths. For yaw angles greater than 15°, the transient yawing moment coefficient overshot the steady yawed coefficient by up to 25%, with the transient yawing moment coefficient reducing to the comparable steady yawed coefficient within two model lengths of cross-wind flow. These results are typical of those expected for a vehicle entering into a region of cross-wind where no transient flow effects occur.

Stewart [55] constructed a similar moving model facility. This consisted of a 24m track, with the models again propelled by rubber shock chord. This larger scale facility allowed the testing of 1/4 scale passenger cars, or 1/10th scale commercial vehicles. The models used were run in proximity to the ground, being supported by struts that projected through the ground plane. The cross-wind tunnel exit was 4.5m in length, creating gusts of between 3 and 5 model lengths. Reynolds number based on model forward speed and length was $1.3 \leq Re_l \leq 1.7 \times 10^6$. Force and moment data were recorded by a five component (no drag) internally mounted balance, with 30Hz low pass filters and a 'no wind' trace used to remove and vibration track noise. In order to give a good comparison with real gusts, turbulence intensity was in the order of Tu = 10%.

The results are too numerous to discuss in detail, however the side force and yawing moment coefficients obtained for a fastback vehicle shape entering a sharp edged cross-wind gust with relative yaw angle of $\psi = 30°$ are presented in figure 2.8. The side force shows a peak transient overshoot of about 15% of the steady yawed value, with this occurring 2 model lengths into the cross-wind gust. The yawing moment also exhibits a transient overshoot, with a peak overshoot of around 150% of the steady yawed value. Both coefficients subsequently decay, and are comparable with the steady yawed flow coefficients after 3 model lengths of cross-wind flow. The transient side force coefficient overshoot must be the result of transient flow effects in the development of the yawed flowfield, with these transient effects also affecting the yawing moment coefficient. Stewart [55] also investigated the effect of various aerodynamic add-on devices, finding that the magnitude of the transient force and moment overshoot was dependent on the geometry tested, however it was significant in all cases.

Macklin *et al* [36] used a similar facility to investigate the transient forces and moments on scale passenger cars, with each of the three generic configurations tested (notchback, squareback and fastback). The Reynolds number for the tests varied in the range $3.4 \times 10^5 \leq Re_l \leq 4.7 \times 10^5$. Comparisons of peak moving model and static model force and moment coefficients were made. These showed that for all three configurations, for all yaw angles greater than $\psi = 15^\circ$, the peak moving model yawing moment coefficients showed a significant overshoot of their static counterparts, however a yaw angle of $\psi = 40^\circ$ was required before any overshoot was observed in the transient side force coefficients. This suggests that for these geometries, under these flow conditions, transient flow effects were only present for yaw angles of $\psi > 40^\circ$.

More recently Chadwick *et al* [56], using the same facility as Macklin *et al* [36], investigated the transient surface pressures, and forces and moments on both square and radiused edged boxes. The models were approximate 1/10th scale. The sharp edged box experienced a transient yawing moment overshoot on entry to the gust (as expected), however no side force overshoot was observed. This can be contrasted to the radiused box, which experienced a transient yawing moment overshoot for $\psi > 10^\circ$ and a transient side force overshoot for $\psi > 25^\circ$. Again, the transient side force overshoot indicates the presence of transient flow development, that is not present for the square edged box, and only occurs for the radiused box at higher yaw angles.

A completely different approach to the dynamic-static technique was adopted by Garry and Cooper [57]. They compared the drag and yawing moment coefficients of a simple tractor-trailer assembly obtained from quasi-steady measurements at yaw to those obtained when rotating the model at yaw rates of up to $64^\circ s^{-1}$ in steady flow over a yaw angle range of $-40^\circ \leq \psi \leq 40^\circ$. Tare measurements were completed in a 'wind-off' situation, such that the dynamic and aerodynamic forces could be separated. They concluded that the magnitude of the drag and yawing moment were unaffected by the rotation, however the dynamic data was phase shifted. This technique provides interesting results, however has little relevance to the sharp edged gust entry, or any other flow situation, as when one end of the model moves away from the wind, the other moves towards it.

2.3.4 The Static-Dynamic Technique

Bearman and Mullarkey [58] used a pair of sinusoidially oscillating aerofoils placed upstream of a 1/8th scale generic passenger car to created flow oscillations in the working section that corresponded to gust angles of $\psi \cong \pm 8^\circ$. Aerodynamic admittances were calculated over a range of gust reduced frequencies and from these they concluded that quasi-steady measurements would safely predict transient forces and moments. It should be noted that the yaw angle of $\psi \cong \pm 8^\circ$ was relatively low and that this simulation is unlikely to represent the entry to a sharp edged gust discussed in the previous chapter.

A unique static-dynamic technique has been used at the University of Durham, where sharp edged, finite length cross-wind gusts were created by the transient interaction of two wind tunnel jets. This method was initially investigated by Scott [59], and then significantly developed by Docton [60, 61] and Docton and Dominy [62, 63]. Results for a simple one-box shape with well rounded corners, subjected to a cross-wind gust of three model lengths at a relative yaw angle of $\psi = 30^\circ$ and a Reynolds number of $Re_l = 3.3 \times 10^5$ indicated delayed leeward side pressure development on entry to the gust. This delayed pressure development, which again suggested the presence of transient flow effects, had a significant effect on both the transient side force and yawing moment coefficients. More detail about this facility is given in Chapter Three.

2.3.5 Advantages and Disadvantages of the Testing Techniques

By far the most promising scale model transient testing results have been obtained from the two fundamentally different dynamic-static track technique and the static-dynamic jet interaction technique. The relative advantages and disadvantages of these techniques are contrasted in table 2.2.

The most fundamental disadvantage of the track technique is vibration associated with model movement along the track. This has an obvious effect on direct force and moment measurements, and is usually removed by subtracting a 'wind-off' measurement from the 'wind-on' measurement. The practical Reynolds number limitation originates from the spatial requirement of the track. To increase Reynolds number either a higher model velocity or a larger model are required. A higher model velocity would require a longer track, (assuming the acceleration remains the same), as would a larger (and heavier) model travelling at the same velocity, (assuming the accelerating force remains the same). The model acceleration also complicates drag measurement, in that the drag component of any balance must by stiff enough to withstand the acceleration force and hence accuracy is compromised. This could be overcome by reducing the acceleration force, however to achieve the same Reynolds number (model velocity) for the same mass (scale) of model, a longer track would be required. The main advantages are the ability to test a range of yaw angles and the availability of ground boundary layer profiles.

The fixed wind tunnel configuration of the static-dynamic jet interaction technique produces cross-wind gusts with a fixed yaw angle. This yaw angle also has a practical minimum, however the yaw angles possible do lie within the range that can be considered as worst cases (section 3.2). The current generation of facility have inherent gust characteristic problems, (section 7.1), however the technique is still under development and it is likely that these will be eradicated. The main advantages lie in the conventional fixed instrumentation, the rapid gust production rate, and the flexibility of gust length. This type of facility also allows transient and steady data to be collected from the same configuration, removing any uncertainty about the validity of comparisons.

	Advantages	Disadvantages
Static-Dynamic Jet Interaction Technique (Stationary Model)	• High gust production rate (up to 1000/hr) • Conventional fixed instrumentation • Can be used with large scale models • Transient and time-averaged conditions can be tested in the same environment • Ability to generate gusts of any length	• Fixed yaw angle ($\psi > 20^o$) • Current generation has inherent gust profile problems
Dynamic-Static Track Technique (Moving Model)	• Can test a range of yaw angles • Correct ground simulation • Good replication of real gust situations • Ability to accurately simulate ground boundary layer profiles	• Inherent model vibration associated with the track signature • Unable to easily perform wake traverses • Practical upper limit on the achievable Reynolds number • Difficulty in directly measuring drag force

Table 2.2 Advantages and Disadvantages of Two of the Transient Cross-Wind Testing Techniques

2.3.6 Empirical and Theoretical Methods

White [64] recorded steady side force and yawing moment data for 144 cars in the MIRA full scale wind tunnel at a yaw angle of $\psi = 20^\circ$. From this he formulated a rating system that would allow the prediction of coefficients for new vehicles. The rating was based around ten categories of vehicle shape that were assessed on a present/absent basis and four categories of vehicle proportion. A linear regression was used that correlated the rating of a specific vehicle to a side force coefficient. Predictions were made for side force coefficients that were with 20% of those measured experimentally. The magnitude of this error is not surprising considering the complicated three dimensional nature of flow around a passenger car, that is not conducive to the simplifications made in this, or any other, empirically based method.

Tran [65, 66] developed an empirical method to predict transient forces on entry to a cross-wind gust from a number of steady flow waistline surface pressure measurements. He measured the differential pressures between pairs of tappings under steady homogeneous yawed flow in a wind tunnel, subsequently defining several pressure coefficient curves that allowed side force and yawing moment coefficients and incident flow velocity and angle to be related to the measured pressures around a vehicle. From the assumption that the coefficients measured in steady, homogeneous flow would also be valid for unsteady, inhomogeneous flow, he combined these coefficients with the transient surface pressures measured on entry to a sharp edged cross-wind region (using a full size vehicle and cross-wind generator) to calculate the transient side force and yawing moment coefficients. The results for a yaw angle of $\psi = 30^\circ$ showed no evidence of a side force overshoot, suggesting no transient flow mechanisms were present, however the familiar yawing moment peak, due to the motion into the gust, was seen at $x/l = 0.5$, where x represents the distance travelled into the gust and l the vehicle length.

Carr *et al* [67] developed an empirical method based on a detailed study of over 300 vehicle configuration. From these data they formulated relations between 61 dimensional parameters and the components of force and moment. The side force and yawing moment data was considered to be valid for the yaw angle range $-20^\circ \leq \psi \leq 20^\circ$, as the coefficients are generally linear within these limits. The method was subsequently validated for 15 full scale vehicles, however as with the empirical method of White [64], the predicted forces and moments did not correlate well with directly measured ones.

Hucho and Emmelmann [68] developed a theoretical prediction method for both steady and transient side force and yawing moment coefficients. A three-dimensional vehicle was represented by a two-dimensional projection of the side area of the vehicle. This projection was further split into vertical sections, with two-dimensional potential flow theory applied to solve for the flow around a plate of infinite width and height equal to the height of a particular vertical section, for a wind velocity equal to the normal component of the cross-wind. The pressure difference across a plate (corresponding to a single vertical section) was taken to be twice the pressure on the front face and by summing of the component sections over the side of the vehicle the side force and yawing moment were obtained. Ground simulation and vertical symmetry were obtained using a mirrored image below the ground plane, with a correction for the flow between the vehicle and ground applied later. Time dependant solutions, obtained by using a time dependant normal component of cross-wind, also provided transient side force and yawing moment coefficients on entry to a sharp edged gust. Calculations conducted for a medium sized passenger car entering such a gust, with a relative yaw angle of $\psi = 30^\circ$, showed that both the side force and yawing moment exhibit significant overshoots on entry to the gust. The magnitudes of the overshoot were seen to decrease for gusts with shallower gust entry profiles, an effect also observed by Stewart [55].

2.4 Computational Fluid Dynamics

No literature review pertinent to vehicle aerodynamics would be complete without reference to some of the computational fluid dynamics (CFD) investigations undertaken. CFD has significant advantages for automotive engineering in that the artificial environment it creates makes the modelling of precise boundary conditions, that can be difficult to achieve experimentally, easier. For example, no difficulty would be envisaged in modelling a skewed velocity profile with the correct turbulence quantities and lengthscales. Other advantages are that unrealistic model mounting facilities are not introduced, for example a wind tunnel model is usually mounted on a sting with the affect this sting has on the flowfield potentially significant. Full scale Reynolds number simulations are also possible. Potentially the most fundamental advantage is that CFD can provide much more information about the flowfield than experimental measurements.

CFD is frequently criticised for not being able to accurately predict absolute magnitudes for the standard coefficients used in the automotive industry. The numerical solutions are sensitive to mesh density, choice of differencing scheme and in particular turbulence model. Perzon *et al* [69] presented CFD drag coefficient (Cx) values for a bluff body, obtained using two different commercial codes (StarCD and Fluent UNS), for a variety of differencing schemes, mesh densities and turbulence models. Their results exhibited a range of $-0.039 \le \Delta Cx \le 0.243$, where ΔCx is defined as the difference between the experimentally and computationally obtained drag coefficients. Axelsson *et al* [70] presented drag coefficients for the generic Volvo EEC concept car. They used the CFX-4 flow solver to investigate the effect of turbulence model. The drag coefficients obtained varied in the range $0.088 \le Cx \le 0.141$, which can be compared to the experimentally obtained value of $Cx = 0.141$.

Gaylard *et al* [71] presented data for two generic vehicle shapes obtained from calculations using StarCD. Comparisons of CFD and experimentally obtained (FSWT) drag and lift coefficients are shown in table 2.3. As can be seen from table 2.3, drag was relatively well predicted, whereas lift was not, an effect they attributed to a fortuitous balancing out of errors for the drag coefficient. They had more success in predicting the trends in both drag and lift for a series of parametric changes. Table 2.4 compares the CFD and FSWT drag and lift coefficients for a notchback vehicle undergoing such a series of changes. As for the baseline cases, drag is in relative agreement (within 6.3%), whereas the absolute differences for lift are substantial, however the trends in both forces as a result of the configuration changes are correctly predicted.

	Drag Coefficient (Cx)		Lift Coefficient (Cz)	
	CFD	FSWT	CFD	FSWT
Notchback	0.271	0.267±0.002	-0.317	-0.081±0.005
Fastback	0.210	0.206±0.002	-0.328	-0.066±0.005

Table 2.3 CFD and Experimental Lift and Drag Coefficients

(from Gaylard *et al* [71])

	Drag Coefficient (Cx)		Lift Coefficient (Cz)	
	CFD	FSWT	CFD	FSWT
Baseline Notchback	0.271	0.267	-0.317	-0.081
Configuration 2	0.297	0.317	-0.447	-0.237
Configuration 3	0.297	0.303	-0.415	-0.200
Configuration 4	0.291	0.299	-0.320	-0.320

Table 2.4 CFD and Experimental Trends in Lift and Drag Coefficients

(from Gaylard *et al* [71])

Okumura and Kuriyama [72] calculated the side force and yawing moment coefficients, using the commercially available Navier Stokes solver SCRYU, for a two-box type vehicle under steady yawed flow conditions for the range of yaw angles $0^\circ \leq \psi \leq 45^\circ$. As they rightly highlight, using CFD to simulate flow under yawed conditions requires significantly more CPU time as the axial symmetry of the geometry cannot be exploited. Their pre-processor allowed CAD data to be directly converted into a structured computational grid which contained 1×10^5 mesh elements. The direct conversion of CAD data allowed significant fine detail resolution. The calculation time was 30 hours using a single processor CRAY Y-MP. A Reynolds number of $Re = 2 \times 10^6$ based on model height was used, with a k-ε turbulence model and wall functions. The intrinsically unsteady nature of the flow at yaw made it necessary to use an unsteady solver. The computations yielded yawing moment coefficients that matched the experimental values to within 3%.

They further investigated the aerodynamic characteristics of a one-box (van) type vehicle under steady yawed flow conditions. This was done to assess the reduction in yawing moment possible from the use of an 'aero-kick' bumper. This bumper was designed to provoke front leeward side flow separation at low yaw angles, therefore reducing yawing moment. The computational results predicted a 26% reduction in yawing moment compared to a 35% reduction from the experiments. These results are significantly different, and it should be noted that for the standard model (non aero-kick bumper) there was a 25% discrepancy between experimental and computational yawing moment. This discrepancy is significantly larger than that of the two-box vehicle, highlighting the somewhat fickle nature of CFD. Okumura and Kuriyama [72] attributed the large errors of the one-box vehicle to the asymmetric separated region under yawed flow and that the nominal freestream direction is diagonally across the cells, although this condition would also be present for the two box vehicle. Remeshing the geometry would permit alignment of the nominal freestream and cell directions, although this would be time and resource consuming should it be necessary for all changes in incident flow angle and clearly cannot easily be applied to transient investigations.

Docton [61] used the commercially available PHOENICS code to model the jet interaction technique of transient cross-wind gust generation. He investigated the flow around a two dimensional square edged geometry. The results showed that a cross-wind gust of up to 7 model lengths was required for the transient forces and moments to develop such that they were comparable with the steady yawed coefficients. This was attributed to delayed flow development on the leeward side. Figure 2.9 presents velocity vectors for the transient flow from the Docton calculation, clearly showing the delayed leeward side flow development.

Okumura and Kuriyama [73] later presented the transient force and moment coefficients for an one-box type vehicle entering a sharp edged cross-wind gust with a relative yaw angle of $\psi = 25^\circ$. The computational grid contained 2.5×10^5 mesh elements, with a calculation time of 100 hours on a SGI Indigo 2. The vehicle entering the cross-wind region was facilitated by the use of a sliding mesh and time dependent mesh elements. The transient yawing moment coefficient exhibited a 20% overshoot of the steady yawed value when the leading edge of the vehicle was 1.4 body lengths into the gust ($x/l = 1.4$), with the side force coefficient showing a small overshoot at $x/l = 2.0$. These results compare well with those obtained experimentally at full scale by Kobayashi and Yamada [38] for an identical vehicle, although it should be noted that the yaw angle for the computational simulation is slightly lower than that of the experiments. Figure 2.10 shows isoplethic surfaces for the vehicle on entry to the gust. The two defined contour levels are set at $Cp_s = 0.8$ and $Cp_s = -1.5$. The first plot (a) is taken at $x/l = 0.0$, i.e. axial flow conditions, where the stagnation region lies on the front of the vehicle, with flow acceleration around the front corners producing two front corner suction regions (one either side of the vehicle). The second plot (b) is at $x/l = 1.4$, the point of maximum yawing moment, where the stagnation region has moved to the windward front corner and there is a significant increase in size of the leeward side suction region. It is the combination of these two effects that is responsible for the large yawing moment overshoot. By the third plot (c) at $x/l = 4.0$, the leeward side suction region has reduced in size, with a corresponding reduction in yawing moment. This is an excellent example of the type of flow visualisation that would be very difficult to achieve with only experimental data.

This brief presentation of CFD results shows that although there is great potential for detailed, accurate, investigations, there is still a considerable need to validate results, limiting the usefulness of CFD as a predictive tool. Baxendale *et al* [74] commented that CFD should not be used for external flows around vehicles without correlation to experimental data, which is clearly the case.

2.5 Importance of Experimental Technique

There are several areas of experimental technique pertaining to ground vehicle testing that are of fundamental importance and have been the subject of many investigations, some of which are reviewed here.

2.5.1 Ground Simulation

Various methods of ground simulation are depicted in figure 2.11, the most common and simplest of these being 2.11a, where the model is directly mounted onto a fixed ground board. This configuration has several drawbacks; firstly the incident airflow has a boundary layer and hence vertical velocity gradient, (this would not exist for a moving vehicle in statistically stationary air), secondly the relative motion between the ground and the vehicle is not modelled and finally the presence and growth of the boundary layer induces a vertical velocity component on the incident flow, which again would not be experienced in a true vehicle environment.

These effects can considerably affect the flow around a vehicle; Baker and Brockie [75] found that using a fixed groundboard underpredicted values of drag coefficient for a range of scale train models. They attributed this to boundary layer effects reducing the average velocity of the flow around the model. Fago *et al* [76] compared drag and lift coefficients for a bluff body with rounded corners, measured using a fixed ground and moving ground condition. They found the drag was significantly lower for the moving ground condition, an affect they attributed to a change in wake structure. As expected, the influence of the ground condition was significantly reduced by increasing the spacing between the model and the ground. Lajos and Hegel [77] observed lateral outflow from the sides of the underbody gap for a 1/5th scale model bus with detailed underbody while using a fixed ground board. The outflow was significantly reduced when a moving ground was adopted. Hackett *et al* [78] observed similar outflow for a 15% scale Ford Cougar with detailed underbody. Wake traverses were conducted with both fixed and moving ground; the fixed ground condition revealed the presence of two side lobes at ground level, with associated total pressure deficit that were not present for the moving ground condition. Howell [79] and Howell and Goodwin [80] commented that although correct ground simulation changes the absolute values of drag and lift, the trends are the same and therefore it is reasonable to use a fixed ground condition in the early development of a passenger car, where comparative testing is more important than absolute magnitudes.

Figures 2.10b to j show several methods that have been used to improve the ground simulation. Methods d-j are only concerned with the removal of the ground boundary layer or the effects thereof, but are simpler to implement than the more realistic moving ground method, c, which not only removes the boundary layer but also simulates the motion between the vehicle and road. One of the main difficulties associated with a moving ground is mounting of the model, as it cannot be supported from below. Generally a sting is used that supports the model from either behind or above, however this can have significant influence on the flow in the backlight region, which is potentially very sensitive to external disturbances. If force measurements are required, it is also necessary to isolate the forces transmitted to the wheels by the road from the measured forces.

A rather unique method of ground simulation was adopted by Papenfuss [81]. He used the track moving model technique, normally reserved for cross-wind simulations, to produce what would be a perfect representation of a vehicle in motion. Moving model techniques however have several disadvantages, as detailed in table 2.2.

The simulation of the correct ground boundary layer profile is significantly harder for a vehicle subjected to cross-wind conditions. Considering a vehicle in an area of perpendicular cross-wind, the cross-wind flow is moving relative to the ground and has a vertical velocity gradient, whereas the relative forward movement between the vehicle and the air has no such gradient. Figure 2.12 depicts two possible boundary layer profiles for simulated cross-wind conditions. If the boundary layer is removed, the profile on the left is achieved, however it can be seen that this is significantly different to the natural boundary layer profile, as seen on the right. For this profile, both yaw angle and resultant velocity vary with height. The only cross-wind method that currently can correctly represent this boundary layer profile is the dynamic-static track technique.

2.5.2 Reynolds Number

The Reynolds number, based on vehicle length, is given by equation 2.1 where ρ is fluid density, u is fluid velocity, l is the vehicle length and μ is the fluid dynamic viscosity.

$$\mathrm{Re}_l = \frac{\rho u l}{\mu} \qquad (2.1)$$

For an average sized passenger car of length 4.0m, travelling at 80km/h, the Reynolds number under standard atmospheric conditions is $Re_l = 5.8 \times 10^6$. Ideally this should be replicated in wind tunnel tests, however the use of small scale models makes this difficult. For a 1/8th scale model this would require a wind tunnel velocity of $178ms^{-1}$, which in addition to requiring a powerful fan motor, would clearly introduce significant compressibility effects. It is common practice to use a significantly lower Reynolds number, however this should be sufficiently high that the flow structures are correct and hence the flow is effectively Reynolds number independent.

Cooper [44] investigated the effects of Reynolds number on the drag of simple box like shapes with radiused corners for a range of $1.6 \leq Re_A \leq 2.6 \times 10^6$, where Reynolds number was based on the square root of base area. He found a significant decrease in drag at $Re_A = 5 \times 10^5$, this being the critical Reynolds number at which transition of the boundary layer to turbulent and hence delayed separation occurred. The critical Reynolds number increased as yaw angle increased for the tested range of $0° \leq \Psi \leq 15°$. Cooper [44] concluded that a minimum test Reynolds number of $Re_A = 2 \times 10^6$ should be used. Interestingly, taking a typical passenger car frontal area of $1.97m^2$ [1] and converting Cooper's minimum test Reynolds number to one based on a vehicle length of 4.0m, yields $Re_l = 5.7 \times 10^6$, which is only marginally below a typical full scale Reynolds number ($Re_l = 5.8 \times 10^6$).

Barth [82] investigated the effect of Reynolds number on the surface static pressure distribution of a two dimensional body with rounded corners, where the ratio of radius of curvature to body length was $r/l = 0.1$. He used a low turbulence wind tunnel and investigated a range of yaw angles from $0° \leq \psi \leq 20°$. The results showed that increasing the Reynolds number from $Re_l = 4.6 \times 10^5$ to $Re_l = 10.3 \times 10^5$ prevented front leeward corner separation, even at 20° yaw, and in this instance he recorded a suction peak in the order of $Cp_s = -2.4$.

Baker and Humphreys [83] presented a series of results obtained for an articulated lorry over a range of Reynolds numbers from $4.4 \times 10^4 \leq Re_l \leq 3.0 \times 10^5$ and turbulence simulations at a range of yaw angles. The side force coefficients showed remarkable agreement over the range of Reynolds number of turbulence intensity for all yaw angles, however the lift coefficients exhibited significant differences for yaw angles of $\Psi > 30^\circ$. The model used for this investigation had sharp edges and therefore was likely to exhibit low Reynolds number sensitivity.

It may be concluded from these investigations that Reynolds number sensitivity is very dependant on geometry and test environment, and therefore it is advisable to conduct sensitivity tests prior to any wind tunnel program. It is most likely that geometries that have relatively large radii corners will be more sensitive to Reynolds number than those with sharp corners, and that for these geometries the Reynolds number required for independence will be significantly higher.

2.5.3 Turbulence Intensity

Assuming that no attempt is being made to model atmospheric turbulence intensities and lengthscales, the wind tunnel turbulence intensity used can have a significant effect on the results. For isotropic turbulence, the turbulence intensity, Tu, is defined in equation 2.2 [84], where u' are the streamwise velocity fluctuations and $\bar{u}$ the mean streamwise velocity.

$$\mathrm{Tu} = \frac{\sqrt{\overline{u'^2}}}{\bar{u}} \qquad (2.2)$$

Bearman and Morel [85] described the presence of freestream turbulence as potentially having three effects on a flowfield: accelerated transition to turbulence in shear layers, enhanced mixing and entrainment, and distortion of free stream turbulence itself by the mean flow. Accelerated transition to turbulence can be expected to have a significant impact on the location of separation and reattachment points. Enhanced mixing and entrainment can be expected, for example, to alter the base pressure in the wake region of a bluff body, and thus affect its drag. Distortion of freestream turbulence by the presence of a bluff body, for example the constraint that there can be no normal turbulent component adjacent to a surface, will mean that the turbulent structure in a boundary or shear layer may be significantly different from that of the free stream.

Hegel and Bearman [86] investigated the effect of free stream turbulence on the force coefficients of a bluff body with rounded front corners for turbulence levels of $0.15\% \leq Tu \leq 10.5\%$. They found that the effects were complex, with the magnitude and direction of any change in drag dependant on the size of the corner radii, but no systematic trend was apparent.

Results presented by Macklin *et al* [87] for the mean force and moment coefficients measured on a 1/5 scale passenger car using the dynamic-static track technique for a range of turbulence intensities ($1.0\% < Tu < 3.4\%$) indicate that the turbulence intensity within this range had little effect on the magnitude of the coefficients.

Wiedemann and Ewald [88] described a method to increase the effective Reynolds number by the introduction of turbulence. Using two different turbulence grids that generated turbulence intensities of $Tu = 2.2\%$ and $Tu = 2.8\%$ they raised the effective Reynolds number by a factor of 2. This method has limitations in that there is a practical limit on the level of freestream turbulence that can be generated, (> 5% difficult), and it decays rapidly.

Bearman [89] commented that generalising about the effects of freestream turbulence is unwise, as clearly seems to be the case. He cited results that show a reduction in drag with increasing turbulence for a circular cylinder, and contrasts these to his own [90], that showed an increase in drag with turbulence for square plates and circular discs mounted normal to the flow. The main geometrical difference accounting for these opposing results was the fixed separation points of the plates and discs.

Notchback

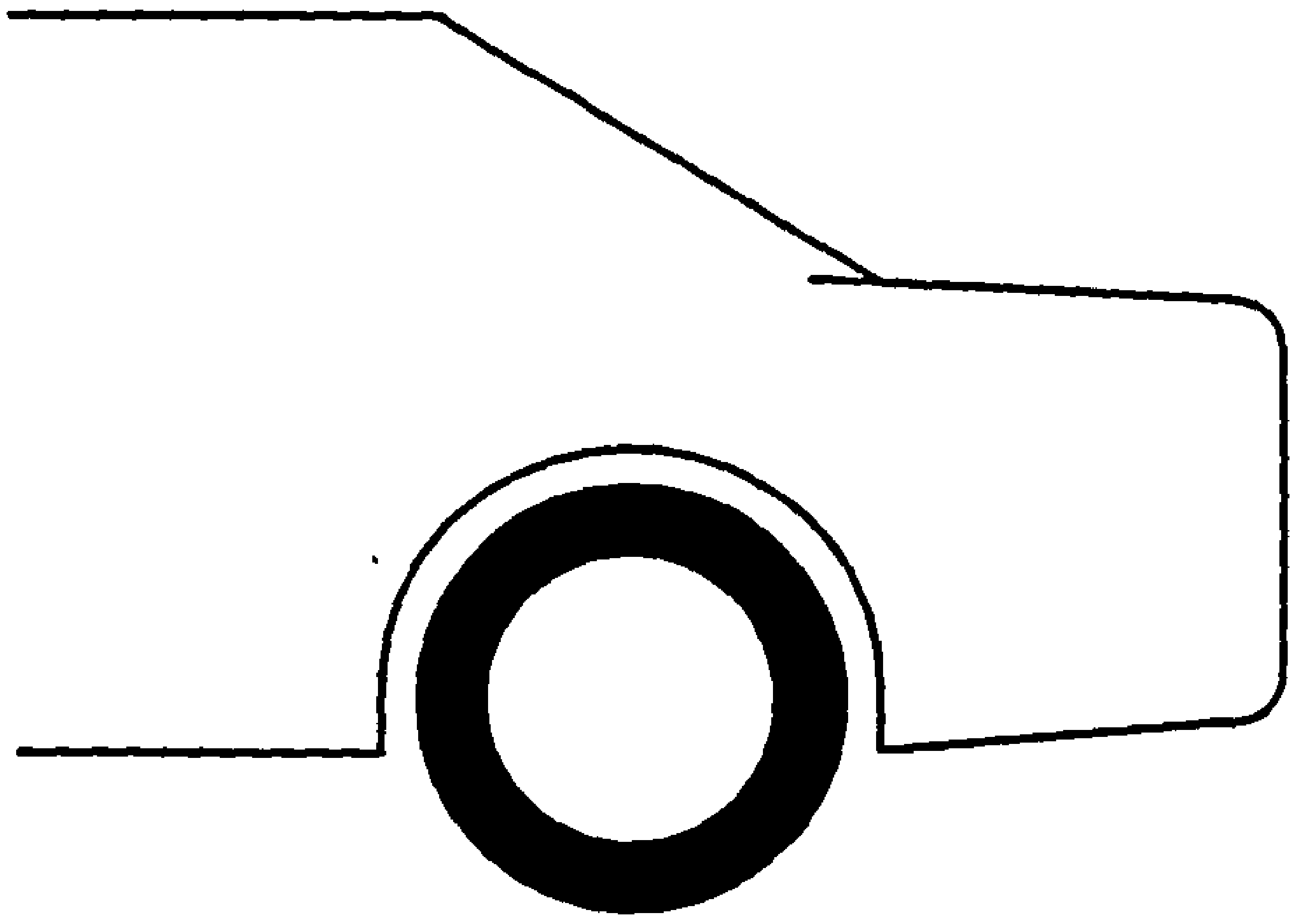

Fastback

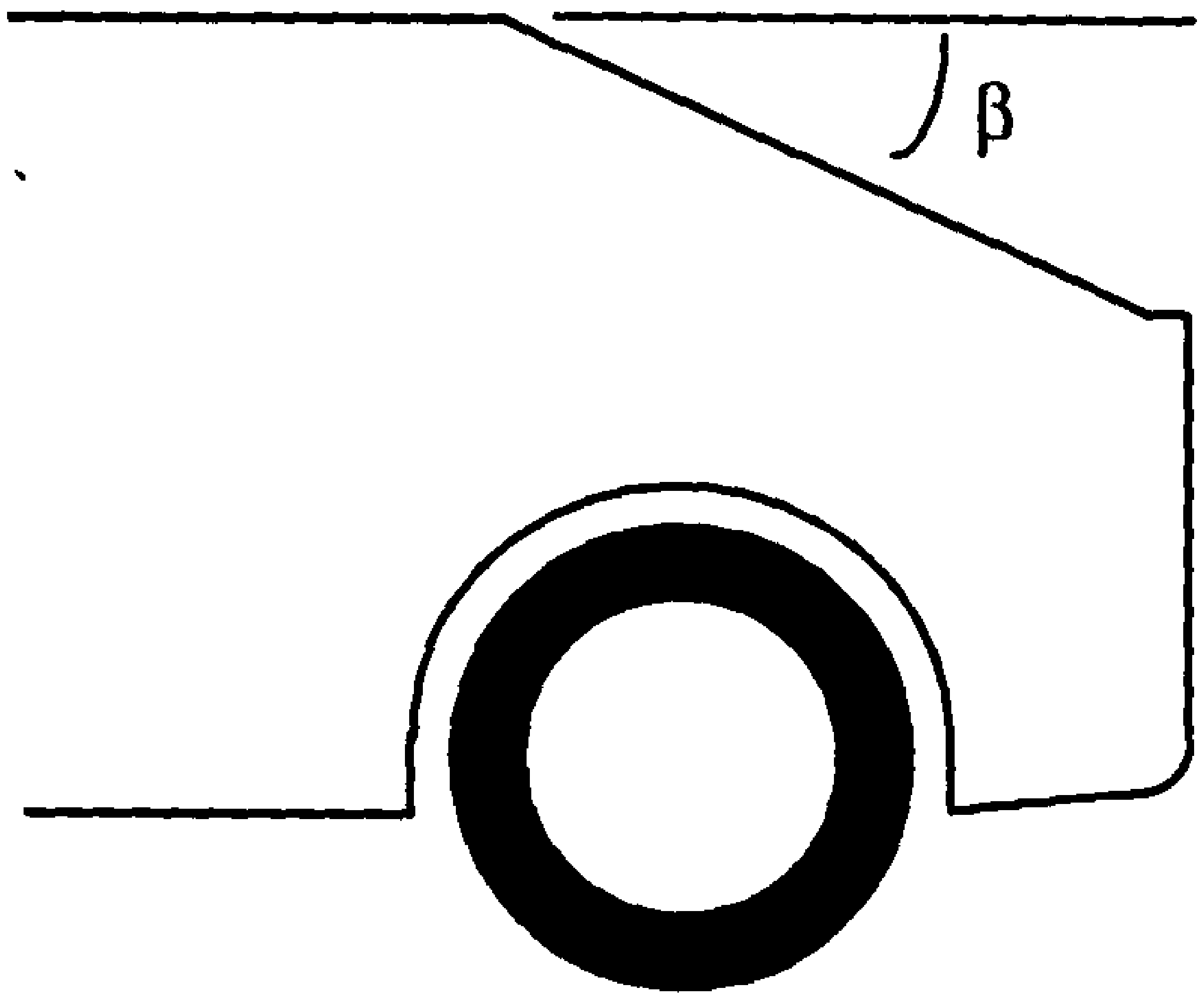

Squareback

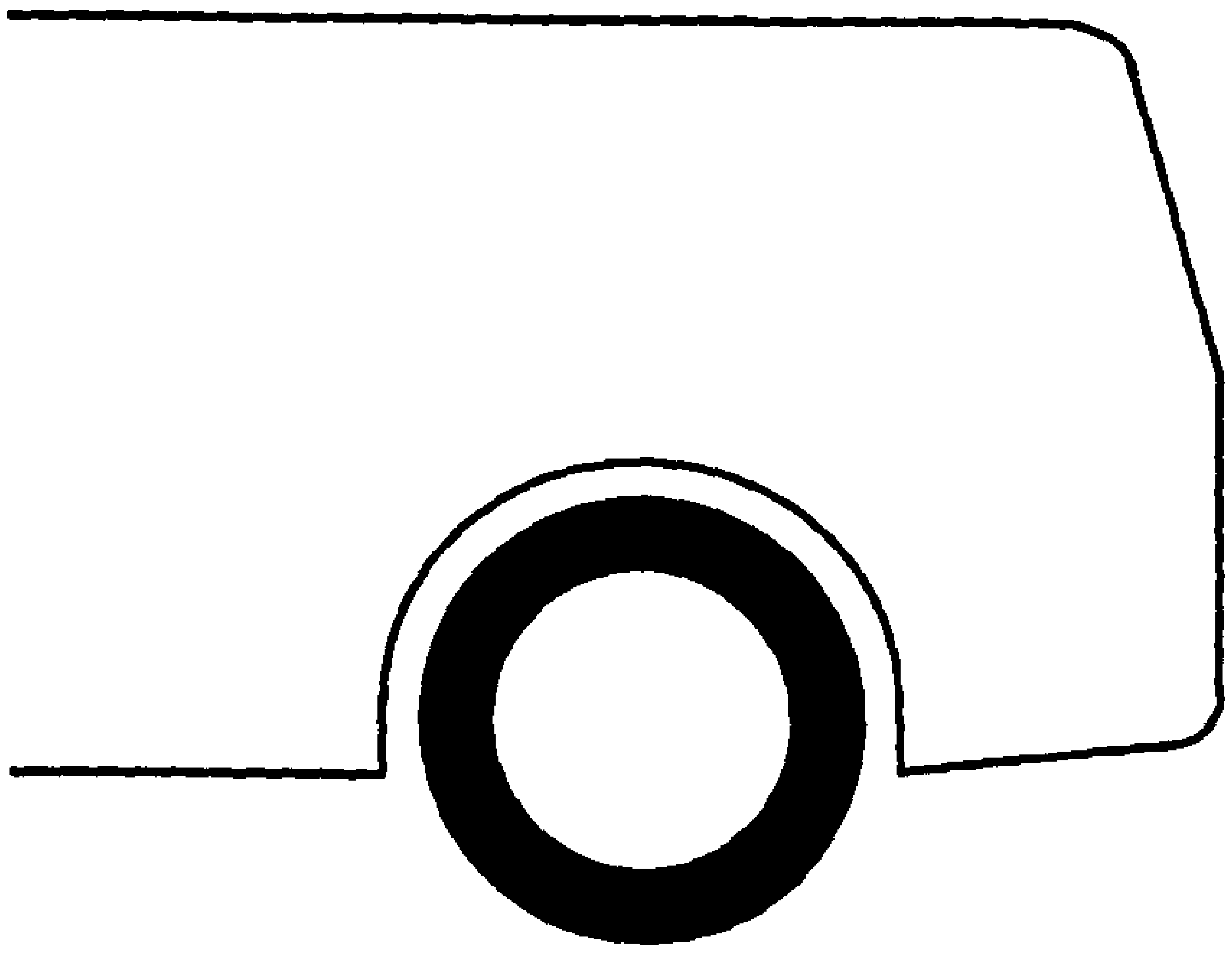

Figure 2.1 Passenger Car Rear End Shapes

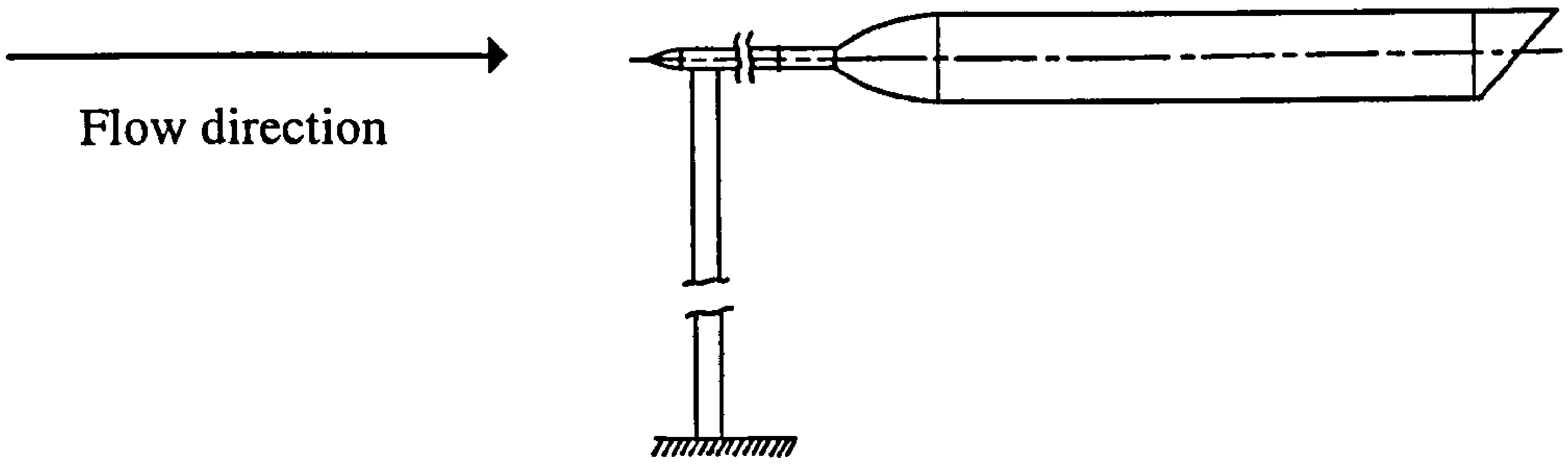

Figure 2.2 Morel's Truncated Cylinder (from Morel [22])

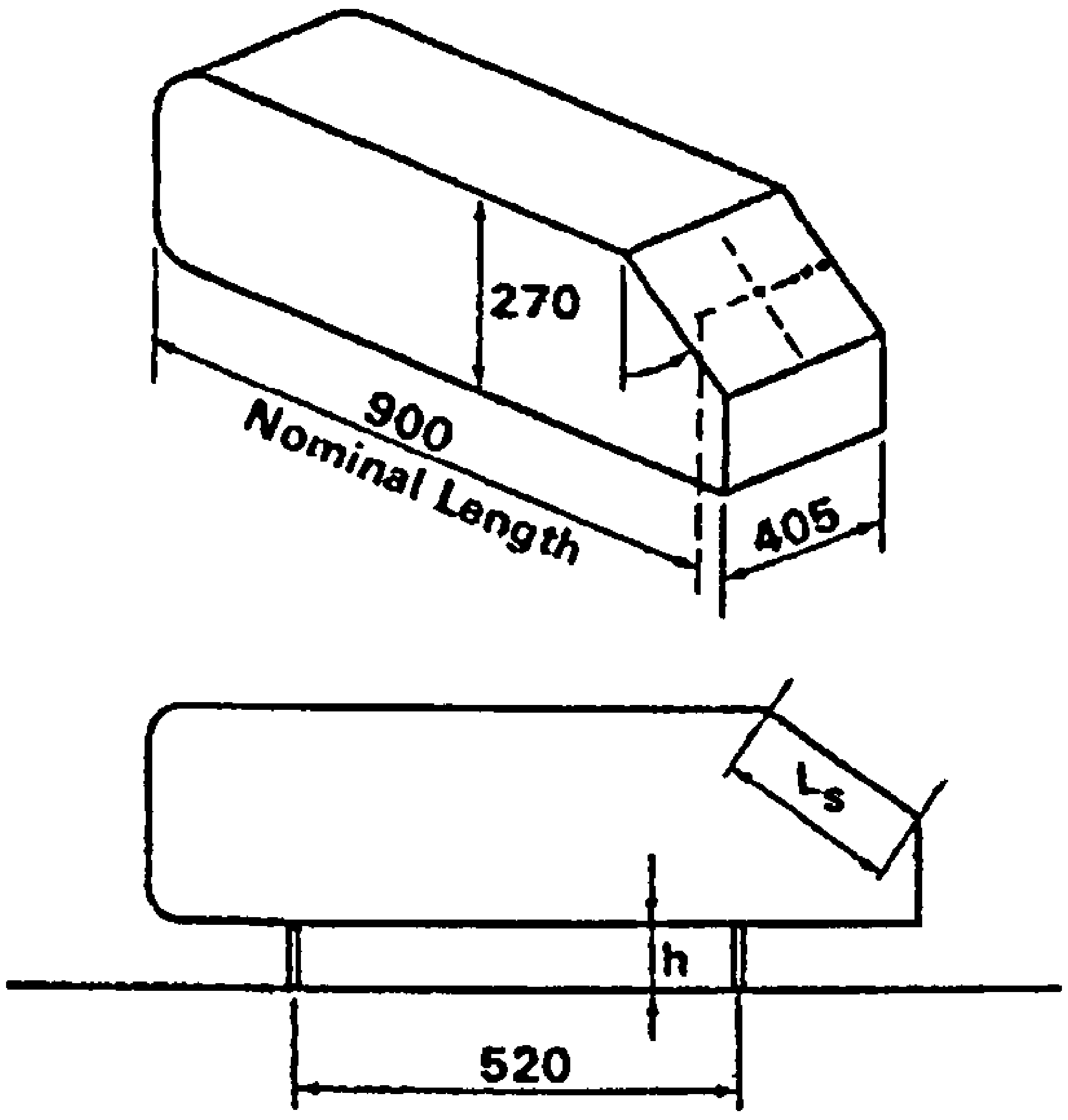

Figure 2.3 The Morel Geometry (from Morel [22])

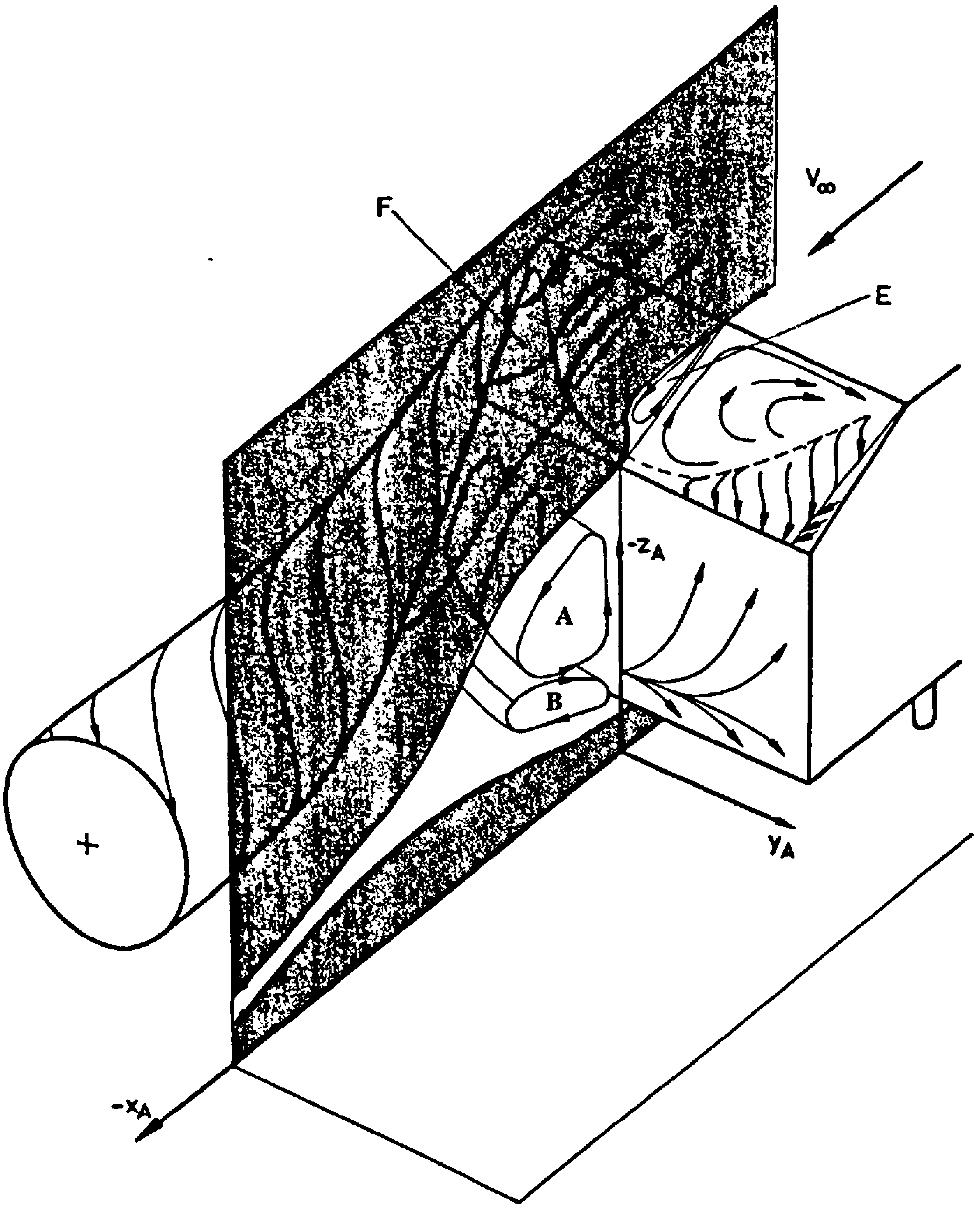

Figure 2.4 Attached Flow Over the Ahmed Geometry Backlight
(from Ahmed *et al* [2])

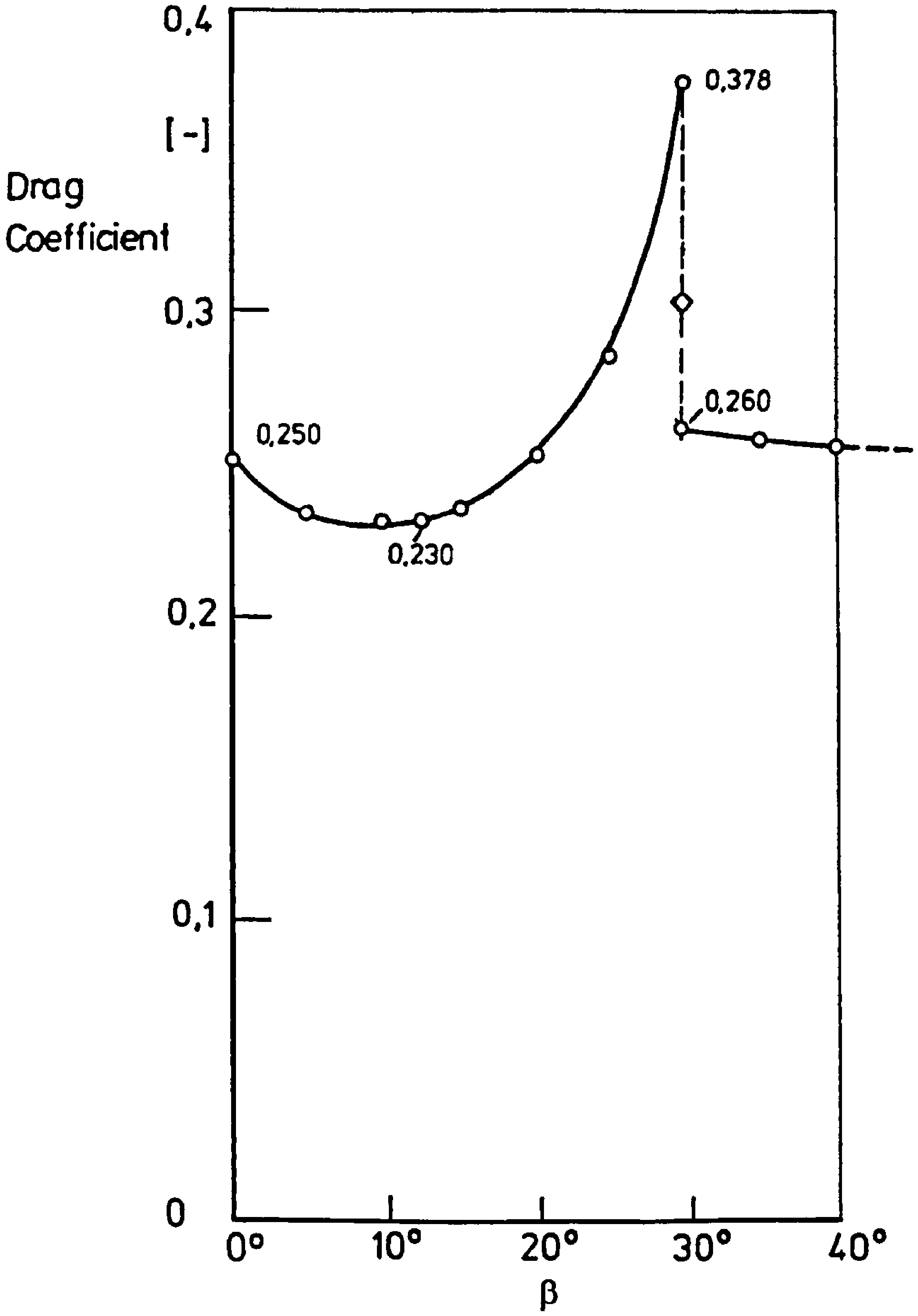

Figure 2.5 Variation of Drag Coefficient with Backlight Angle for the Ahmed Geometry (from Ahmed *et al* [2])

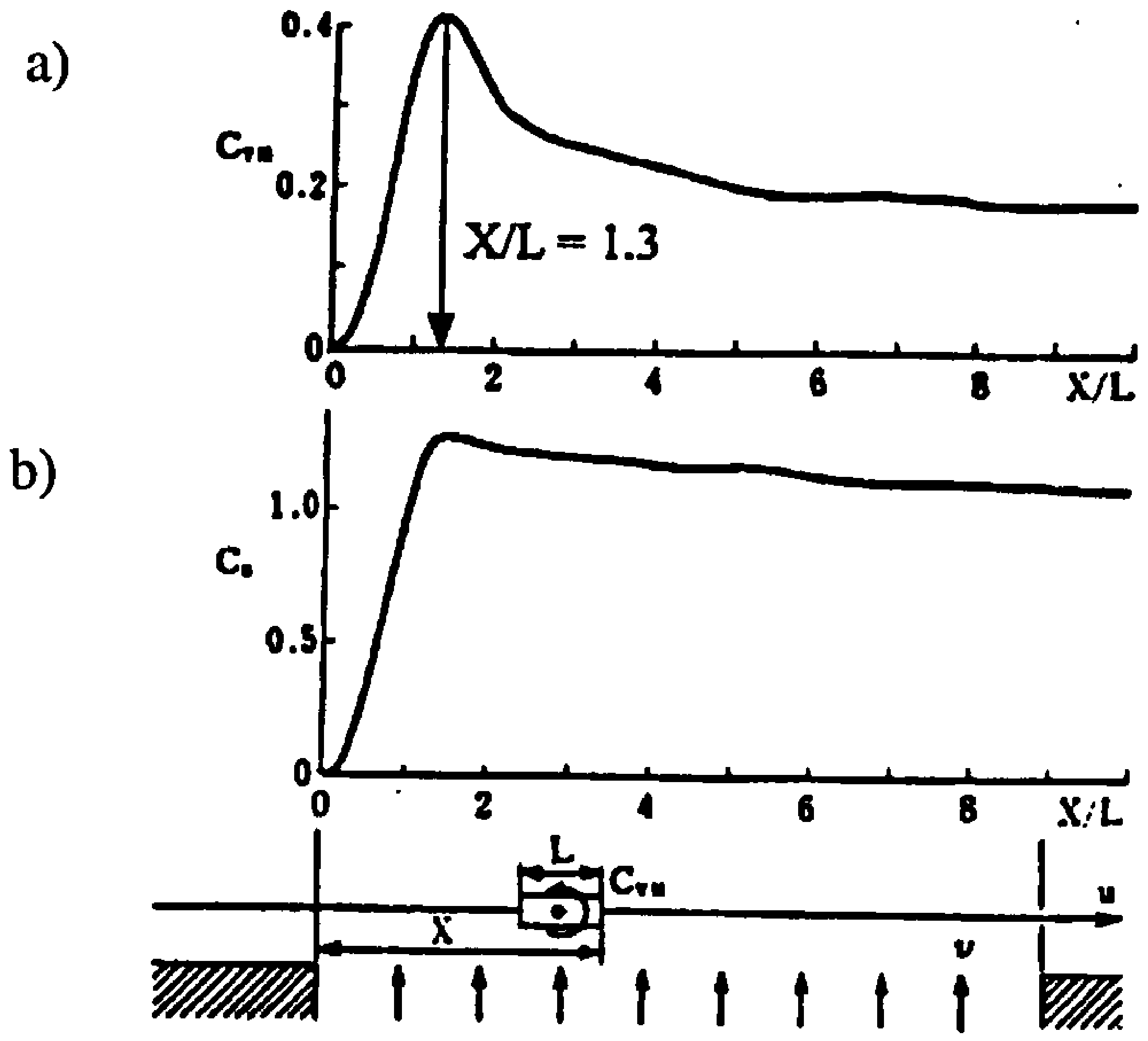

Figure 2.6 Transient (a) Yawing Moment and (b) Side Force Coefficients (from Kobayashi & Yamada [37])

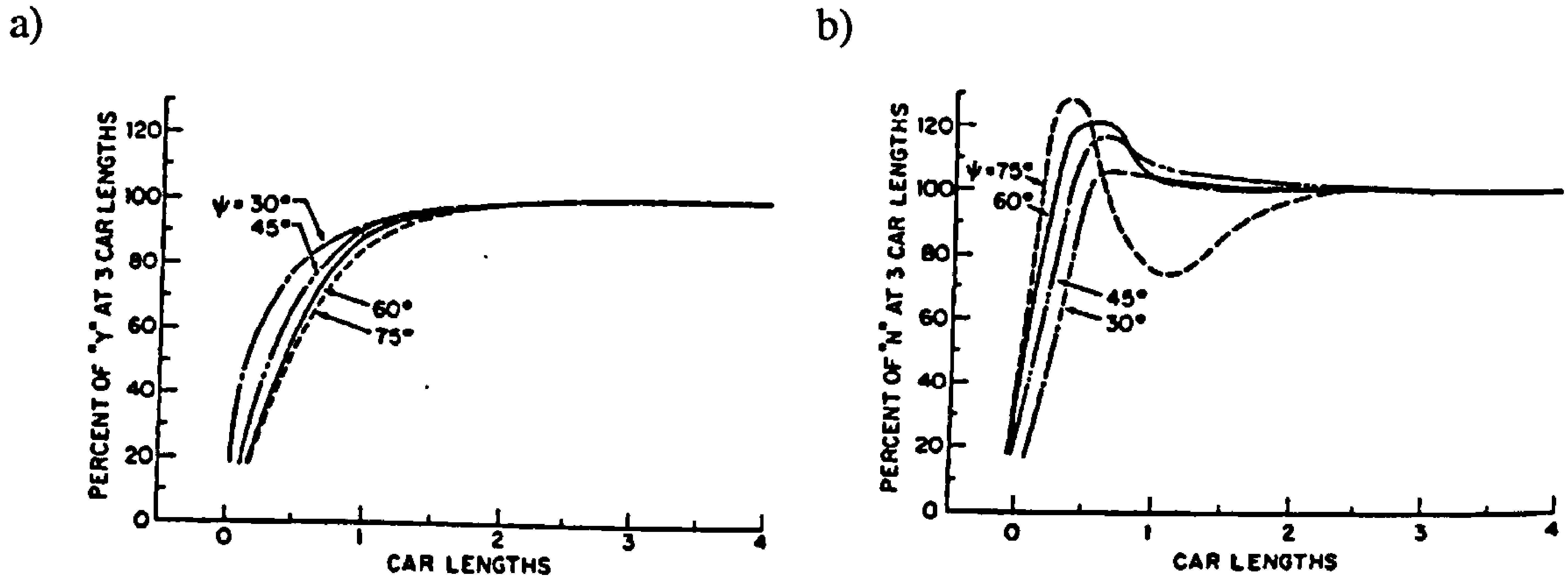

Figure 2.7 Transient (a) Side Force and (b) Yawing Moment Coefficients for a Notchback Vehicle Entering into a Sharp Edged Gust (from Beauvais [54])

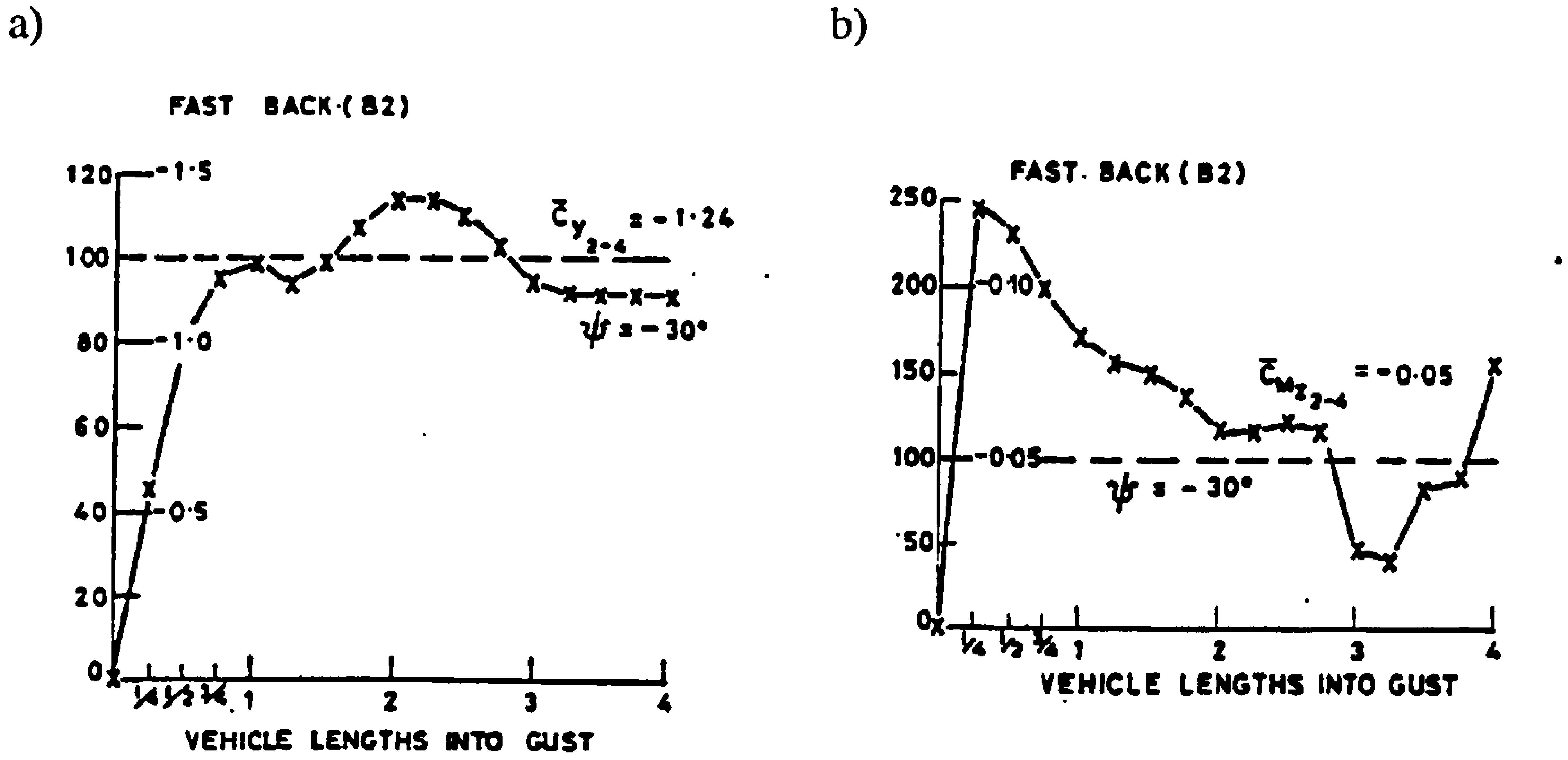

Figure 2.8 Transient (a) Side Force and (b) Yawing Moment Coefficients for a Fastback Vehicle Entering into a Sharp Edged Gust (from Stewart [55])

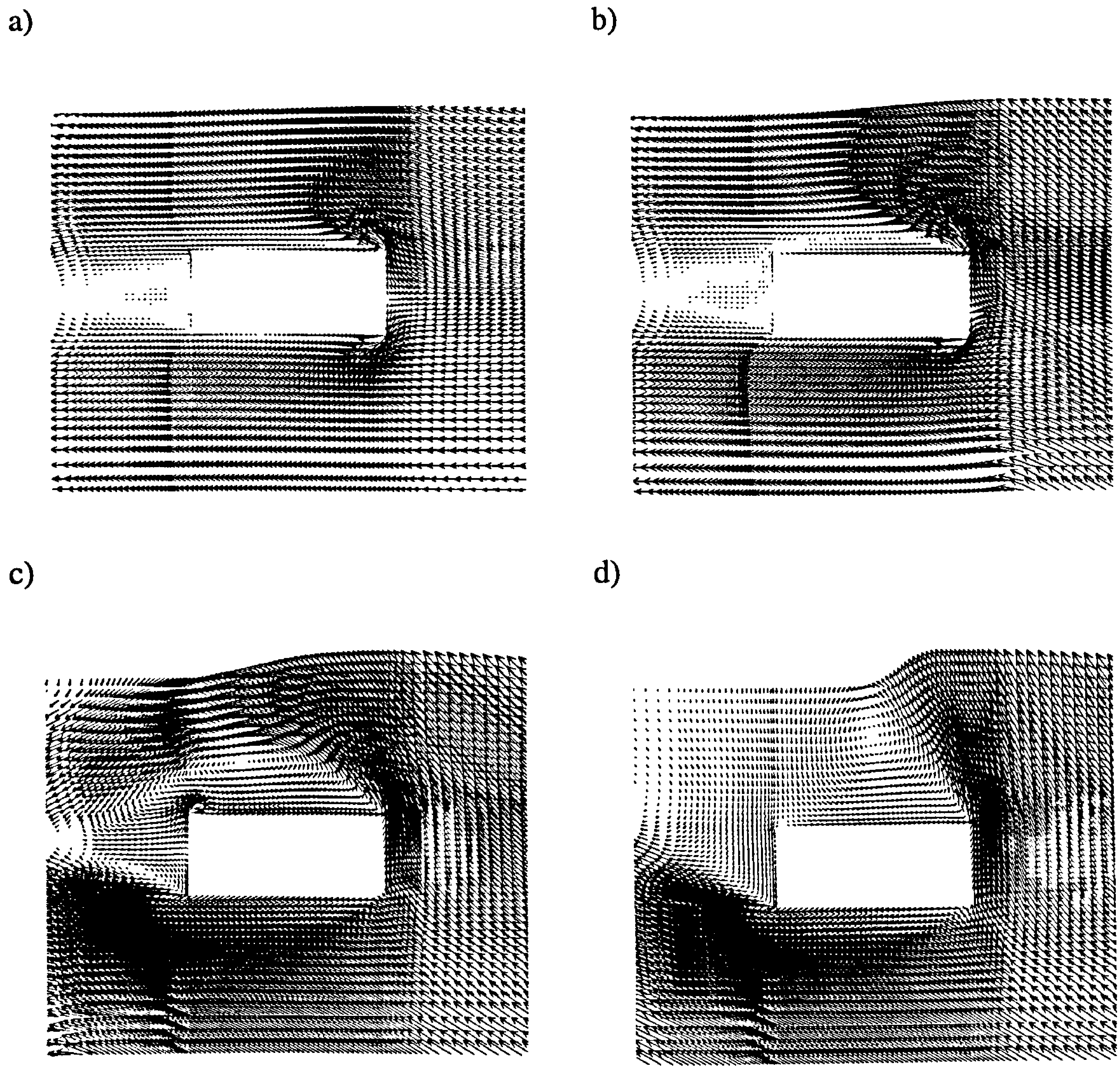

Figure 2.9 Transient CFD Velocity Vectors (from Docton [61])

a) Axial Flow

b) Gust Leading Edge at Model Leading Edge

c) Gust Leading Edge Downstream of Model Trailing Edge

d) Fully Developed Yawed Flow

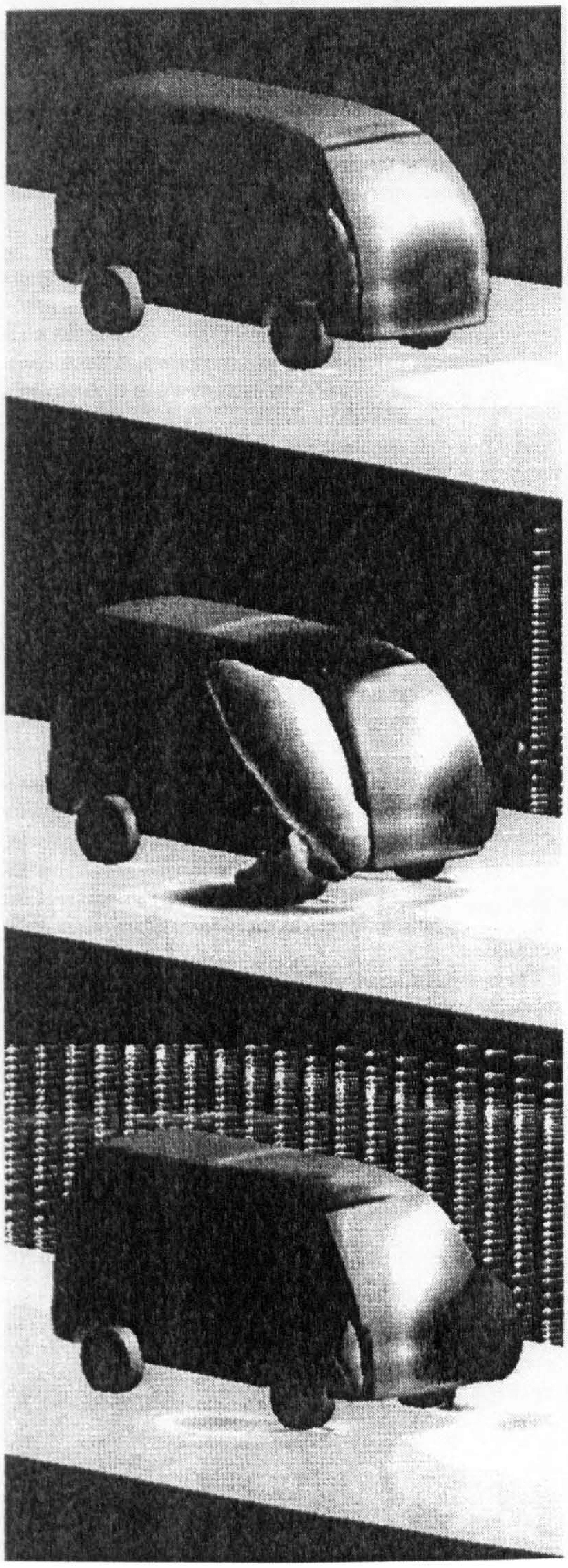

a) x/l = 0.0

b) x/l = 1.4

c) x/l = 4.0

Figure 2.10 Isoplethic Surfaces for Entry into a Sharp Edged Gust (from Okumura and Kuriyama [73])

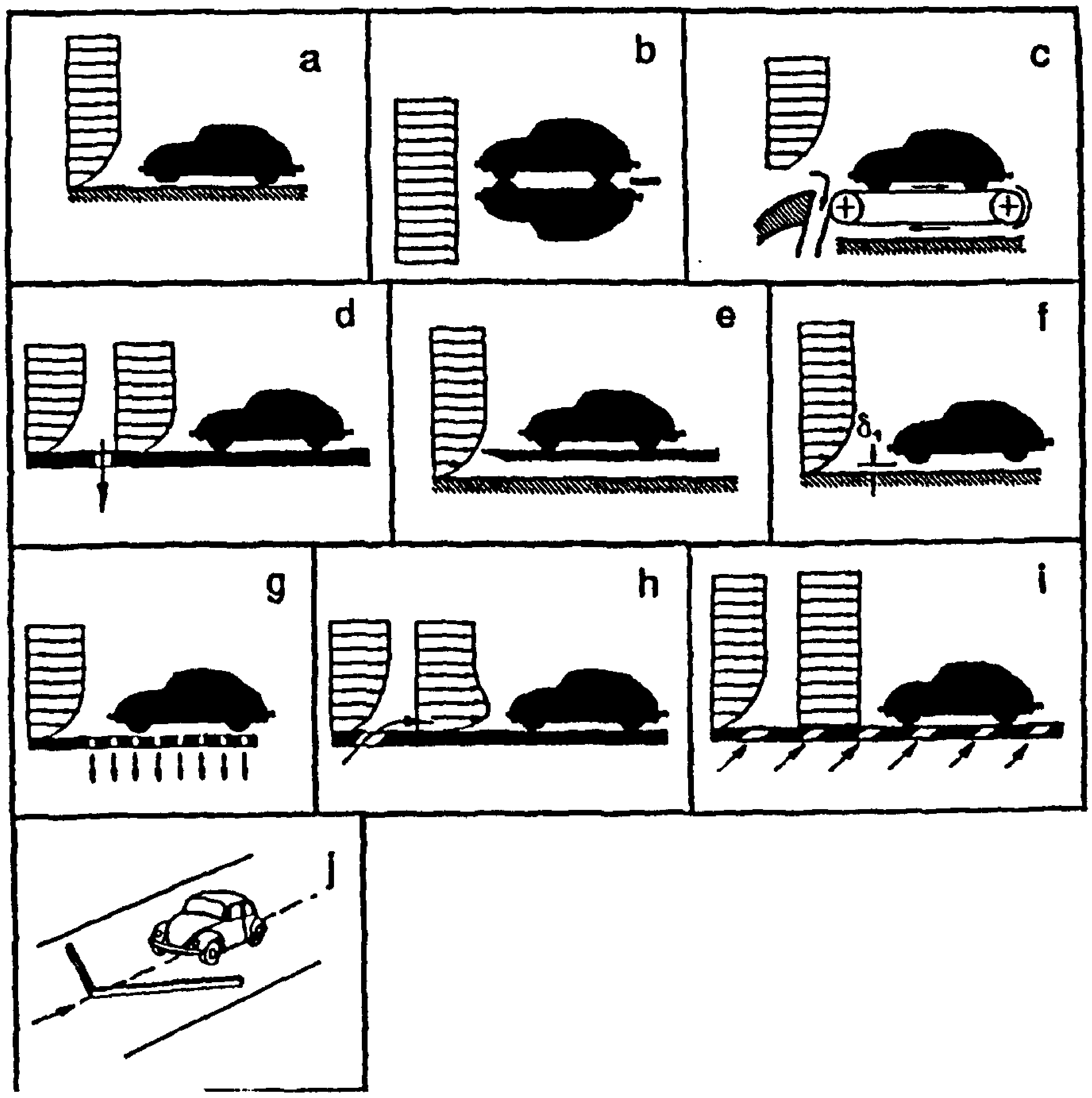

Figure 2.11 Ground Simulation Techniques (from Hucho [6])

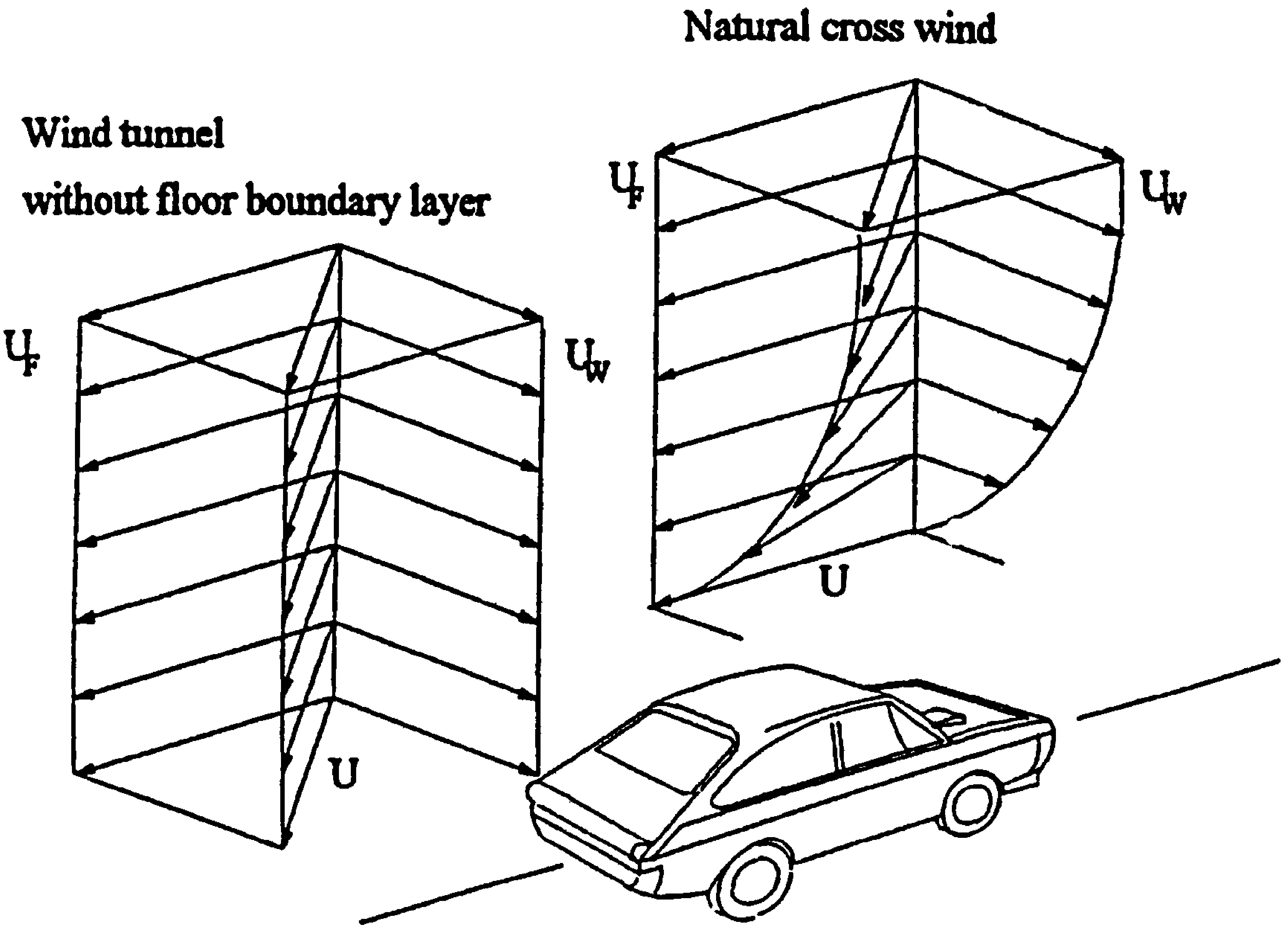

Figure 2.12 Possible Cross-Wind Boundary Layer Profiles (from Macklin *et al* [36])

Chapter Three

The Static-Dynamic Jet Interaction Technique

3.1 Theoretical Operation

The objective of the static-dynamic jet-interaction technique was to produce repeatable, sharp edged, finite length cross-wind gusts with as conventional a wind tunnel configuration as possible. This cross-wind gust characteristic was chosen as it is generally considered to be a worst case scenario (section 1.2). The advantage of using a relatively conventional wind tunnel configuration is that it permits the use of already well developed test techniques and instrumentation.

The cross-wind gust is generated by the introduction of additional fluid, from a second wind tunnel, into the working section of a conventional open working section wind tunnel. The development of the gust profile is carefully controlled by manipulation of the boundary conditions at the exit of this second tunnel. A schematic plan of the required wind tunnel configuration is shown in figure 3.1. The exit plane of the cross-wind tunnel is nominally blocked, thus the model is subjected to axial flow. To generate a cross-wind gust an open aperture of finite length is allowed to pass along the exit plane of the cross-wind tunnel (from upstream to downstream) such that cross-wind fluid exits into the working section. The movement of this aperture is analogous to that found in many cameras, where the passing of an open aperture over a film allows light to project onto the film. To generate the required gust profile the speed of propagation of this aperture and the axial component of velocity of the incoming cross-wind fluid are matched to the axial velocity of the main wind tunnel.

As the nominally yawed cross-wind fluid enters the working section, it displaces the fluid from the main jet in a cross-stream direction. This continues to such an extent that as the leading edge of the aperture reaches the model, far downstream in the working section, all fluid of interest in the working section originates from the cross-wind tunnel. Thus the model is subjected to flow at a predefined relative yaw angle. On passing of the trailing edge of the aperture, the flow in the working section returns to the axial condition.

A simplified development of the flow is shown schematically in figure 3.2. Here the model is represented by the solid black square and the boundary between the cross-wind tunnel and the working section as the thick black line. At time t = 1, the cross-wind exit is blocked, thus the model is subjected to axial flow only. At time t = 2, the aperture is positioned such that cross-wind fluid enters the working section into cell B2. The yaw angle achieved in cell B2 is much lower than that finally attained. The entire flow and leading edge of the aperture move downstream with a velocity of u, consequently when the aperture has reached column 3, the fluid previously in cell B2, which is now in cell C3, is again acted on by flow from the cross-wind tunnel. Thus this fluid element moves further across the working section while continuing with an unchanged axial component. New flow enters the working section from the cross-wind tunnel and as it merges with a flow that already exhibits a small yaw component the resulting merged yaw angle (cell B3 at t = 3), is slightly greater than that of its neighbours (cells B2 and C3). As the aperture moves further downstream, (t = 4-12), this process continues until the influence of the cross-wind jet has extended to the entire width of the flowfield.

At time t = 13, the perpendicular leading edge of the gust has moved down the working section (at a velocity equal to the axial velocity, u), such that it lies just in front of the model. The model now undergoes an abrupt change from axial to yawed flow and remains subjected to yawed flow until the trailing edge of the aperture reaches the same axial location as the model, when a similarly abrupt return to axial flow occurs. Throughout the duration of the development of the cross-wind gust fluid is entering the working section from the main (axial) jet, this fluid is displaced by the fluid from the cross-wind jet such that it exits out of side (or lower face in figure 3.2) of the working section. This main jet curvature has been omitted in figure 3.2 to clarify the area of influence of the cross-wind fluid.

3.2 Implementation of the Technique

A facility of this type, suitable for testing 1/8th scale passenger cars, was constructed by Docton [61]. The main axial flow was provided by the University of Durham automotive wind tunnel (0.85m x 0.55m working-section). This tunnel is of open jet open return type with a maximum freestream velocity of $27ms^{-1}$. A second cross-wind tunnel was built to provide flow for the cross-wind gust.

This facility generated cross-wind gusts of 1.5m in length (3 model lengths). Data published by Kobayshi and Yamada [38] suggested that a cross-wind gust of up to 7 model lengths were required for full flow development, however the shorter gust length was considered sufficient for investigation of the initial transient response. The relative yaw angle of the cross-wind gusts was $\psi = 30°$. Much of the published data from steady cross-wind testing, for example Macklin *et al* [36], has shown the maximum steady peak side force and yawing moment coefficients to occur around this yaw angle.

The working section Reynolds number under axial flow conditions, which was limited by the mass flow from the cross-wind tunnel, was $Re_l = 3.3x10^5$. Docton [61] thoroughly investigated the possibilities for control of the cross-wind tunnel exit boundary, concluding the best option was to use a vertically mounted flexible belt mounted parallel to the axis of the main tunnel. Figure 3.3 shows the facility used by Docton.

The belt contained several apertures for the creation of the cross-wind gusts. On initiation of a run, it would be rapidly wound from the upstream to the downstream spool by means of a motor. A length of belt was permitted for acceleration purposes, after which there were four apertures, two in the top half of the belt, and two in the bottom half. The apertures in the top half allowed cross-wind tunnel fluid to exit into the working section, thus creating the cross-wind gust, while the apertures in the lower half allowed cross-wind fluid to exit below the working section. The apertures were configured such that the open exit area of the cross-wind tunnel remained almost constant, helping the cross-wind tunnel fan to operate at an almost fixed point on its characteristic.

After each belt run (two cross-wind transients) the belt had to be manually rewound onto the upstream spool. This was a time consuming process, restricting the number of cross-winds gusts that could be generated within realistic timescales, however the gust production rate did represent an improvement on the dynamic-static track method. The length of cross-wind gust that could be generated was restricted by the mass of, and the flexible nature of, the belt. The mass was limited by the available drive torque, while the flexible nature led to increased tracking problems with increasing belt length.

Docton [61] conducted a survey of the empty working section of this facility, confirming the generation of sharp edged, finite length, cross-wind gusts was as expected. Figure 3.4 shows the transient response as found at the model centre in the empty working section. This was measured using a 5-hole probe system designed for optimum transient response. Prior to onset of the cross-wind gust the yaw angle at the model centre is nominally zero. An undershoot occurs before rapid transition to the yawed flow regime, which is maintained for the duration of the gust, before an equally rapid return to axial flow conditions. Inspection of the axial velocity component shows that, within the constraints of the unsteady flow, matching of the axial velocities of the main and cross-wind tunnels was achieved.

3.3 Facility Development

Docton's [61] method of gust generation had inherent limitations. Aerodynamic unsteadiness in the working section produced a noisy signal, this could have been minimised by ensemble averaging however the labour intensive gust generation process was not conducive to this. In addition, the relatively short gust length was unlikely to allow full transient flow development to be observed.

Ideally a fully automated repeating transient gust generation facility with the possibility of varying the gust length was required. The development, manufacture and testing of such a facility was undertaken by the current author and is detailed in the remainder of this Chapter. From reviewing the work of Docton [61], it was apparent that the only requirement was an improved method of controlling the cross-wind tunnel boundary condition. The rapid gust production rate of this new facility would not only allow ensemble averaging, but also offer the possibility of conducting wake traverses, yet untried because of the large number of gusts required (several 1000s).

3.3.1 Vertical Axis Shutter Concept

Careful consideration of the proposed concepts for controlling the cross-wind tunnel boundary showed a vertical axis shutter system to have the greatest potential. Two rows of vertically mounted, sequentially opening, shutters were placed at the exit plane of the cross-wind tunnel (figure 3.5).

The top row of shutters allowed cross-wind fluid to exit into the working section. Each top row shutter was connected to its bottom row counterpart by a gear mechanism, such that when one opened the other closed. This maintained a constant open exit area irrespective of which top row shutters were open. Each shutter pair was individually actuated allowing sequential opening of the shutters. Thus, the top row of shutters could be opened and closed in a 'Mexican wave' fashion, giving an effect analogous to the open aperture moving down the cross-wind tunnel exit plane.

Control of the dwell time each linked shutter pair was open for allowed the gust length to be set, with the speed of propagation of the gust leading and trailing edges controlled by the timing of adjacent shutter opening and closing.

3.3.2 Conceptual Development of the Shutter System

The design of the shutter system was split into three areas; the aerodynamic considerations, shutter actuation and the mechanical design of the support system. Before construction of the final system, a single pair of vertically linked shutters were manufactured and tested to assess the assumptions about inertial effects, bearing friction and actuator speed made during the design process.

The aerodynamic design was dominated by the potential effects of shutter chord length. A short chord is desirable on two accounts. Firstly, it represents less of a percentage of the cross-wind gust length, making the gust propagation process less 'discrete'. Secondly, it minimises the disturbance to the cross-wind fluid of an opening shutter. During the opening process, each shutter acts as a rotating bluff body in the cross-wind fluid. This inevitably disturbs the passing fluid, however using a shorter shutter chord minimises this disturbance. Turbulence suppression devices, such as screens or honeycomb section, could also be used to reduce any flow disturbance caused by the opening shutters.

Various concepts for shutter actuation were considered, including connected mechanical levers, rotating shafts with cams and pneumatics. The only concept that provided an effective opening system, within the cost constraints, was found to be solenoid actuation.

3.3.3 Design Implementation

Consideration of the above factors led to a shutter chord length of 68.5mm, which offered a good compromise between cost and performance for a yet unproved design. This chord length required two rows of 30 shutters to cover the cross-wind tunnel exit plane. Figure 3.6a shows a schematic plan view of part of the shutter system taken along section B-B' (figure 3.6b), with 3.6b being a schematic front elevation of two shutter pairs along section A-A' (the aspect ratio of the shutters has been decreased to fit on the page). Directional control of the cross-wind fluid was provided by the static guide vanes between shutters and the honeycomb flow straightener downstream of the shutters.

The solenoid actuated opening was provided by Mechetronics D5 solenoids; these provide 40N of force over a 24.0mm stroke length when operated at the rated 12V. The linear to rotational motion translation required for shutter opening was achieved by lever arms. To decrease the shutter opening times the solenoids were supplied at 60V for the duration of shutter opening, with the shutters held open for the remainder of the dwell time by a separate 24V supply. The low duty cycle (< 1%) prevented any potential overheating problems that could have been caused by the voltage over-rating of the solenoids.

Power for the 60V supply was provided by 5, 12V, 7Ah batteries. The 24V supply was 2, 12V, 17Ah batteries. This was sufficient for approximately 3000 cross-wind gusts, with the gusts generated at a rate of 1000/h. Recharging of the whole battery supply was possible overnight. Solenoid control was by an Amplicon PC14AT and an Amplicon PC14A I/O boards. Each board contained 6, 8 bit digital output ports, with one board used to control to 60V supply and the other for the 24V supply. The I/O boards were mounted in a dedicated PC, with the outputs routed to the individual solenoid control transistors through a buffer board.

For reasons of economy shutter closure was spring actuated. Thus shutter closure was significantly slower than shutter opening, an effect likely to smear the gust trailing edge, however at this stage the aerodynamic effects at the trailing edge were of secondary importance. It is for this reason that no detailed analysis of the transition from yawed to axial flow conditions for either the experimental facility or the aerodynamic models is included.

The honeycomb flow straightener (figure 3.6a) covered the full length of the upper row of shutters. Due to its length, and the fact the flow through the honeycomb is not perpendicular to its face, it was necessary to manufacture it from several sections. Each of these sections was similar to the shape depicted in figure 3.6a. Great difficulty was encountered in joining adjacent honeycomb sections in a manner that ensured flow straightening occurred but without increasing the local blockage of the honeycomb. This problem later manifested itself as uneven total pressure loss through the honeycomb along its length, leading to some total pressure gradients in the working section. The honeycomb also introduced an asymmetry in exit conditions between the top and bottom rows of shutters, such that although the open exit area remained constant for the duration of a cross-wind gust, some change in the cross-wind fan operating point was expected.

3.3.4 Other Aspects of the Facility

As discussed in section 2.5.1, ground simulation is a potentially important aspect of experimental technique. This is particularly pertinent for this facility where the model is mounted a significant distance (2.4m) along the ground board. A rolling road was not available for the early tests, so the simplest approach of boundary layer removal by use of a raised section of ground board was adopted. This raised ground board was mounted 70mm above the main board, which had been shown by a five hole probe survey to be above the boundary layer. The aerodynamic model centre was 470mm from the leading edge of the raised board, which extending a further 1030mm behind the model centre. This is well within the recommendations made by Garry *et al* [91].

Early flow measurements conducted in the empty working section indicated that the cross-wind jet had a tendency to ride up over the main jet. Thus a roof section was fitted that covered the full width of the working section, but finished at the leading edge of the raised ground board. The roof was not required to extent beyond here as by this downstream position full gust development has taken place, with the open jet nature of the remainder of the working section avoiding any potential problems of a high blockage ratio.

The completed facility, with the roof of the working section removed, is shown in figure 3.7.

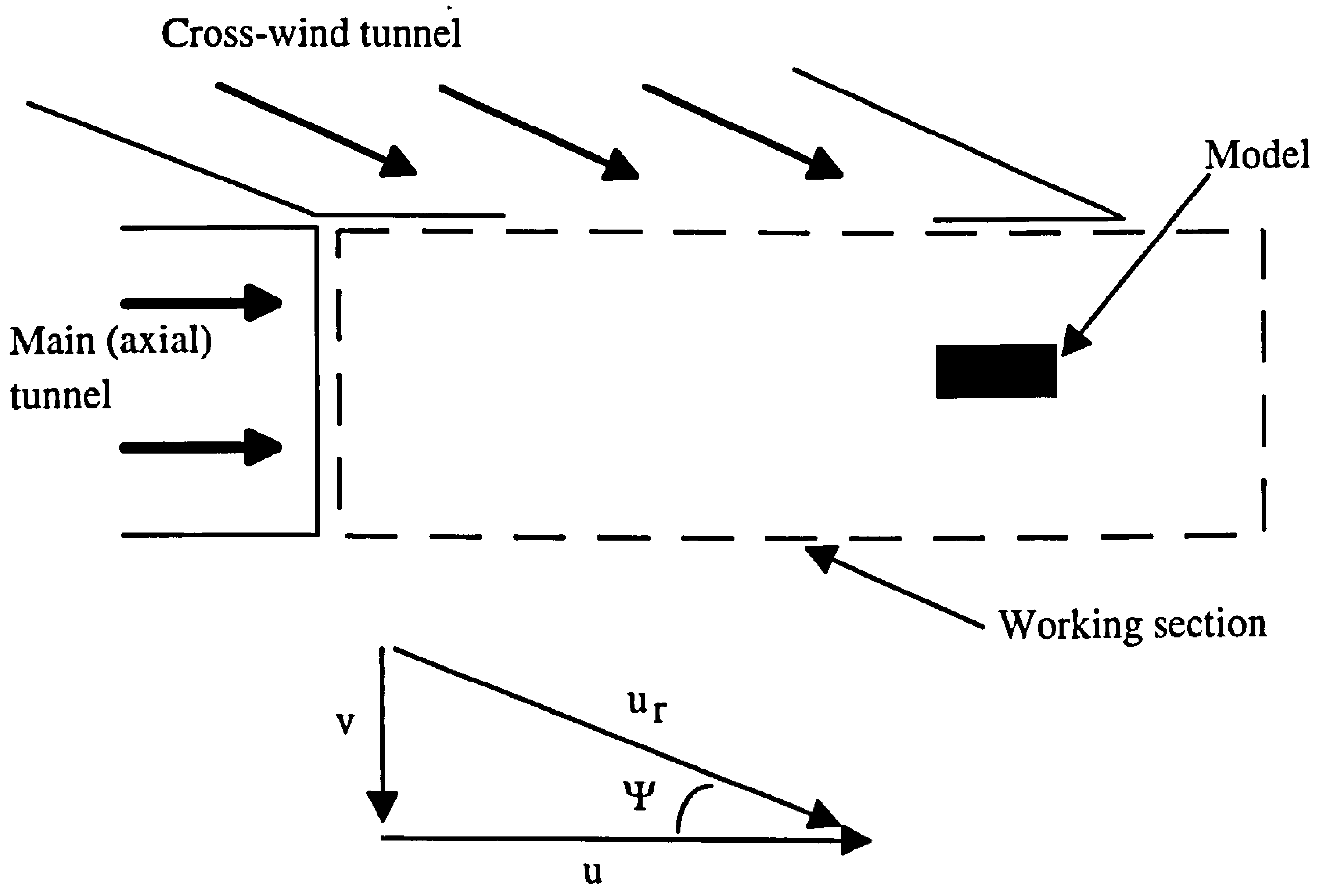

Figure 3.1 Schematic Plan of the Wind Tunnel Configuration and Velocity Triangle

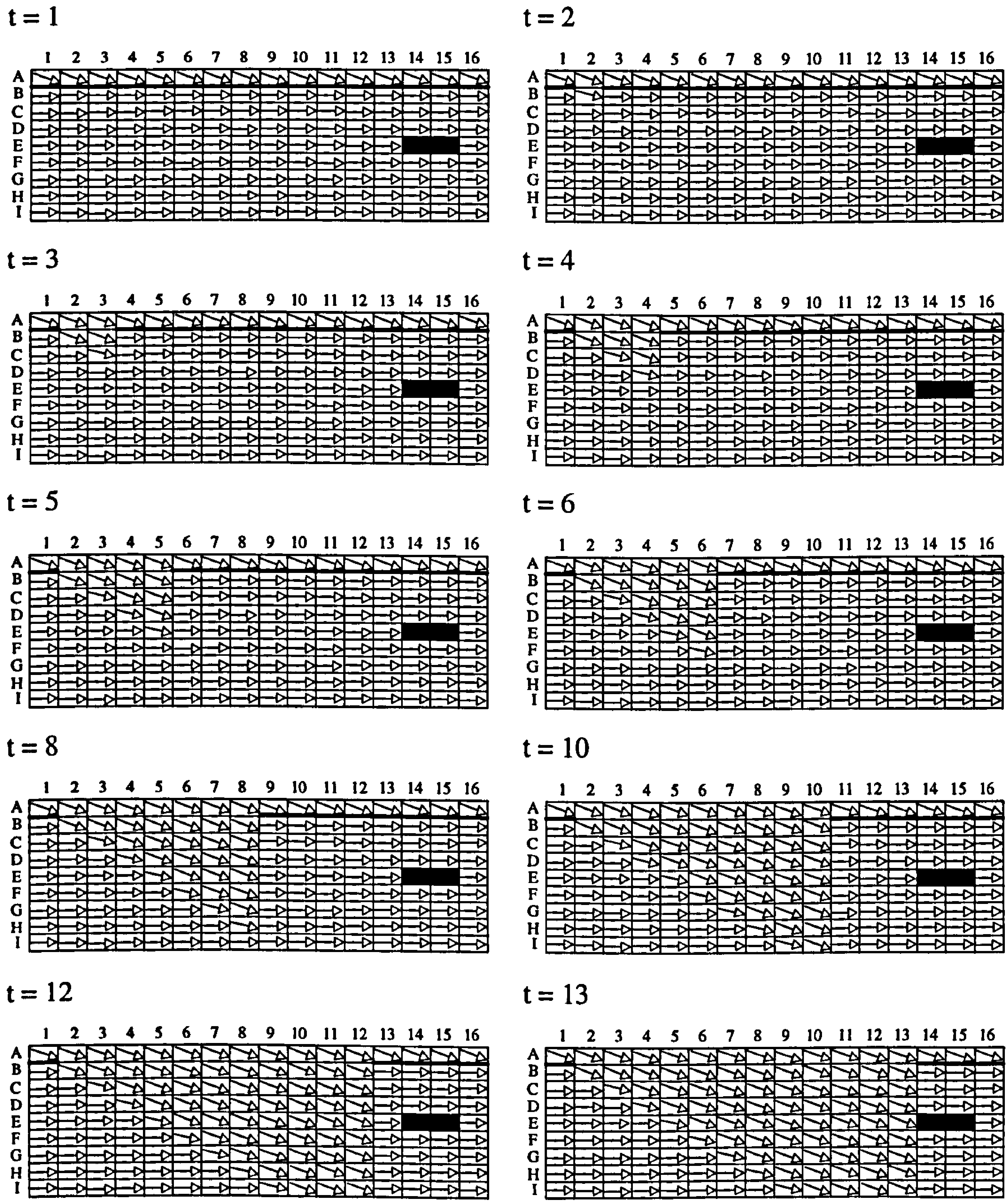

Figure 3.2 Transient Cross-Wind Flow Development

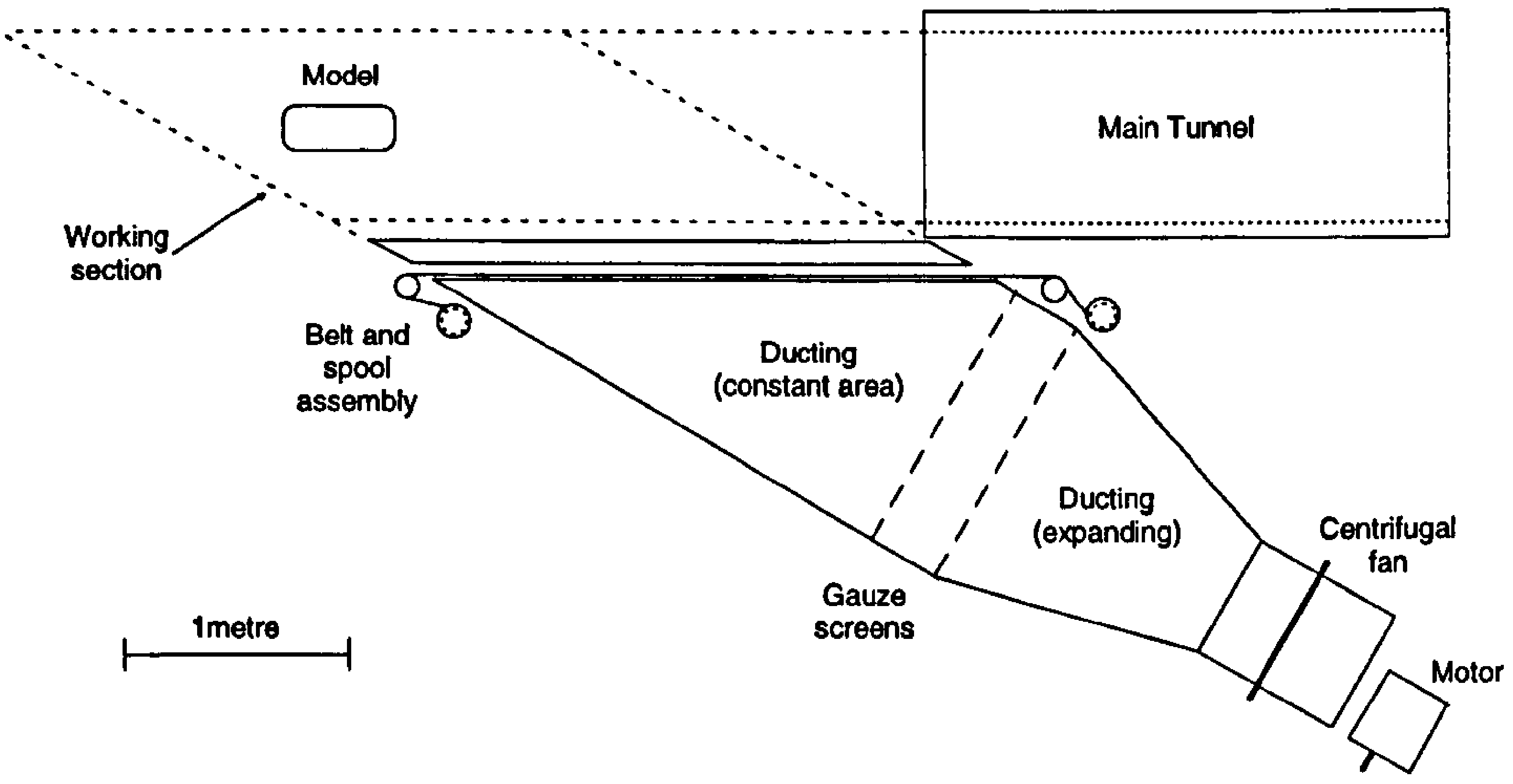

Figure 3.3 The Cross-Wind Generation Facility Used by Docton (from Docton [61])

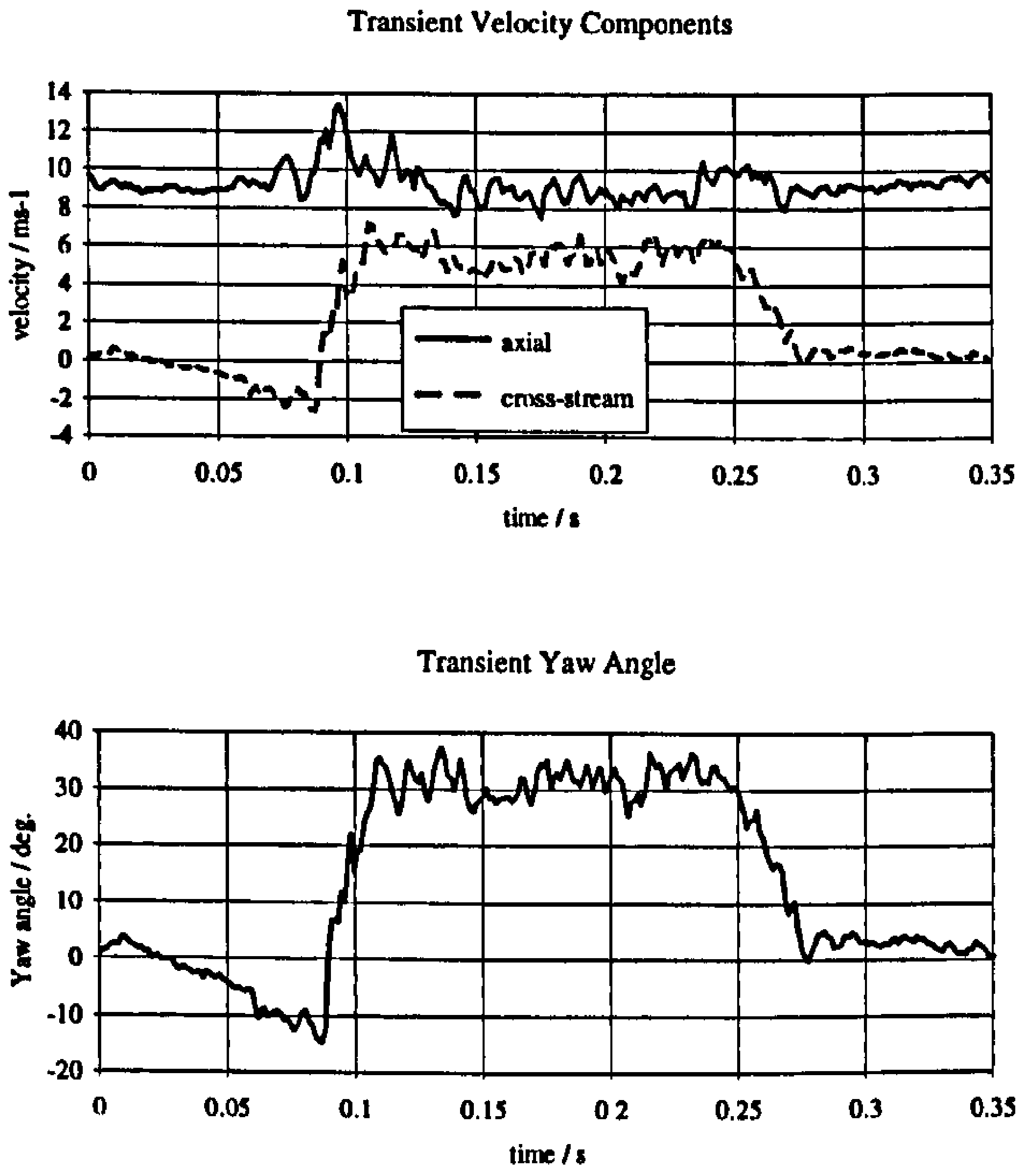

Figure 3.4 The Docton Facility Gust Characteristics (from Docton [61])

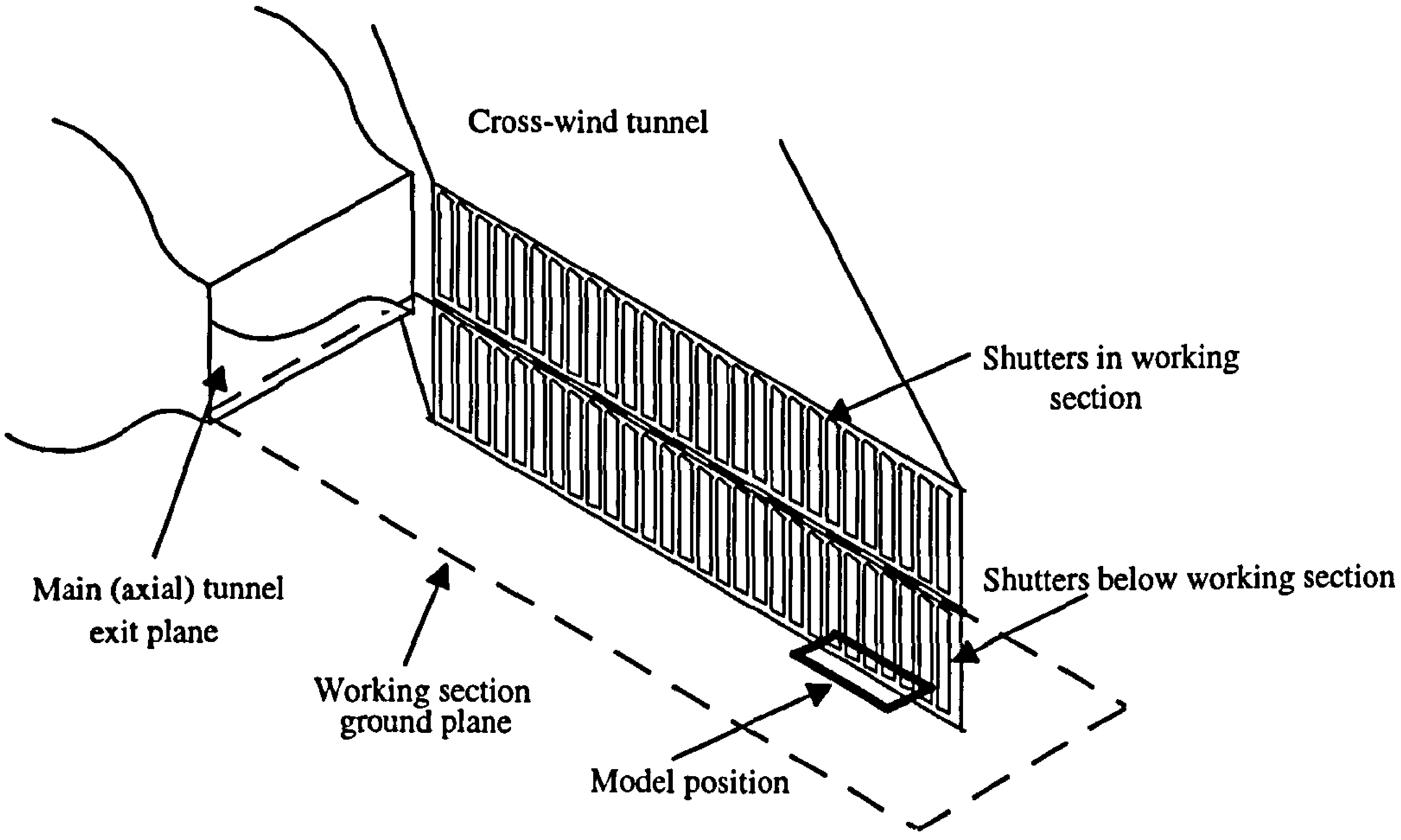

Figure 3.5 The New Cross-Wind Tunnel Configuration
(from Dominy and Ryan [43])

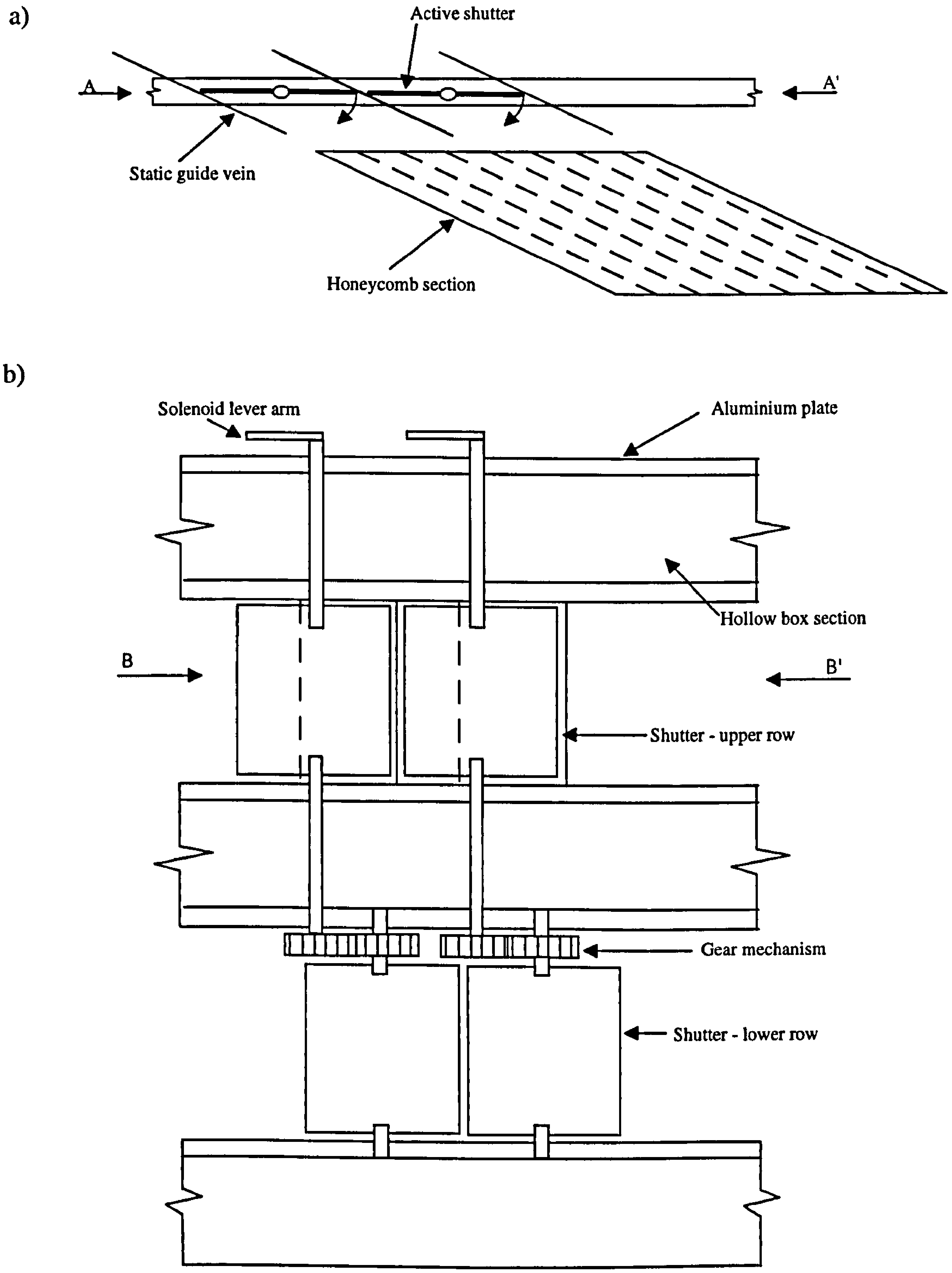

Figure 3.6 The New Cross-Wind Tunnel Shutter Assembly
- a) Plan View, b) Front Elevation

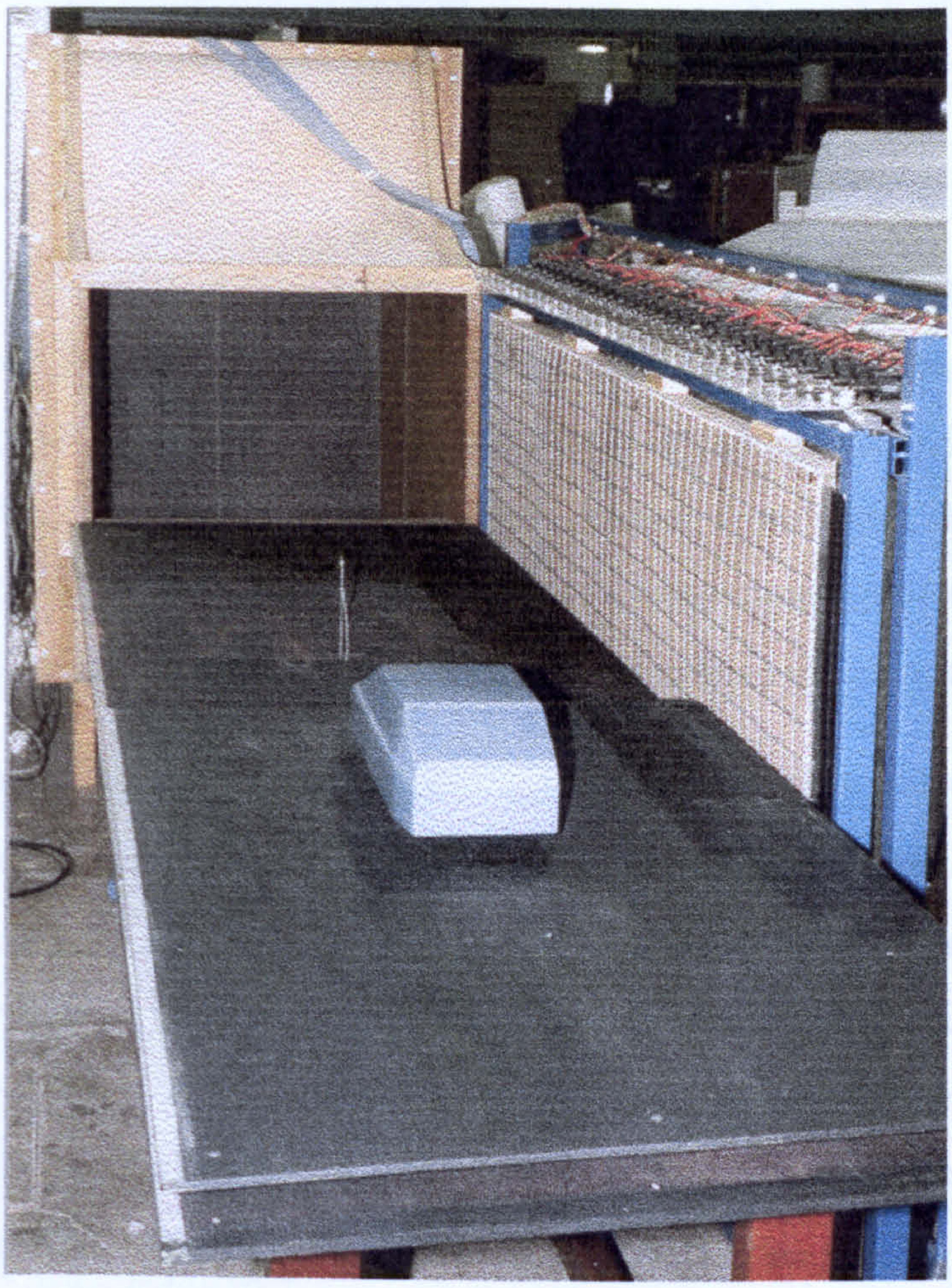

Figure 3.7 The Developed Transient Cross-Wind Facility

Chapter Four

Instrumentation and Aerodynamic Models

4.1 Introduction

To commission the facility measurement of the flow in the empty working section was essential. Several appropriate methods of measurement exist, including pressure probes, hot wires or hot films. The use of pressure probes is advantageous in that they provide a means of pressure measurement at the point of interest, from which the velocity can be calculated. Hot-wires or films can only provide information about the velocity field. Pressure probes are also much more robust and cheaper than the alternatives.

Five hole pressure probes are frequently utilised at the University of Durham for aerodynamic investigations and hence the necessary instrumentation and expertise for their use exists. For reasons of economy the pressure transducers of the available probes were mounted remotely from the probe head. The length of tubing required to connect to the probe head limits the frequency response of the probe, however Sims-Williams [92, 93] recently used a system for the dynamic correction of pressure probes that provides an excellent frequency response up to 250Hz (this can be contrasted to hot wires where a frequency response of up to 50kHz is easily obtained [94]). This upper frequency permits the resolution of all aerodynamic effects corresponding to greater than 8.5% of model length.

After facility commissioning, aerodynamic measurements on two vehicle like geometries were conducted. These consisted of surface static pressure, direct force and moment and wake traverse measurements. The surface static pressure data were acquired using a scanivalve system that had been dynamically corrected in a similar manner to the five hole probe. Force and moment measurement was by means of a new two component internal balance that was designed with the emphasis on dynamic response. Finally, the wake traverses were conducted using the five hole probe system that had been used for the empty working section survey.

4.2 Aerodynamic Models

4.2.1 The Docton Geometry

Preliminary aerodynamic investigations were conducted on the two-dimensional 'Docton' geometry. The model geometry and dimensions are shown in figure 4.1. This geometry is essentially a cuboid of aspect ratio 3.36:1.37:1.00 (l:w:h), but with well rounded corners. The ratio of corner radii to model length (r/l = 0.1) is significantly larger than that found on production vehicles. This parameter has been shown by Cooper [44] to be significant in determining the cross-wind response of a vehicle, with large radii enhancing yawing moment.

For simplicity, two-dimensional flow was promoted by fitting end plates on a geometry where the height to width aspect ratio is only 0.74. The initial motivation for Docton to manufacture a model with such a low aspect ratio was two fold. Firstly, the area blockage of this model in the axial jet is 6%. If the model had occupied the height of the tunnel the blockage ratio would have been 23%, which is unacceptable even for an open jet tunnel. Secondly, his belt and spool assembly produced cross-wind gusts with a height of 0.35m, which needed to be greater than the model height.

Each side of the model was instrumented with 37 pressure tappings at mid height, the location of these tapping being shown in figure 4.2. As can be seen from figure 4.2, the tappings are concentrated around the corner radii, where movement of lines of flow separation and reattachment is expected. The pressure tappings were constructed from 1.0mm internal diameter stainless steel hypodermic tubing.

To maximise the frequency response of the model/balance system for transient force and moment measurements a second lighter version of the Docton geometry was manufactured. This was constructed from high density foam and fitted with wooden end plates, producing a model with a mass of 1.05kg. This compared favourably with the original model mass of 2.61kg.

For the surface static pressure readings and wake traverses the model was mounted from below in the working section using three 25mm diameter supports. The lighter model, used only for the force balance measurements, was mounted by a single underfloor sting at the model centre.

Figure 4.3 shows key points on the perimeter of the Docton geometry in the non-dimensional form 's/S', which is used in later results ('s' is the distance around the perimeter from the front centre of the model and 'S' is the half perimeter). The moment centre for the Docton geometry was taken on the axial centreline at x/l = 0.5 from the front of the model.

4.2.2 The Durham Geometry

To assess the transient cross-wind response of a more realistic vehicle shape the generic three dimensional 'Durham' geometry was used (figure 4.4). This geometry, which is very similar to that used by Davis [33] and Bearman and Mullarkey [58], exhibits certain vehicle-like features such as A-pillars, C-pillars, a slanted windshield and backlight, boat-tailing (plan form tapering) and tumbleholm (vertical tapering), however much of the complicated detail of a real vehicle is omitted. The A-pillars are particularly pronounced and likely to produce strong A-pillar vortices. The basic geometry had the critical backlight angle of 30°, [2, 21], however as a bi-stable flow condition was undesirable, a backlight angle of 25°, which should promote attached flow, was used throughout these investigations.

Each side of the model was instrumented with 57 pressure tappings, the upper surface having a further 100. Again the pressure tappings were 1.0mm diameter hypodermic tubing. The tappings, as shown in figure 4.5, are essentially equally distributed on a 40mm grid, but are more concentrated in regions where strong pressure gradients were expected (for example around the side front corner). The lower surface of the model was not instrumented as it was considered that the inappropriate ground boundary condition and the flow interference created by the model supports and instrumentation cabling would lead to erroneous results.

A second lighter Durham geometry was manufactured for the purposes of direct force and moment measurement. This geometry was mainly constructed from thin (1.6 or 1.2mm) aluminium sheet, with the rounded front section sculpted from wood. The model mass was 1.46kg, compared with 3.77kg of the original model. The moment centre for the Durham geometry was taken as mid height on the axial centreline at $x/l = 0.55$.

The model mounting system used for both pressure data and force measurements was identical to that used for the Docton geometry.

4.3 The Five Hole Pressure Probe

4.3.1 The Probe

The probe, which was the same probe as used by Docton [61], was of the forward facing pyramid type (as classified by Dominy and Hodson [95]), with a cone angle of 45°. The probe is shown schematically in figure 4.6. It is constructed from 5, 1.0mm internal diameter 300mm long hypodermic tubes sheathed in a 6.0mm internal diameter tube and held together with epoxy. The large bore of the individual tubes produces a relatively intrusive probe, however they help maintain a good frequency response, which was vital for Docton [61] who used the probe without dynamic correction.

The probe was calibrated to ±35° (2.5° increments) in both yaw and pitch using a dedicated calibration facility. Probe calibration was at a freestream velocity of 12.9ms^{-1} ($p_{dyn} \cong 100$Pa), which corresponds to a probe Reynolds number (based on diameter) of $Re_d = 5090$. Although this velocity is higher than the free-stream velocity in the working section (11.3ms^{-1}), it was the lowest achievable with this calibration facility. A Reynolds number sensitivity investigation was not undertaken, but pyramid type probes have previously been shown to be relatively insensitive to Reynolds number [95]. The probe calibration maps and coefficient definitions are seen in Appendix A. To minimise errors, the probe was calibrated using the same pressure transducers and data acquisition system used for the experimental investigations. To reduce the peak yaw angles experienced by the probe in the working section it was mounted at an angle of 12° to the axial direction; thus it would be expected to be nominally subjected to flow with a relative yaw angle of ±12°. The probe was positioned in the working section using a 4 axis (3 linear and 1 angular) traverse system controlled by the data acquisition desktop PC. The unsteady pressure correction technique of Sims-Williams [92, 93] (section 4.5) was applied to all transient five hole probe data.

4.3.2 The Pressure Transducers

Five fast response (rise time ≅ 200μs) SensorTechnics 103LP10DPCB ±1000Pa pressure transducers with onboard power supply stabilisation, signal amplification and precision temperature compensation [96] were used for measurement of the individual five hole probe pressures. The transducers were operated in differential mode, with a common 12V power supply. The transducers were regularly, simultaneously calibrated against a silicon oil micromanometer with the individual calibration slopes stored in a lookup table. A further two identical pressure transducers were used for measurement of the wind tunnel reference conditions.

4.4 The Scanivalve System

Surface static pressures were measured using a 48 channel scanivalve mounted inside the model. The unsteady pressure correction technique of Sims-Williams [92, 93] (section 4.5), was applied to correct for amplitude and phase distortion caused by the pressure tapping, tubing and scanivalve system. Passive improvement of the dynamic response was also achieved by minimising the lengths of tubing connecting the pressure tappings to the scanivalve, and the scanivalve to the pressure transducer. The pressure transducer used was from the bank of five, with data acquisition and scanivalve stepping controlled by the desktop PC.

4.5 Unsteady Correction Technique

To accurately measure unsteady pressures a system is required that does not either attenuate (including resonance) or phase shift the pressure signal between the point of measurement and the pressure transducer. Attenuation is caused by viscous losses in the tube, with a phase lag generally occurring due to the length of tubing. Both these can be minimised by shortening the lengths of tubing between the point of measurement and the pressure transducer, however this is not always practical. For example, the 4 axis traverse system used in these investigations requires a minimum tube length of 1.0m to connect the probe to the pressure transducers. A further reduction in attenuation can be achieved by increasing the diameter of the tubing, but this has practical limitations. For many experimental situations the absolute phase of a signal is not required, more the relative phase between signals recorded at different points in space. If this is the case, providing a constant tubing length is used the phase need not be corrected and the attenuation limited by use of a short length of tubing.

Several methods have previously been implemented to improve the dynamic response of tubing systems. The simplest of these, as used by Duell and George [97] for example, is to place a restrictors within the tubing system. Here two different diameter tubes are connected in series, the smaller diameter tube acting as the restrictor. The restrictor damps out the standing waves that are responsible for resonance within the system. Duell and George [97] applied this method to a tubing length of 12.5cm, successfully moving the resonant frequency to over 500Hz, which was above their range of interest. This method however increases the viscous damping of the system (due to the reduced diameter tubing) and makes no active attempt to correct the phase shift.

More recently Rediniotis and Pathak [98] modelled a tubing system as a second order dynamic system. For simplification, the second order model was reduced to a first order model. This placed some restrictions on its application (it could now only be used for critically damped or overdamped systems), but allowed easy measurement of the constants associated with the system, subsequently allowing them to correct for amplitude distortion, but not phase distortion. They found a good frequency response could be achieved for frequencies of up to 120Hz when using tubing of 0.25mm internal diameter and 0.3m length.

By far the most promising method for dynamic correction is that used by Irwin *et al* [99] and more recently applied by Ishihara and Takagi [5] and Sims-Williams [92, 93]. This method, known as the inverse transfer function (ITF) method, actively models both amplitude and phase distortion. The transfer function of a tubing system is measured by applying a test signal of varying frequency and amplitude to one end of the system. The test signal is directly measured and then compared with the recorded signal at the pressure transducer end of the system. Comparison of these signals in the frequency domain allows a complex transfer function (amplitude and phase), which is valid over the range of frequencies of the test signal, to be calculated for the tubing system. This complex transfer function can then be applied to any signal recorded at the downstream end of the tubing to accurately infer the applied signal.

This method has been successfully applied to both the five hole probe and scanivalve system used in these experiments. For both corrections a swept sine wave with upper and lower limits of 3Hz and 300Hz was used as the exciting signal. This was applied into a small chamber that contained either the probe head, or a representative pressure tapping, through an audio loudspeaker. The chamber also contained the pressure transducer used to measure the test signal. Five hundred sets of 1024 points were recorded and Fast Fourier transforms (FFT's) of the fluctuating pressure signals calculated. A transfer function was then calculated for each of the sets and the 500 transfer functions averaged. An extrapolation to zero Hertz was made using the assumption of an amplitude ratio 1.0 and phase shift of 0.0° at 0Hz. For the five hole probe individual transfer functions were calculated for each tube. The transfer function for the centre hole of the Docton five hole probe is shown in figure 4.7. The noise above 300Hz is caused by a lack of signal above this frequency.

For correction of a particular experimental pressure signal, FFT's of the time domain data were calculated and then divided by the relevant tubing transfer function. All data above 250Hz was truncated and an inverse Fourier transform (IFT) taken to yield amplitude and phase corrected time-domain data. This method is fully discussed by Sims-Williams [100].

4.6 The Two Component Force Balance

Measurement of unsteady forces using a force balance is inherently difficult. Force measurement is achieved through deflection, and hence any balance possesses elasticity. This when combined with the finite mass of a balance produces system that is dynamically characterised by damped simple harmonic motion. Mullarkey [101] states that the useful upper bound of frequency response of a balance is between half and one third of the resonant frequency, although this depends on the level of damping.

The force balance used by Docton [61] was relatively heavy, with six degrees of freedom and low capacity (6kg) load cells reducing the overall stiffness and hence resonant frequency. His balance was also externally mounted, allowing the model to act as a pendulum mass. For the experiments undertaken by the current author a new balance was designed and manufactured, with the emphasis on stiffness, low mass, and minimising the size such that it could be internally mounted in either of the aerodynamic models.

To achieve these criteria the balance was restricted to two components. This allowed measurement of a single force and moment component for a given balance orientation, however the balance could be mounted in any orientation, hence all six components could be measured. Measurement of only two components requires the remaining four to be eliminated at the point of measurement. This was achieved by making the balance relatively stiff in all other directions and transmitting force to the load cells by means of thin steel rods. These thin rods allow transmission of tension or compression, but have negligible resistance in bending. A schematic of the balance configuration is shown in figure 4.8.

Force measurement was by means of two bespoke ‘S-beam’ load cells, as shown in figure 4.9. The load cell geometry was based on the Graham & White 535Q series cell which had been used in Docton’s balance. This design was chosen as sufficient data were available to allow the design to be extrapolated to a much higher capacity, in this case a nominal capacity of 60kg, which was expected to yield a significant increase in balance stiffness. Although this capacity was an order of magnitude higher than that of the cells used by Docton [61], the specific output (V/kg) was kept constant through higher signal amplification. Deflection measurement was by means of 4, 350Ω foil backed strain gauges configured in a full bridge circuit, which also provided temperature compensation. Signal amplification was external, using a gain of 1000, with noise reduction achieved by ensemble averaging (section 5.1.3).

The balance was calibrated in the side force/yawing moment configuration. The effect of cross-loading the balance was investigated for a limited number of loading configurations. This led to the conclusion that cross-coupling between components had not been entirely eliminated on this simple balance design, however for the expected loadings the force and moment data would be within 5% of the actual load.

Although the balance was designed to have a high natural frequency, serious problems of balance resonance were encountered when measuring transient forces. Figure 4.10 shows unfiltered autospectral density functions of side force and yawing moment coefficients for the Docton geometry when subjected to the standard 5.0m (10 model lengths) transient cross-wind gust. The balance/model system is clearly resonating at approximately 30Hz. The balance could not easily be further stiffened, thus a low pass digital filter was used to eliminate unwanted frequencies. Figure 4.11 is the autospectral density of the empty working section yaw angle. This shows that although the gust is sharp edged the aerodynamic input is dominated by the lower frequency aspects. Filtering at a low frequency will undoubtedly remove some of this data, however the detrimental effects should be limited.

A digital filter is defined by two parameters, the cut-off frequency, f_c, and the stop frequency, f_s. The resonant frequency of the balance dictated that the stop-frequency had to be below 30Hz. An unavoidable consequence of digital filtering is 'ringing', which manifests itself as damped oscillations in the filtered time domain data [102]. Ringing is a consequence of sharp edges in the frequency response of a filter, with the oscillations being at the frequency of these edges. To avoid removing important data a high cut-off frequency is desirable, however for a fixed stop frequency this inevitably leads to sharper edges and enhanced ringing. The effects of ringing can be minimised using a optimised filter geometry (shape), for example that proposed by Hamming [103].

Numerous filter geometries were investigated, with changes made to the cut-off frequency, the stop frequency and the filter geometry. The most effective filter was found to be an empirical design proposed by the author, with the geometry was based on circular arcs. The cut-off frequency is a mere 5Hz, with a stop frequency of 18Hz. Figure 4.12 shows the frequency response of this filter. This was used to filter all transient load cell output voltage time histories prior to application of the force balance calibration matrix (applying the force balance calibration and then filtering produces identical results).

Figure 4.13 shows typical transient side force and yawing moment data for the Docton geometry. The ringing has clearly affected the side force coefficient, but to a much lesser extent the yawing moment coefficient. Comparison of the respective side force and yawing moment autospectral densities (figure 4.10) illustrates that the side force contains a relatively high amount of information around 18Hz, the cut off frequency. Thus, the ringing appears to be mainly associated with the filter geometry around this frequency.

The effect of the low pass filter on transient data is seen in figure 4.14. Here the unfiltered empty working section yaw angle is compared with the same data after filtering. The main effect of filtering is to increase the rise time of the yaw angle as the high frequency components are removed, with truncation of both the under and overshoot spikes. There is little evidence of filter ringing, again inspection of the yaw angle autospectral density (figure 4.11) shows a relatively small amount of information around 18Hz.

4.7 Data Acquisition

Data acquisition was by an Amplicon PC30-PGH, 12 bit ADC card run on a MS-DOS based desktop PC. This card has a maximum of 16 analogue input ports, with an additional three 8 bit I/O ports. The card was operated in differential input mode, limiting the number of inputs to 8. The input range was set to 0-10V, with each channel having an individual software controlled gain setting of either 1, 2, 4 or 8.

The data logging and post-processing software used was custom written in FORTRAN. Data acquisition for each transient cross-wind gust was triggered by a signal from the shutter control software, thus ensuring consistent ‘zero’ times. All data was logged in sets of 1024 points at a sampling rate of 800Hz. Anti-aliasing was provided by a set of matched second order 250Hz low pass analogue filters.

4.8 Experimental Accuracy

Errors in aerodynamic measurements have been classed by Gossweiler *et al* [104] as being either systematic or random. Systematic errors are those that occur, and in theory can be compensated for, whereas random error cannot be compensated for. For example, when considering a five hole probe systematic errors will occur in the measurements due to thermal shift of both zero values and sensitivity of the pressure transducers, with random errors occurring due to aerodynamic effects around the probe head that have not been calibrated for.

4.8.1 Logger Card

Probably the smallest contribution to error, but one that is common to all data acquisition, is the quantization error of the logger card. The maximum quantization error is ±1/2 LSB (least significant bit) [105], this corresponds to 1.22×10^{-3}V for the card used, which typically equates to 0.5Pa for the pressure transducers or 0.05N for the load cells. This error is random as it cannot be compensated for.

4.8.2 Pressure Transducers

The pressure transducers have a small systematic error that is mainly due to temperature shifts. The pressure transducer specification [96] quotes typical values of thermal shift in the range 0 - 50°C of ±0.5% of full scale for both offset and sensitivity. This corresponds to an absolute value of 5Pa over 50°C, however in the vicinity of the wind tunnel temperature variations of more than 10°C are rarely experienced, reducing the error accordingly.

Errors in offset voltages through long term creep were virtually eliminated through the daily acquisition of datum values, as were variations in long term sensitivity through frequent calibration.

4.8.3 Five Hole Probe Data

The largest magnitude of error in the flowfield data will undoubtedly be from the five hole probe, with the errors originating from several sources.

The flow in the majority of the empty working section is at or near freestream velocity, this being near the calibration velocity of the probe, and hence Reynolds number errors should be small. This is not the case in the wake of the bluff bodies, where for the majority of the wake the local Reynolds number is likely to be substantially lower that that of the freestream. Areas of higher than freestream Reynolds number will also exist, but the increase here are not likely to be substantial. Dominy and Hodson [95] report that for a 60° forward facing cone probe errors as high as 5% in yaw angle and 6% in dynamic pressure were found by increasing the probe Reynolds number from $Re = 1.0 \times 10^4$ to $Re = 2.1 \times 10^4$. The probe used for the current experiments is of the pyramid type, with the sharp edges fixing the separation points, even at incidence, and hence the Reynolds number sensitivity should be somewhat lower. Dominy and Hodson [95] also investigated the effect of turbulence on probes. They concluded that freestream turbulence is most likely to affect probes that are sensitive to Reynolds number, as turbulence mainly affects the size and position of separated regions. Thus the turbulence intensity sensitivity of this probe is expected to be low.

Random errors will originate from dissimilarity in flow around the probe head for a given flow condition between the calibration process and the experiments, mainly due to flow hysterisis. Errors of this nature may occur as early on as the calibration process, with the calibration map not being a true representation of the probe. Treaster and Yocum [106] suggested that a probe should be calibrated a number of times in the same manner, and these calibrations averaged to minimise this error. A potential improvement on this would be to calibrate the probe a number of times, but vary the order of calibration, i.e. change the order of pitch and yaw angle incidences, and average these calibrations.

The transient nature of the flow would normally accentuate any hysterisis effects. The parameter of interest is reduced frequency, as defined in equation 4.1. Here f_{red} is the reduced frequency, f is a characteristic frequency, d a characteristic dimension and u the freestream velocity.

$$f_{red} = \frac{2\pi f d}{u} \tag{4.1}$$

A flow with a reduced frequency of order 1 or greater can be expected to exhibit transient effects, however if the reduced frequency is well below 1 the flow can be considered quasi-steady [107]. A typical reduced frequency for the flow around the probe can be calculated using the time for the flow to change from nominally axial to yawed to form the characteristic frequency (1/0.028s), the probe diameter (6.0mm) for the dimension and the freestream velocity (11.3ms^{-1}). This yields f_{red} = 0.12, which is well within the bounds of quasi-steady flow and hence the steady probe calibration can be considered appropriate. The reduced frequency in other parts of the flowfield, especially the model wakes, may vary substantially from this.

The relatively large probe diameter (6.2mm) will cause measurement errors in regions of either high shear or where there is small scale unsteadiness. For either case the error will be caused by the different tubes of the probe head being subjected to different flow conditions. For the case of high shear, this error will give a incorrect value for yaw or pitch and is likely to overpredict both total and static pressure. In the case of unsteadiness, the error will depend on the exact nature of the unsteadiness.

4.8.4 Force Balance Data

Force balance errors will originate from calibration errors and hysterisis effects in the load cells, however in both cases these are likely to be significantly less than the maximum 5% error possible from cross-coupling (section 4.6).

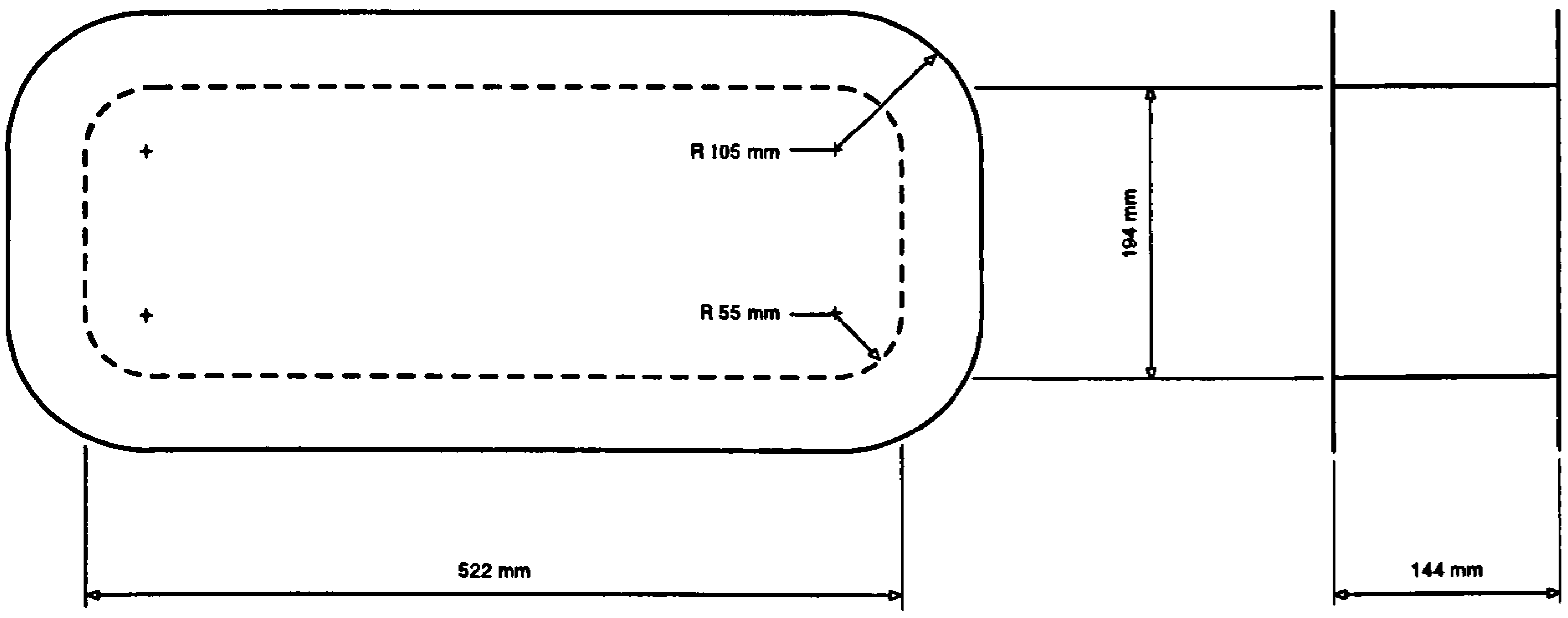

Figure 4.1 The Docton Geometry (from Docton [61])

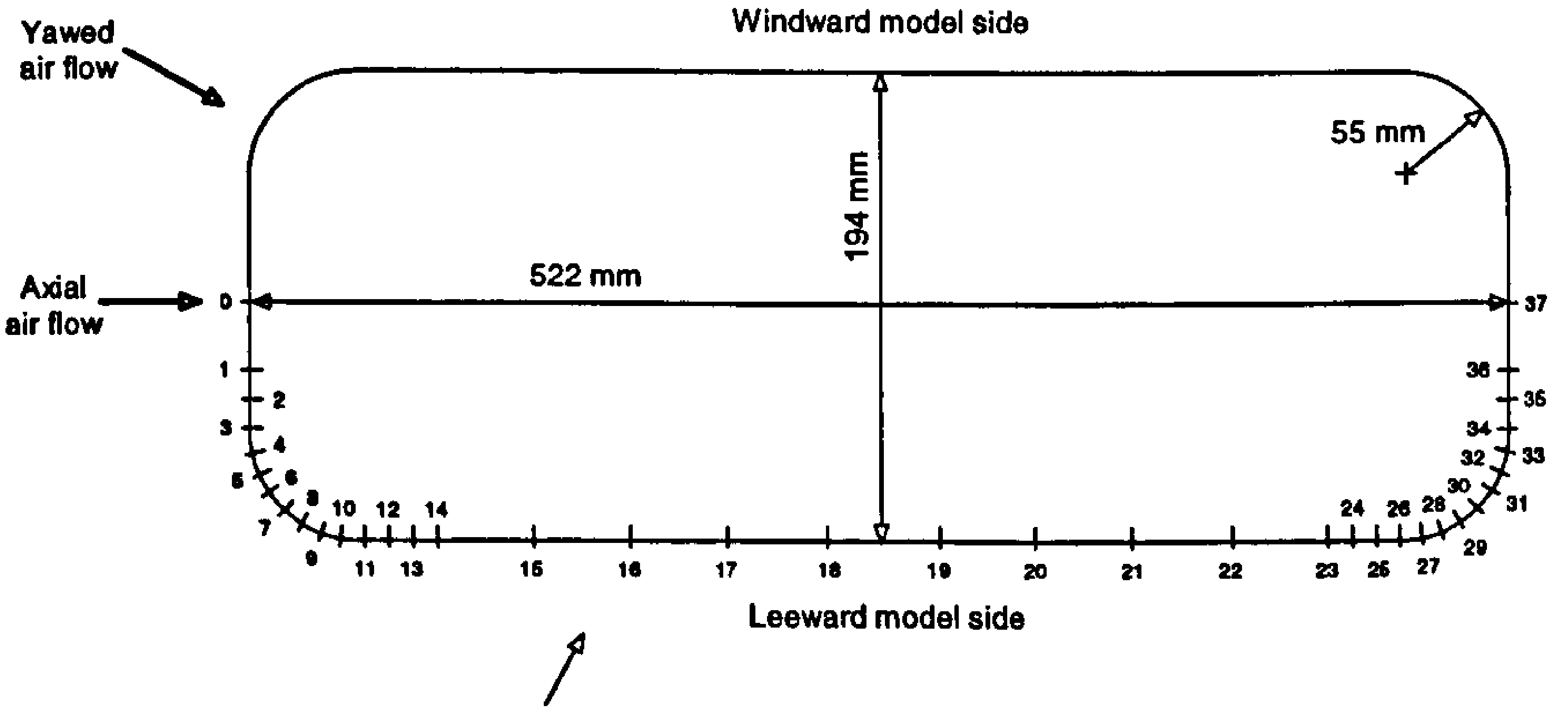

Pressure tapping position and number (indicated down leeward model side only, windward model side tappings gained by symmetry about axial centre line).

Figure 4.2 Location of Pressure Tappings on the Docton Geometry (from Docton [61])

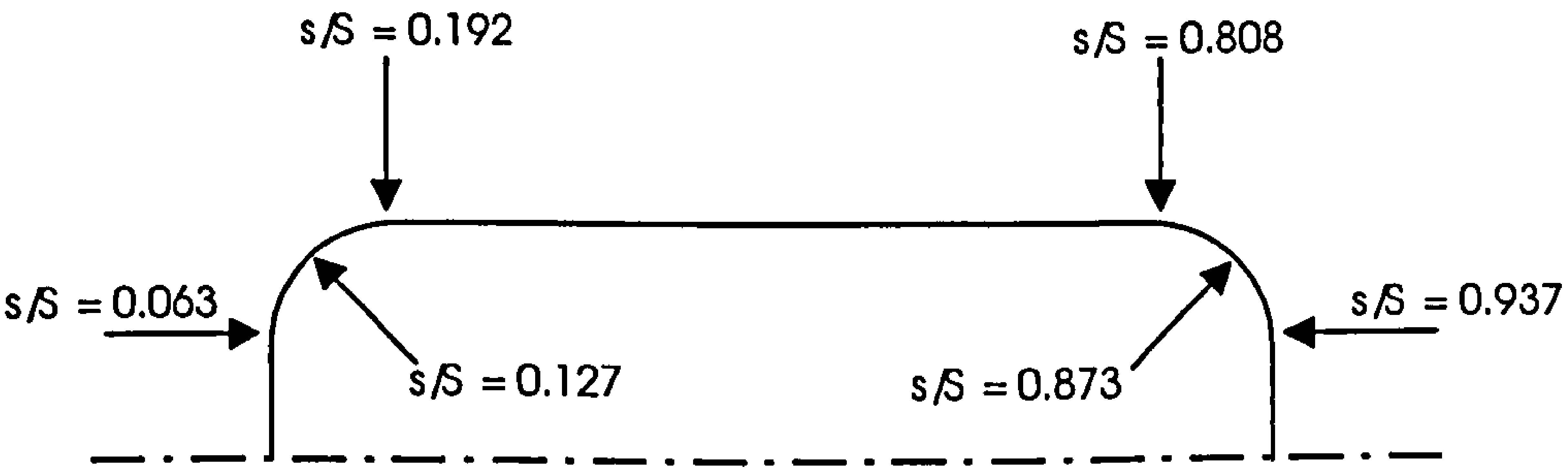

Figure 4.3 Key Points on the Perimeter of the Docton Geometry

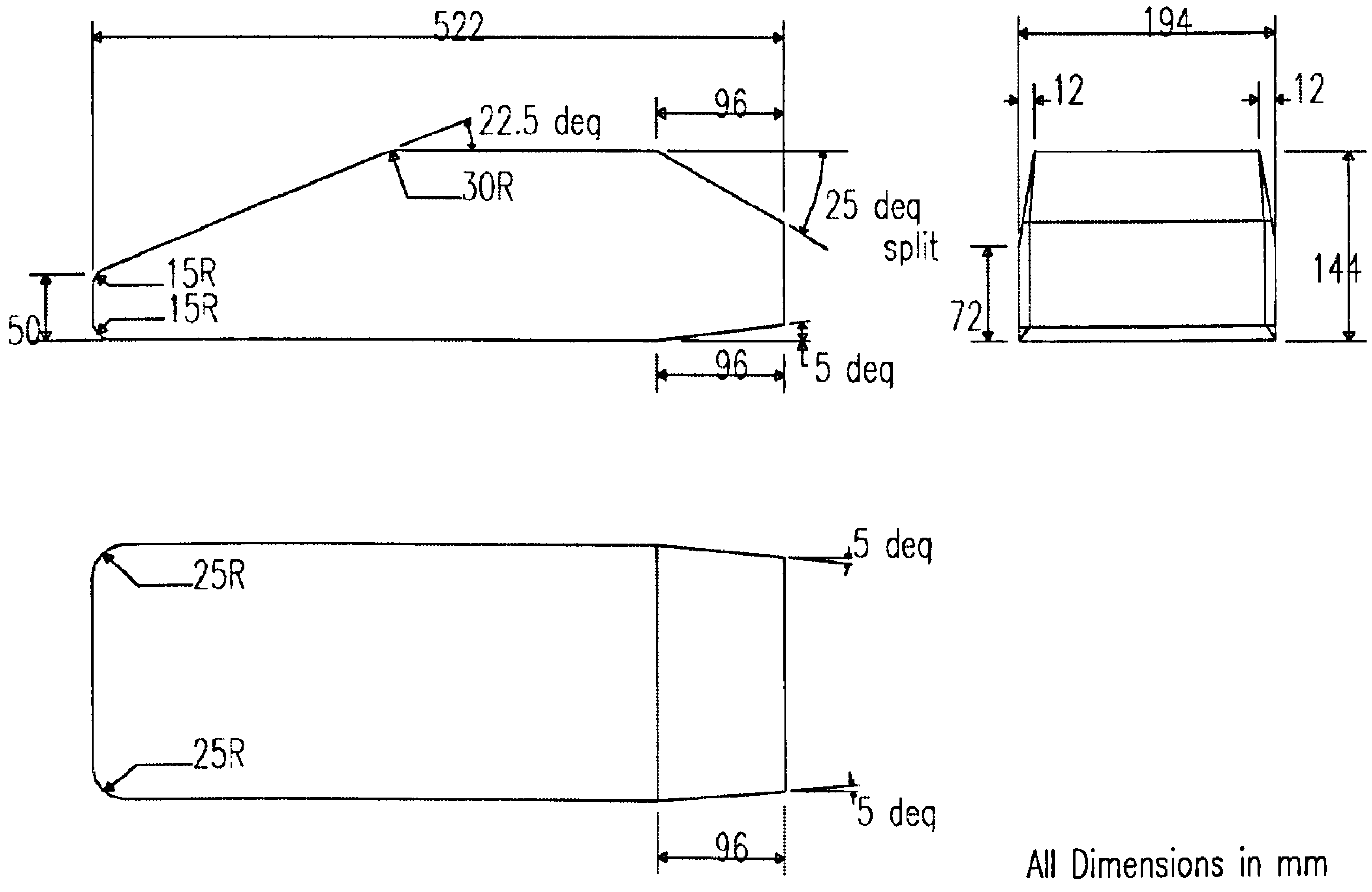

Figure 4.4 The Durham Geometry

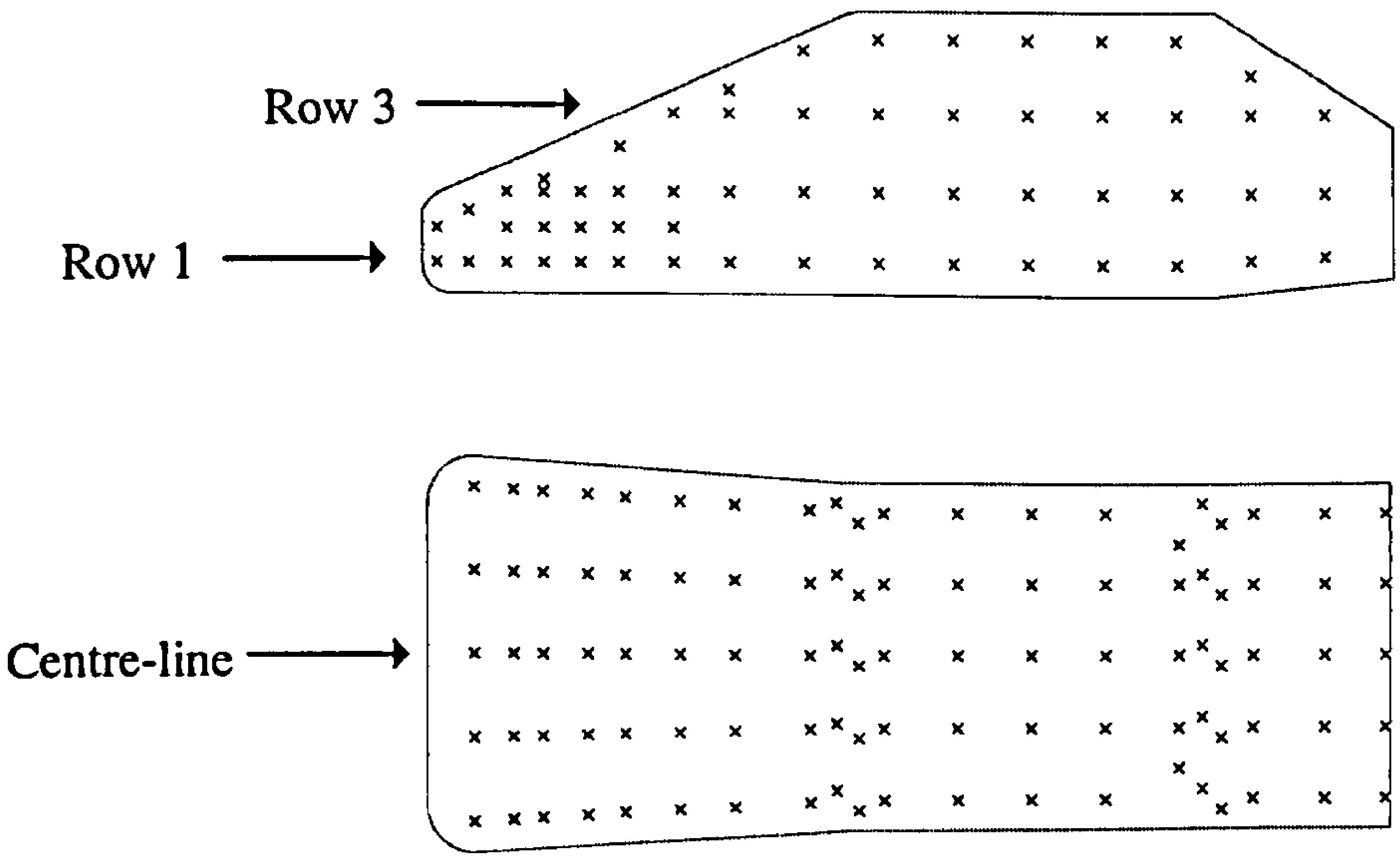

Figure 4.5 Location of Pressure Tappings on the Durham Geometry

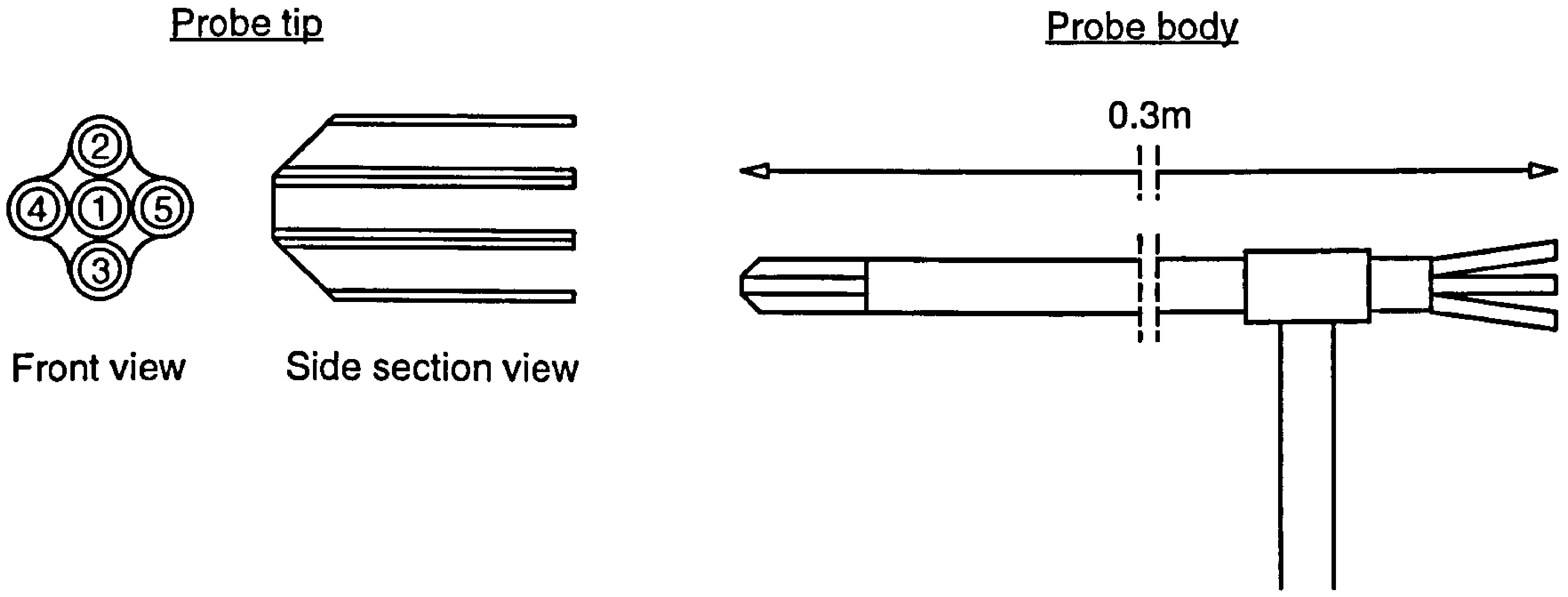

Figure 4.6 The Five Hole Probe (from Docton [61])

a) Amplitude

b) Phase

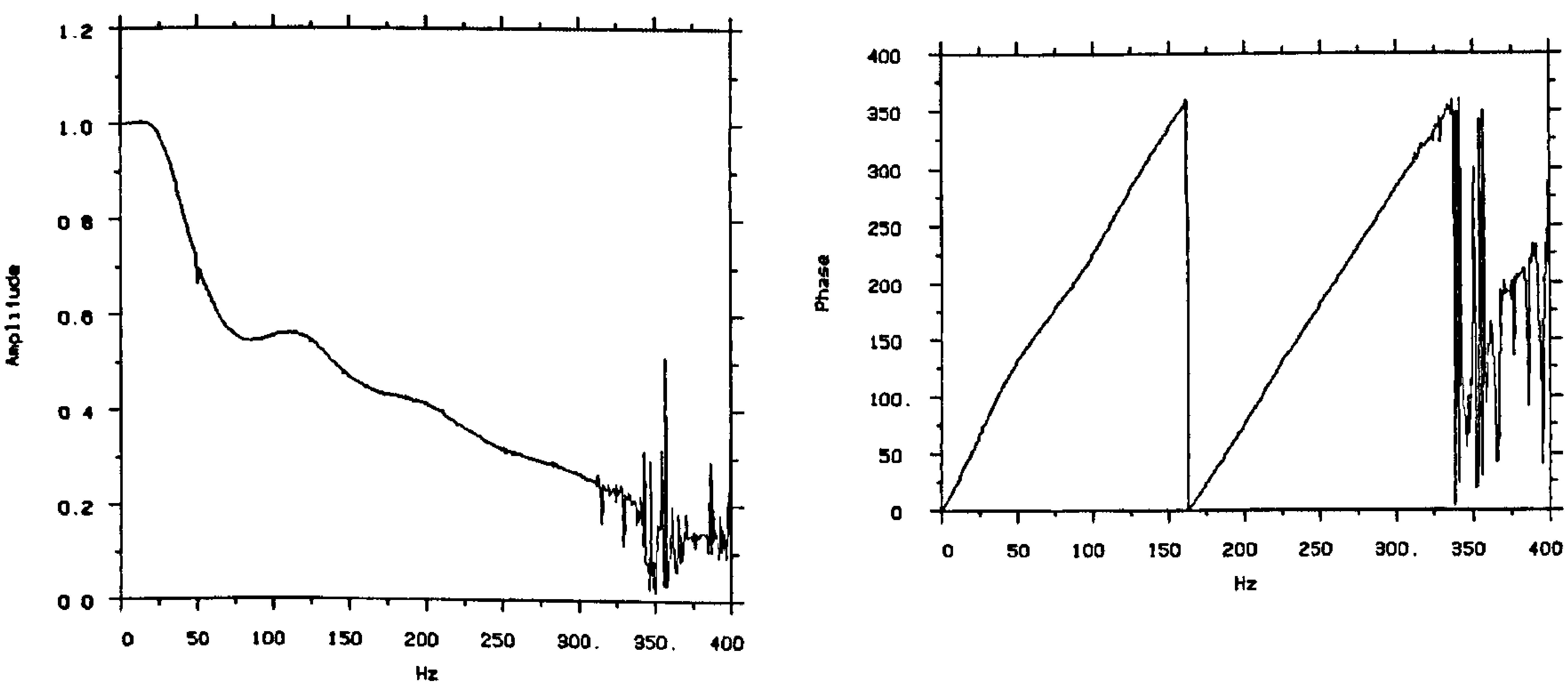

Figure 4.7 Five Hole Probe a) Amplitude and b) Phase Transfer Function Characteristics

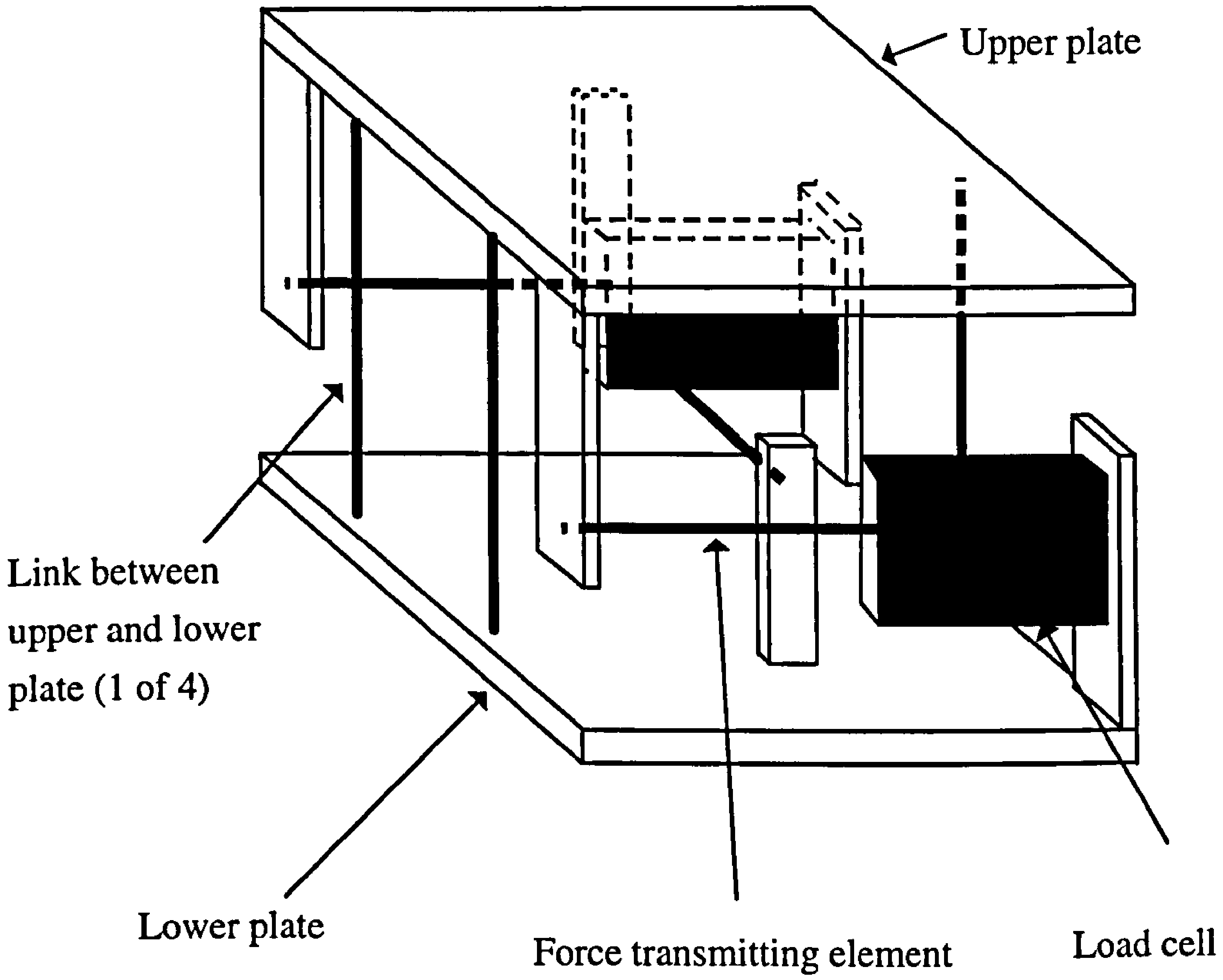

Figure 4.8 Two Component Force Balance Configuration

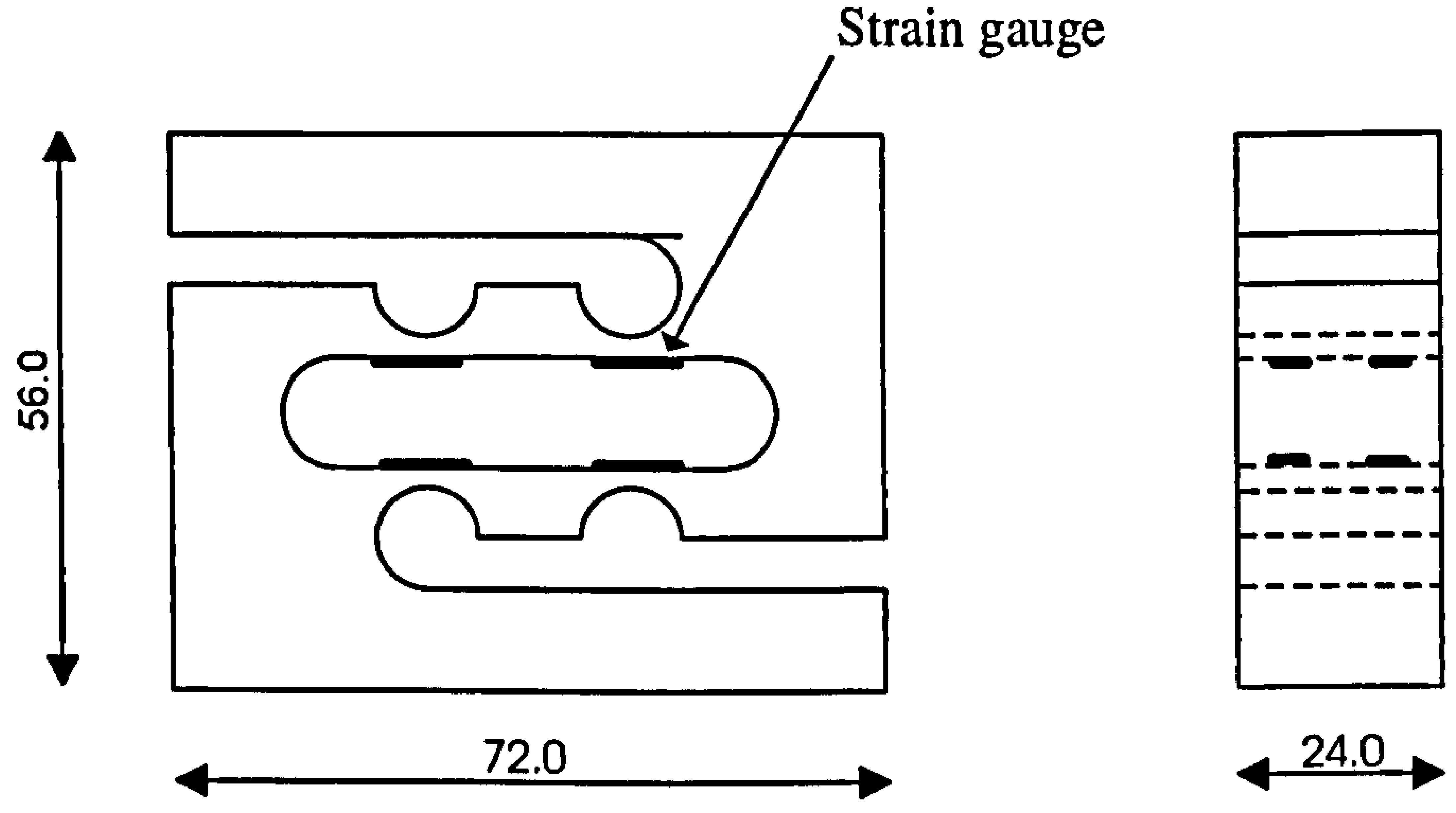

Figure 4.9 Schematic of an S-beam Load Cell (dimensions in mm)

a) Side Force Coefficient

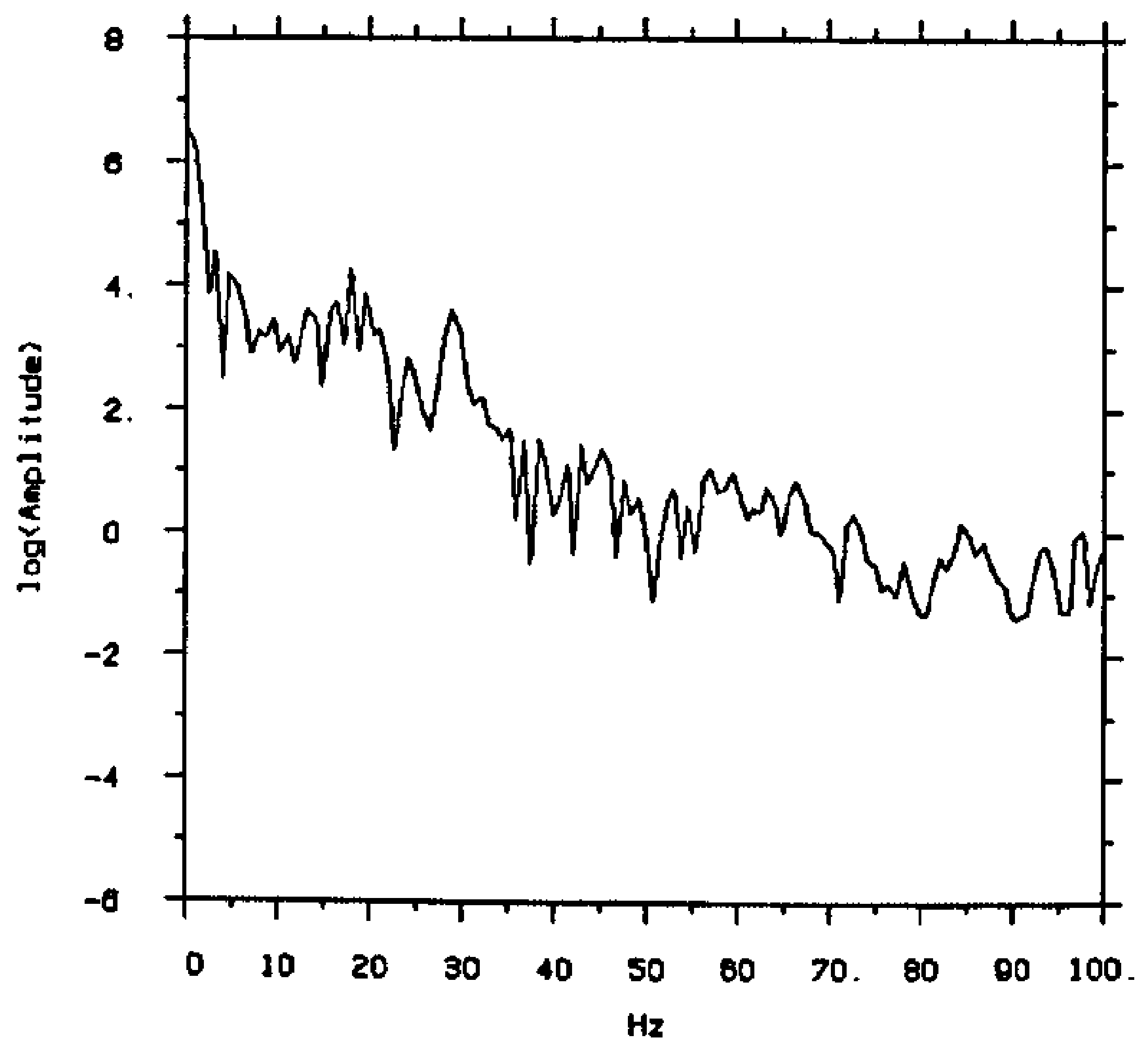

b) Yawing Moment Coefficient

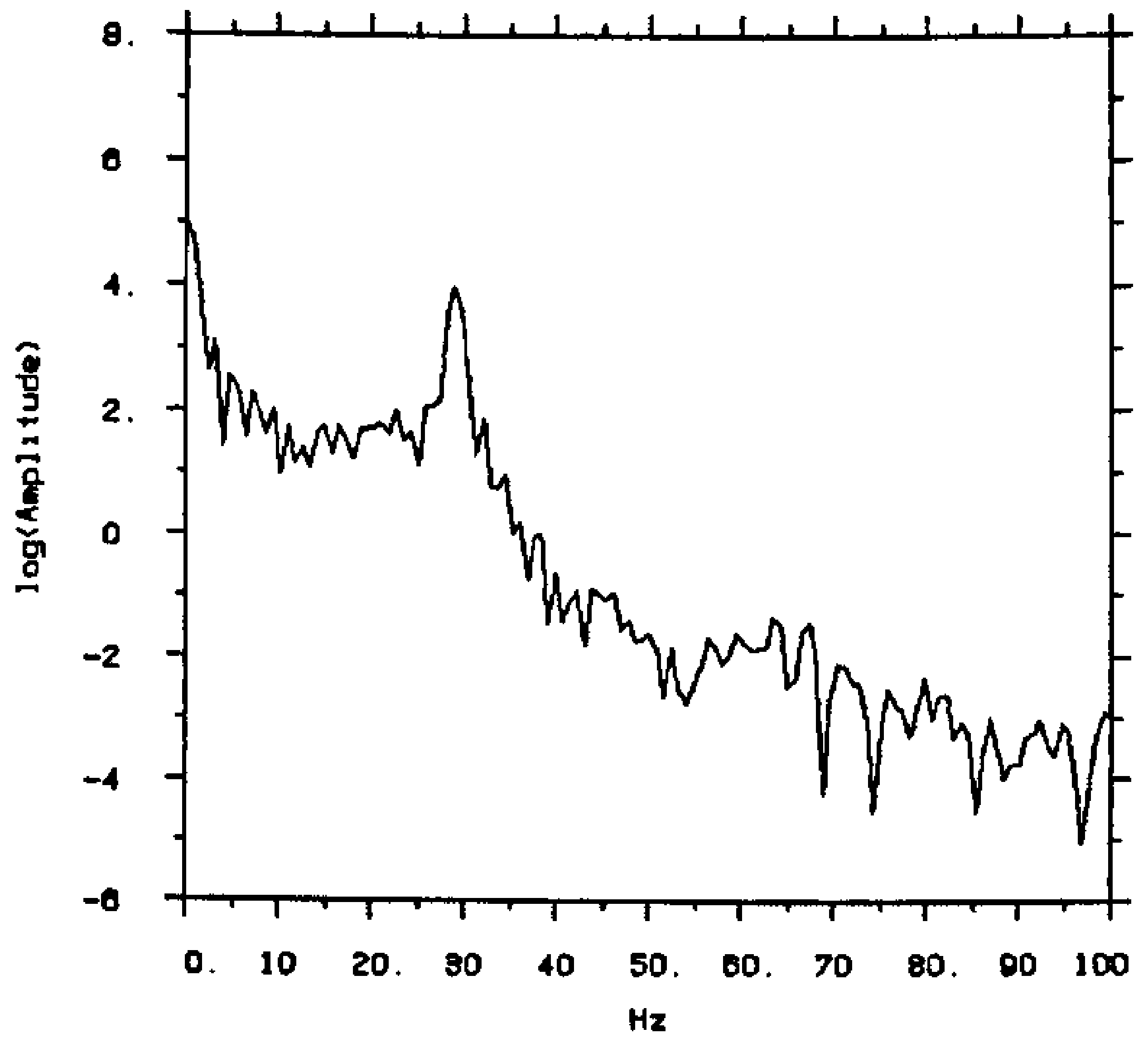

Figure 4.10 Docton Geometry Transient a) Side Force and b) Yawing Moment Coefficient Autospectral Densities

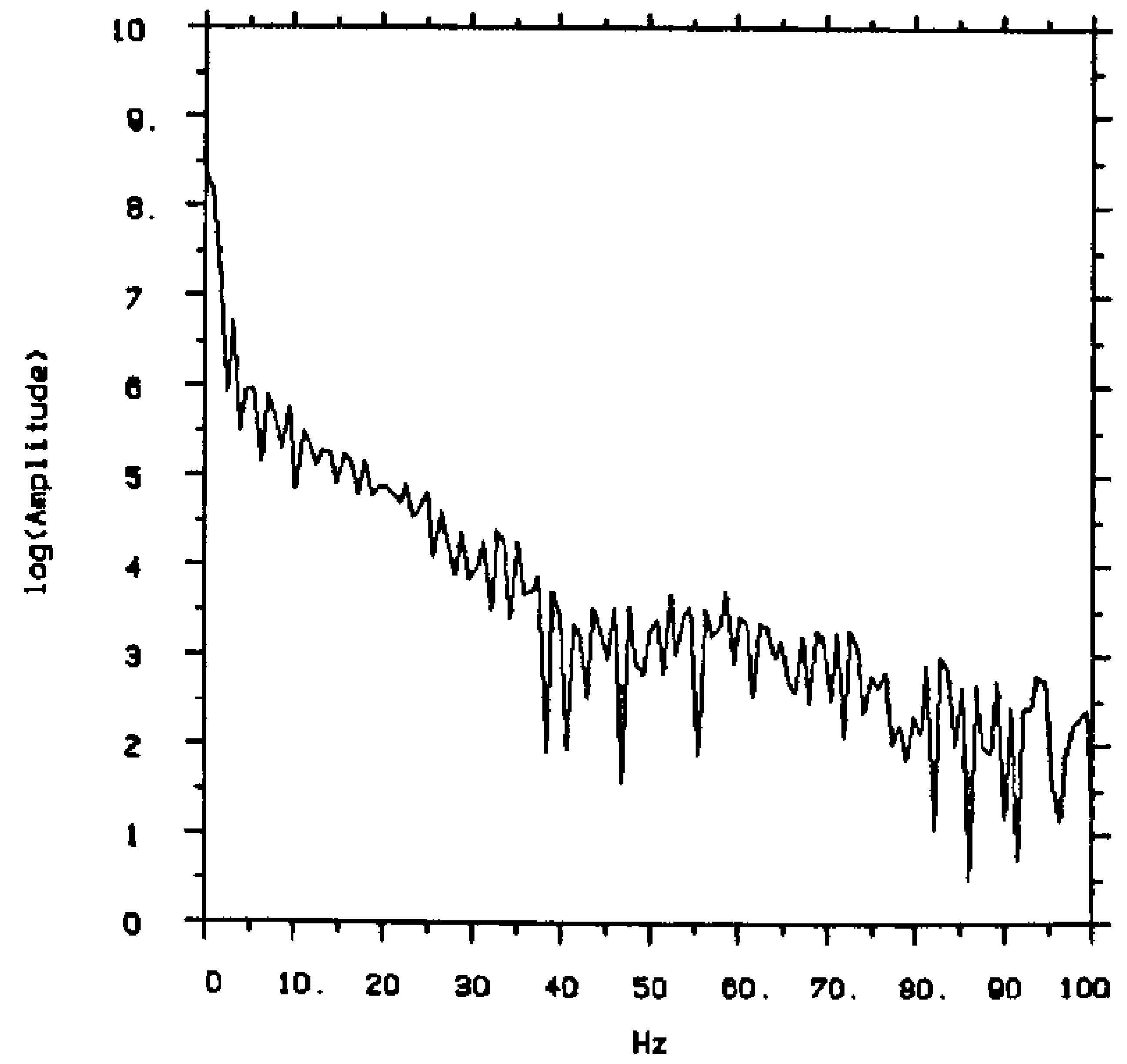

Figure 4.11 Empty Working Section Yaw Angle Autospectral Density

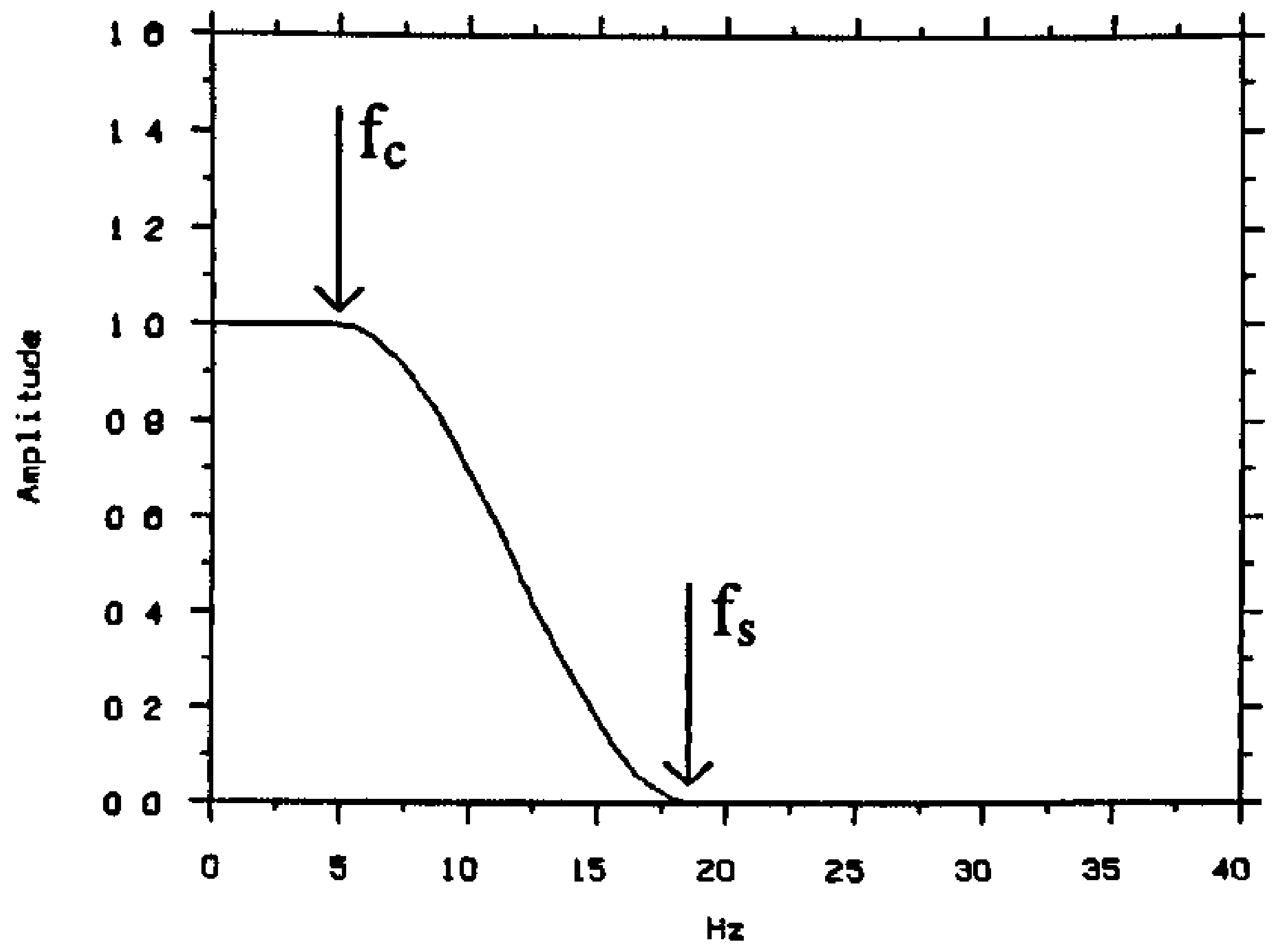

Figure 4.12 Force Balance Low Pass Filter Geometry

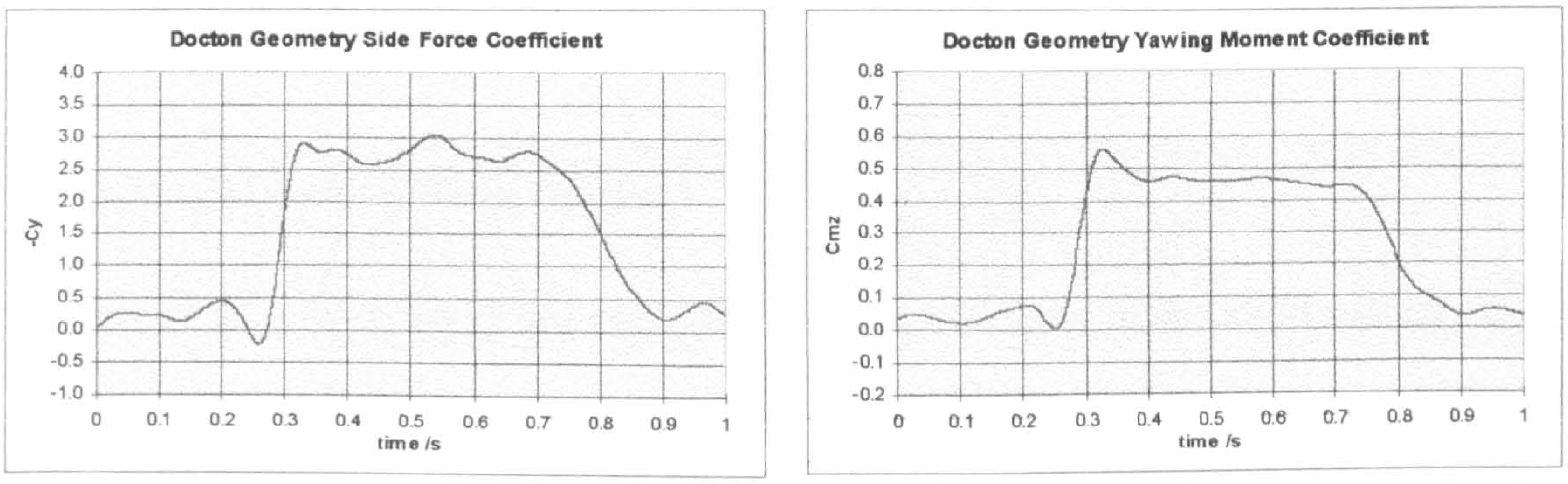
a) Side Force

b) Yawing Moment

Figure 4.13 Typical Side Force and Yawing Moment Force Balance Data

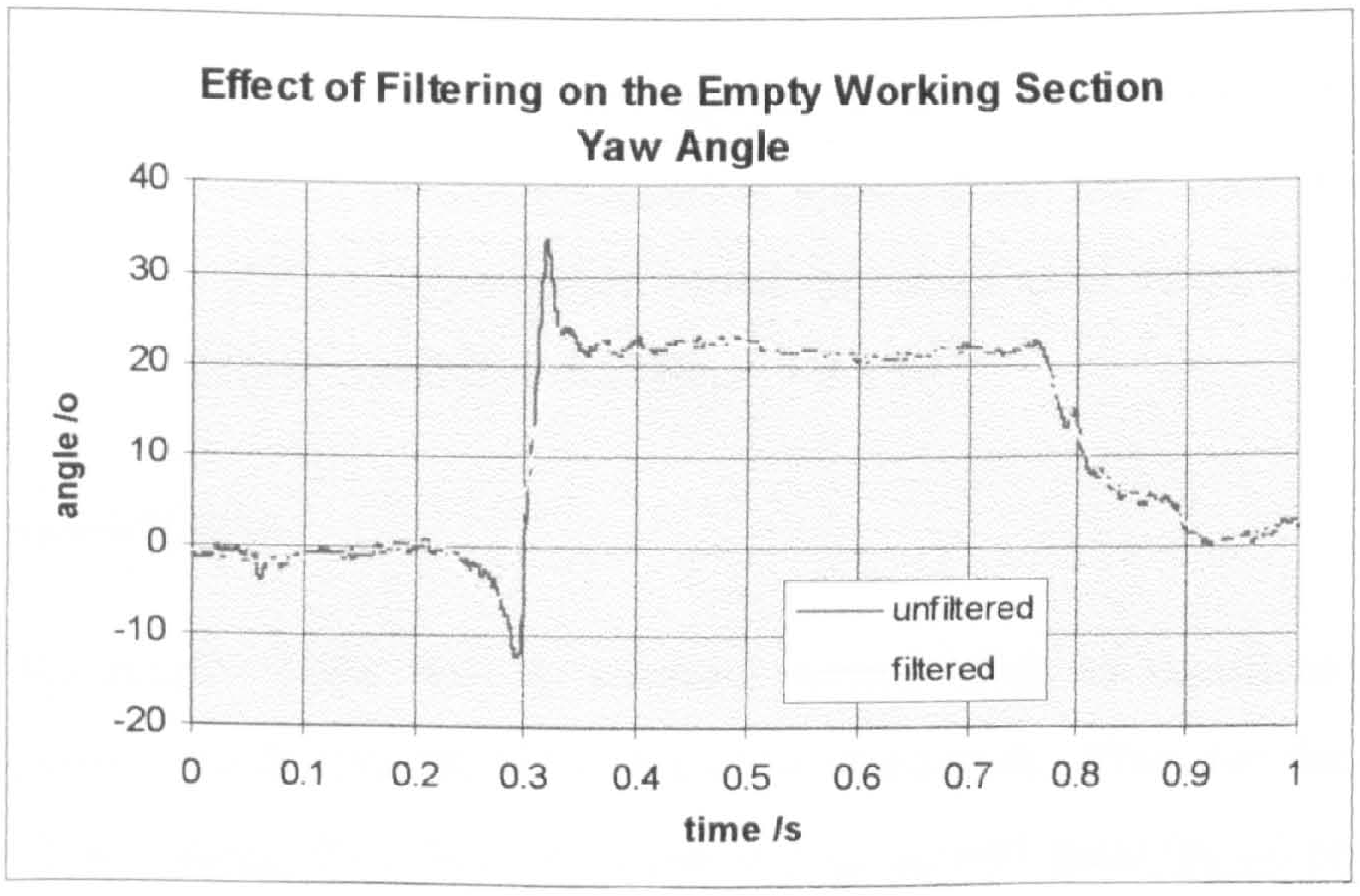

Figure 4.14 Effect of Low Pass Filtering on the Empty Working Section Yaw Angle

Chapter Five

Experimental and Computational Investigations

5.1 Experimental Technique

5.1.1 Cross-Wind Gust Matching Process

Correct formation of the cross-wind gust requires matching of the axial velocity of the main tunnel, the axial component of the cross-wind tunnel and the speed of propagation of shutter opening (section 3.1). Matching of the two tunnel velocities was achieved by examination of the axial velocity component, measured at the model centre in the empty working section, for a set of gusts, and if necessary adjustment of the axial tunnel velocity. The correct shutter propagation speed was then set to be the nominal tunnel axial velocity, as measured during the matching process. It was found that changes to the axial tunnel velocity (and shutter propagation speed) were rarely required, hence the tunnel matching process was only repeated at approximate four week intervals. The nominal experimental Reynolds number, based on tunnel axial velocity, model length, and standard atmospheric conditions was $Re_l = 3.9 \times 10^5$.

5.1.2 Non-Dimensionalisation

The transient nature of the flow in working section leads to significant changes in dynamic pressure during the duration of a cross-wind gust. Thus for the purposes of non-dimensionalisation, the reference dynamic (p_{dyn_ref}) and static (p_{s_ref}) pressures were measured on a daily basis under steady axial freestream conditions, prior to any transient experiments. All non-dimensional coefficients, as defined in equations (5.1-5.7), are then formed using these reference pressures.

Total pressure coefficient:

$$Cp_o = \frac{p_o - p_{s\_ref}}{p_{dyn\_ref}} \qquad (5.1)$$

Static pressure coefficient:

$$Cp_s = \frac{p_s - p_{s\_ref}}{p_{dyn\_ref}} \qquad (5.2)$$

Velocity coefficient:

$$Cv_i = \frac{v_i}{u_{ref}} \qquad (5.3)$$

where v_i represents a velocity in one of the three orthogonal directions x, y or z and u_{ref} is the reference freestream axial velocity, as defined in (5.5).

Reference freestream velocity:

$$u_{ref} = \sqrt{\frac{2 \times p_{dyn\_ref}}{\rho}} \qquad (5.5)$$

where ρ is the density of air.

General force coefficient:

$$Cf = \frac{F}{p_{dyn\_ref} \times A} \qquad (5.6)$$

where F is a force and A the model frontal area.

General moment coefficient

$$\mathrm{Cm} = \frac{\mathrm{M}}{p_{dyn\_ref} \times A \times l} \tag{5.7}$$

where M is a moment and l is the model length.

Empty working section data are presented as working section yaw angle, ψ, as defined in (5.8).

$$\psi = \tan^{-1}\left(\frac{-v}{u}\right) \tag{5.8}$$

where v is the cross-stream velocity and u the axial velocity.

Wake data are presented as non-dimensional vorticity, ξ, as defined in (5.9).

$$\xi = \frac{l}{u_{ref}} \times \left(\frac{\partial w}{\partial y} - \frac{\partial v}{\partial z}\right) \tag{5.9}$$

5.1.3 Ensemble Averaging

The rapid nature of gust production possible with this new facility (1000/hr) allows phase synchronised averaging of data to improve the signal to noise ratio (so called 'ensemble averaging'). The phase synchronisation is realised through the trigger signal that initiates data logging at a fixed time prior to every cross-wind gust (section 4.7). The effect of varying the number of averages used for a particular data set was investigated for both typical five hole probe and surface static pressure tapping data.

Figure 5.1 shows total pressure coefficient (Cp_o) against time for a fixed point in the wake of the Durham geometry (x/l = 1.5, y/l = -0.24, z/l = 0.24 where x is the axial distance from the nose of the model, y the cross-stream distance from the model centreline, z the vertical distance above the groundboard, and l the model length), as recorded by the five hole probe. The number of gusts used to create each average is given by 'n-ens'. It is apparent from these results that ensemble averaging is essential for the collection of meaningful aerodynamic data. Although the signal to noise ratio continues to increase throughout the range of gust numbers used, experimental run and battery charge time dictate a practical maximum. Thus all five hole probe data were averaged over 20 cross-wind gusts.

Figure 5.2 shows that a similar increase in quality of static pressure coefficient data (Cp_s) for a surface pressure tapping is also achieved by ensemble averaging. These data are for tapping 7 on the front leeward corner of the Docton geometry (figure 4.2), a position at which the flow remains attached for the duration of a cross-wind gust (figure 6.11, s/S = 0.127). Again an ensemble average of 20 gusts were used for all surface static pressure data, with this offering a good compromise between data quality and time requirements.

5.2 Experimental Investigations

5.2.1 General Overview

The first part of the experimental investigation was to conduct a survey of the empty working section under both transient and nominally steady (time-averaged) axial and yawed flow conditions. This was required to provide accurate information about the gust characteristics that the aerodynamic models would be subjected to. For all the transient investigations a cross-wind gust length of 5.0m was used.

This was followed by aerodynamic investigations on the two models. These primarily consisted of surface static pressure distribution measurements, wake surveys and direct force and moment measurements. Data was collected for both transient and steady axial and yawed flow conditions. Again, a cross-wind gust length of 5.0m (10 model lengths) was used for all transient investigations. The main focus of the analysis was to investigate if any differences occur in the force and moment coefficients between transient and comparable steady flow conditions, and if so, what were the flow structures responsible for these differences.

5.2.2 Empty Working Section Survey

The empty working section survey was conducted in the x-y plane (horizontal) at a height equal to the mid height of the aerodynamic models. The gridpoint spacing was 100mm in both directions, giving an overall grid dimension of 29 x 9 points. The survey was completed for steady axial, yawed and transient flow conditions. The steady yawed flow was created using both cross-wind and axial jets. The limited range of the traverse system, and in the case of the transient flow the number of cross-wind gusts available from a single battery charge, required the survey be completed in several sections. The subsequent successful assembly of these sections gave good confidence in the repeatability of the wind tunnel configuration and experimental technique. The transient survey required some 5,500 cross-wind gusts.

A 'pseudo' turbulence intensity was measured at the assumed model centre under steady axial and yawed flow conditions. This was done using a single element hot-wire mounted in a vertical orientation. The turbulence intensity was taken as the quotient of the resultant velocity standard deviation, $\sigma(u_r)$, and mean, $\bar{u}_r$, expressed as a percentage, as defined in equation (5.10).

$$Tu = \frac{\sigma(u_r)}{\bar{u}_r} \times 100 \qquad (5.10)$$

5.2.3 The Docton Geometry

In addition to surface static pressure and force measurements, an x-y plane (horizontal) wake survey was conducted around the sides and rear of the Docton geometry. The grid used was of non-uniform density, however had an average spacing of about 25mm. The grid contained some 560 points, requiring nearly 12,000 cross-wind gusts.

Docton geometry direct force measurements were limited to side force, yawing moment and drag components, with each of these being measured under steady axial, yawed and transient flow conditions.

The steady yawed flow condition was created by subjecting the model to flow from both jets, as opposed to yawing the model in the working section, as this permits exact comparison with the fully developed transient yawed flow.

5.2.4 The Durham Geometry

More detailed investigations were made into the flow structure of the Durham geometry. In addition to the surface static pressure and direct force measurements several wake surveys were conducted.

Steady axial, yawed and transient wake surveys were conducted at three y-z (vertical, perpendicular to the freestream direction) planes downstream of the model. The downstream distances used were $x/l = 0.75$, 1.3 and 1.5, where x represents distance from the leading edge of the model and l is the model length. The surveys were conducted on a 20mm x 20mm grid, with each plane having 29 points in the cross-stream direction and 12 in the vertical direction, thus requiring over 7,000 cross-wind gusts per plane.

Quasi-steady wake surveys were conducted at $x/l = 1.5$ for yaw angles of $\psi = 0^0, 7^0, 14^0$ and 22^0. For these surveys the relative yaw angle of the flow to the model was obtained by yawing the model in the working section, and subjecting it to only the main jet. The surveys were conducted with the traverse plane perpendicular to the main axis of the geometry for all yaw angles, allowing direct comparison with the other wake surveys.

Two steady wake surveys (axial flow and $\psi = 22^\circ$ yawed flow) were conducted on a 10mm grid spacing and used for the purposes of wake integration. The finer grid spacing was used in an attempt to improve the accuracy of the integration. The yawed flow condition was again created by yawing the model in the axial jet. This produced problems of blockage, whereby the model was in close proximity to the shear layer at the leeward side of the tunnel, however it was thought to be preferable to the yawed flow condition created using both jets, which exhibits some spatial total pressure variations (section 7.1.1).

The method used for the wake integration was that of the simple momentum equation. Although the wake surveys were carried out over a large area ($-0.7 \leq y/l \leq 0.7$ and $0.04 \leq z/l \leq 0.46$) the area used for the integration was reduced. It was hoped that this would increase accuracy by eliminating any effects of the free shear layers at the sides of the jet. For the axial flow case, the area used for the integration was $-0.31 \leq y/l \leq 0.31$ and $0.04 \leq z/l \leq 0.46$, and for the yawed flow case the area was $-0.27 \leq y/l \leq 0.57$ and $0.04 \leq z/l \leq 0.46$. The contribution made to drag and side force from the groundboard boundary layer was kept to a minimum by not surveying below $z = 20$mm ($z/l = 0.04$).

The wake integration method allows the drag and side forces to be split in viscous and vortex terms. The viscous term represents energy loss through fluid entrainment into the boundary layer and wake of the body, while the vortex term represents the energy required to maintain secondary flow. In addition, the numerical evaluation of drag or side force from discrete data points in the wake allows comparison of the relative contributions from these discrete points - so called ‘microdrag’ and ‘microside’. The wake integration method, including viscous and vortex terms and microdrag and microside is fully discussed in Appendix B.

Force balance data were recorded for all six components of force and moment under steady axial, yawed and transient flow conditions.

5.3 Computational Fluid Dynamics

Computational investigations were initially undertaken using the commercially available PHOENICS code, as used by Docton [61]. This code proved to have serious limitations, in that difficulty was encountered in obtaining a solution for a two-dimensional computation of the flow around a radiused body (the Docton geometry), and hence was abandoned. Simulations were subsequently undertaken using the commercially available StarCD code (version 3.10) and in the light of experimental data obtained from the empty working section these computations were focused on the flow in the empty working section.

The advantages of conducting a computationally based investigation were twofold. Firstly, it allowed the wind tunnel configuration, including the boundary conditions, to be easily manipulated, and secondly it permitted more detailed quantitative analysis of the flowfield parameters. The CFD subsequently provided significant insight that could not have been achieved experimentally. The investigation was limited to the empty working section, with a two-dimensional assumption made that significantly reduced hardware demands and calculation times.

As the computation was not required to provide a solution for regions of separated or stagnating flow, which have caused significant solution problems for flow around bluff bodies, for example see [108, 109, 110], it was considered that parameters such as turbulence model, differencing scheme and solution method would have little effect on the results, and it is for this reason that they are not discussed in detail.

5.3.1 Computational Grid and Boundary Conditions

Figure 5.3 shows a schematic of the outline of the computational grid used (A-C-D-E). The extent of the working section, as defined by the ground board, is shown by the dashed line. A representative model position is shown by the black rectangle, although no model was included for these calculations. The grid consisted of approximately 27,000 identical cells of aspect ratio 1.02 (264 in the streamwise direction and 104 in the cross-stream direction). A solution was obtained for an approximate 61,000 cell grid (grid density increased by a factor of 1.5 in both directions) that showed little difference to the 27,000 cell grid, suggesting the solution from the coarser grid was relatively grid independent.

The transient cross-wind boundary condition was prescribed as follows. The cross-wind shutter inlet region (A-B in figure 5.3) was split into 30 discrete inlets such that each inlet represented a single shutter exiting into the working section. The computation time domain was split into 61 discrete time regions. For the initial time region, the entire boundary A-B was represented as a solid wall. As the computation stepped through the time regions, discrete wall boundaries were replaced by inlet boundaries, with the required inlet conditions, in a process analogous to the opening of the shutters in the experimental facility. The change from wall to inlet condition for each inlet was instantaneous, such that it represented a shutter opening in an infinitesimal time. Each inlet region remained as an inlet for a predetermined time, equal to the shutter open time in the experimental facility, before reverting back a wall condition. The inlet conditions were prescribed as fixed velocity components, equal to those from the experimental facility.

The axial jet inlet boundary, which was not time dependent, was also set as a fixed velocity inlet. Boundaries B-C, C-D and D-E (figure 5.3) were fixed pressure boundaries, and hence were located sufficiently far from the working section that this condition would have little affect on the flow in the region of interest. Boundary E-F was set as a wall boundary. For an accurate replication of the experimental facility boundary E-F should have been of the fixed pressure type, however this led to numerically unstable solutions, and hence the wall condition was imposed.

5.3.2 Solution Method

The solution was calculated as an incompressible flow field. The standard k-ξ turbulence model was used with a self-filtered central differencing scheme. Self-filtered central differencing is a blended upwind and central differencing scheme with the blending factor determined by the local gradients, such that in areas of steep gradients the blending factor has a strong bias towards the central differencing scheme [111]. Wall functions were used for solid boundary conditions.

Prior to a transient solution being undertaken a steady solution was calculated for the axial flow condition. From this starting condition a full transient solution took around 2hrs to converge.

The main area of investigation for the CFD study was the effect of the rough honeycomb flow straightener and associated thick boundary layer along the cross-wind inlet. Two conditions were examined. The first modelled the wall as a smooth surface with a no-slip condition imposed. The second modelled the wall as a rough surface, which consequently produced a much thicker boundary layer. Selection of wall roughness parameters was by comparison of the region of total pressure loss along the wall from the steady axial flow computation to that observed under comparable conditions in the experimental facility.

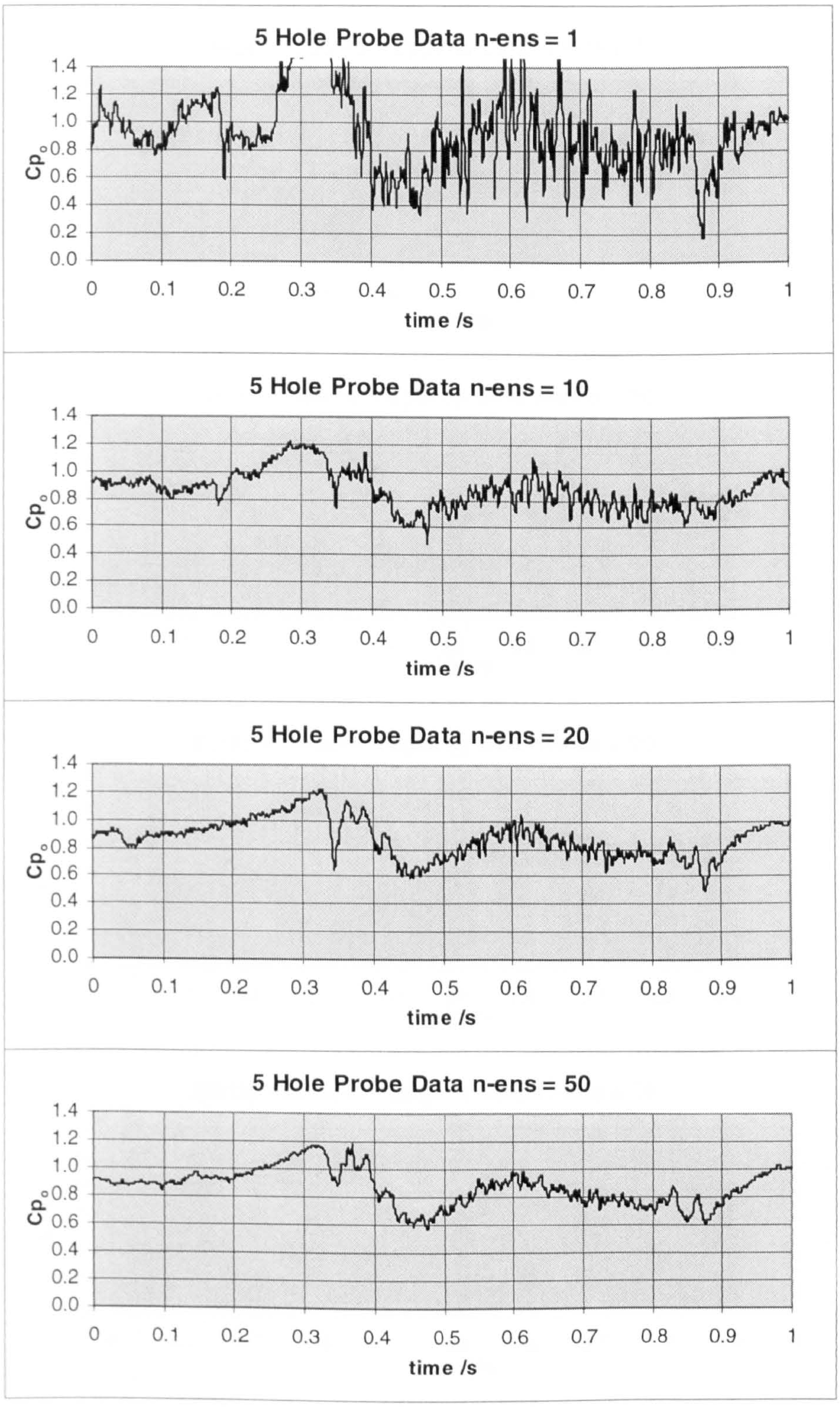

Figure 5.1 Effect of Ensemble Average on Five Hole Probe Data

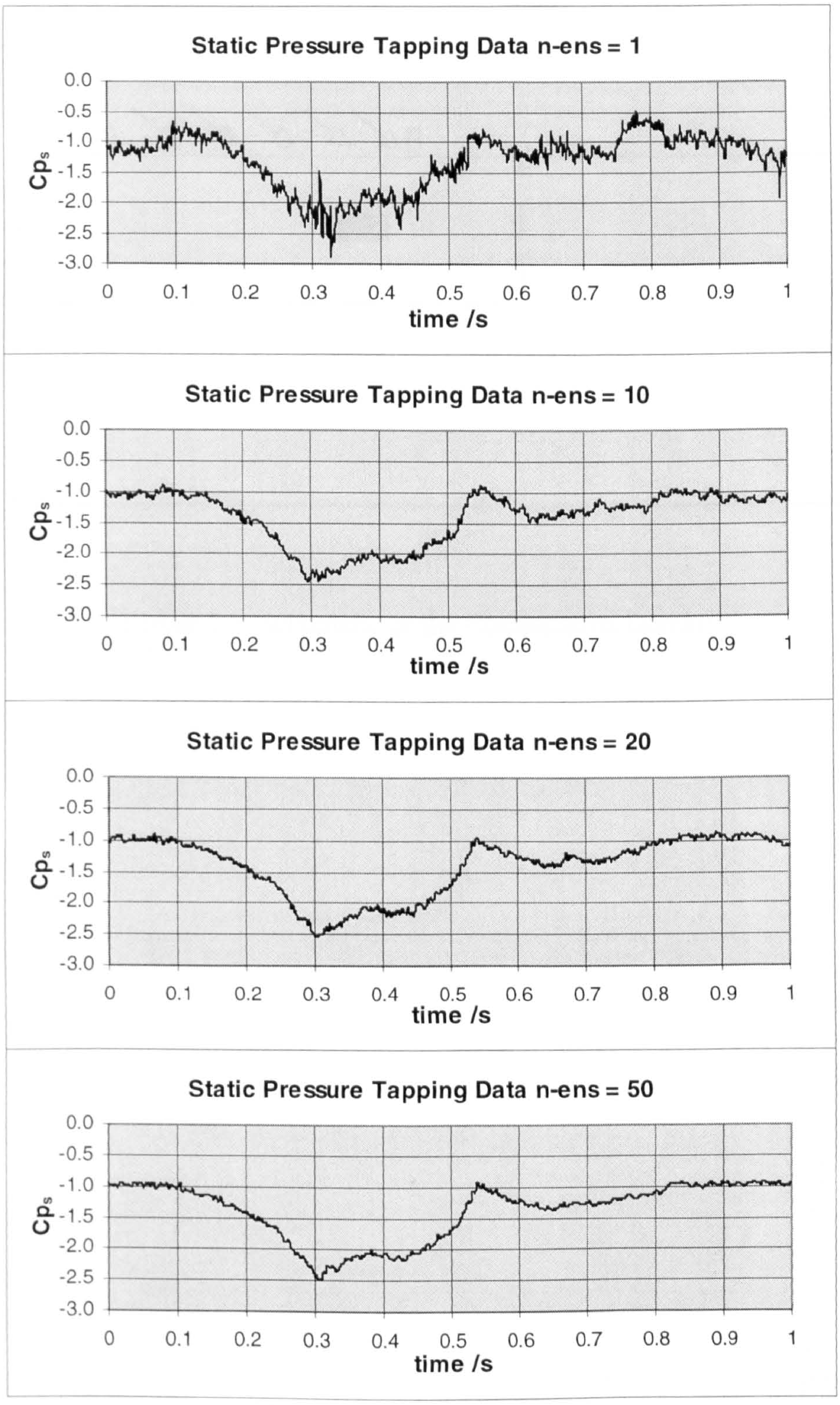

Figure 5.2 Effect of Ensemble Average on Static Pressure Tapping Data

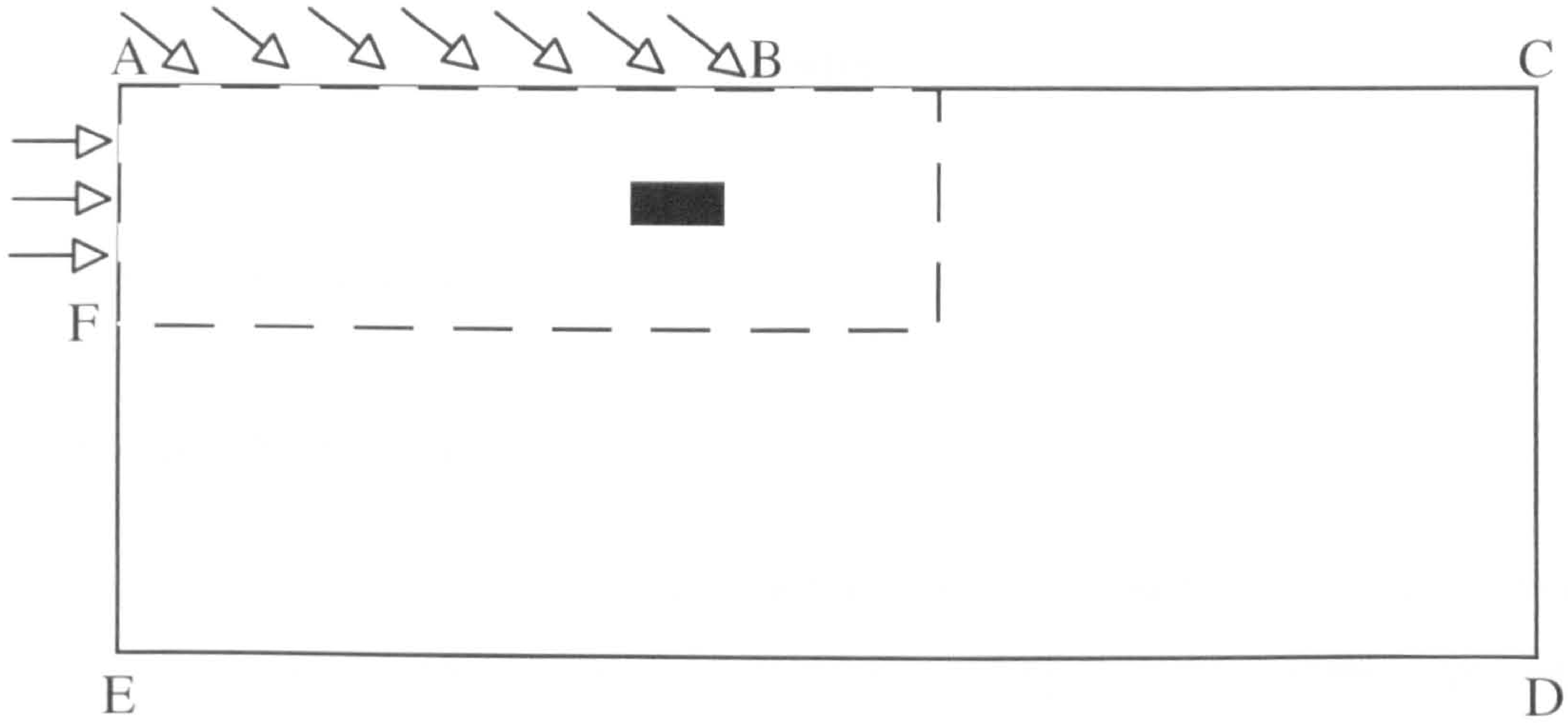

Figure 5.3 Schematic of the Computation Domain

Chapter Six

Results

6.1 Empty Working Section

6.1.1 Empty Working Section Survey

Figures 6.1 - 6.6 show contours of the important flow quantities in the empty working section as the transient cross-wind gust develops. They are: yaw angle (figure 6.1), cross-stream (y) velocity coefficient (figure 6.2), modified velocity vectors (figure 6.3), total pressure coefficient (figure 6.4), streamwise (x) velocity coefficient (figure 6.5) and static pressure coefficient (figure 6.6). Contour intervals for each quantity are defined on the last sheet of each figure. No data is available for x < 200mm, as the presence of a concrete pillar beside the wind tunnel prevented the traverse from reaching this region, however the flow in this region was of little interest as it was upstream of the cross-wind inlet. Similarly the furthest reach of the traverse in the y direction was 800mm. This was limited by the length of the probe mounting stem. Lengthening the stem would have allowed the traverse to travel further, but also increased the amplitude of vibration at the probe head, and hence a practical maximum length was used. The modified velocity vectors of figure 6.3 are velocity vectors with each vector having its axial direction component reduced by a velocity corresponding to the freestream velocity. Thus they are what an observer would see if moving along the working section at a velocity equal to the axial velocity. This adds clarity to the processes occurring at the leading edge of the cross-wind gust.

Animations of the empty working section yaw angle (ewsyaw.avi) and total pressure coefficient (ewscpo.avi) are available on the CD-ROM that accompanies this Thesis.

These may be viewed on any Windows based media player. The animations cover the time period $0.0\text{s} \leq t \leq 1.0\text{s}$ with the frames at 6.25×10^{-3}s increments.

With the exception of the CFD all zero times are synchronised.

6.1.2 Associated Results

Figure 6.7 shows total pressure, as recorded in the cross-wind tunnel upstream of the shutter mechanism at a position corresponding to fluid that subsequently passes through the upstream shutters. The first shutter opens at $t = 0.089$s.

Figure 6.8 shows time dependent total pressure coefficient traces for two positions in the working section, as indicated on the graphs.

6.1.3 Gust Characteristics at the Model Centre

Figure 6.9 presents time histories of empty working section yaw angle, streamwise and cross-stream velocity coefficients, and total, dynamic and static pressure coefficients. The time histories are for $x = 2400$mm, $y = 400$mm, $z = 97$mm, which corresponds to the model centre in the working section at mid-model height. Comparisons are drawn with the steady axial and yawed flow conditions for yaw angle and dynamic pressure coefficient. The steady axial flow pseudo turbulence intensity, as defined in equation 5.10, was $Tu = 3.4\%$, with the steady yawed flow pseudo turbulence intensity being $Tu = 2.6\%$. The axial flow condition represents the turbulence intensity of the main jet, whereas the yawed flow turbulence intensity is that of the cross-wind jet.

6.2 The Docton Geometry

6.2.1 Surface Static Pressure Data

Figure 6.10 and 6.11 show respectively steady axial and yawed, and transient pressure distributions around the Docton geometry. The surface static pressures are plotted against 's/S', the non-dimensional distance around the model perimeter, where 's' is the distance of the tapping around the perimeter and 'S' is the half perimeter of the geometry. Pressures are plotted against this quantity as it allows better resolution of the pressures on the front and rear faces.

Figures 6.12 - 6.14 are the integrated pressure side force, yawing moment and drag coefficients. The integrated pressure side force is obtained by multiplying the surface static pressure (figure 6.10 and 6.11) by a projected area (as viewed in the y direction) for each tapping and summing these over the surface of the model. It should be noted that a positive pressure on the windward side contributes a negative side force, whereas a positive pressure on the leeward side contributes a positive side force. The yawing moment is obtained in a similar manner, however the distance from the moment centre to each tapping is included, as are the contributions from the front and rear faces of the model. The drag coefficient is obtained in a similar manner to the side force, however the faces of interest are the front and rear faces of the model. The yawed side force is nominally negative (away from the cross-wind), but for ease of viewing -Cy has been plotted. This is true for all subsequent side force graphs.

The forces and moments, as directly measured by the two component balance, are presented in figures 6.15 - 6.17.

6.2.3 Wake Traverse Data

Figure 6.18 presents the transient total pressure coefficient obtained from the two dimensional horizontal (x-y) wake traverse around the sides and rear of the Docton geometry. The domain is non-dimensionalised by 'l', the model length. The model outline is shown by the thin black line, with the white region being excluded from the probe measurements. Data that was out of range of the probe calibration is presented as black in this and all subsequent figures. An animation of the total pressure coefficient (docwkcpo.avi) is available on the accompanying CD-ROM. This covers the time period $0.0s \leq t \leq 1.0s$ with the frames at $6.25 \times 10^{-3}s$ increments.

6.3 The Durham Geometry

6.3.1 Steady Flow

Figures 6.19 - 6.22 present results for steady axial flow and figures 6.23 - 6.26 results for steady yawed flow. Figure 6.19 and 6.23 are the surface static pressure distributions under axial and yawed flow respectively. Contour plots of the surface static pressures are shown, along with line graphs corresponding to discrete sets of pressure tappings which aid a more quantitative analysis of the surface pressures. To aid clarity different contour levels are used for each surface of the model. For the geometry sides, two rows of tappings are shown, 'lw' corresponds to lower windward, row 1 in figure 4.5, with 'uw' being upper windward, corresponding to row 3 in figure 4.5. Similarly 'll' and 'ul' for the leeward side. The upper surface line graph is from the centreline of the geometry (figure 4.5). The line graphs show surface static pressure coefficient against 'x/l', where x is the axial distance from the nose, and l the length of the model.

Figures 6.20 and 6.24 show surface oil flow visualisation, using flourescent dye and photographed under ultra-violet light, for steady axial and yawed flow respectively.

Figures 6.21 - 22 and 6.25 - 26 are contour plots of vorticity and total pressure coefficient contours from the wake surveys. Contour plot domains are non-dimensionalised by l, the model length. Figure 6.27 shows contour plots of vorticity from the quasi-steady wake traverse (5.2.4).

6.3.2 Transient Flow

Time-dependent surface static pressure data for times t = 0.10s, 0.30s and 0.34s are presented in figures 6.28 - 6.30. Note again that for reasons of clarity different contour levels are used for each surface of the model. These three times correspond to an axial flow condition (t = 0.10s), approximate cross-wind onset (t = 0.30s) and approximate post cross-wind yaw angle overshoot (t = 0.34s). The latter two are only approximate, as at any one time during transient flow development different parts of the model are subjected to different flow conditions. Side data for two subsequent times are shown in figures 6.31 and 6.32. The first time (t = 0.47s) is when the transient side force equals the steady yawed side force, with the second time (t = 0.52s) corresponding to the maximum transient side force and yawing moment. Figures 6.33 and 6.34 show roof surface static pressures at times of t = 0.45s, 0.55s, 0.74s and 0.76s. The first time (t = 0.45s) is when the transient upper surface lift equals the steady yawed upper surface lift, and the second time (t = 0.55s) the maximum upper surface lift. The final two times (t = 0.74s and t = 0.76s) correspond to anomalies in the upper surface lift occurring near the end of the cross-wind gust. Note should be made of the change in contour interval between figures 6.33 and 6.34, which was made in an attempt to detect the source of these relatively small anomalies. Animations of the Durham geometry surface static pressure for the windward side (durwincp.avi), leeward side (durleecp.avi) and upper surface (durroocp.avi) are available on the CD-ROM. Integrated pressure side force, yawing moment and upper surface lift coefficients are shown in figures 6.35 - 6.37.

Figure 6.38 shows selected transient vorticity and total pressure coefficient contours for the x/l = 0.75 wakeplane, with similar contours for the x/l = 1.5 wakeplane shown in figure 6.39. The time regions for these two sets are shifted by approximately the time taken for freestream flow to propagate between the two planes (0.035s). Subsequent vorticity and total pressure coefficient contours at times t = 0.52s and t = 0.57s for the x/l = 1.5 wakeplane are shown in figure 6.40. Animations of vorticity (durwkvor.avi) and total pressure coefficient (durwkcpo.avi) for the x/l = 1.5 wakeplane are available on the CD-ROM.

The six components of force and moment, as measured by the two-component force balance in its different orientations, are shown in figure 6.41, with comparisons made with the corresponding steady forces and moments. Autospectral density functions of these forces and moments are seen in Appendix C.

6.3.3 Wake Integration

The drag and side force coefficients, as obtained from the wake integration, are shown in table 6.1.

	Steady Axial Flow	Steady Yawed Flow
Cx	0.40	0.98
Viscous Cx	0.36	0.82
Vortex Cx	0.04	0.16
Cy	0.02	-0.85
Viscous Cy	0.02	-0.78
Vortex Cy	0.0	-0.07

Table 6.1 Durham Geometry Wake Integration Results

Figure 6.42 shows the total pressure coefficient, microdrag and viscous and vortex contributions to microdrag, as obtained from the axial flow survey. The total pressure coefficient contours show the extent of the survey plane, with the integration carried out over the reduced area shown in the microdrag contours (section 5.2.4). Figure 6.43 shows the yawed wake traverse total pressure coefficient contours and microdrag and microside contours. Again the extent of the traverse is indicated in the total pressure coefficient contours, with the integration performed over the area shown in the microdrag and microside contours.

6.4 Computation Fluid Dynamics

Figure 6.44 shows the empty working section yaw angle as obtained from the CFD simulation. Attempts have been made to synchronise the CFD and experimental times, however difficulty in estimating the exact time between the shutters opening and cross-wind fluid entering the working section for the experimental facility means this may not be exact. The corresponding total pressure coefficient contours are shown in figure 6.45.

Figure 6.46 and figure 6.47 show the empty working section yaw angle at x = 2400mm, y = 632mm. Figure 6.46 is with the rough honeycomb flow straightener modelled along the cross-wind inlet and figure 6.47 is the smooth wall with the no-slip condition.

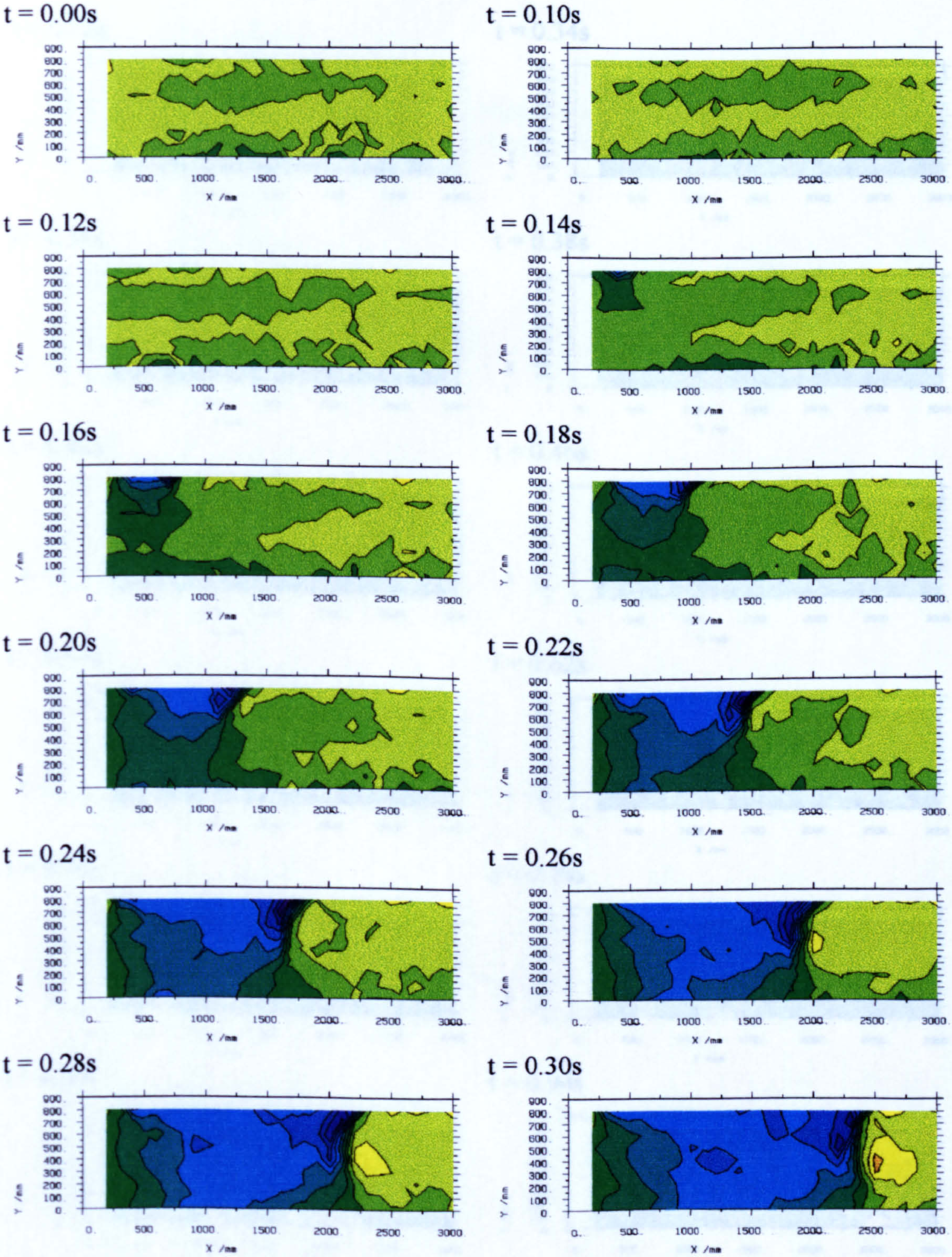

t = 0.00s

t = 0.10s

t = 0.12s

t = 0.14s

t = 0.16s

t = 0.18s

t = 0.20s

t = 0.22s

t = 0.24s

t = 0.26s

t = 0.28s

t = 0.30s

Figure 6.1 (page 1 of 3) Empty Working Section Transient Yaw Angle

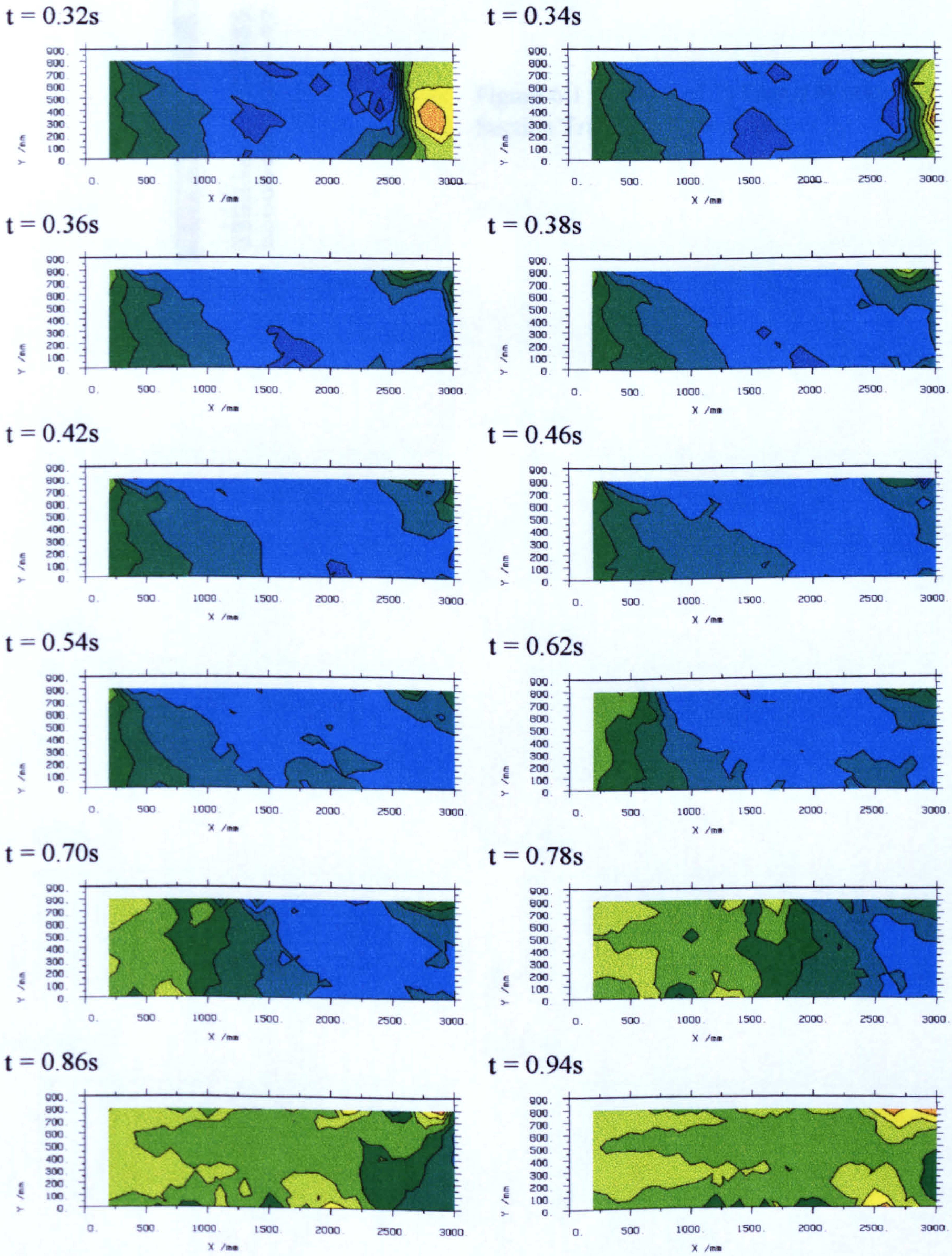
t = 0.32s

t = 0.34s

t = 0.36s

t = 0.38s

t = 0.42s

t = 0.46s

t = 0.54s

t = 0.62s

t = 0.70s

t = 0.78s

t = 0.86s

t = 0.94s

Figure 6.1 (page 2 of 3) Empty Working Section Transient Yaw Angle

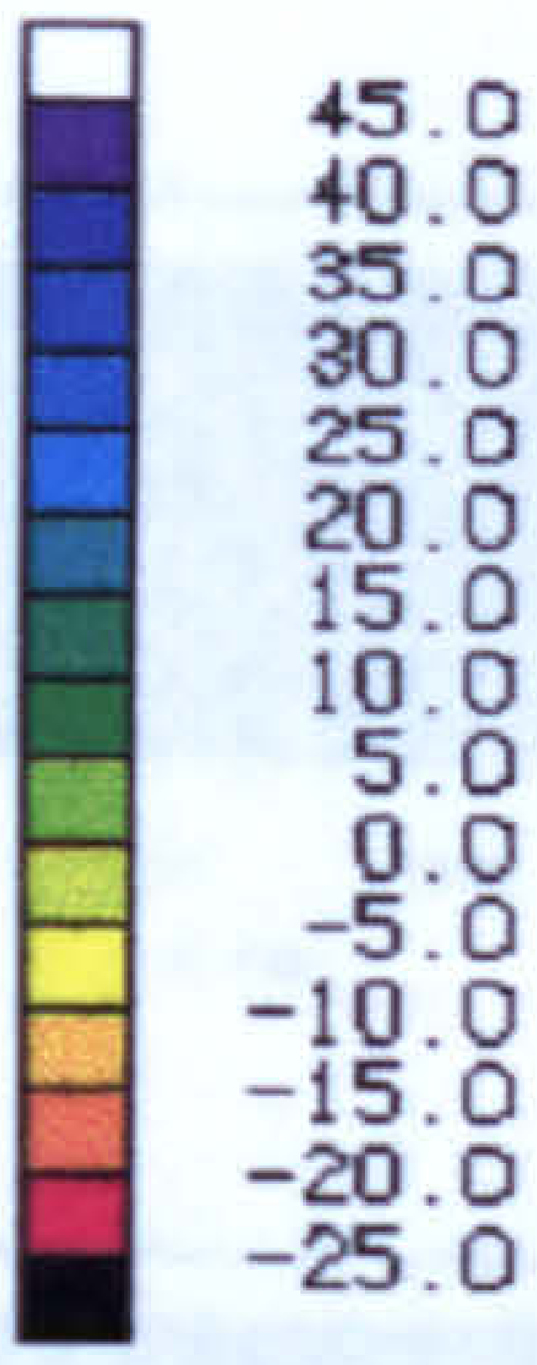

Figure 6.1 (page 3 of 3) Empty Working Section Transient Yaw Angle

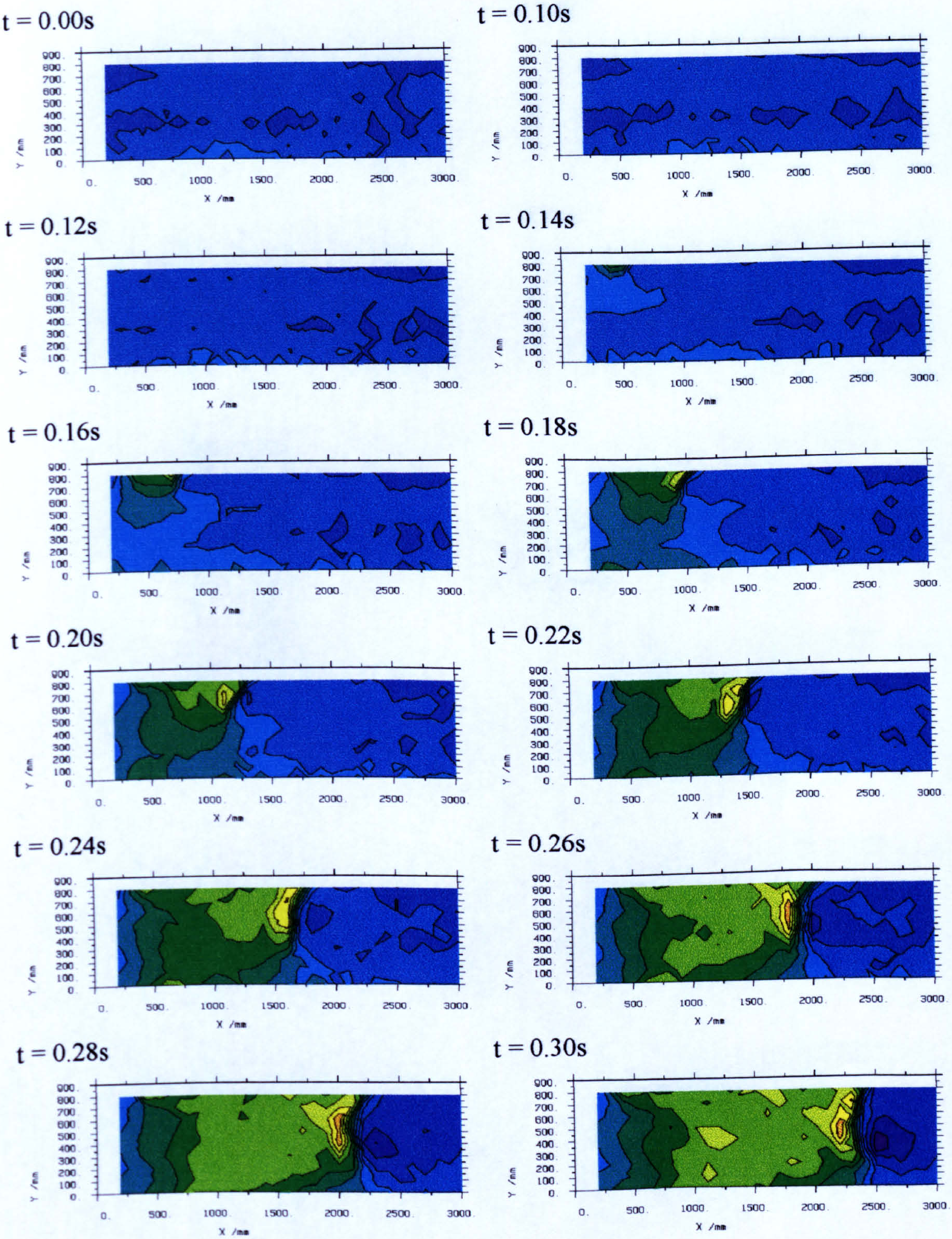

t = 0.00s

t = 0.10s

t = 0.12s

t = 0.14s

t = 0.16s

t = 0.18s

t = 0.20s

t = 0.22s

t = 0.24s

t = 0.26s

t = 0.28s

t = 0.30s

Figure 6.2 (page 1 of 2) Empty Working Section Transient Cross-Stream Velocity Coefficients

t = 0.32s

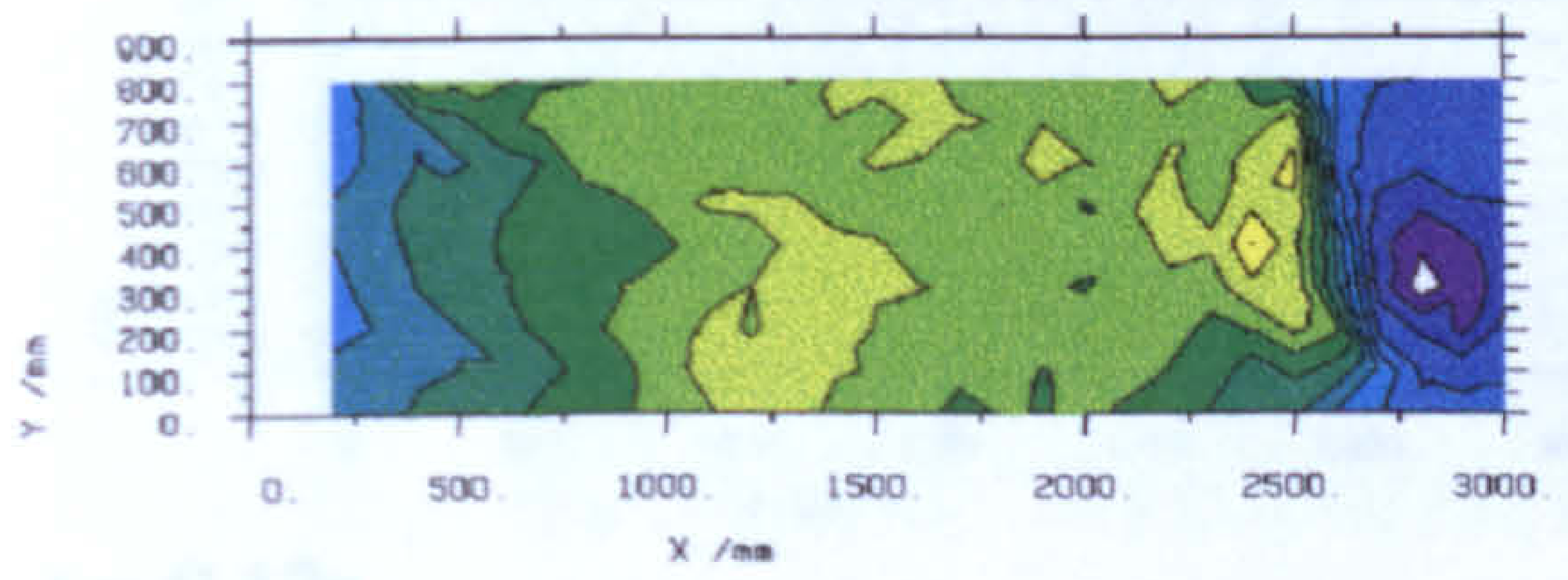

t = 0.34s

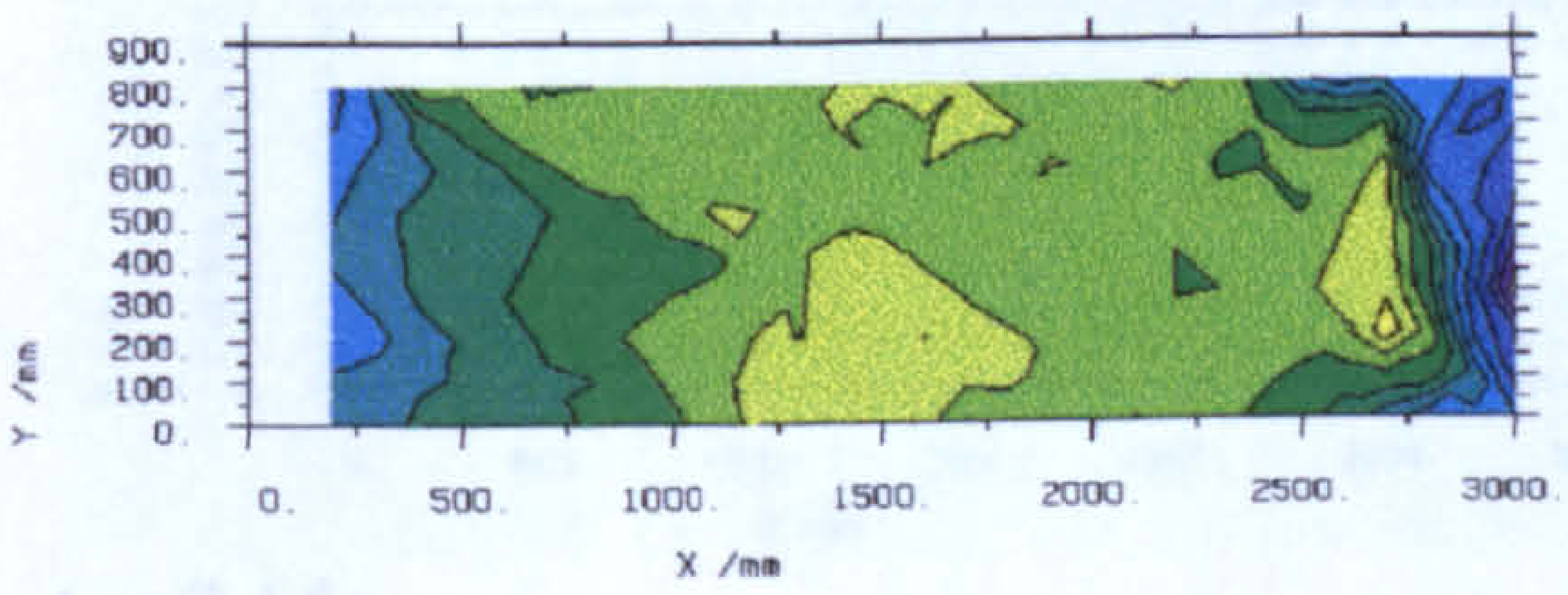

t = 0.36s

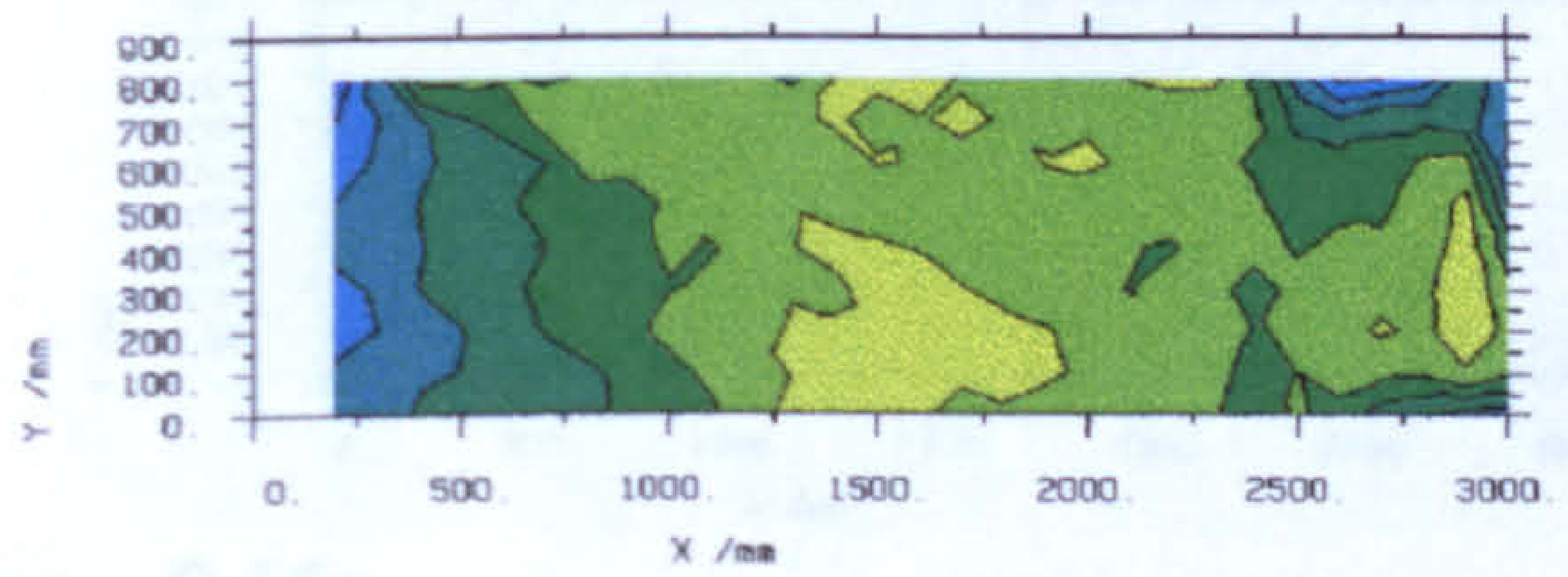

t = 0.38s

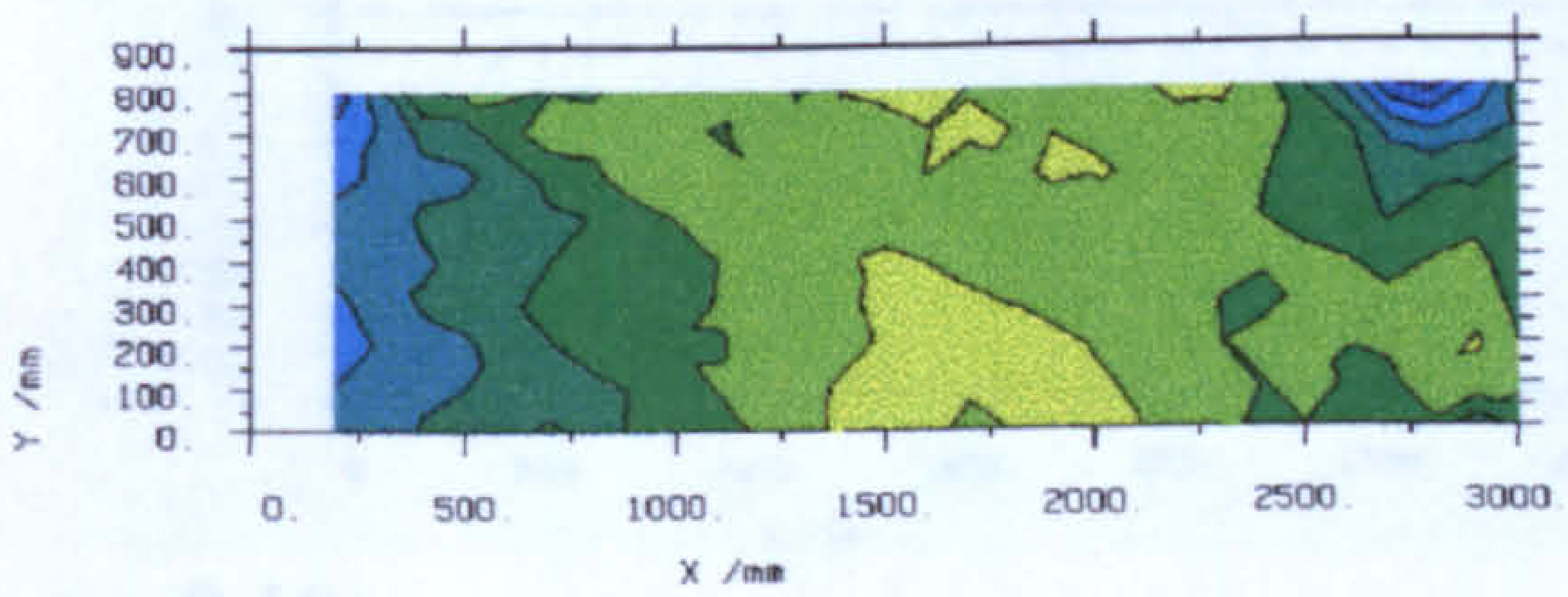

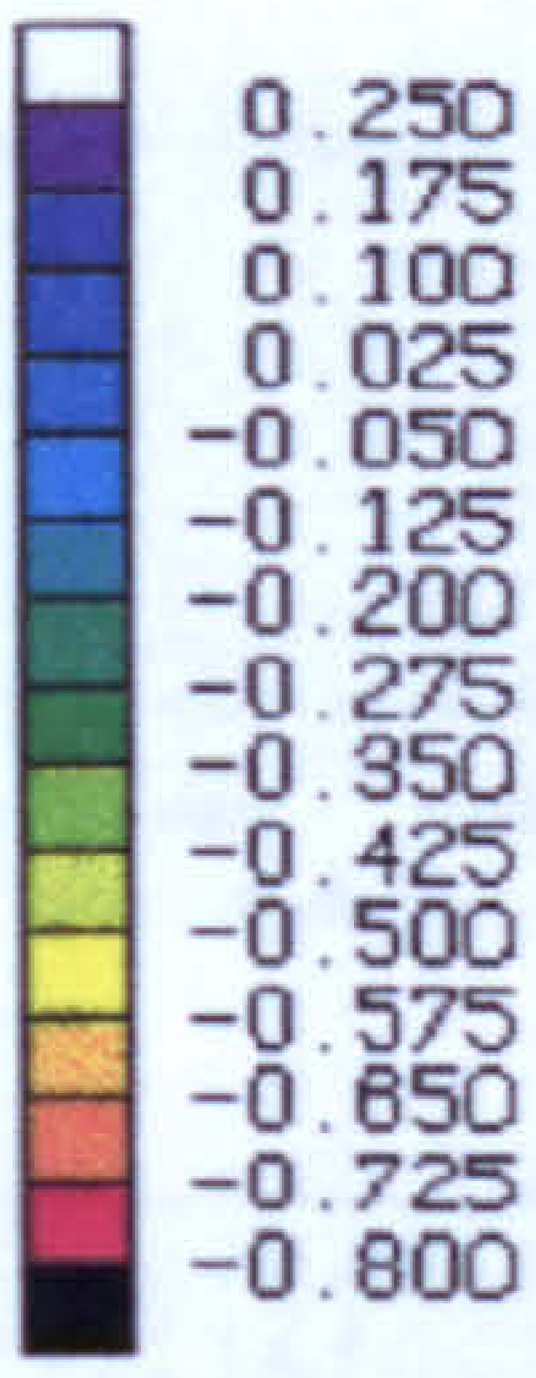

Figure 6.2 (page 2 of 2) Empty Working Section Transient Cross-Stream Velocity Coefficients

t = 0.00s

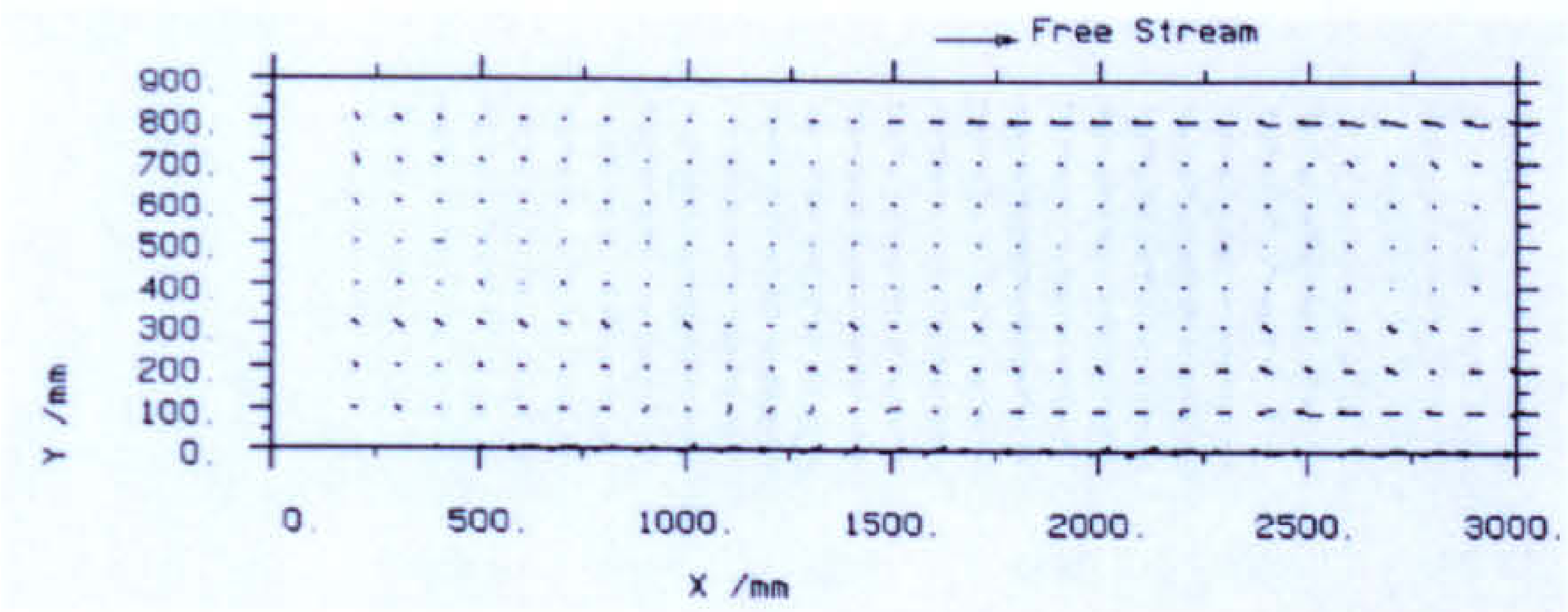

t = 0.10s

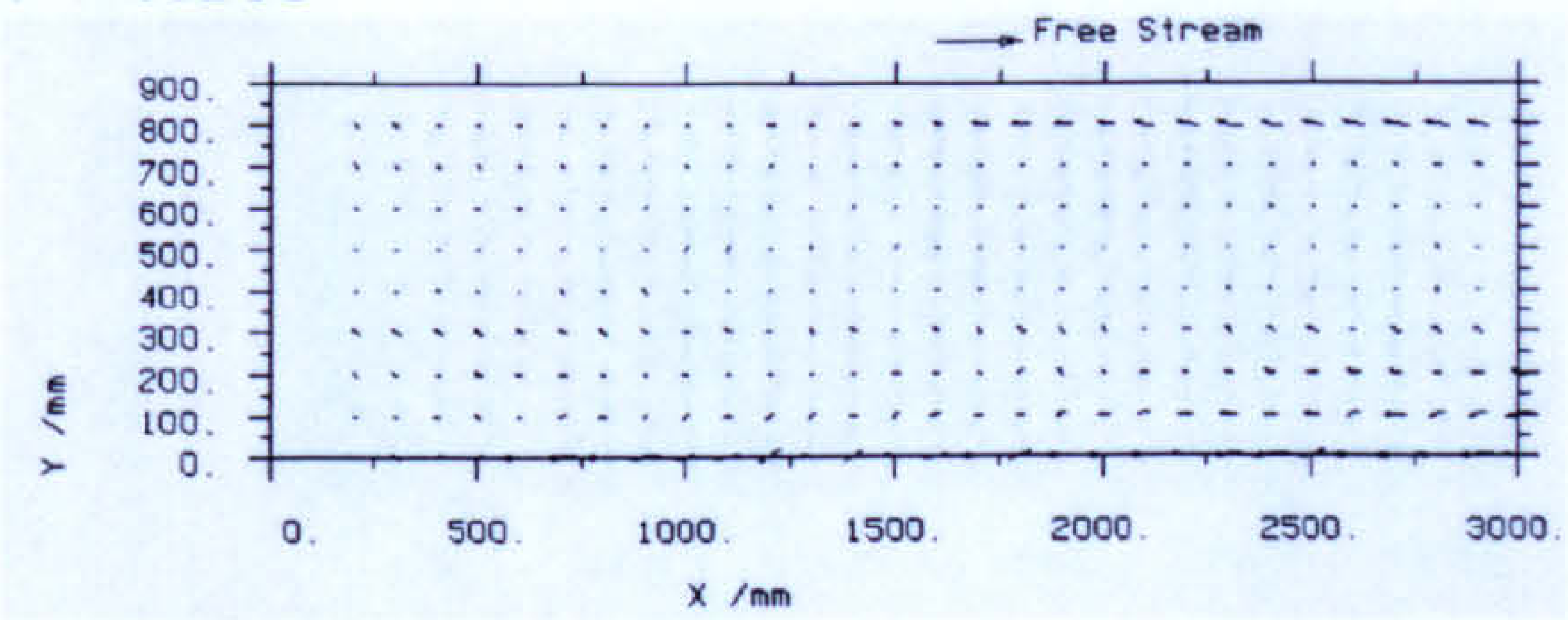

t = 0.12s

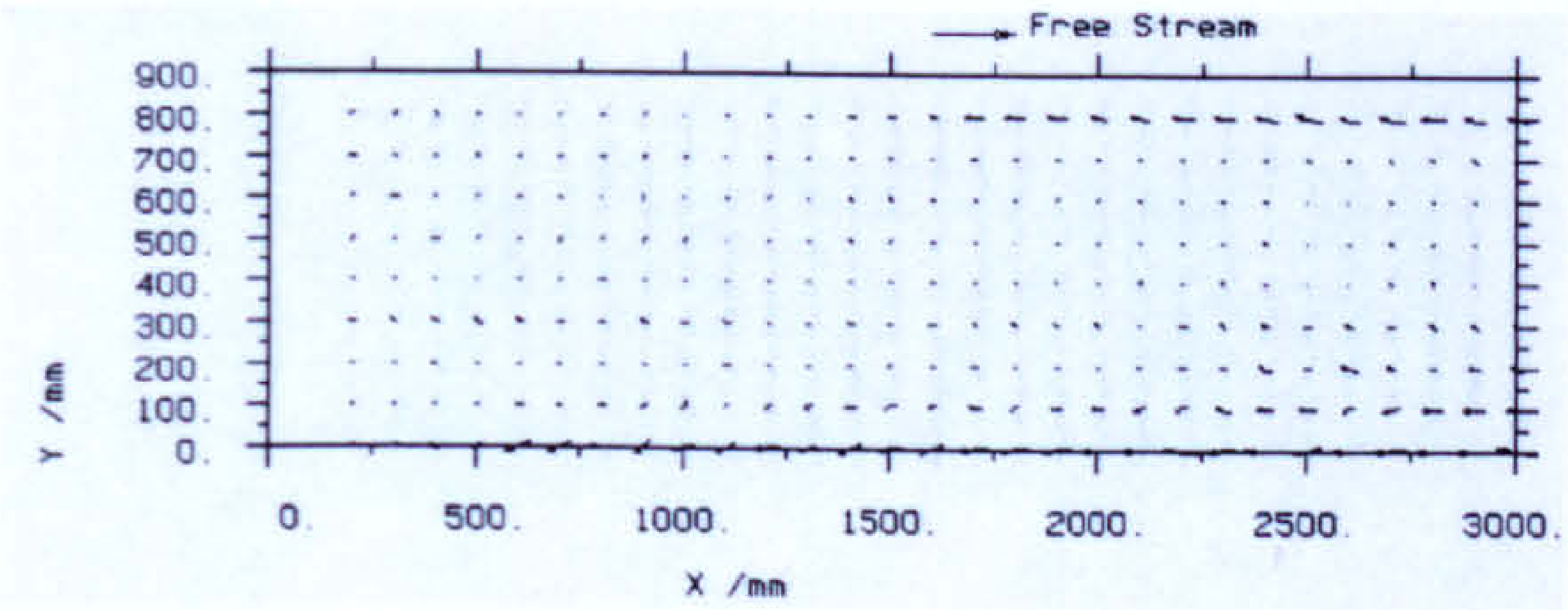

t = 0.14s

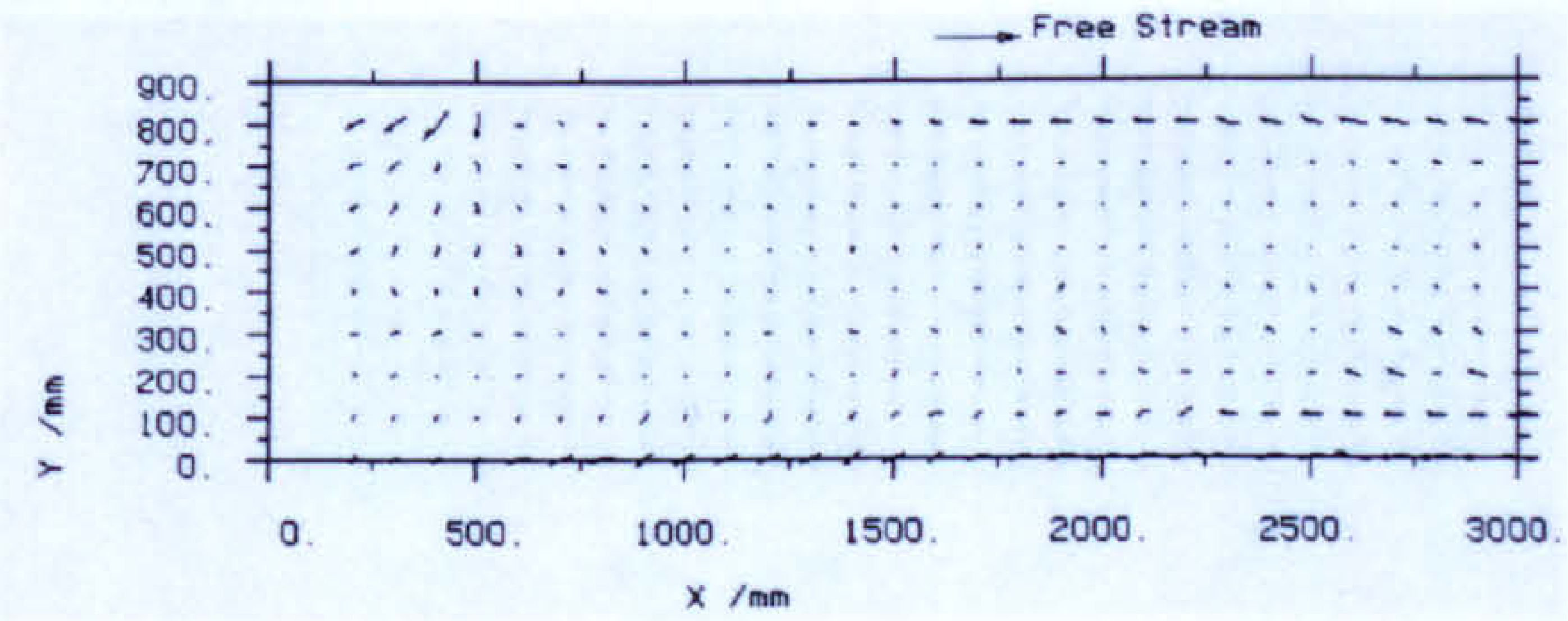

t = 0.16s

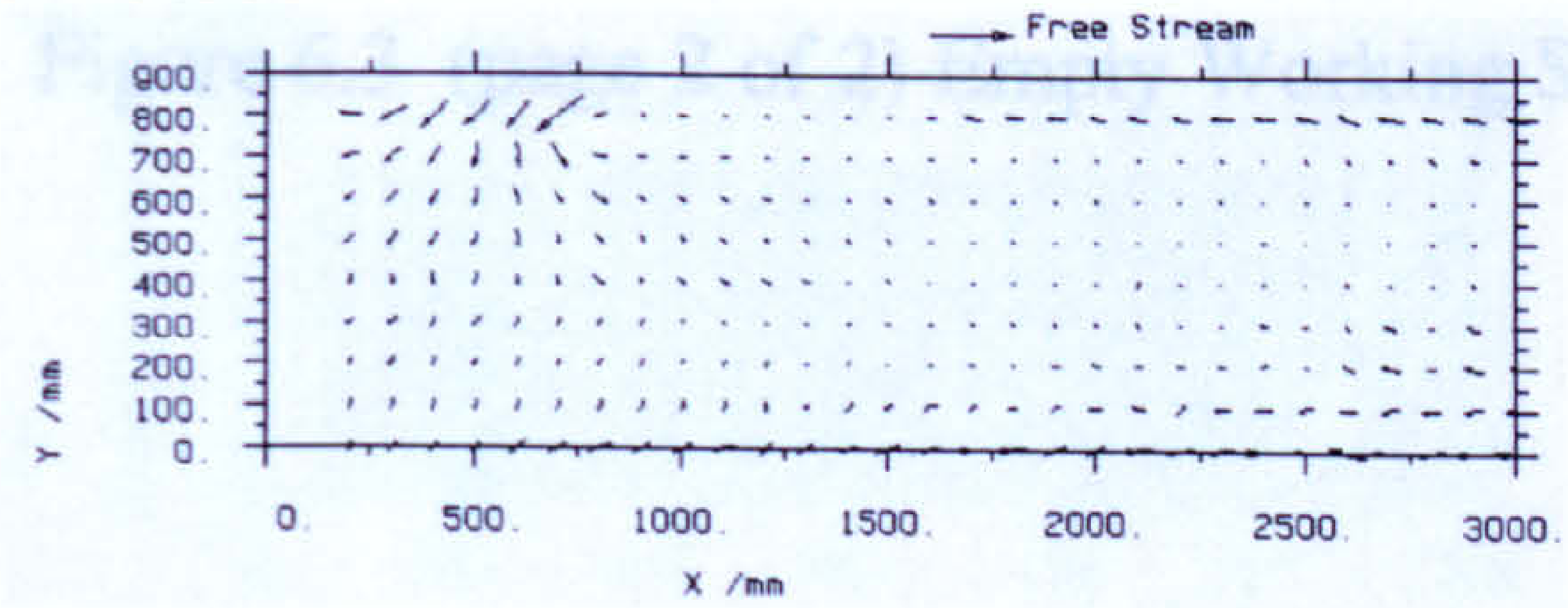

t = 0.18s

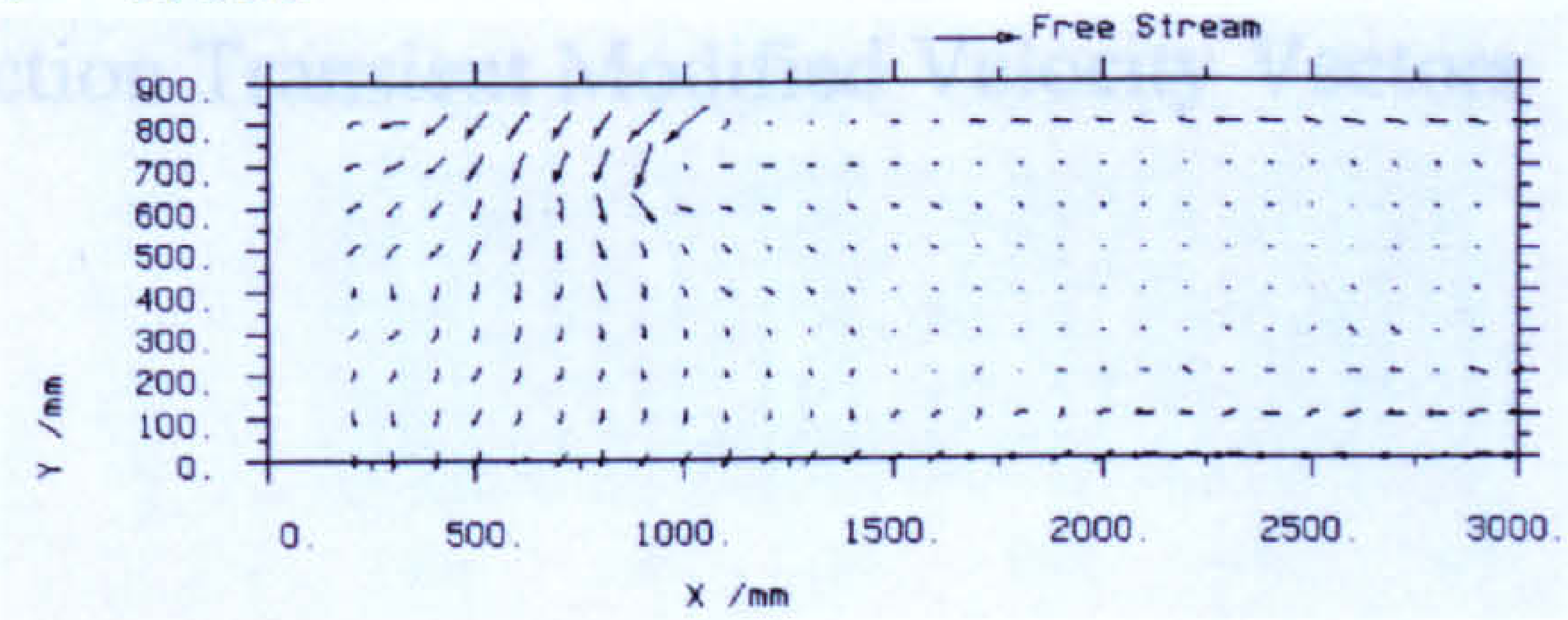

t = 0.20s

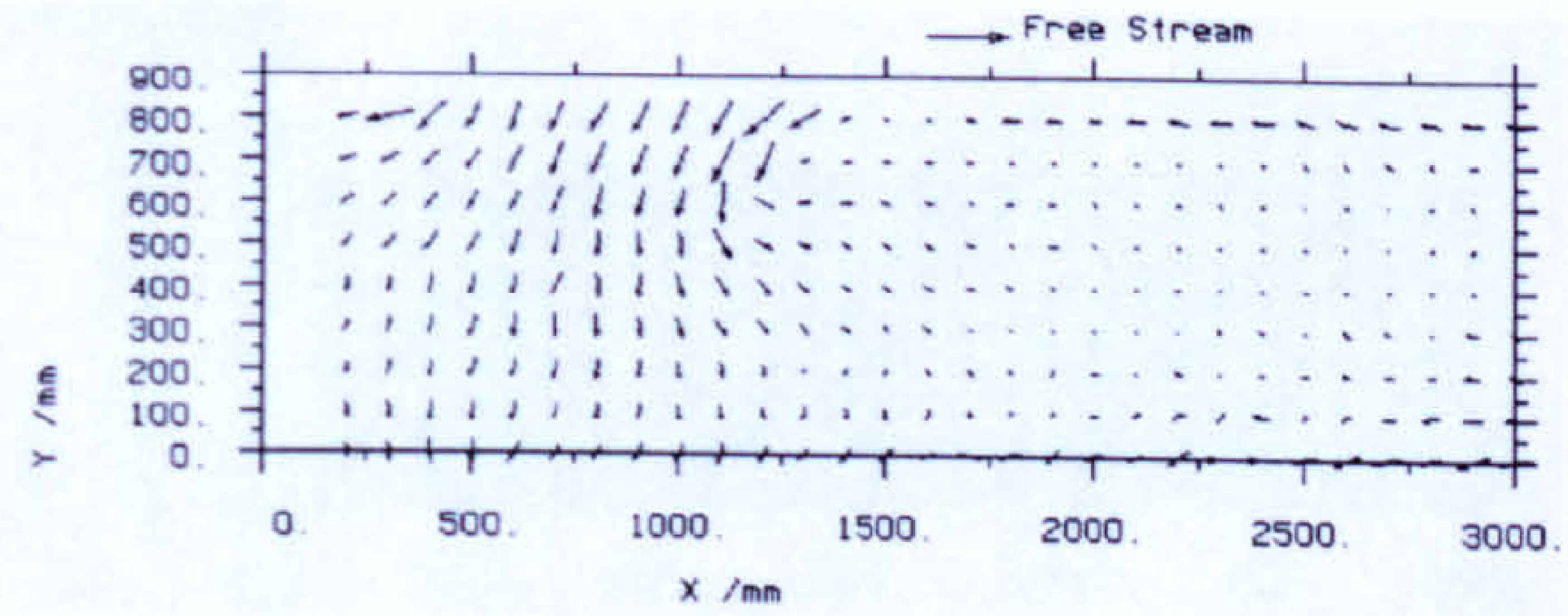

t = 0.22s

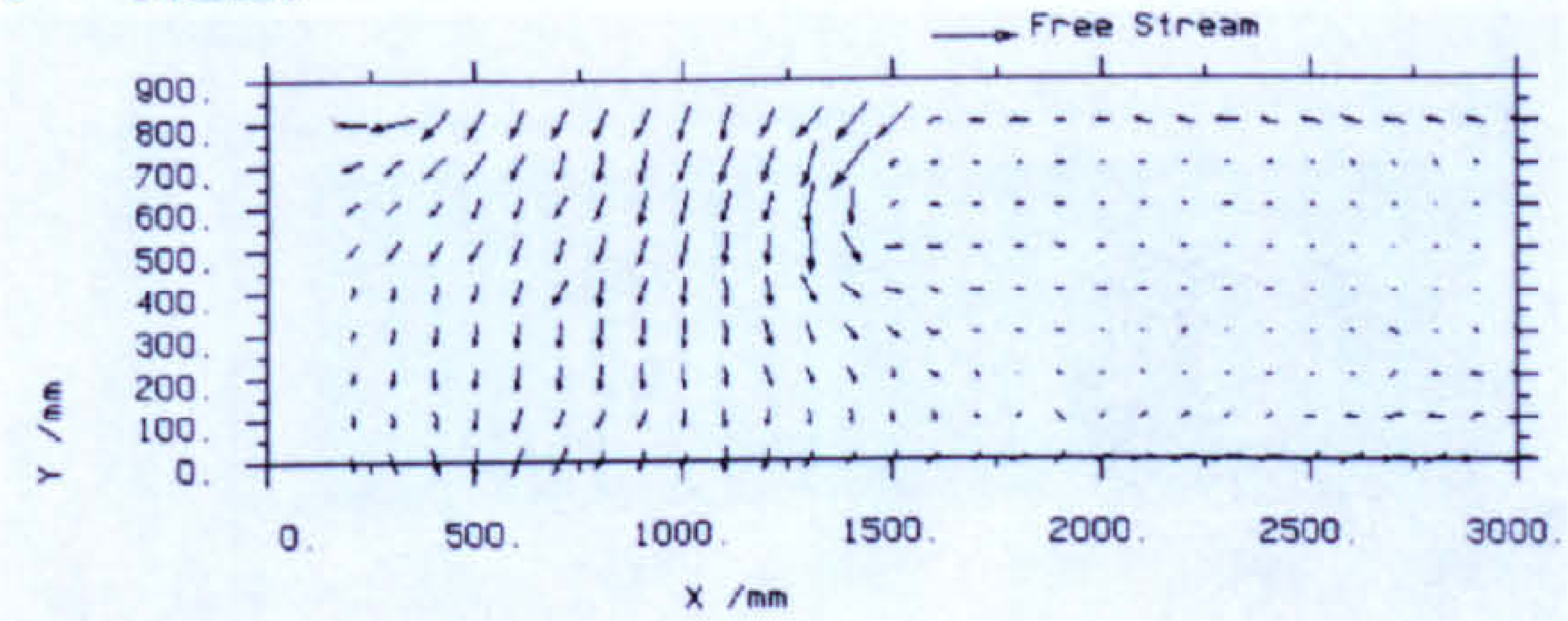

t = 0.24s

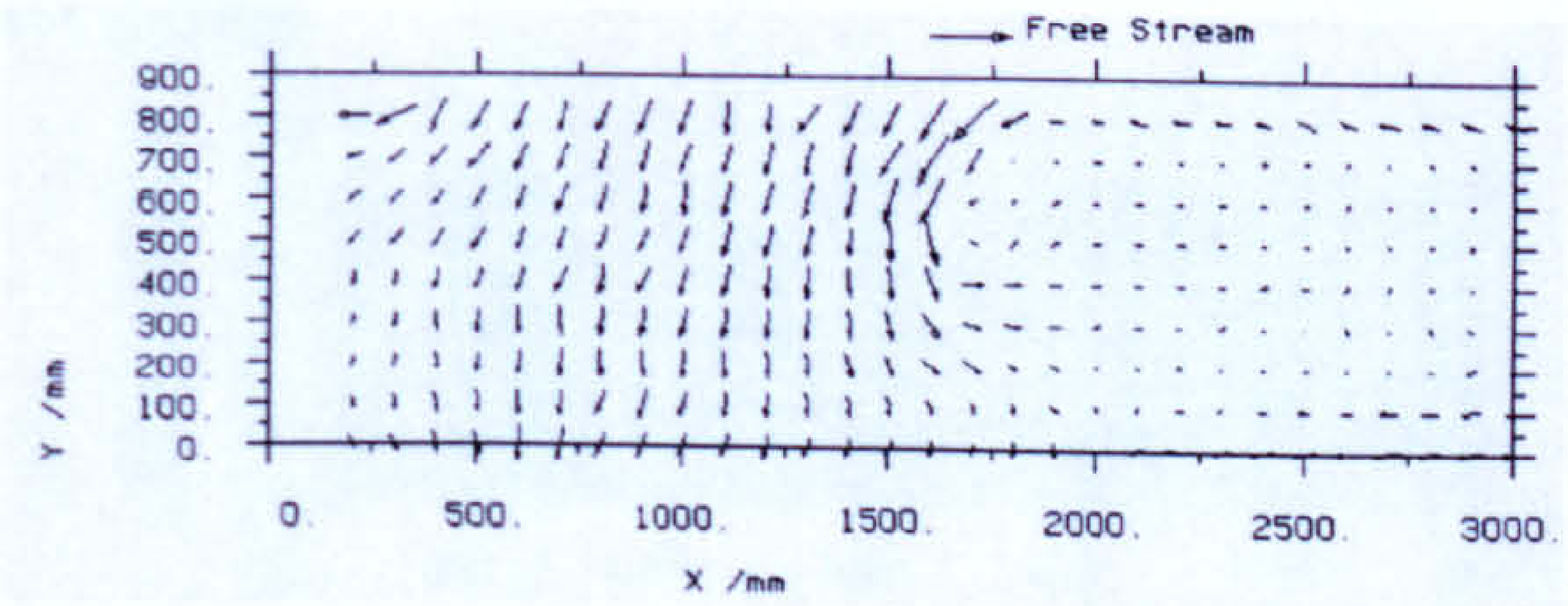

t = 0.26s

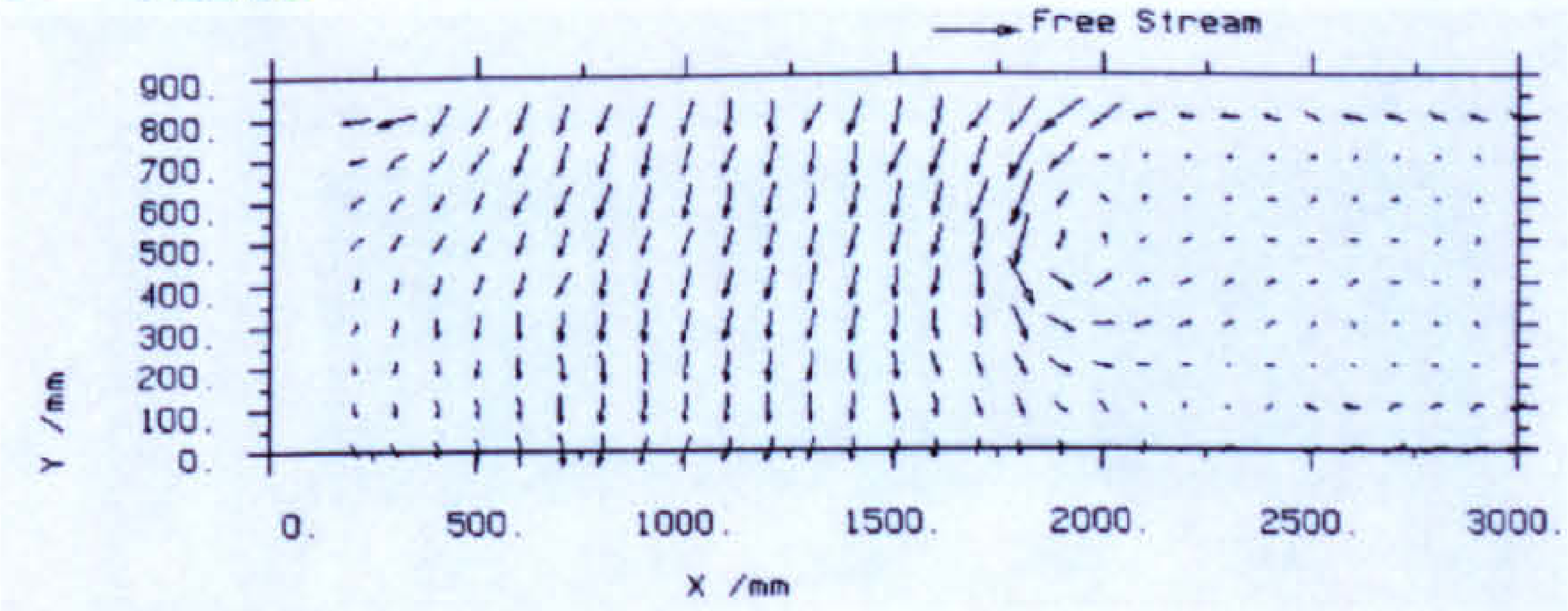

t = 0.28s

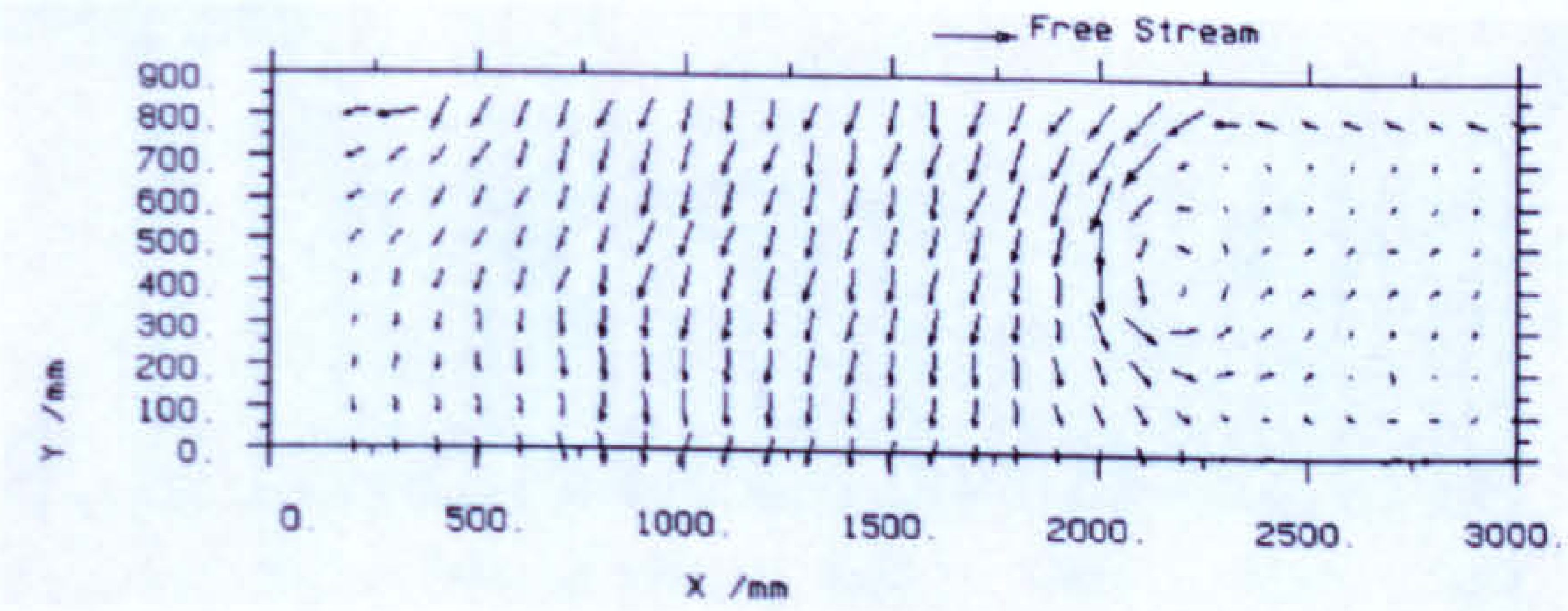

t = 0.30s

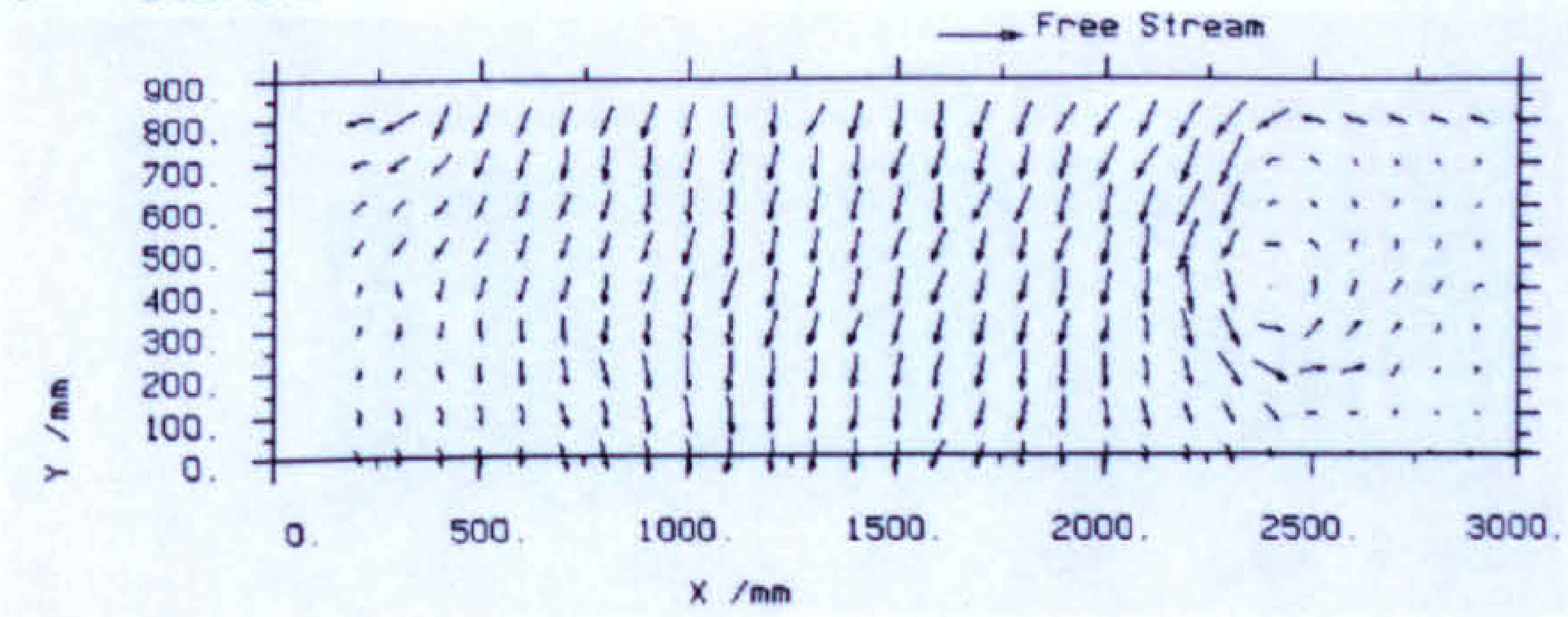

Figure 6.3 (page 1 of 2) Empty Working Section Transient Modified Velocity Vectors

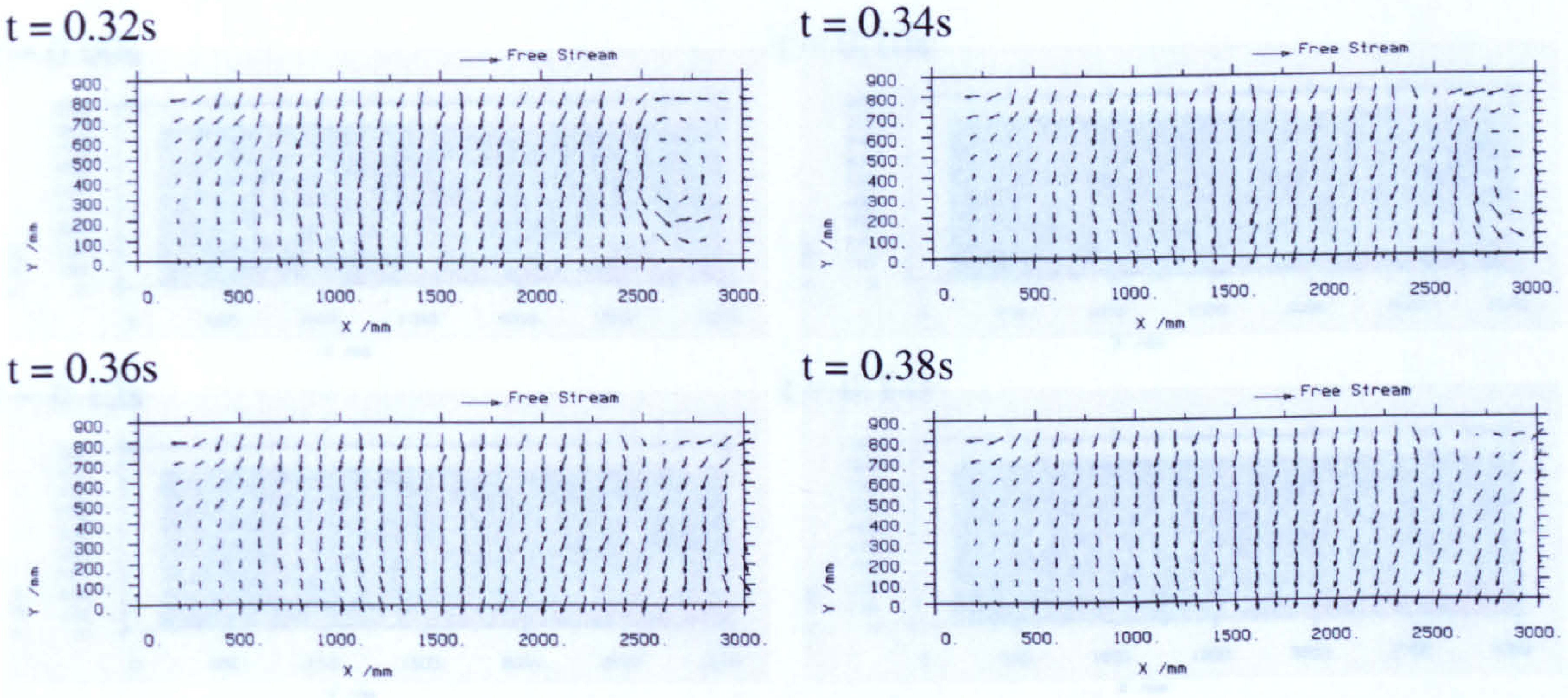

Figure 6.3 (page 2 of 2) Empty Working Section Transient Modified Velocity Vectors

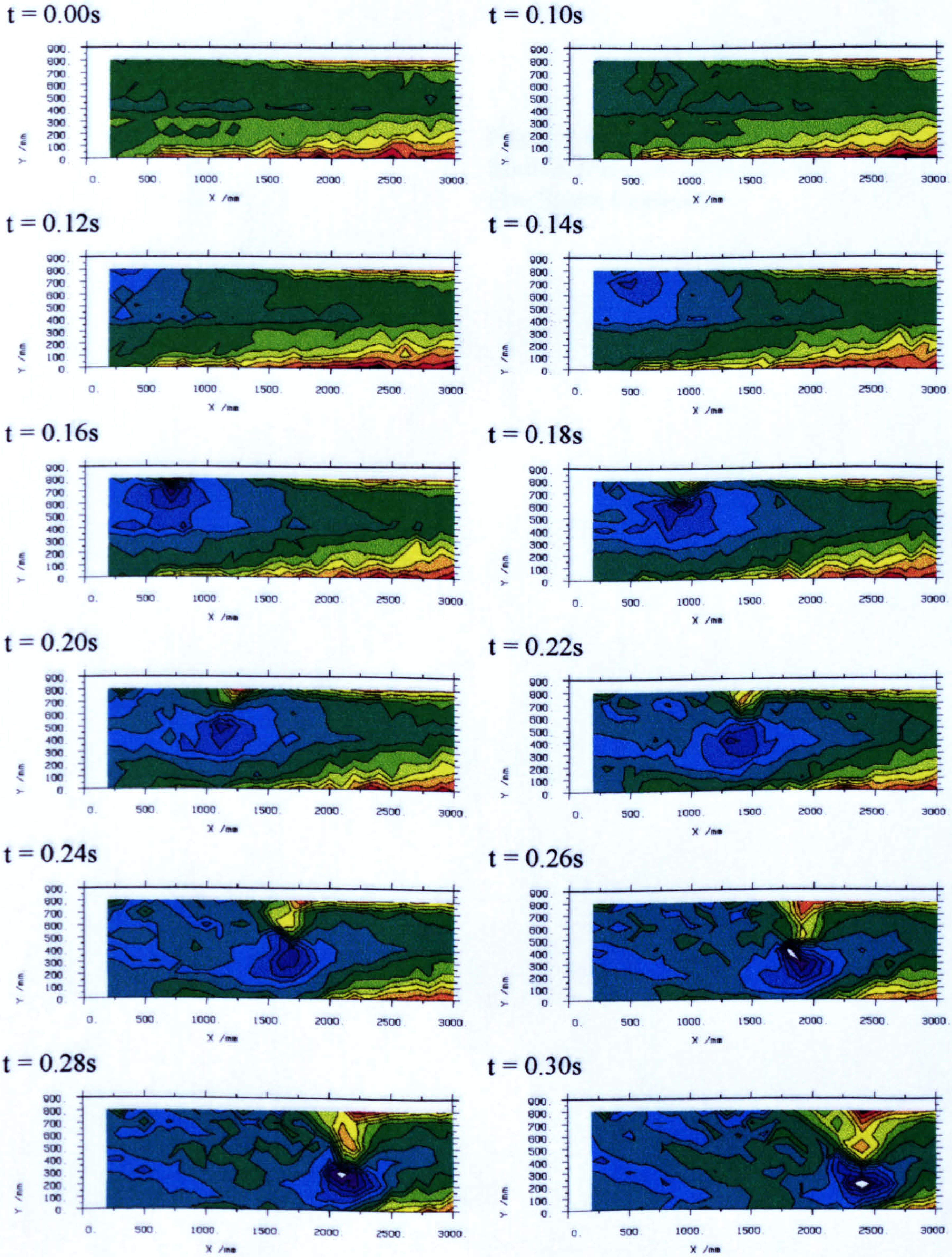

Figure 6.4 (page 1 of 3) Empty Working Section Transient Total Pressure Coefficient Contours

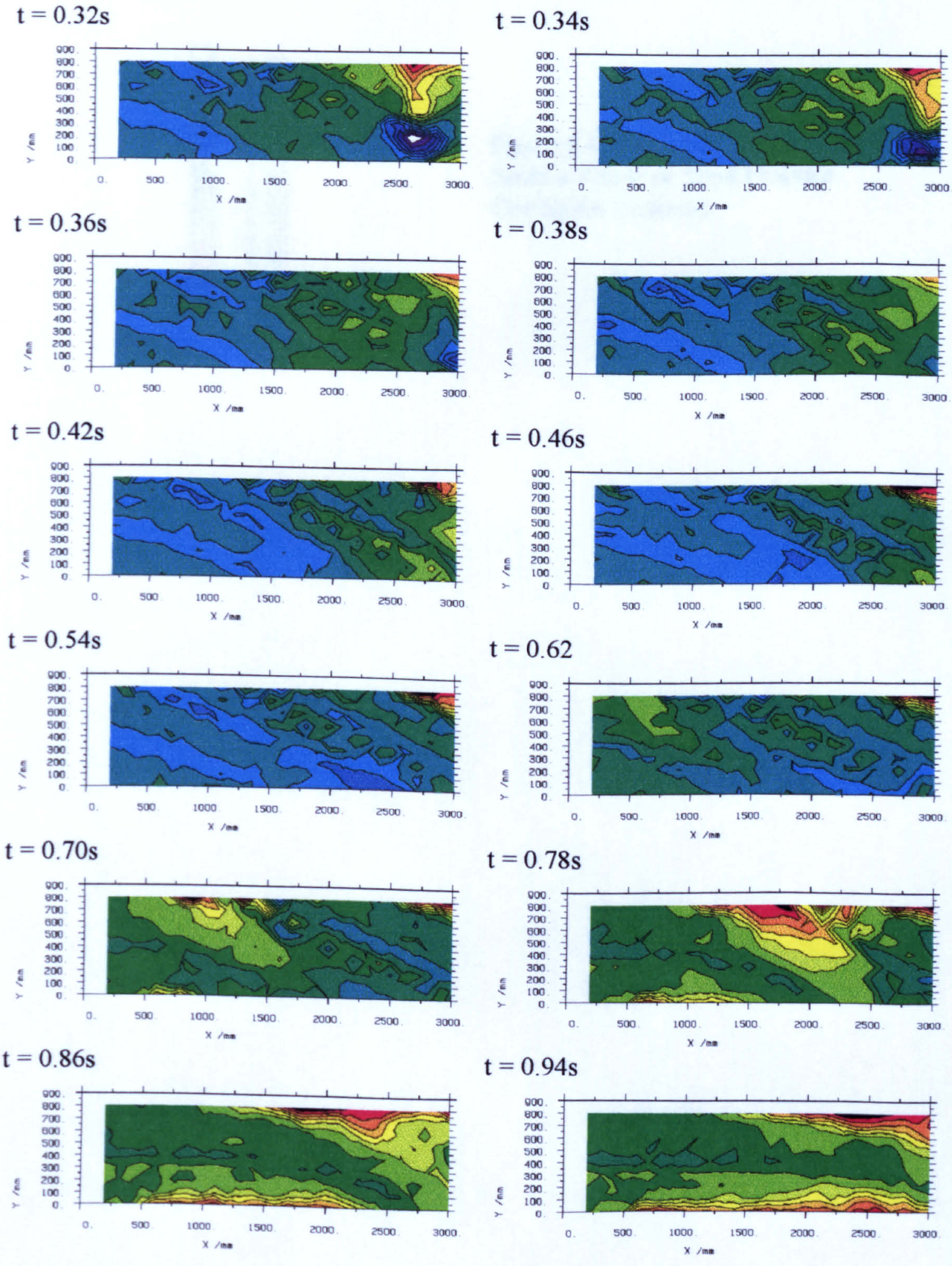
t = 0.32s
t = 0.34s
t = 0.36s
t = 0.38s
t = 0.42s
t = 0.46s
t = 0.54s
t = 0.62
t = 0.70s
t = 0.78s
t = 0.86s
t = 0.94s

Figure 6.4 (page 2 of 3) Empty Working Section Transient Total Pressure Coefficient Contours

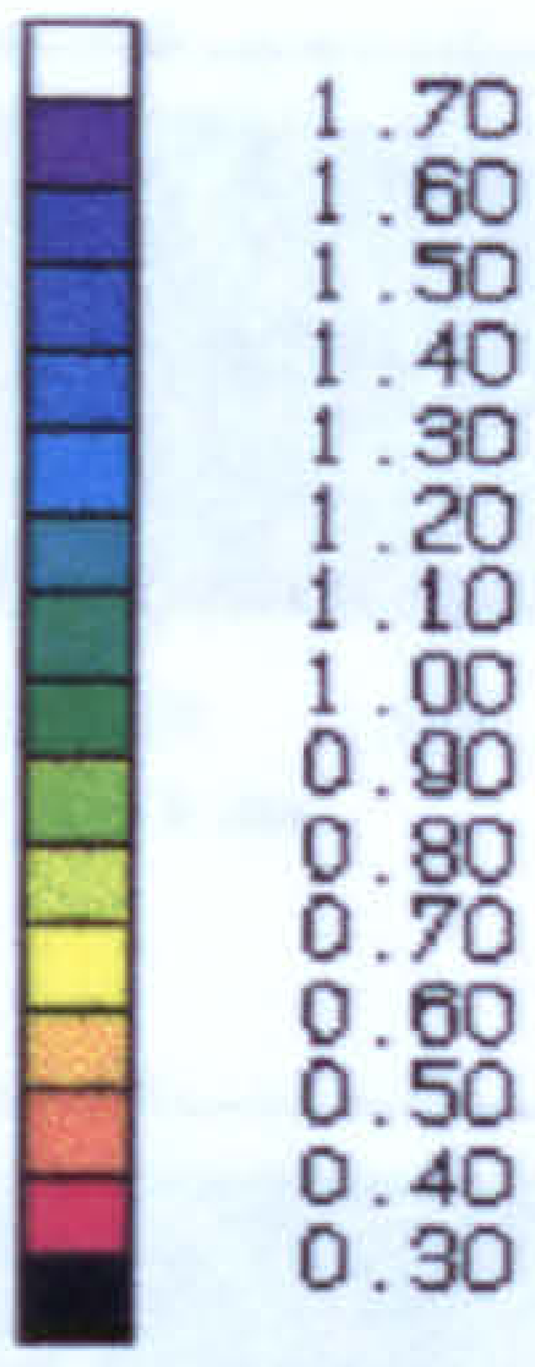

Figure 6.4 (page 3 of 3) Empty Working Section Transient Total Pressure Coefficient Contours

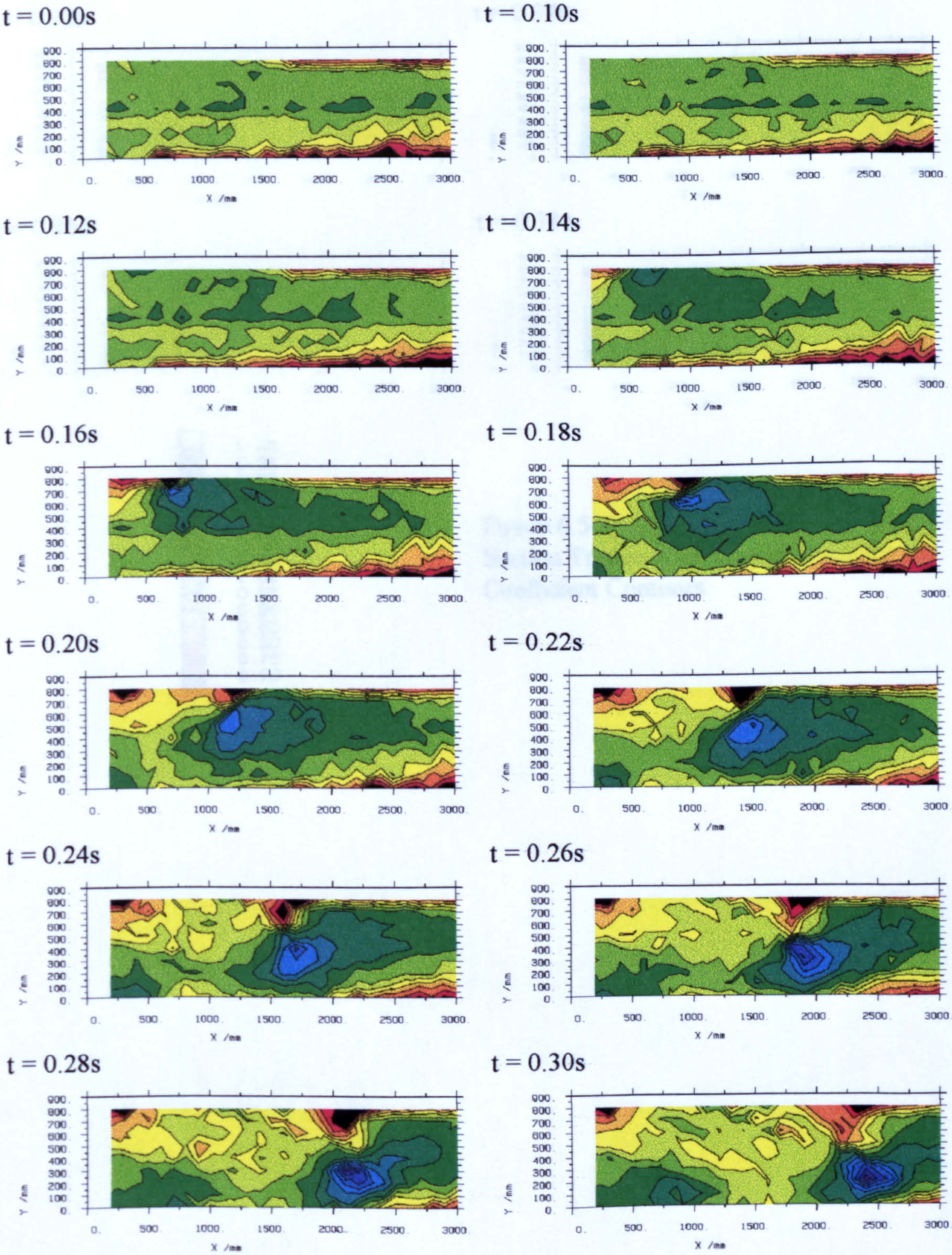

t = 0.00s

t = 0.10s

t = 0.12s

t = 0.14s

t = 0.16s

t = 0.18s

t = 0.20s

t = 0.22s

t = 0.24s

t = 0.26s

t = 0.28s

t = 0.30s

Figure 6.5 (page 1 of 2) Empty Working Section Transient Streamwise Velocity Coefficient Contours

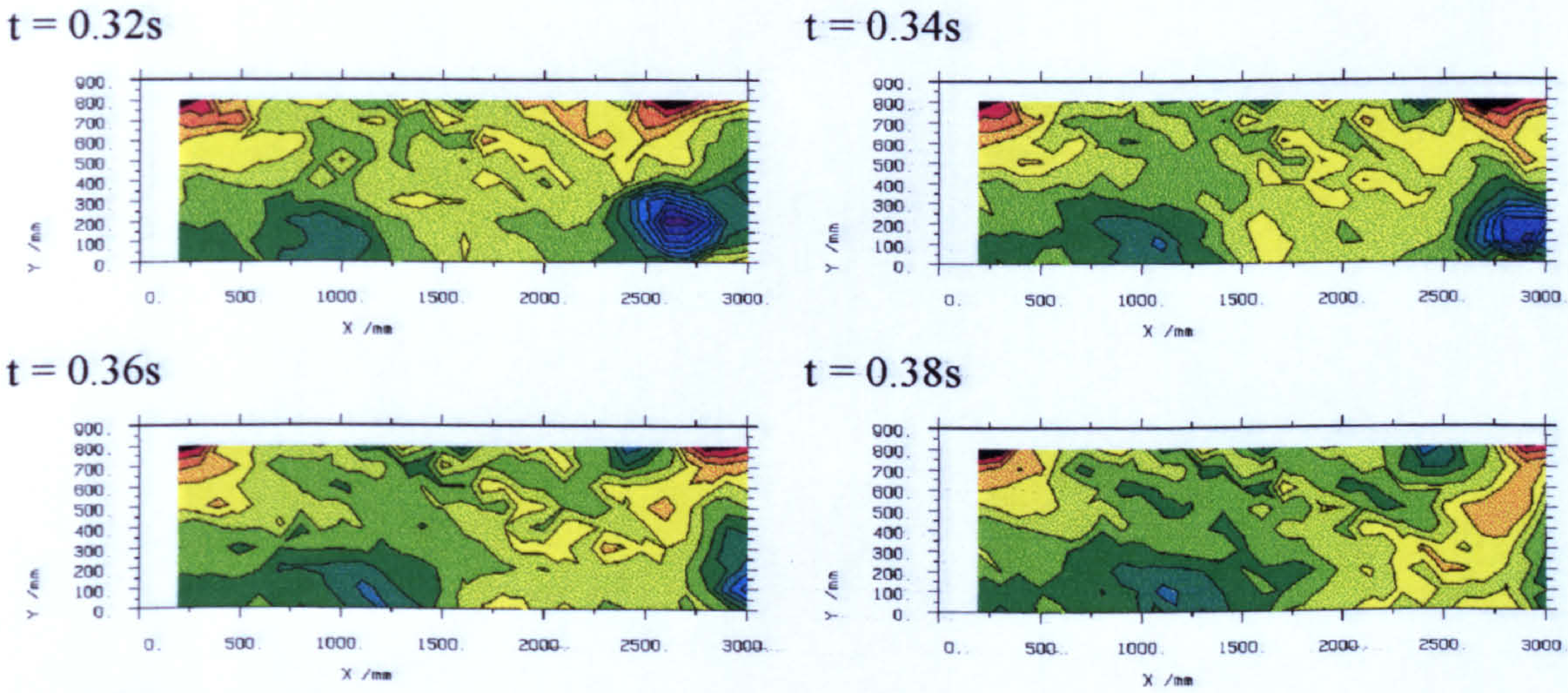

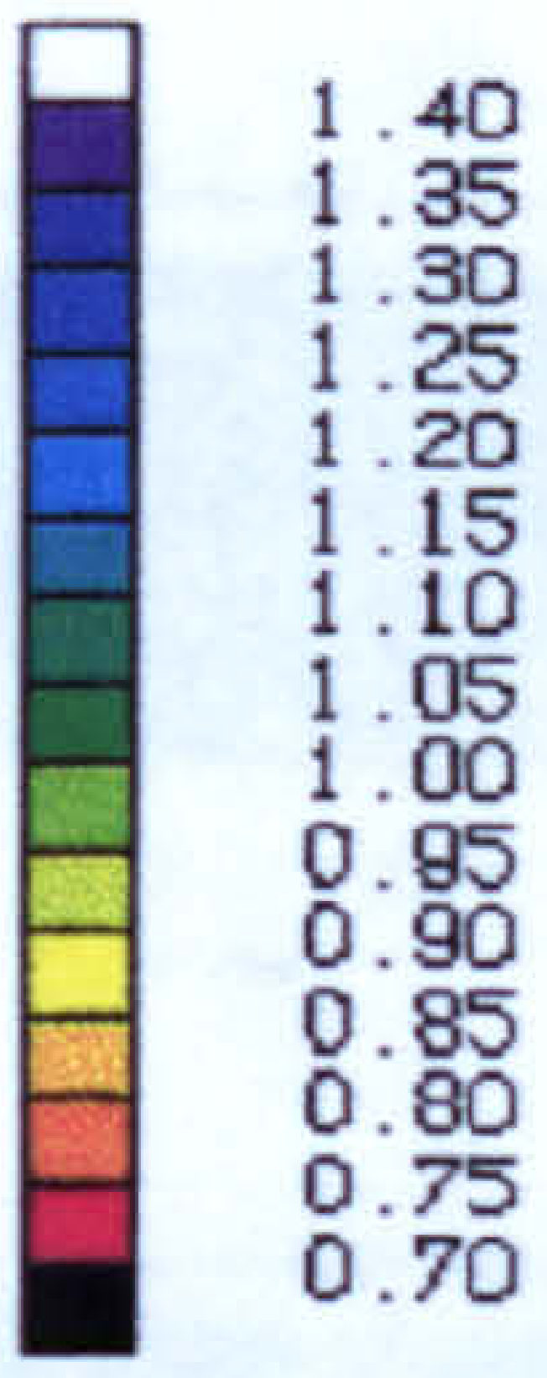

Figure 6.5 (page 2 of 2) Empty Working Section Transient Streamwise Velocity Coefficient Contours

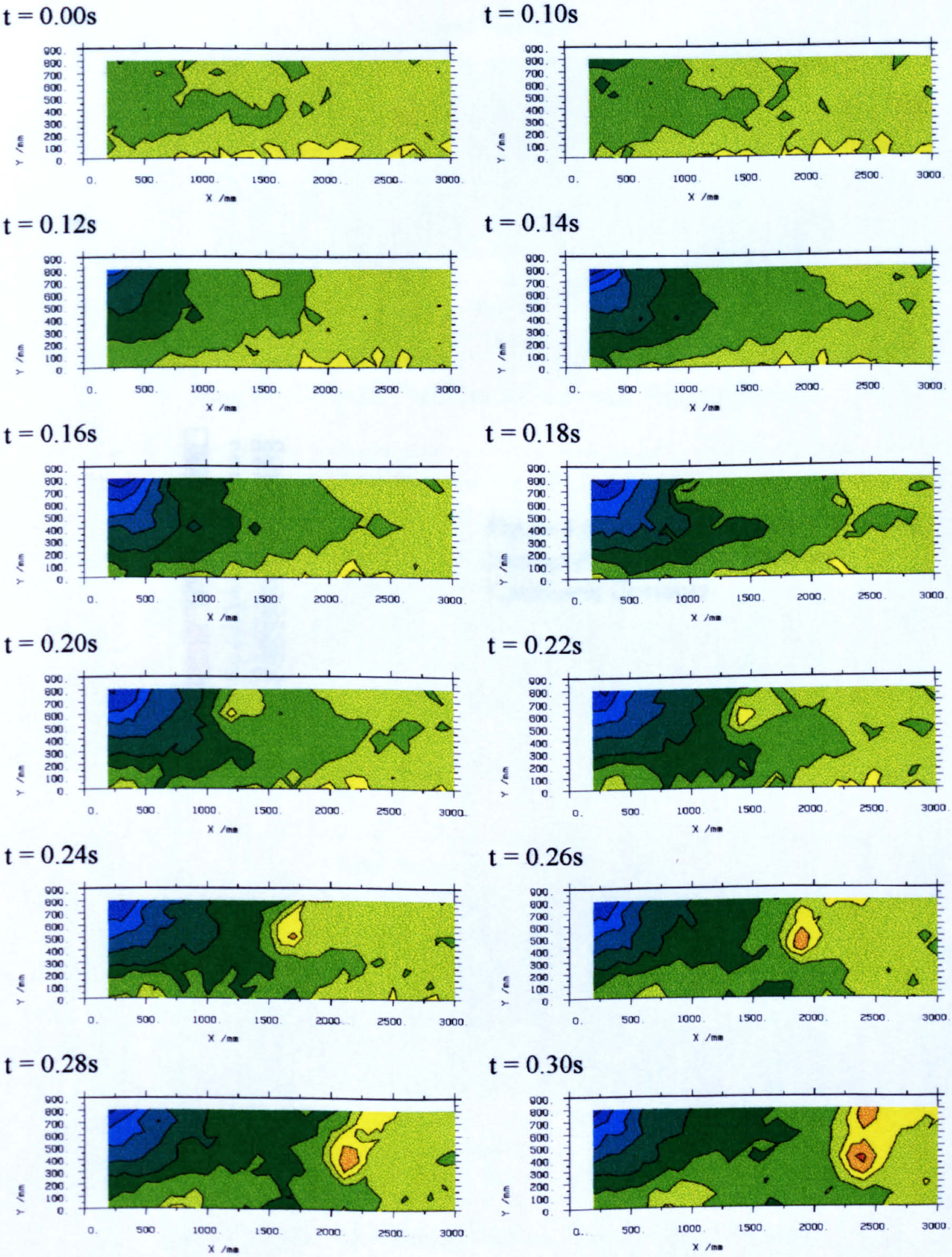

t = 0.00s

t = 0.10s

t = 0.12s

t = 0.14s

t = 0.16s

t = 0.18s

t = 0.20s

t = 0.22s

t = 0.24s

t = 0.26s

t = 0.28s

t = 0.30s

Figure 6.6 (page 1 of 2) Empty Working Section Transient Static Pressure Coefficient Contours

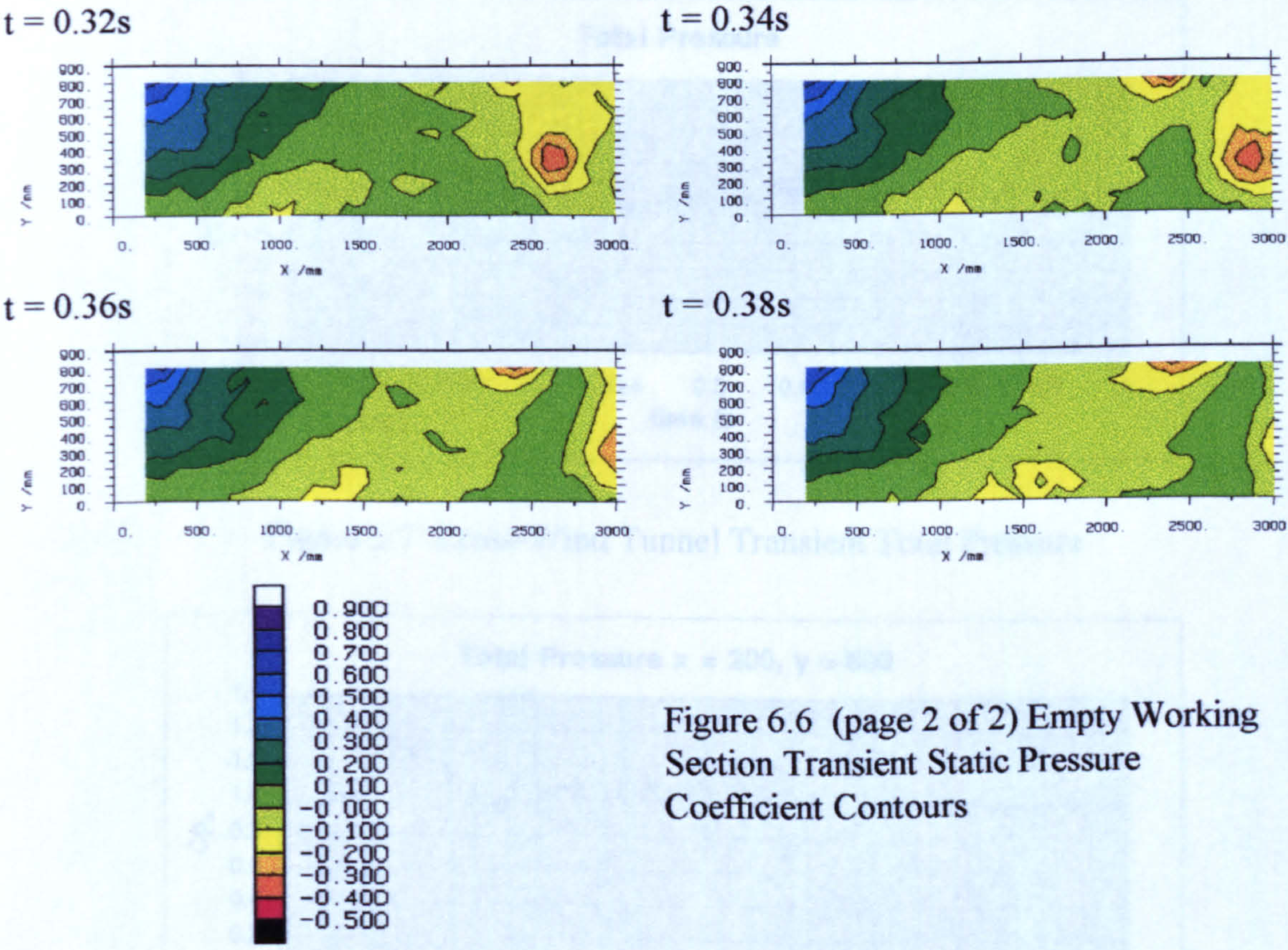

Figure 6.6 (page 2 of 2) Empty Working Section Transient Static Pressure Coefficient Contours

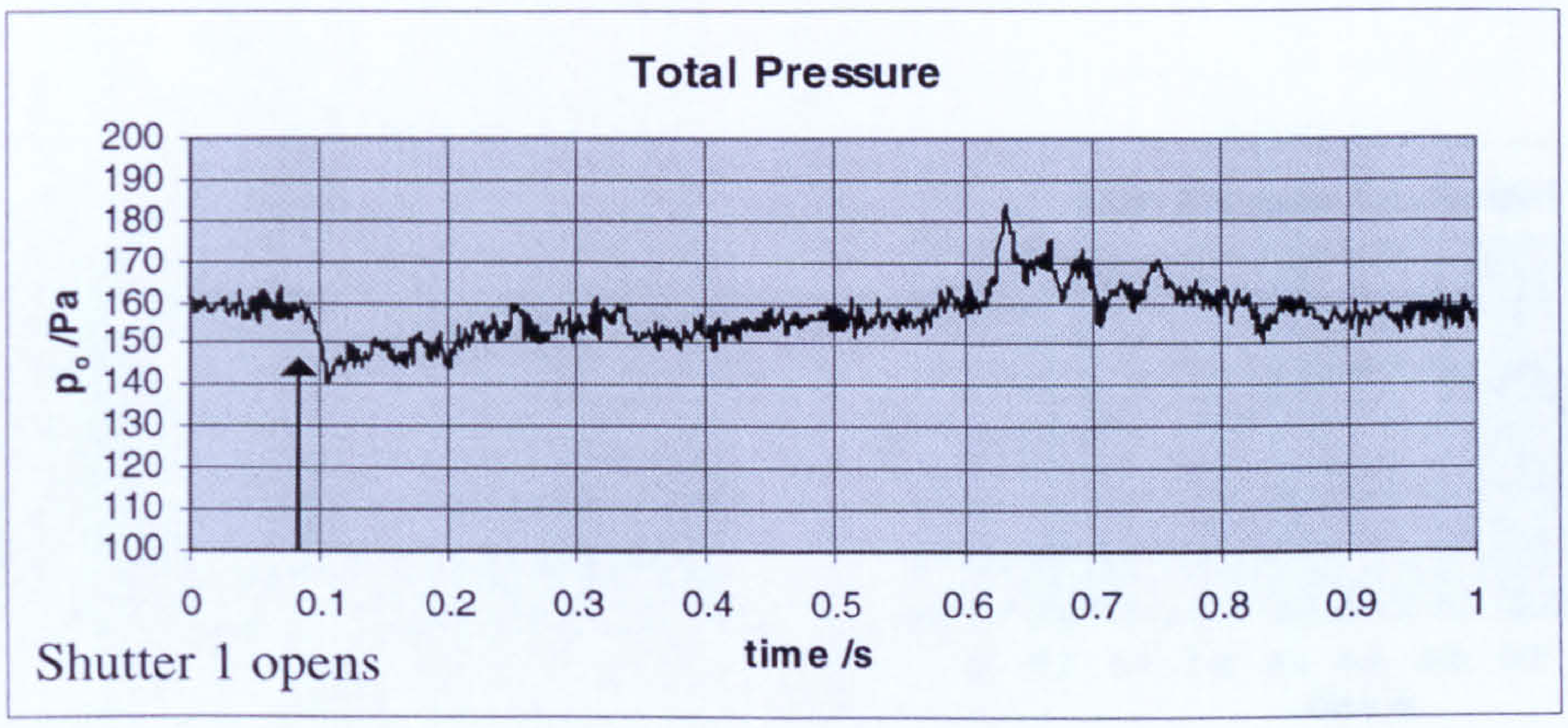

Figure 6.7 Cross-Wind Tunnel Transient Total Pressure

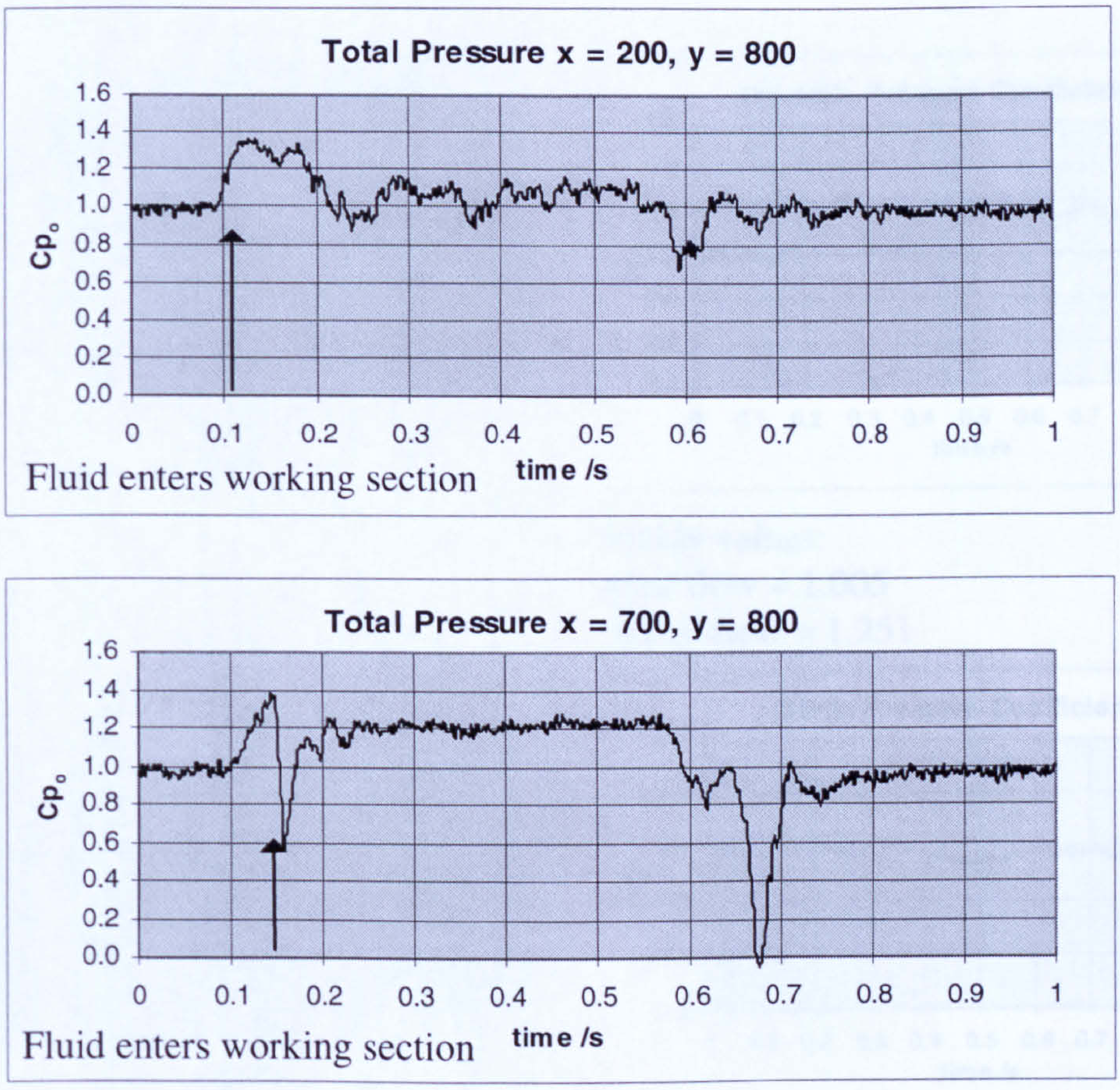

Figure 6.8 Empty Working Section Transient Total Pressure

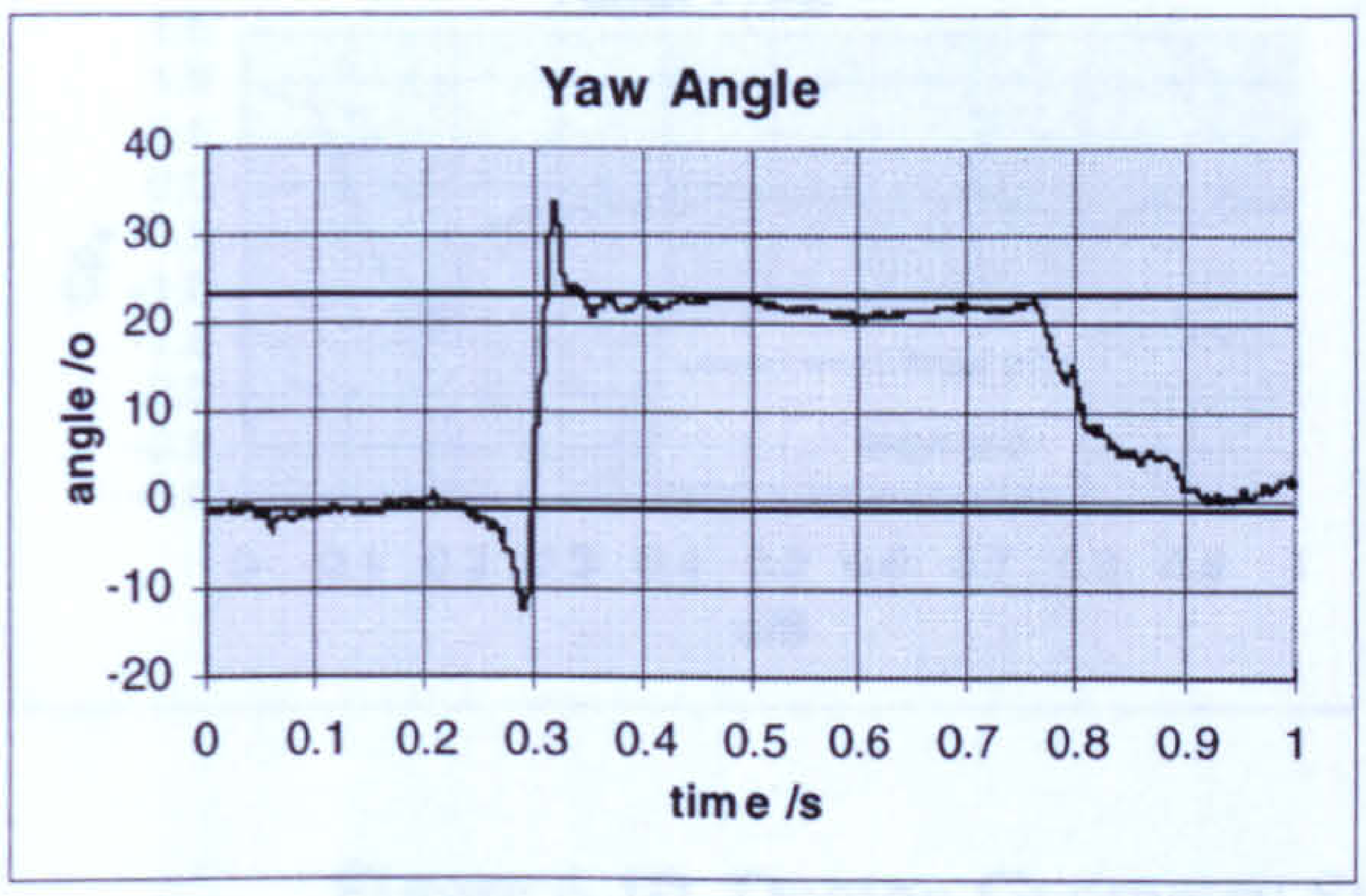

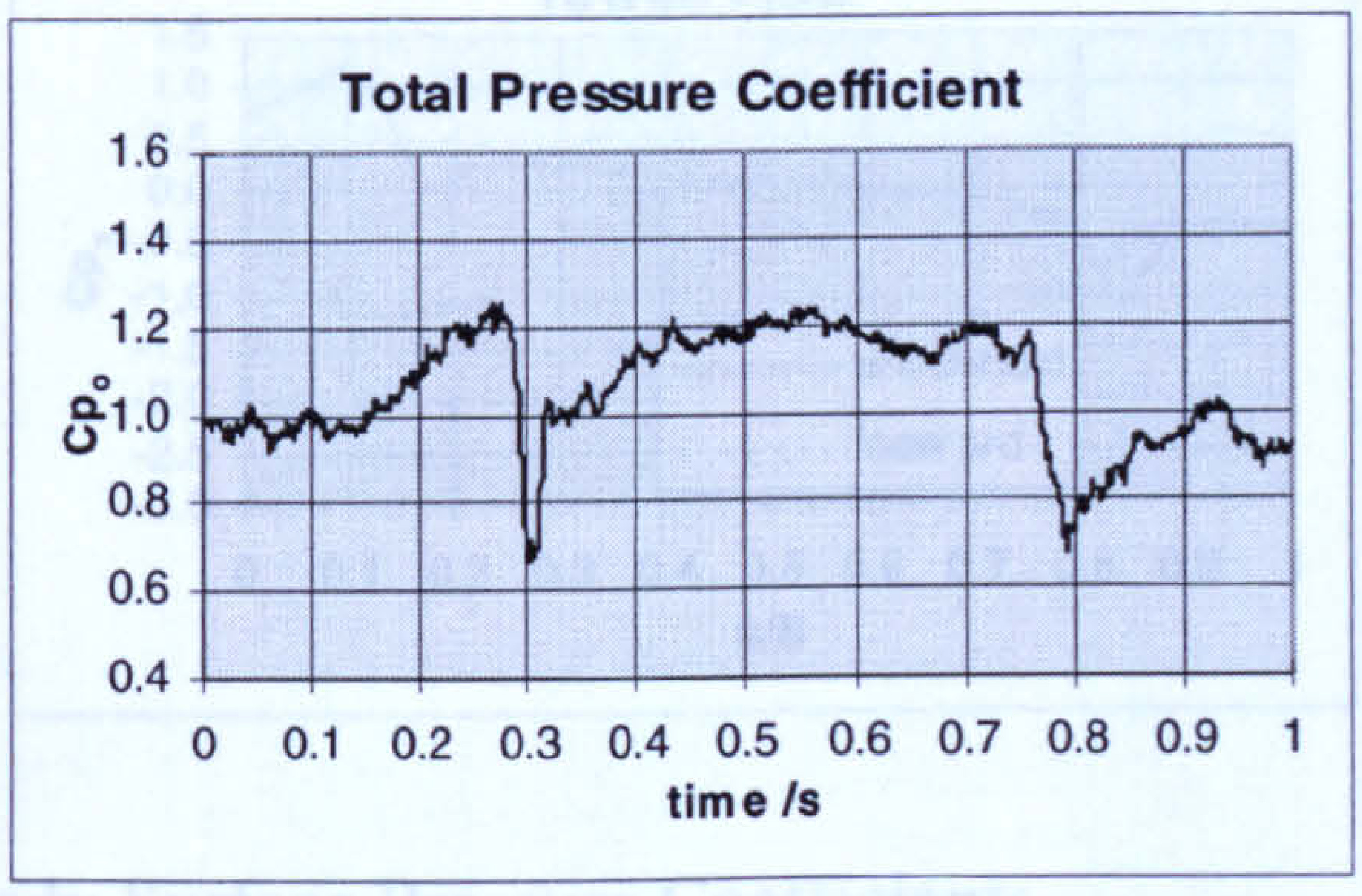

Steady values:
axial flow = -0.952°
yawed flow = 23.1°

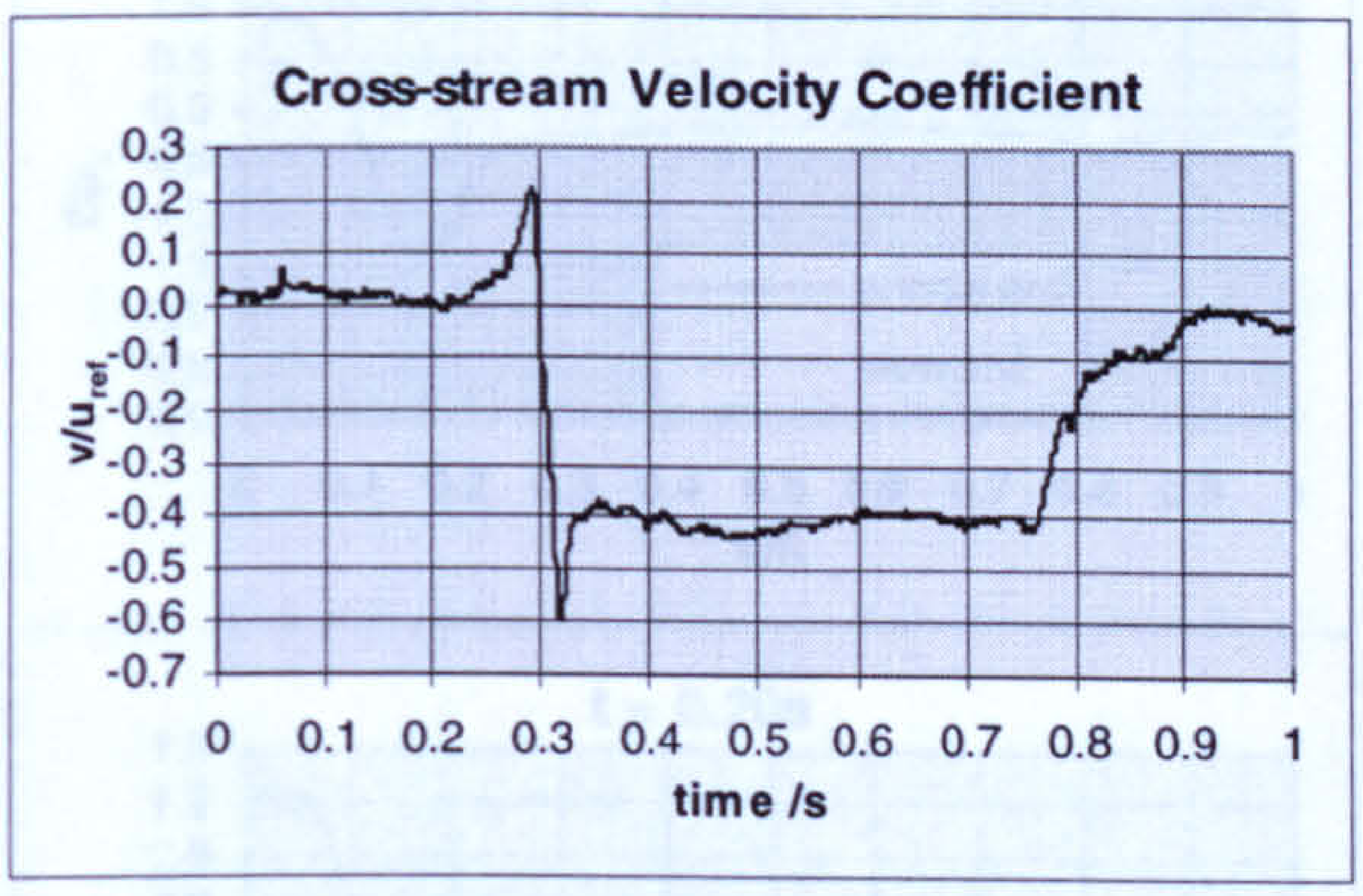

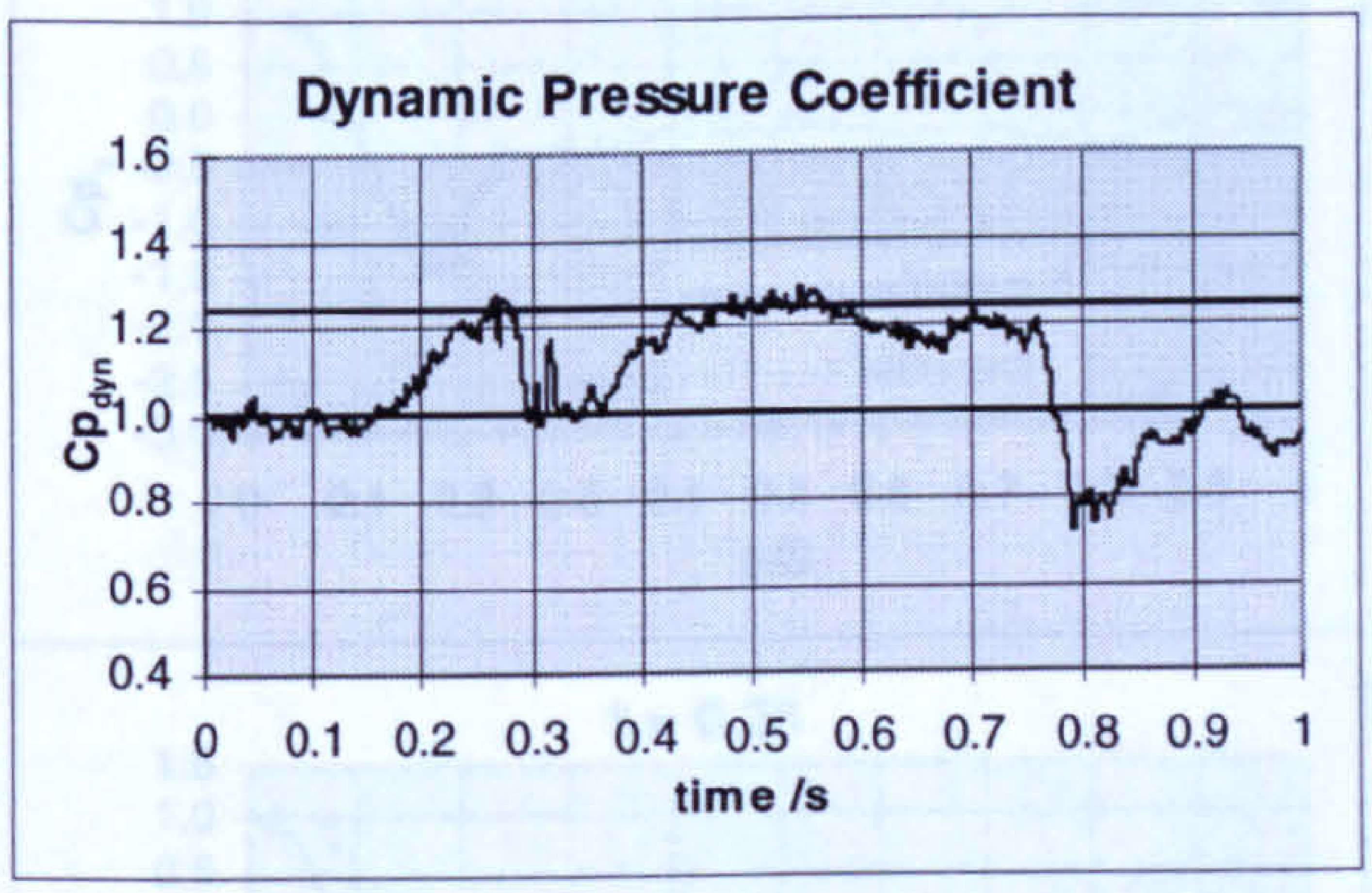

Steady values:
axial flow = 1.005
yawed flow = 1.251

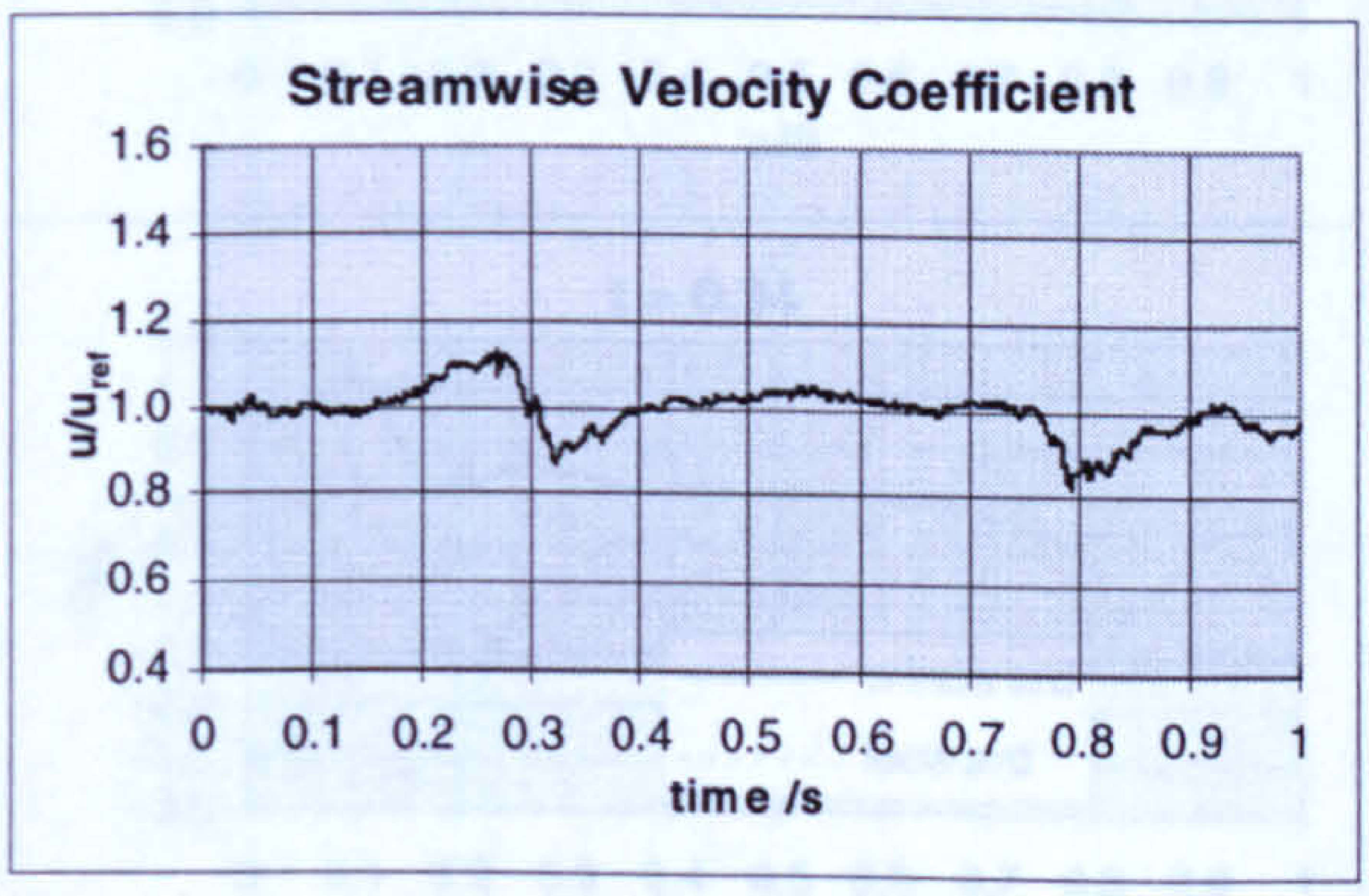

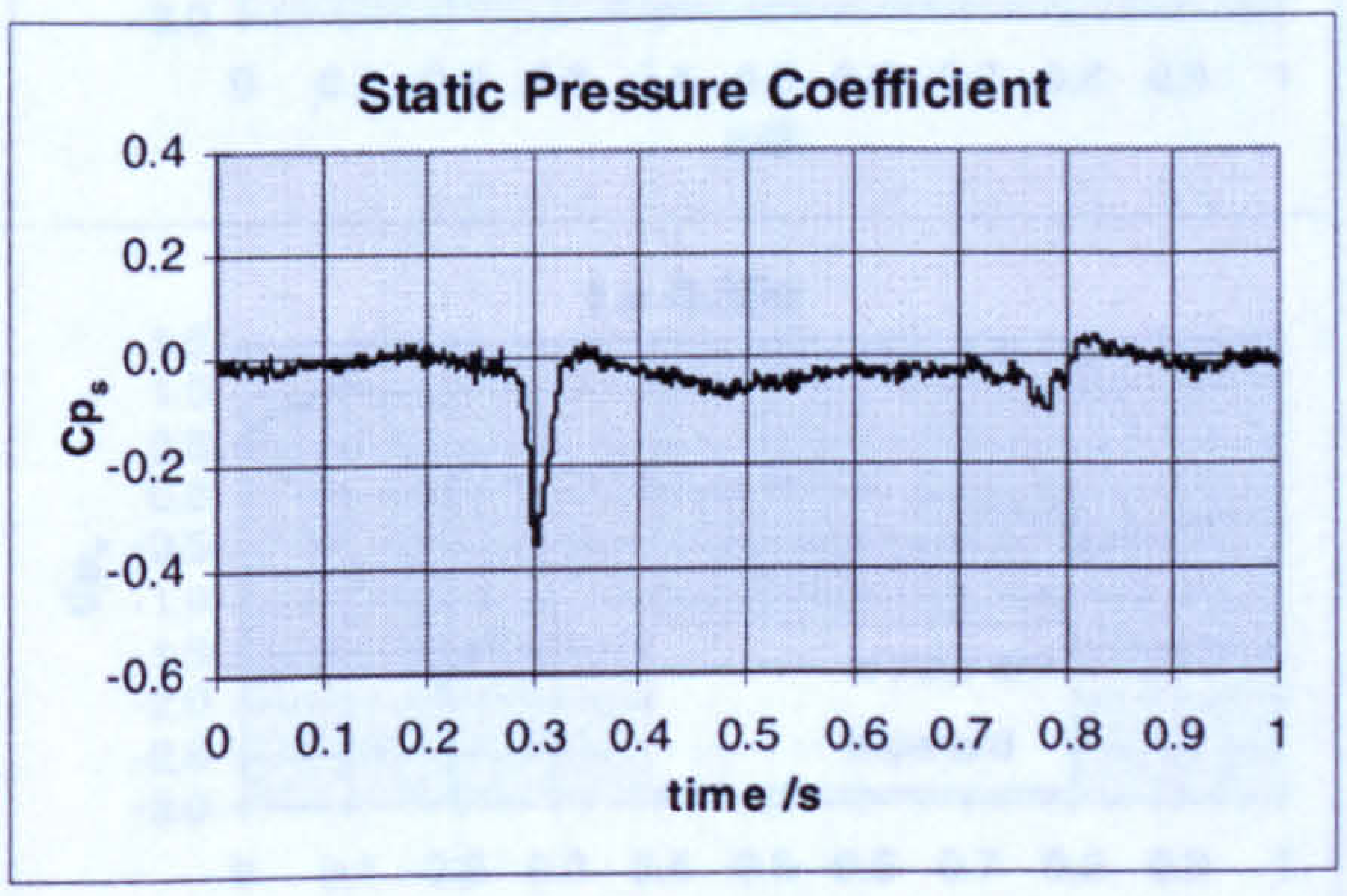

Fgure 6.9 Gust Characteristics at the Model Centre

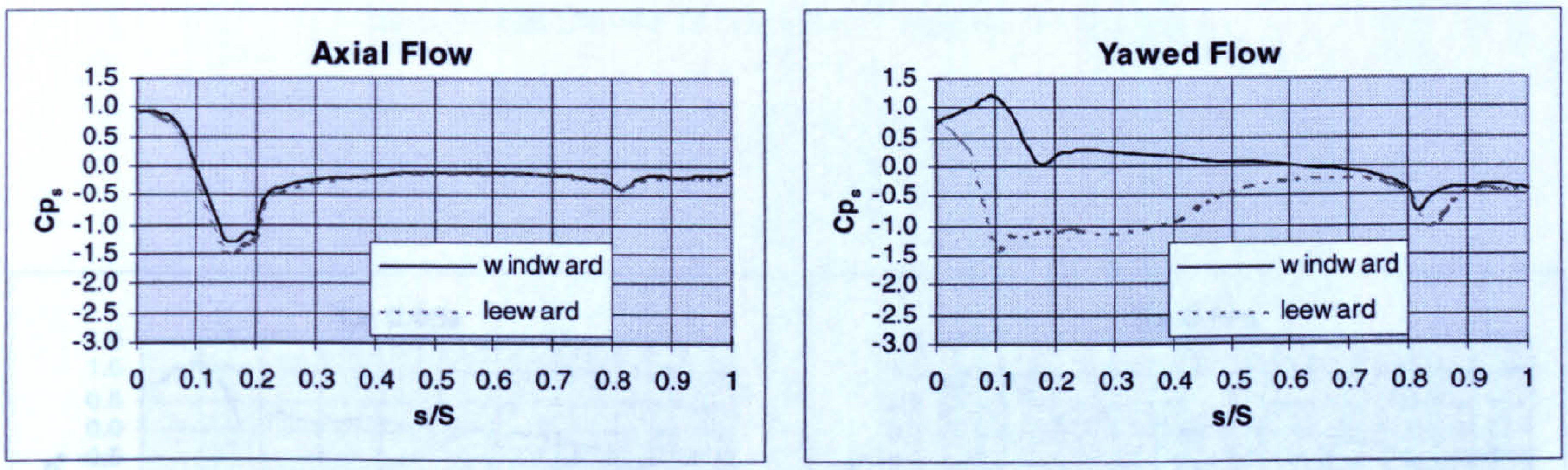

Figure 6.10 Docton Geometry Steady Surface Pressure Coefficients

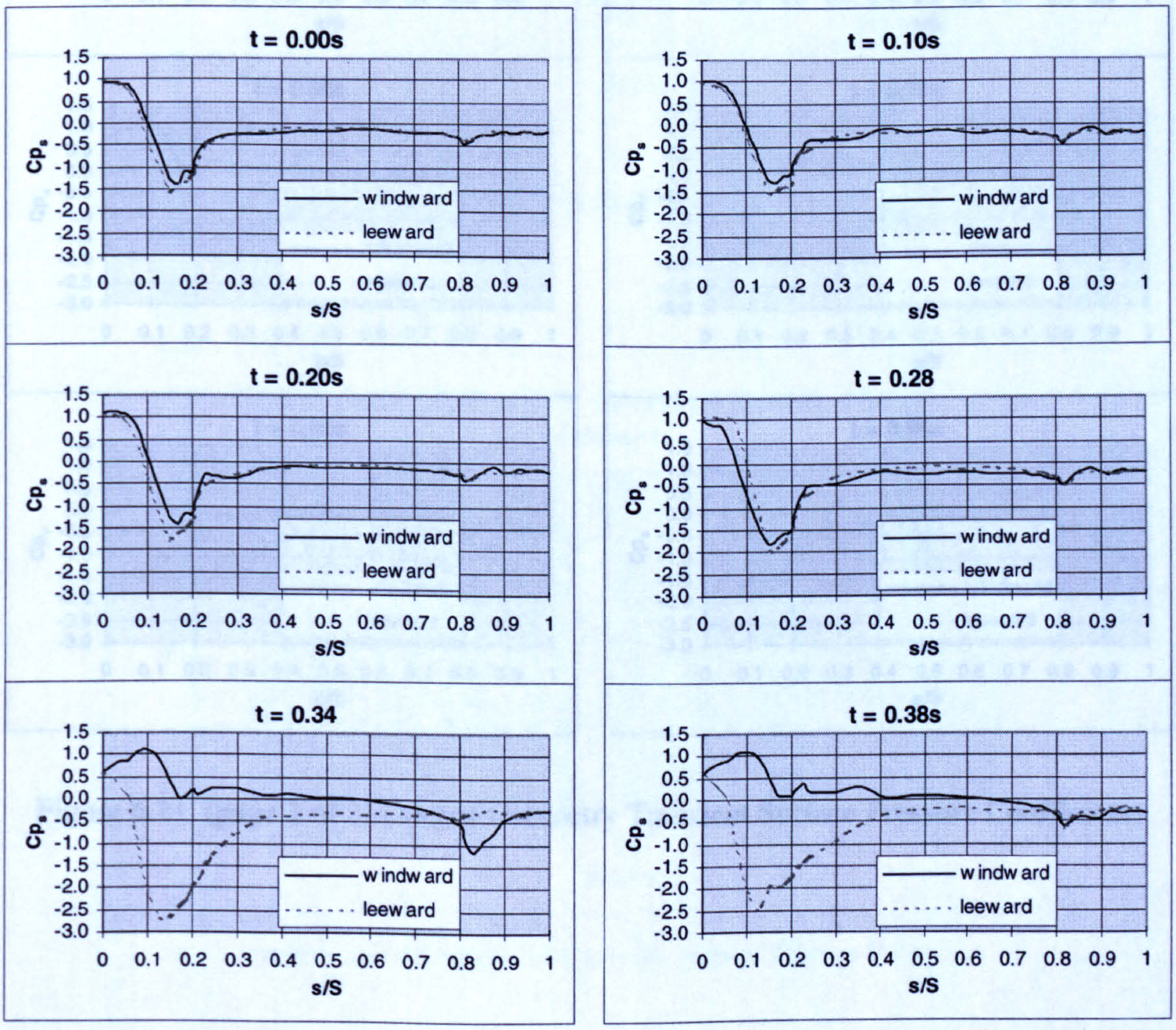

Figure 6.11 (page 1 of 2) Docton Geometry Transient Surface Pressure Coefficients

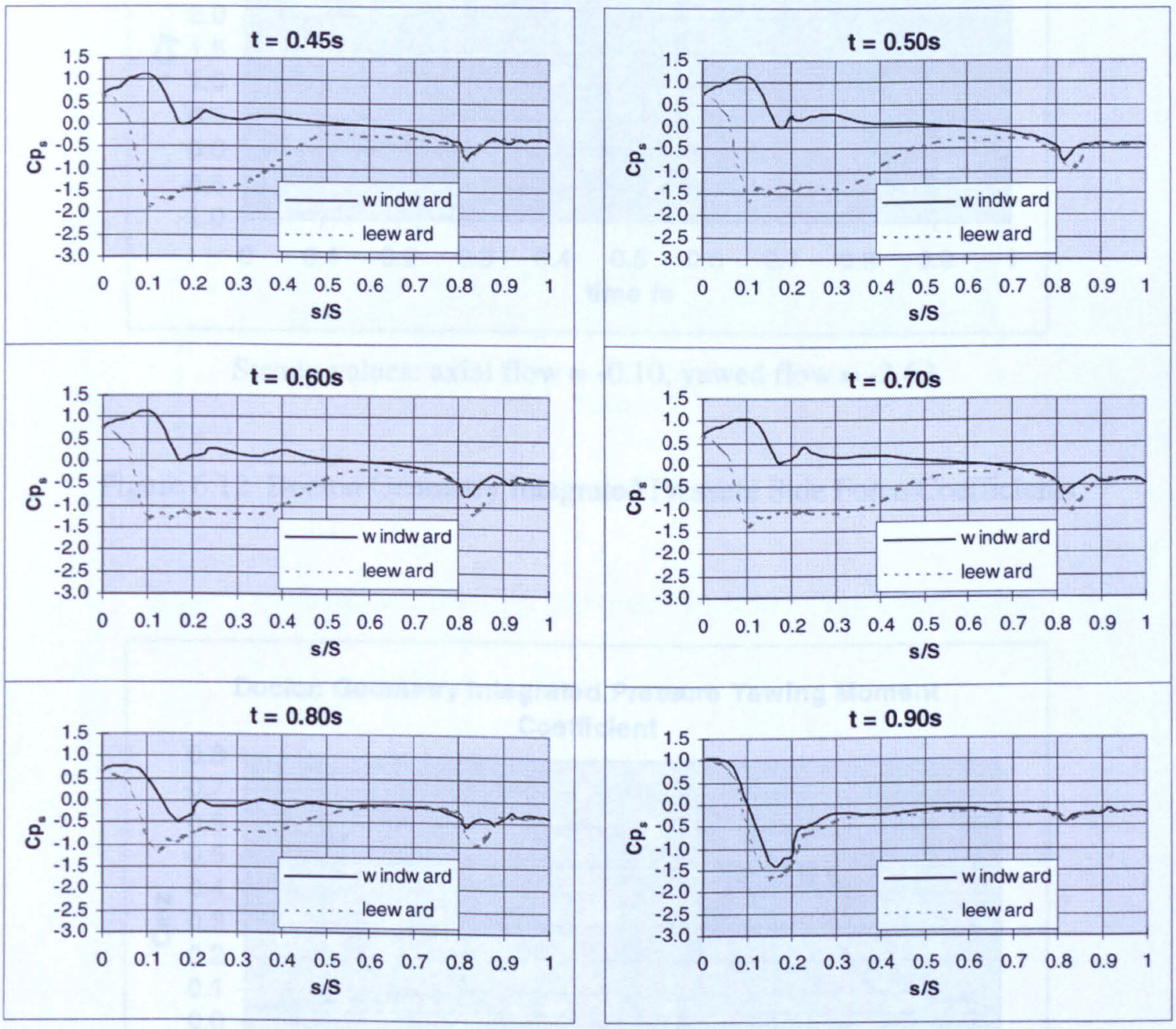

Figure 6.11 (page 2 of 2) Docton Geometry Transient Surface Pressure Coefficients

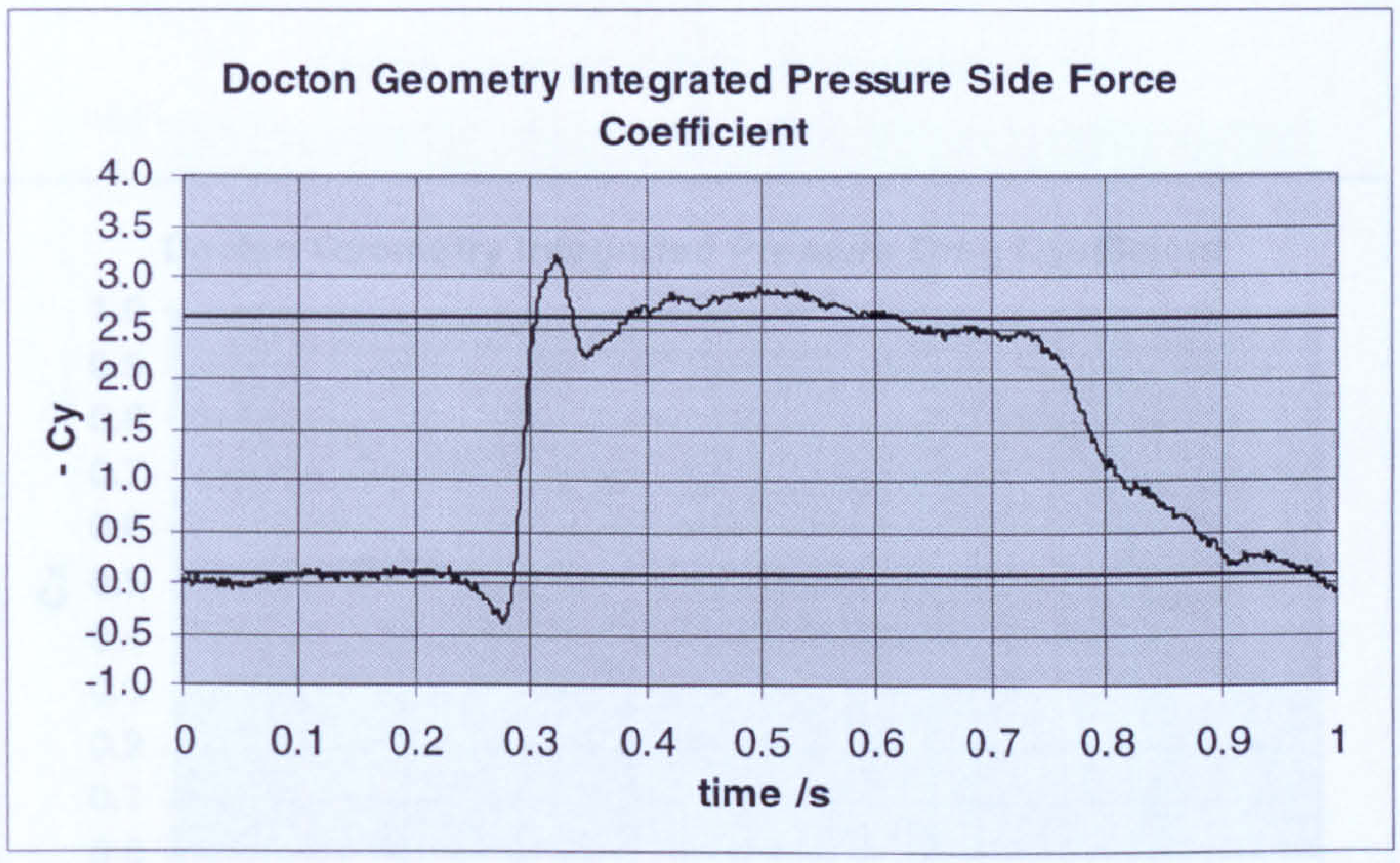

Steady values: axial flow = -0.10, yawed flow = -2.62.

Figure 6.12 Docton Geometry Integrated Pressure Side Force Coefficients

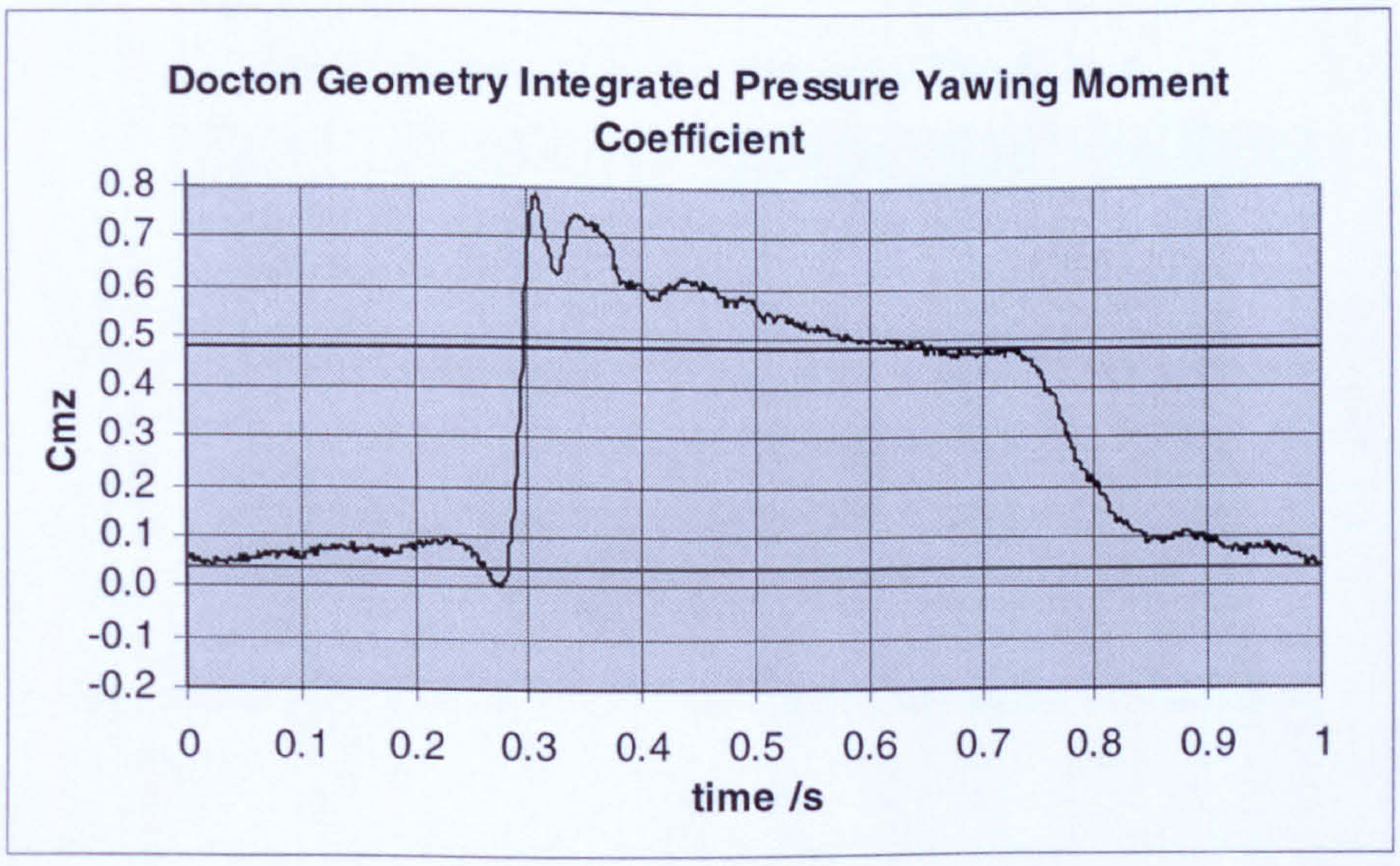

Steady values: axial flow = 0.04, yawed flow = 0.48.

Figure 6.13 Docton Geometry Integrated Pressure Yawing Moment Coefficients

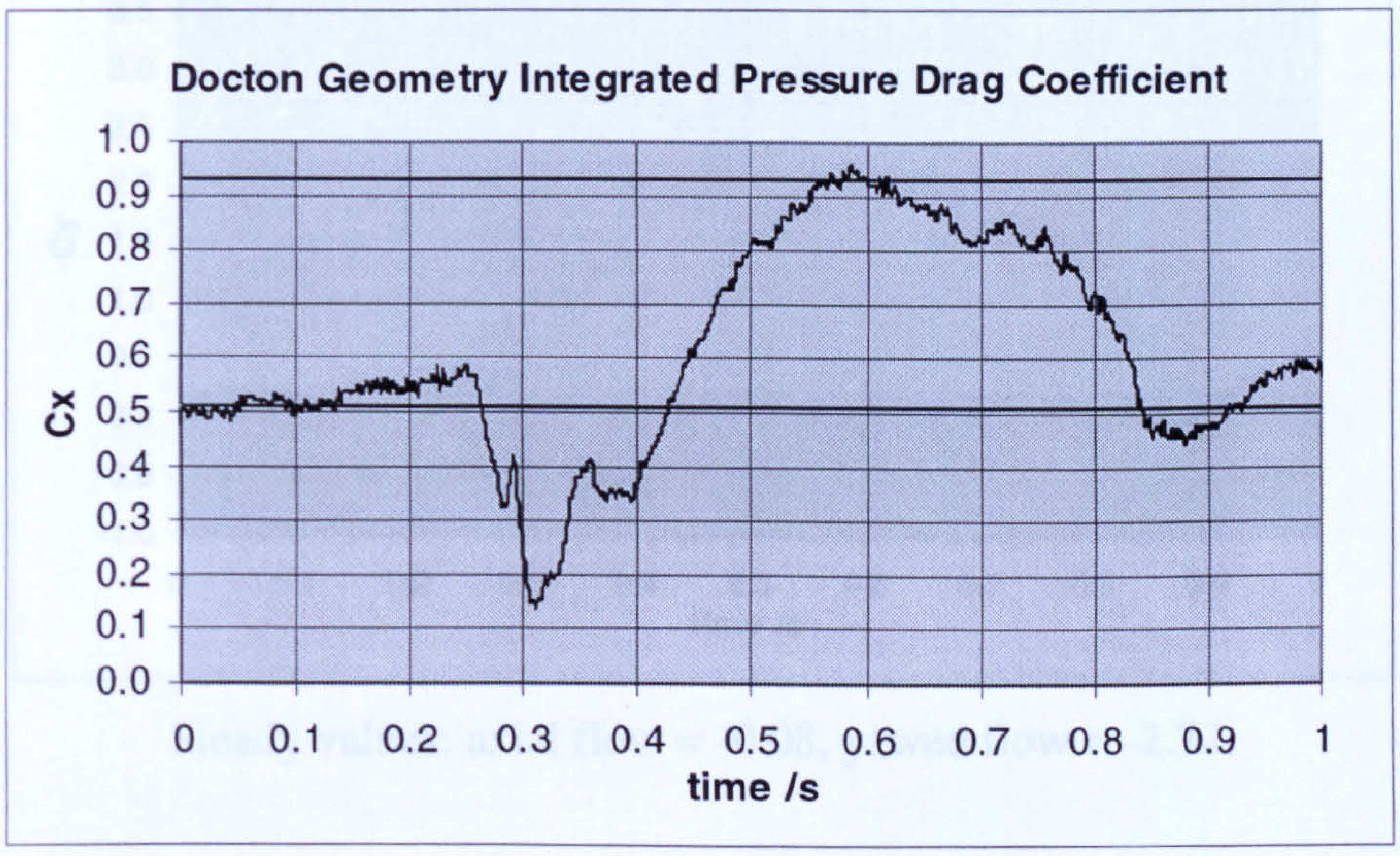

Steady values: axial flow = 0.51, yawed flow = 0.93.

Figure 6.14 Docton Geometry Integrated Pressure Drag Coefficients

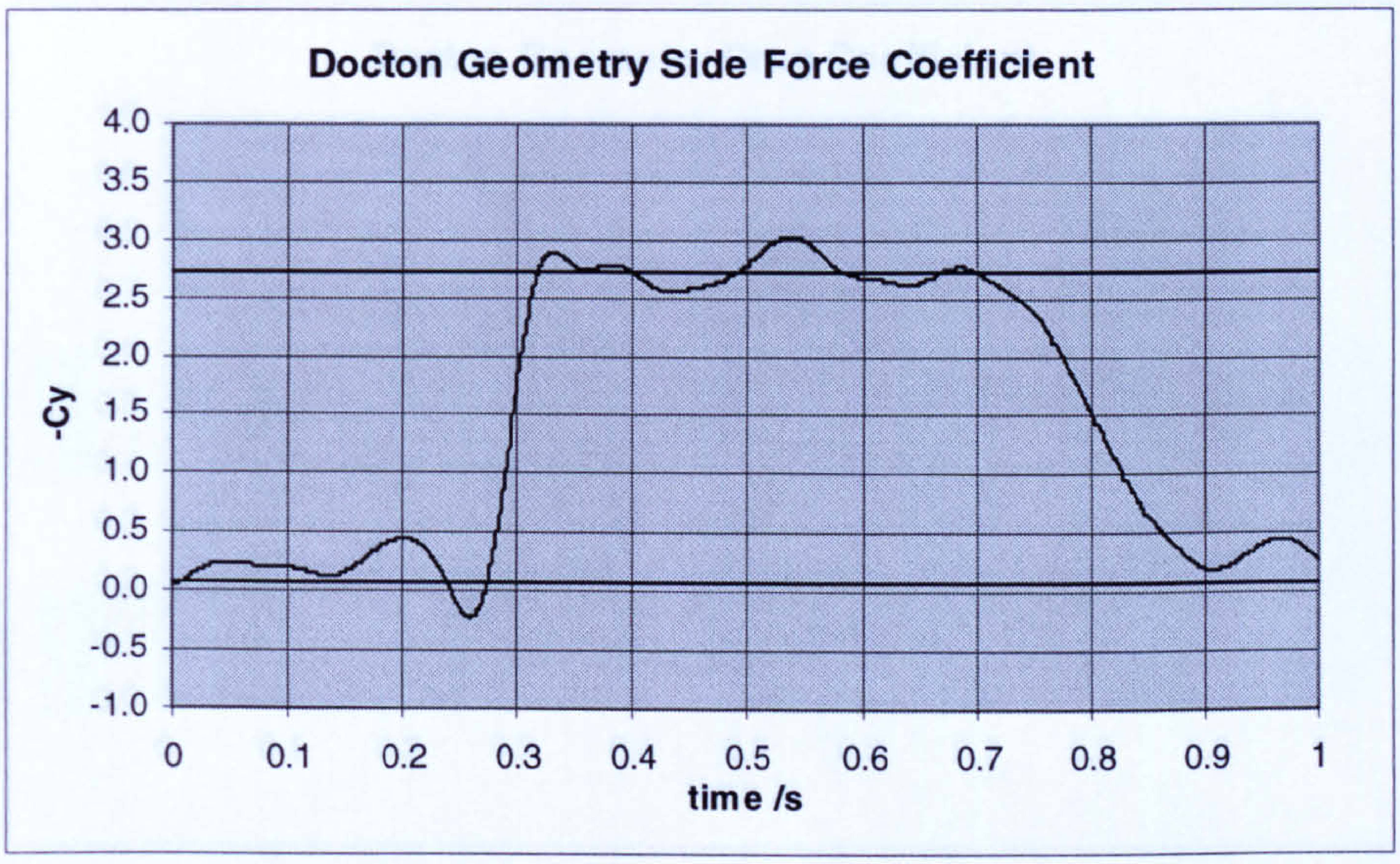

Steady values: axial flow = -0.08, yawed flow = -2.72.

Figure 6.15 Docton Geometry Side Force Coefficients

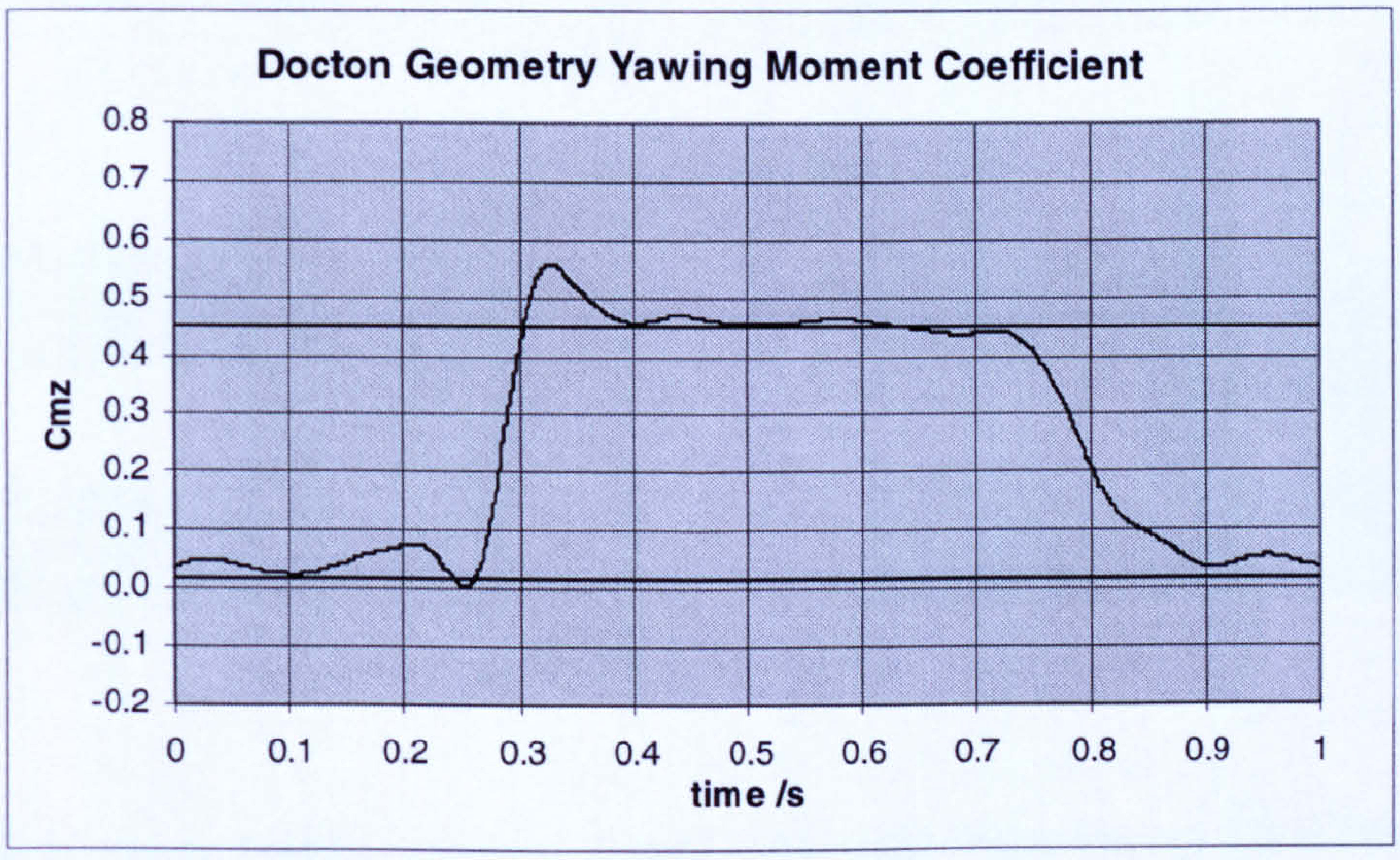

Steady values: axial flow = 0.02, yawed flow = 0.45.

Figure 6.16 Docton Geometry Yawing Moment Coefficients

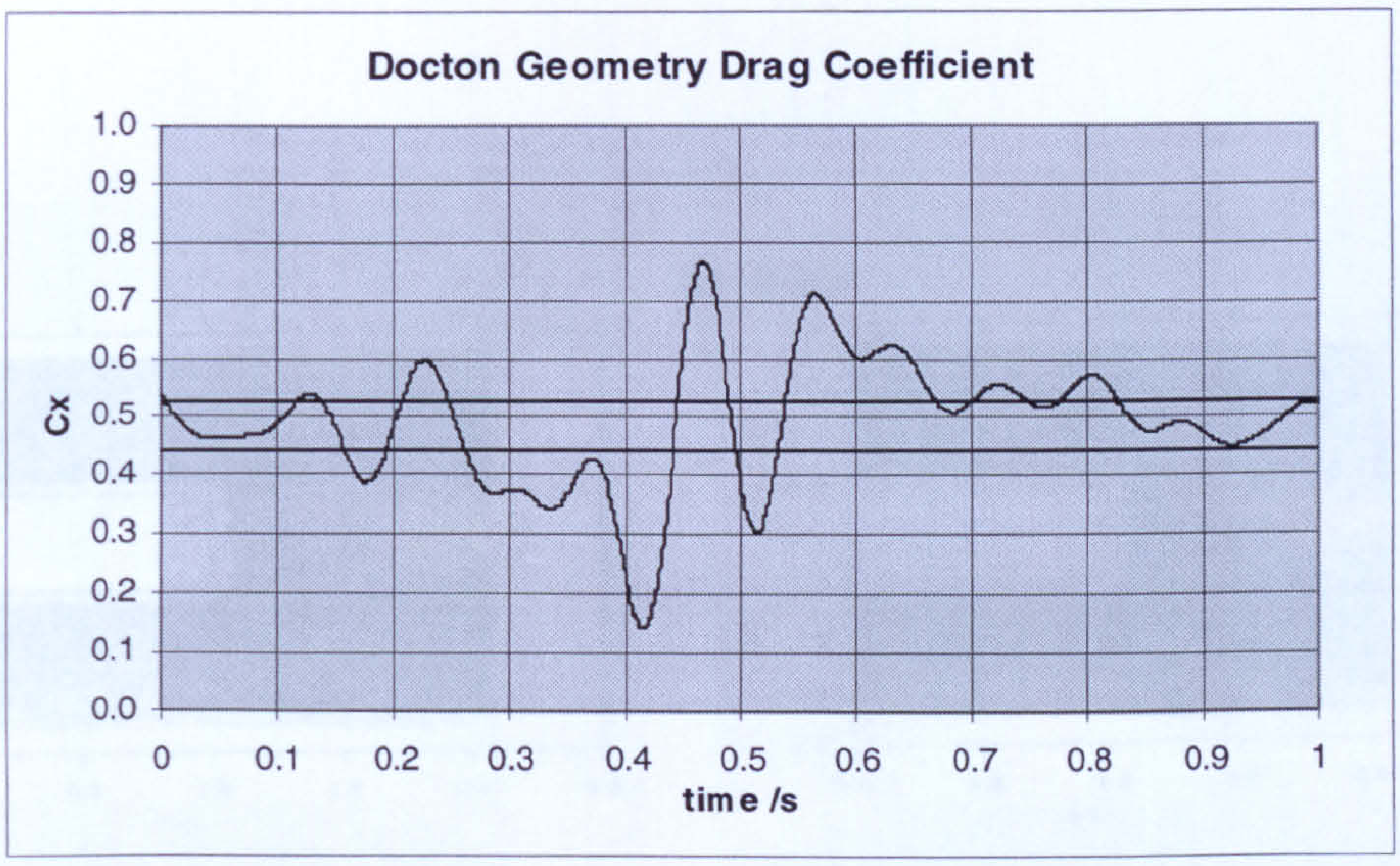

Steady values: axial flow = 0.44, yawed flow = 0.53.

Figure 6.17 Docton Geometry Drag Coefficients t = 0.00s t = 0.10s

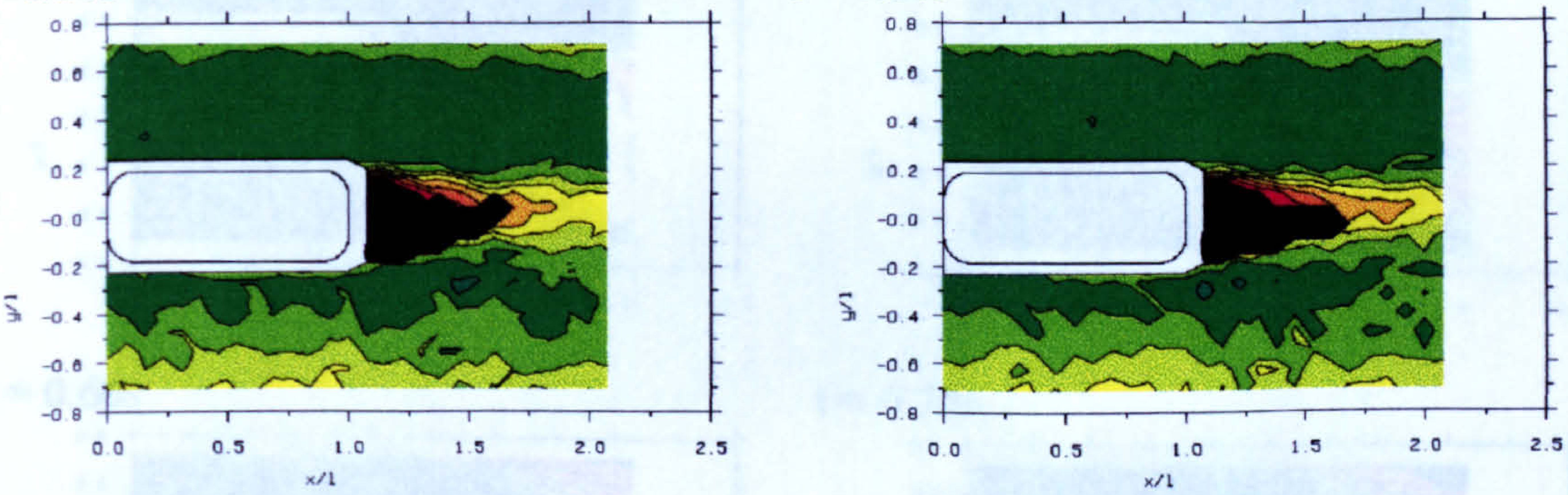

t = 0.20s t = 0.28s

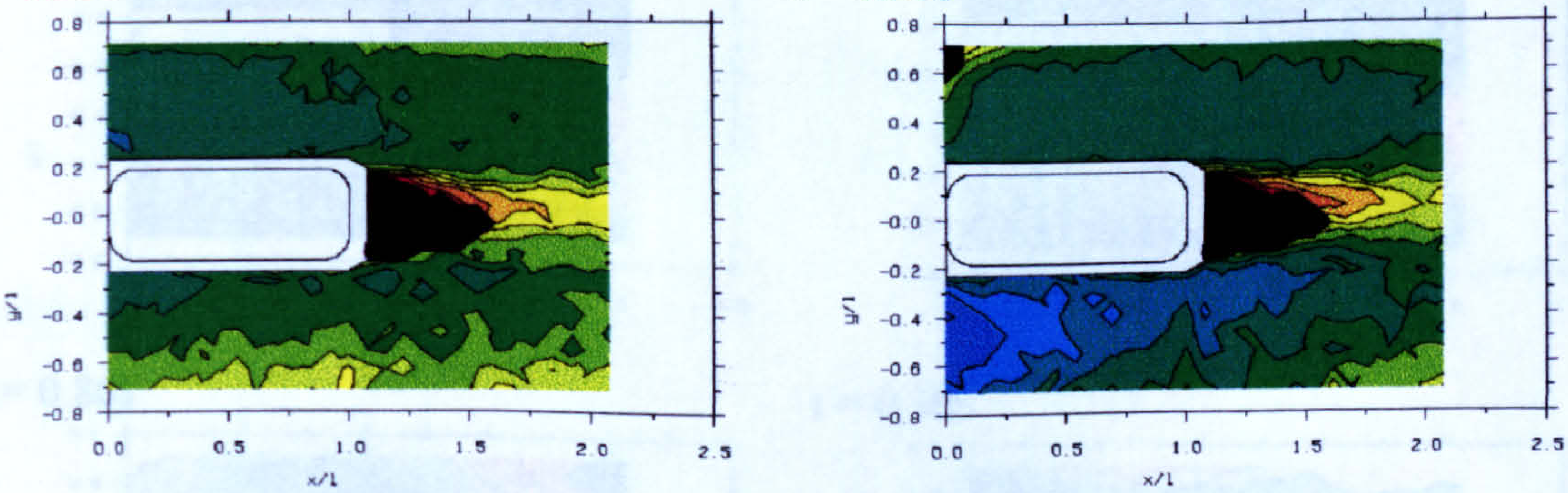

t = 0.34s t = 0.38s

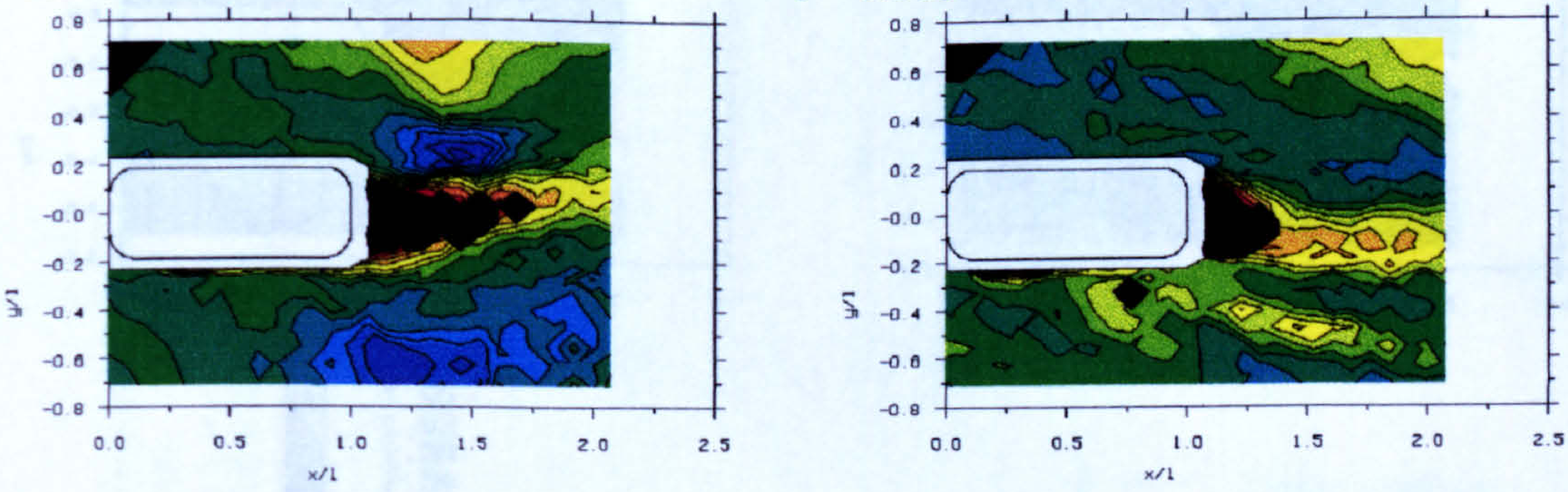

Figure 6.18 (page 1 of 2) Docton Geometry Transient Wake Survey Total Pressure Coefficient Contours

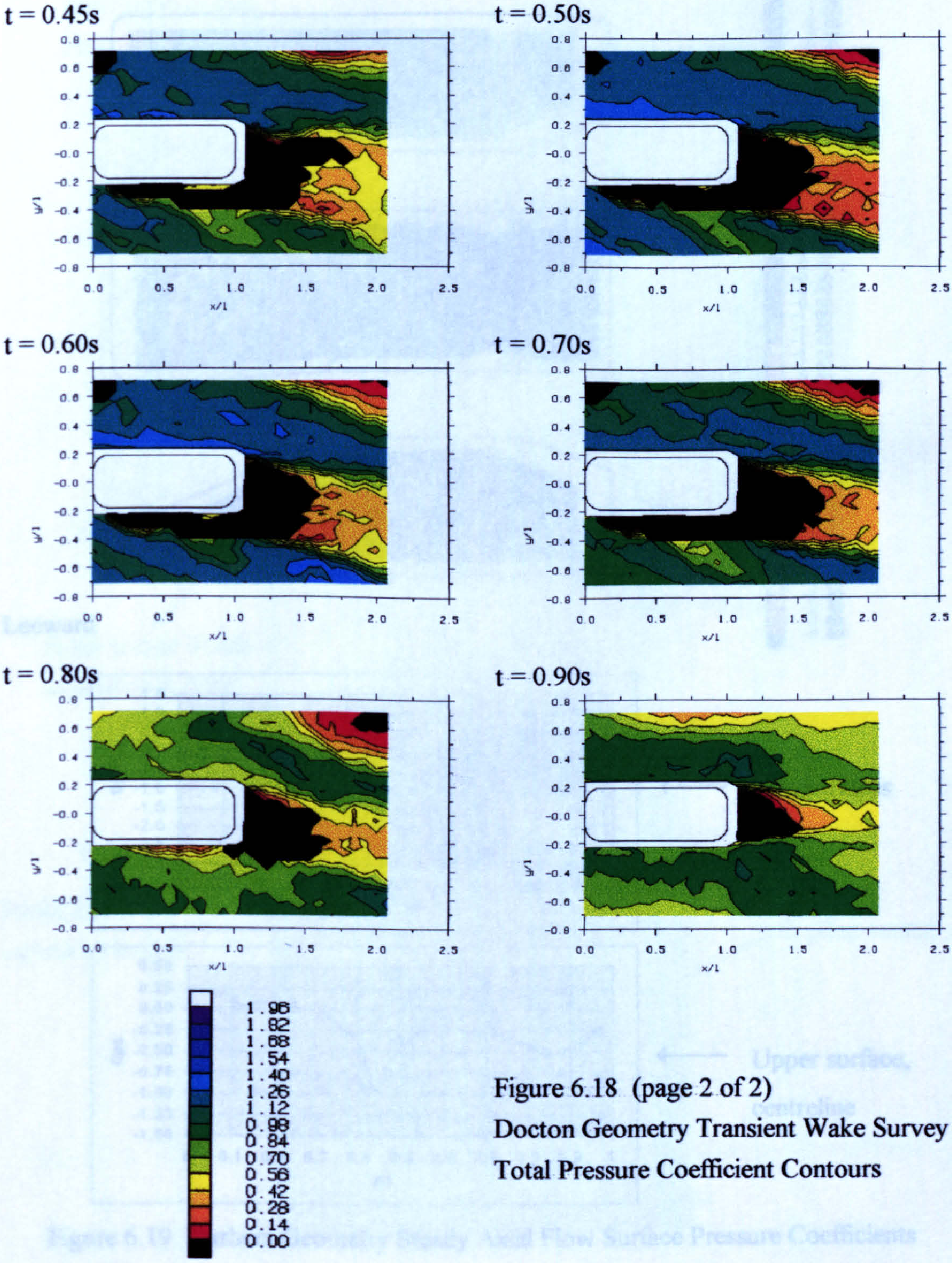

Figure 6.18 (page 2 of 2)
Docton Geometry Transient Wake Survey
Total Pressure Coefficient Contours

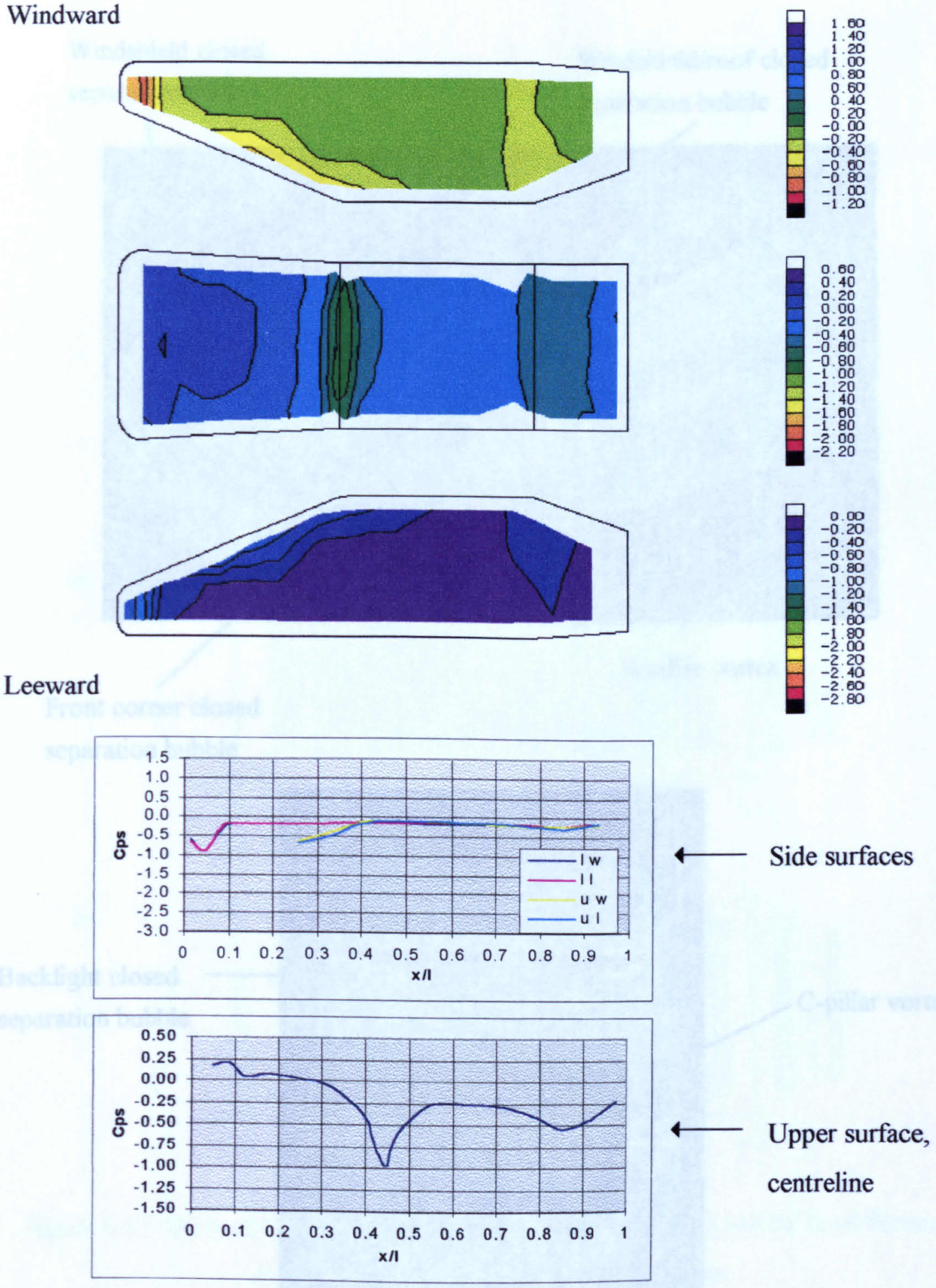

Figure 6.19 Durham Geometry Steady Axial Flow Surface Pressure Coefficients

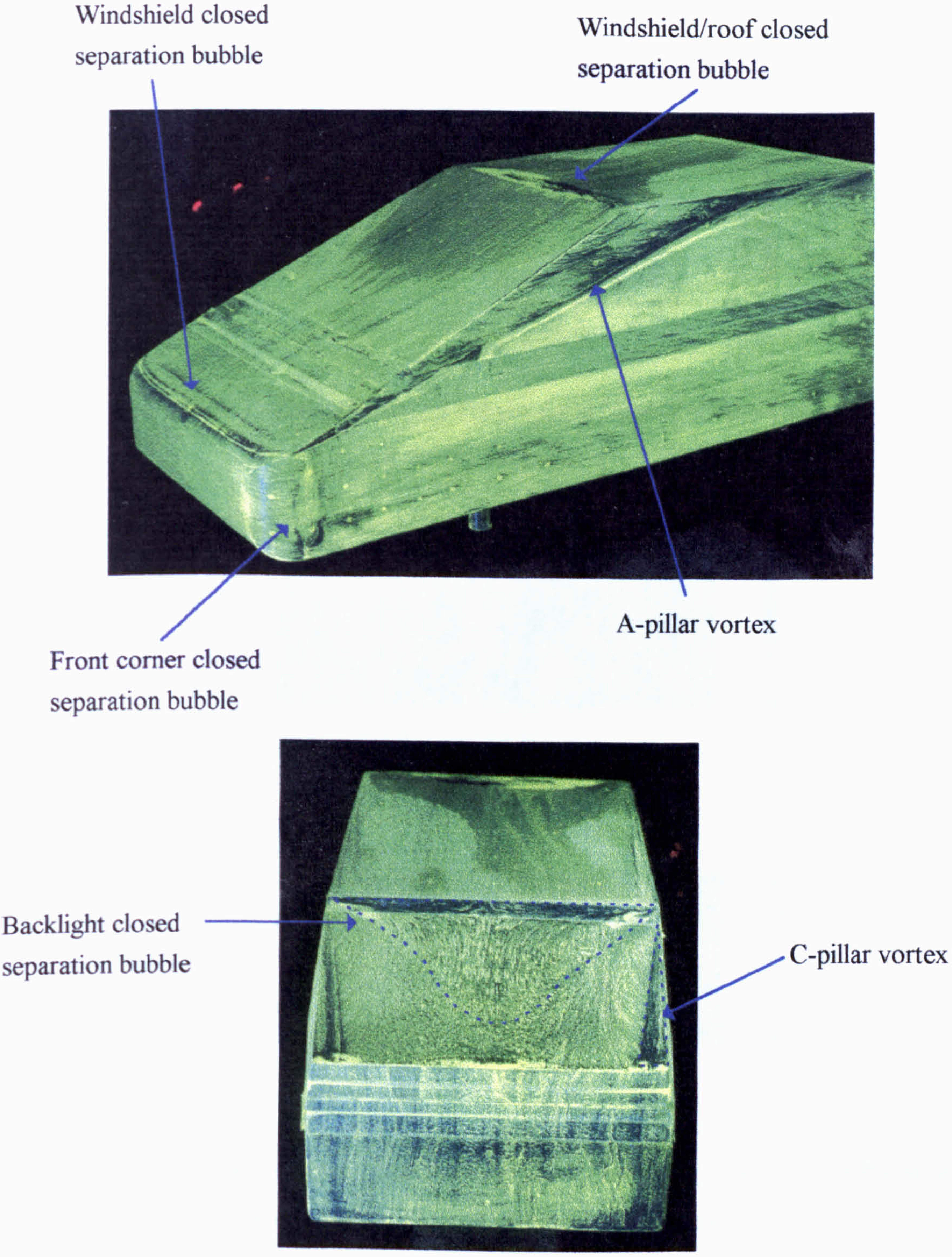

Figure 6.20 Durham Geometry Axial Flow Oil Flow Visualisation

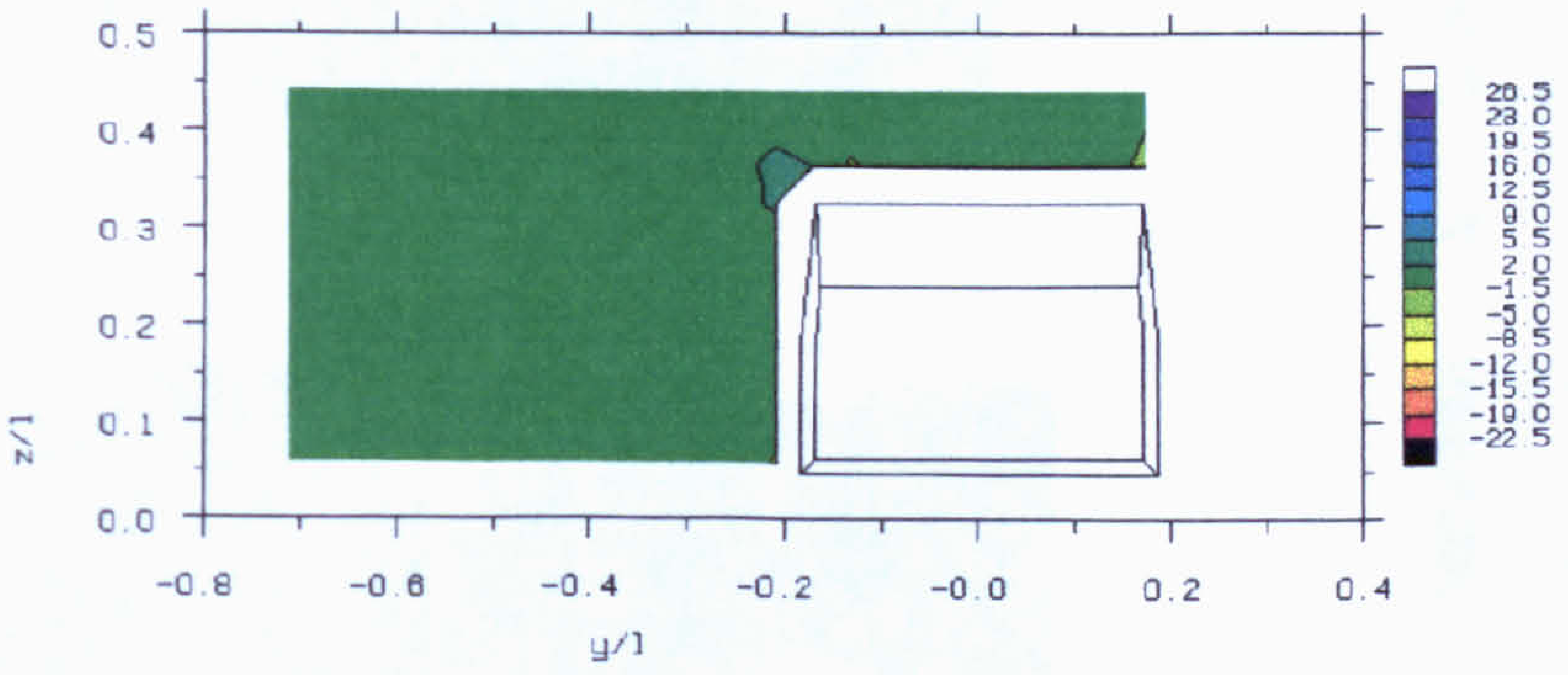

Figure 6.21 Durham Geometry Steady Axial Flow Vorticity Contours x/l = 0.75 Wakeplane

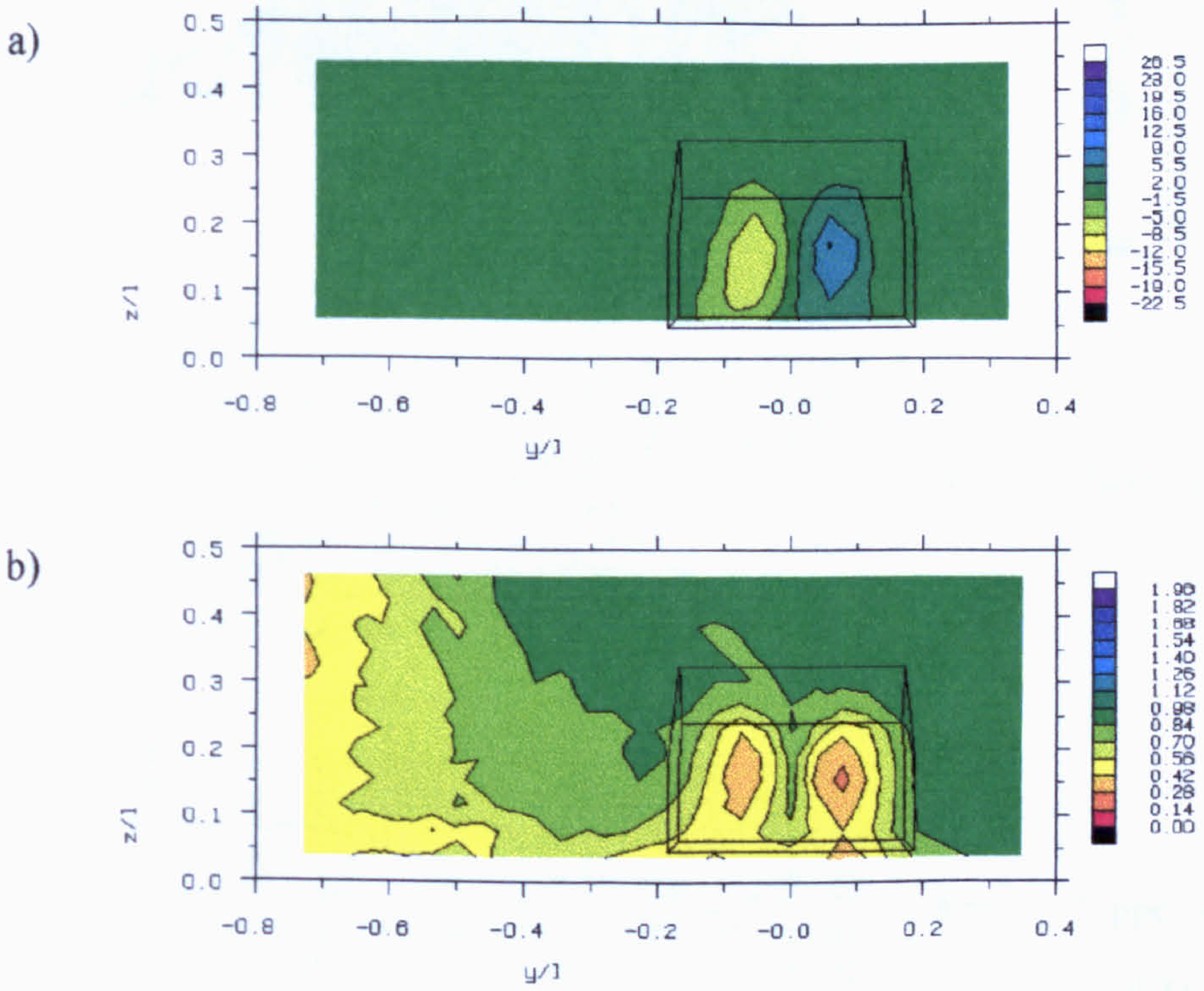

Figure 6.22 Durham Geometry Steady Axial Flow a) Vorticity and b) Total Pressure Coefficient Contours x/l = 1.50 Wakeplane

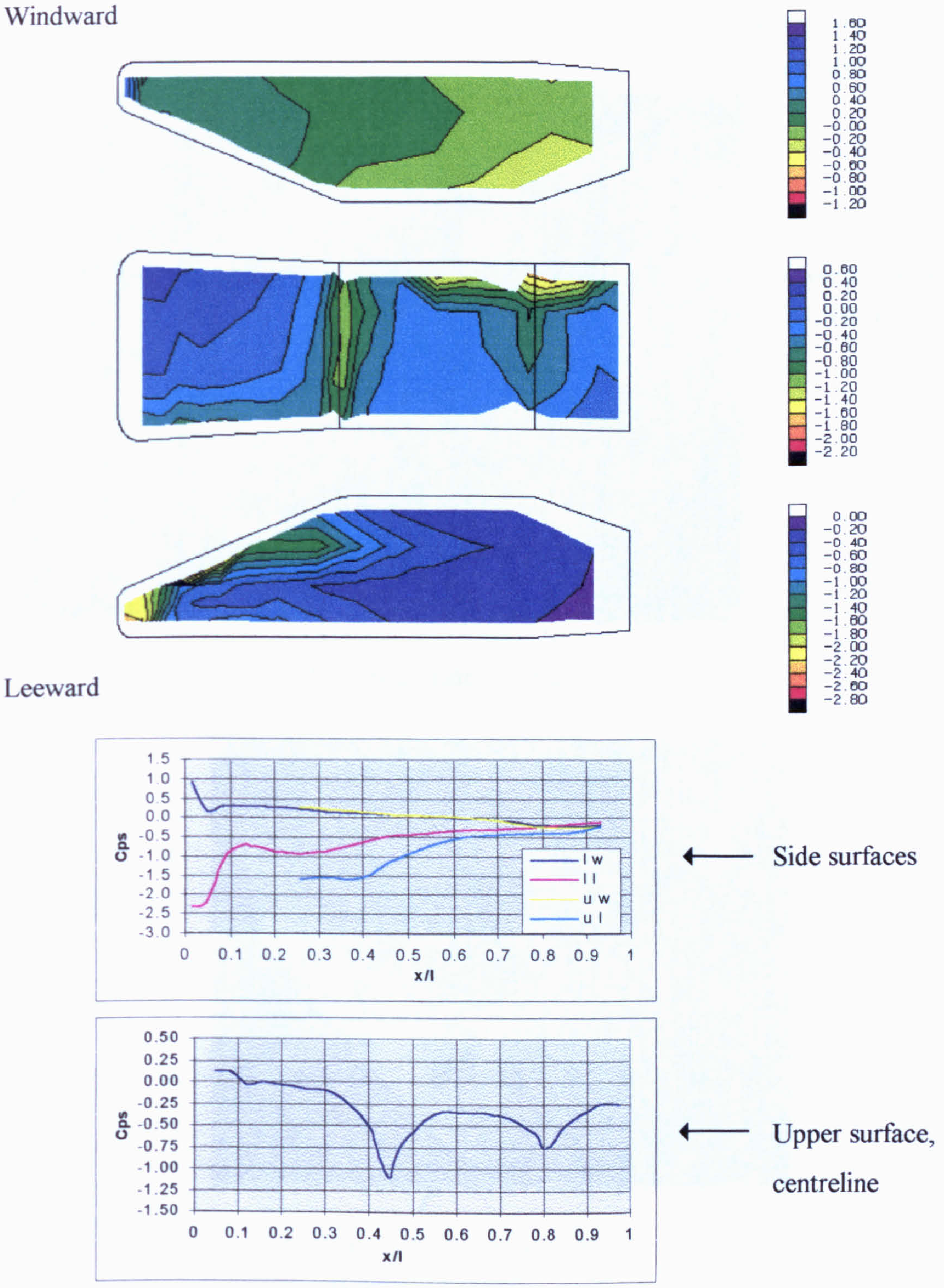

Figure 6.23 Durham Geometry Steady Yawed Flow Surface Pressure Coefficients

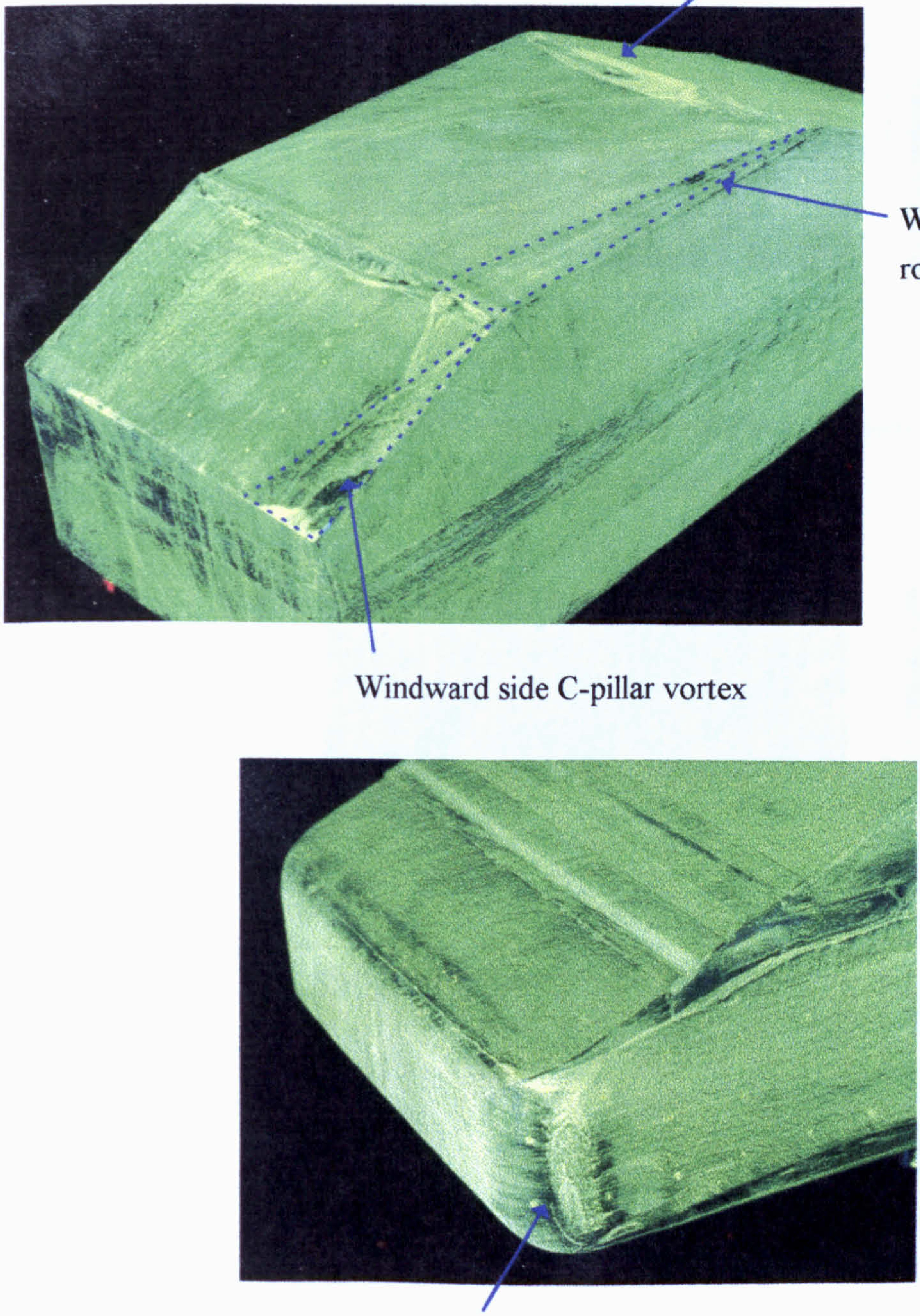

Windshield/roof closed separation bubble

Windward side roof vortex

Windward side C-pillar vortex

Leeward front corner closed separation bubble

Figure 6.24 Durham Geometry Yawed Flow Oil Flow Visualisation

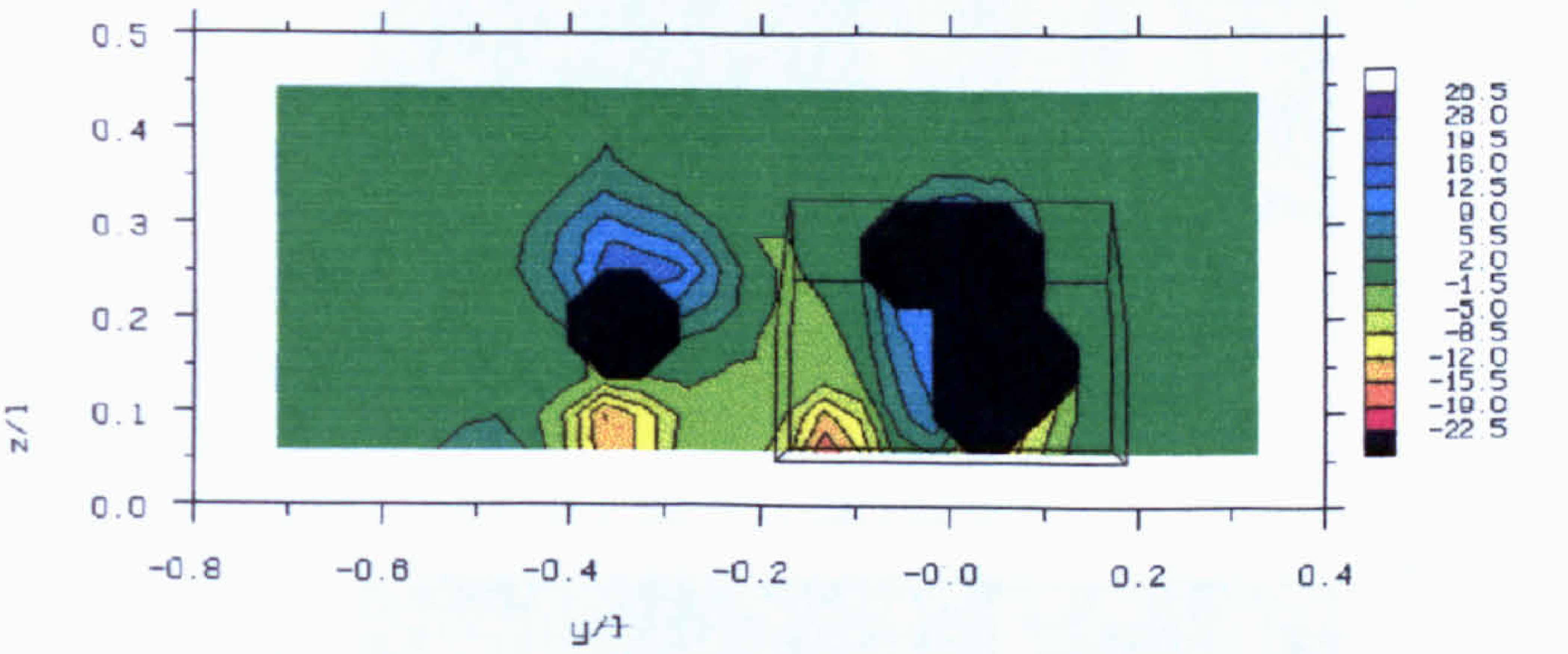

Figure 6.25 Durham Geometry Steady Yawed Flow Vorticity Contours x/l = 1.30 Wakeplane

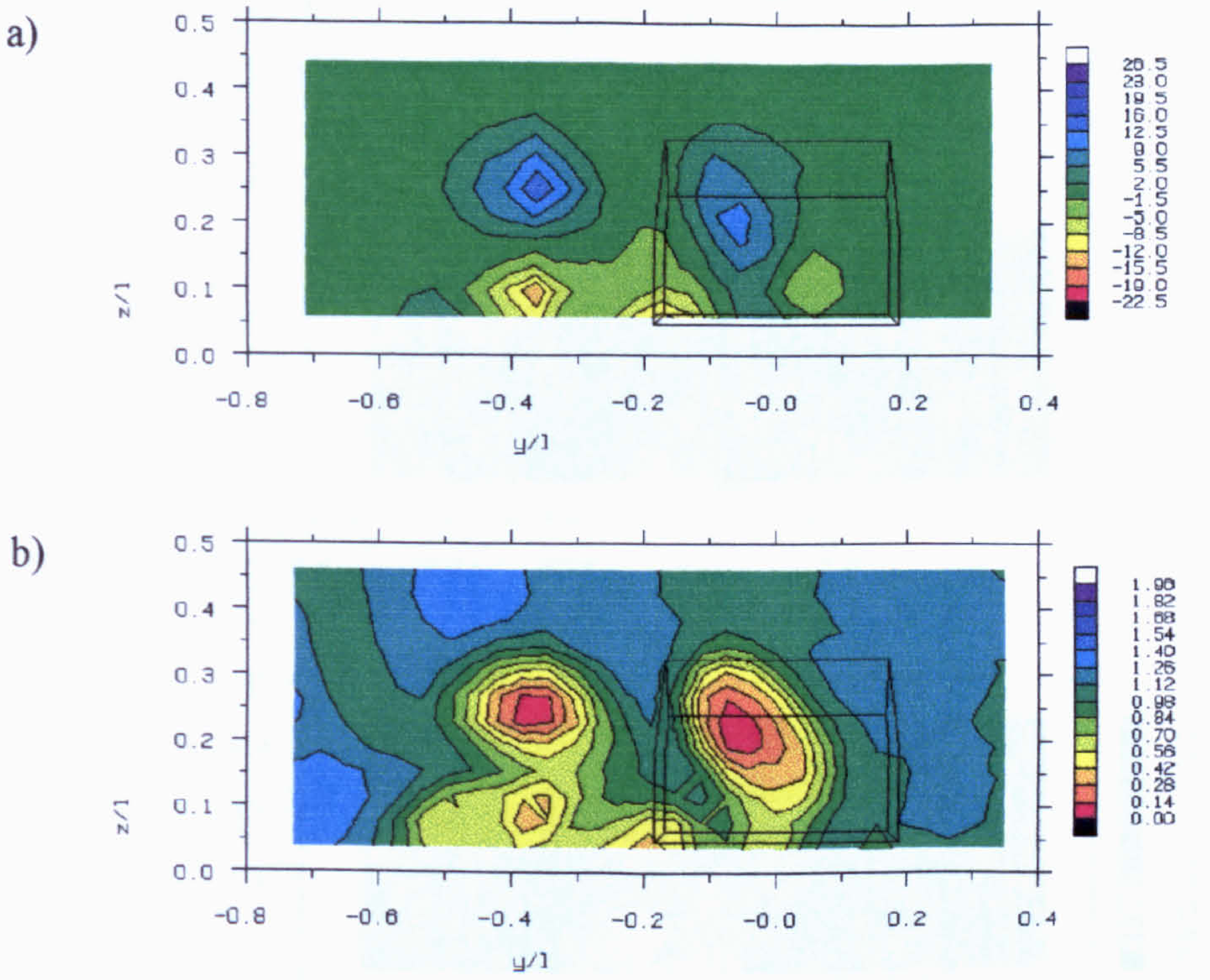

Figure 6.26 Durham Geometry Steady Yawed Flow a) Vorticity and b) Total Pressure Coefficient Contours x/l = 1.50 Wakeplane

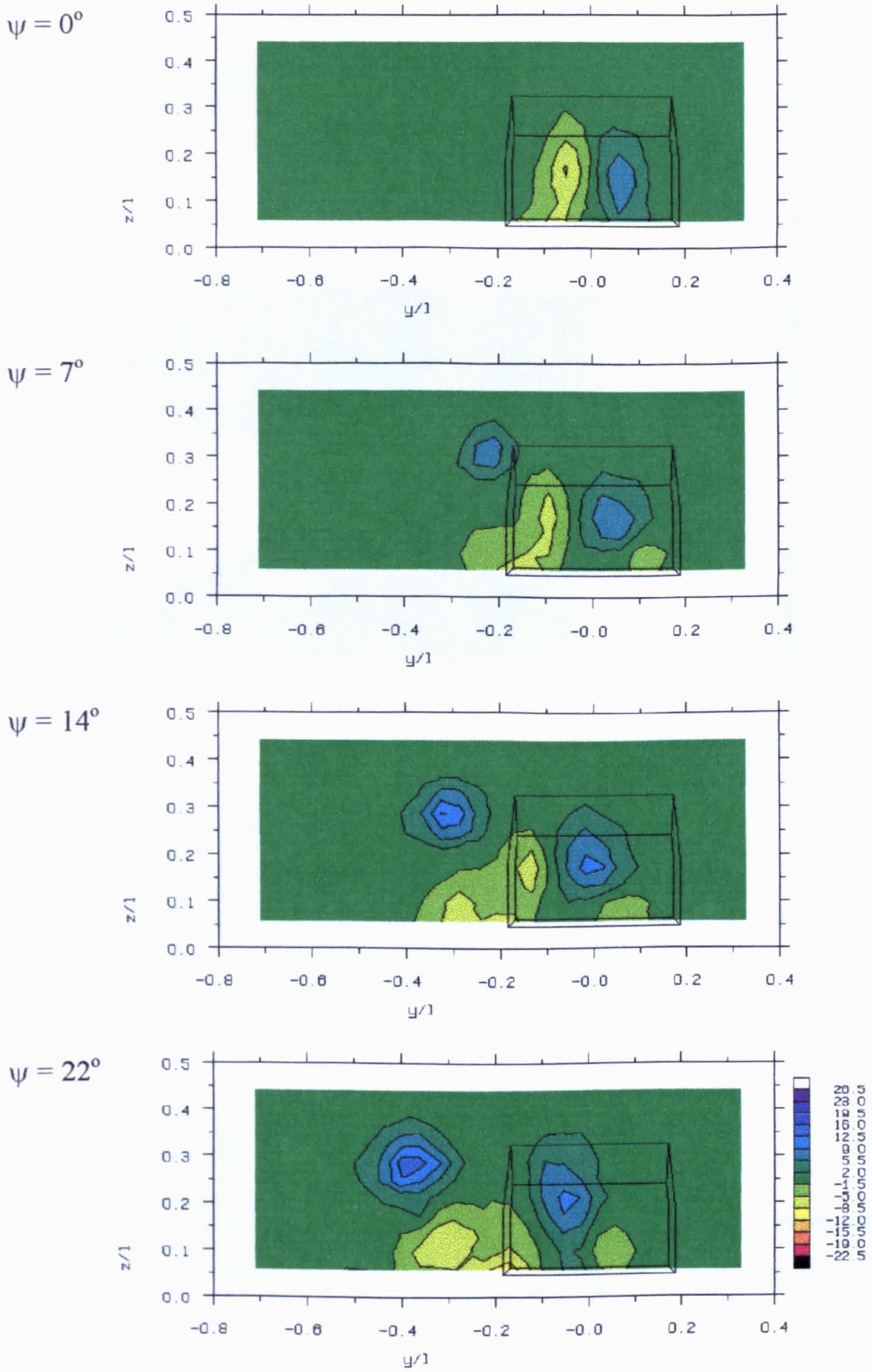

Figure 6.27 Durham Geometry Quasi-Steady Vorticity Contours
x/l = 1.5 Wakeplane

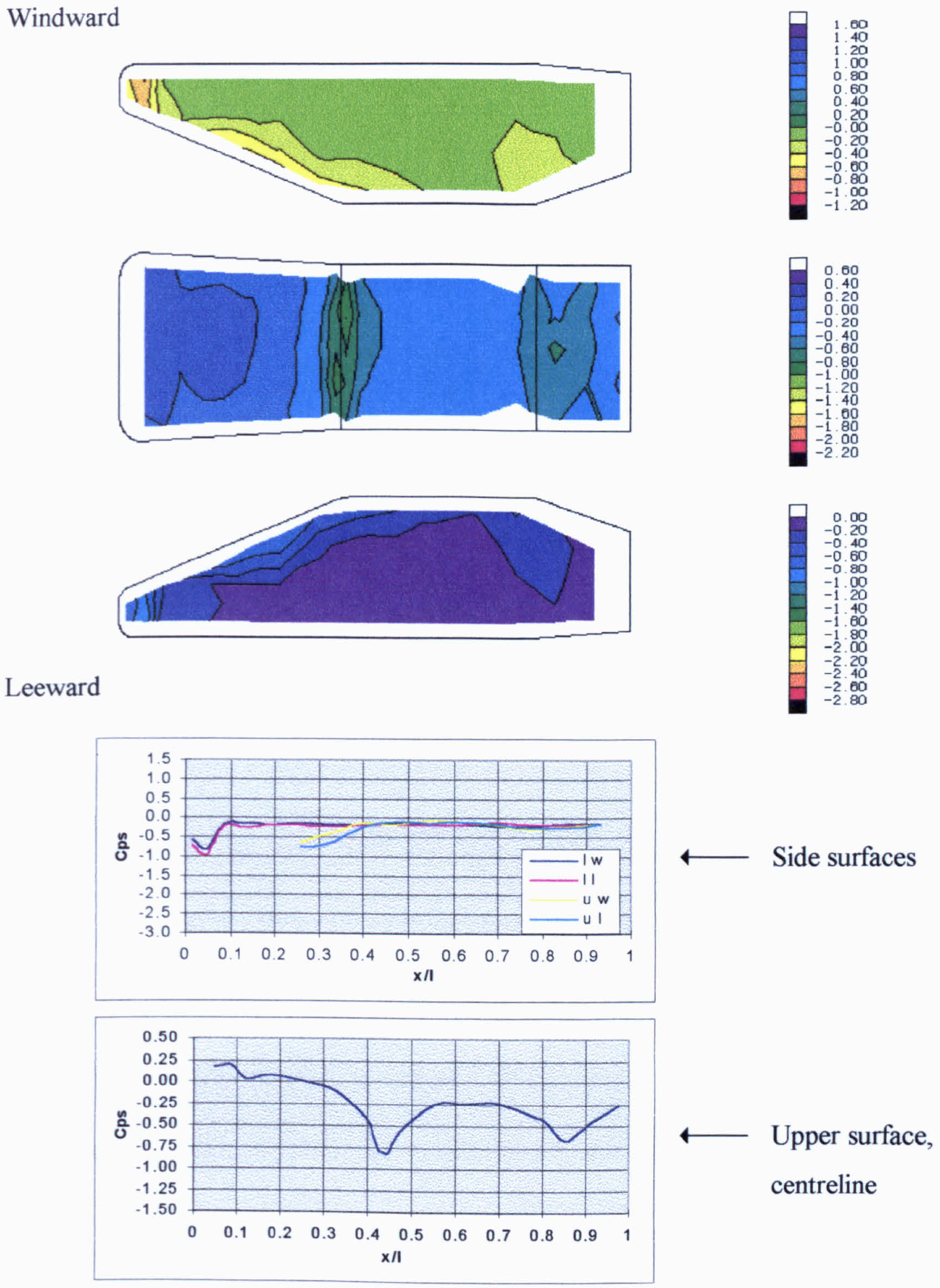

Figure 6.28 Durham Geometry Transient Surface Pressure Coefficients

t = 0.10s

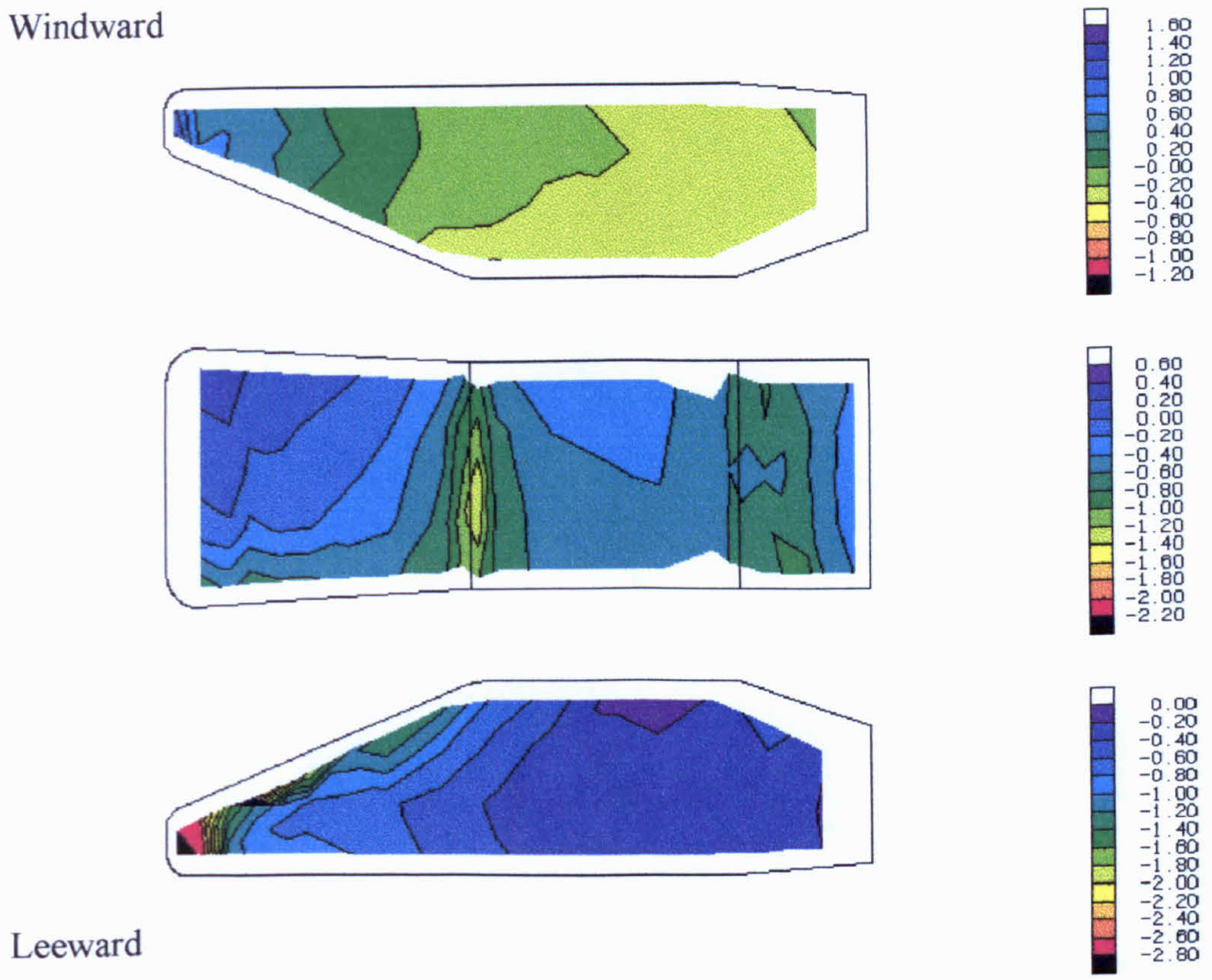

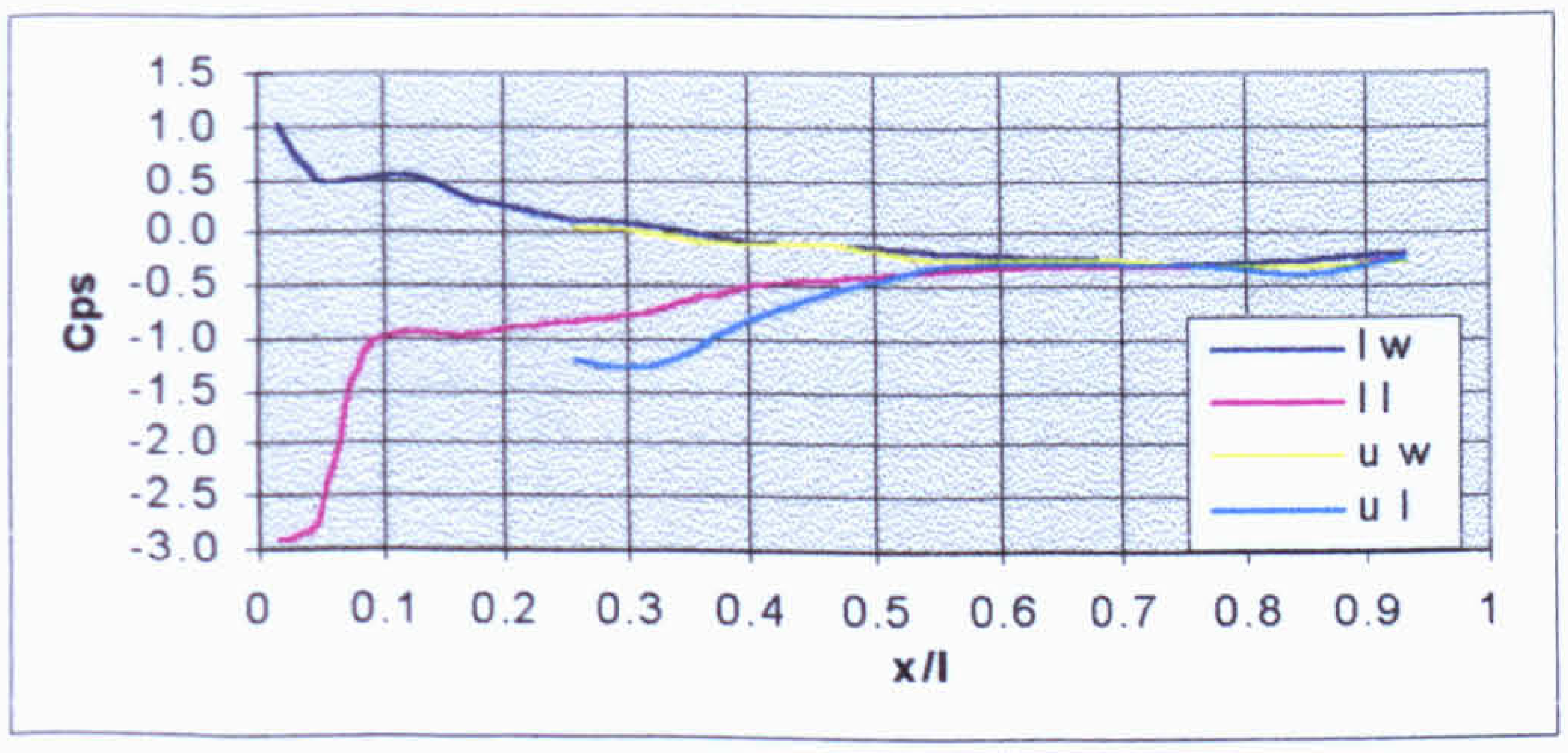

← Side surfaces

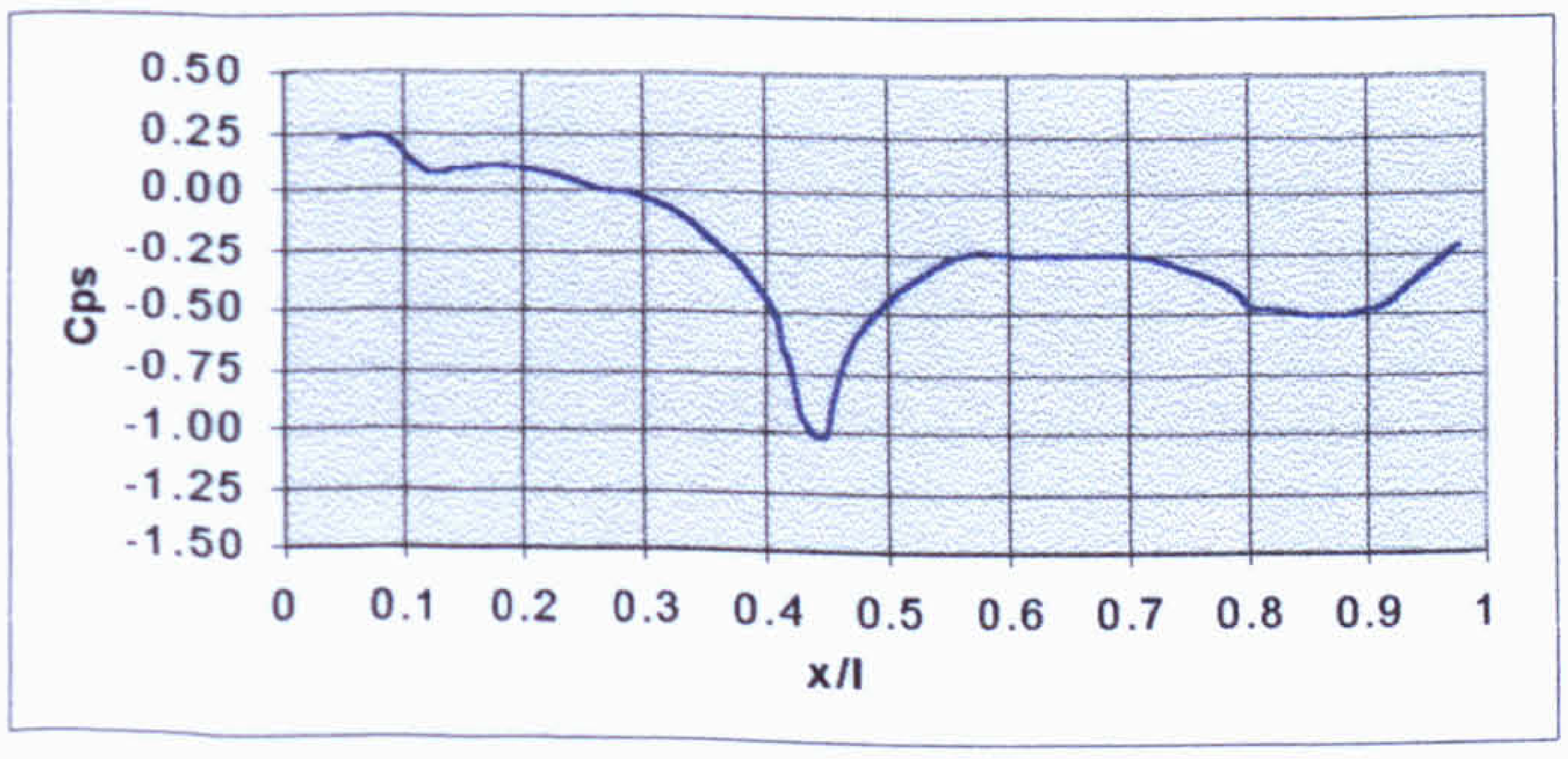

← Upper surface, centreline

Figure 6.29 Durham Geometry Transient Surface Pressure Coefficients

t = 0.30s

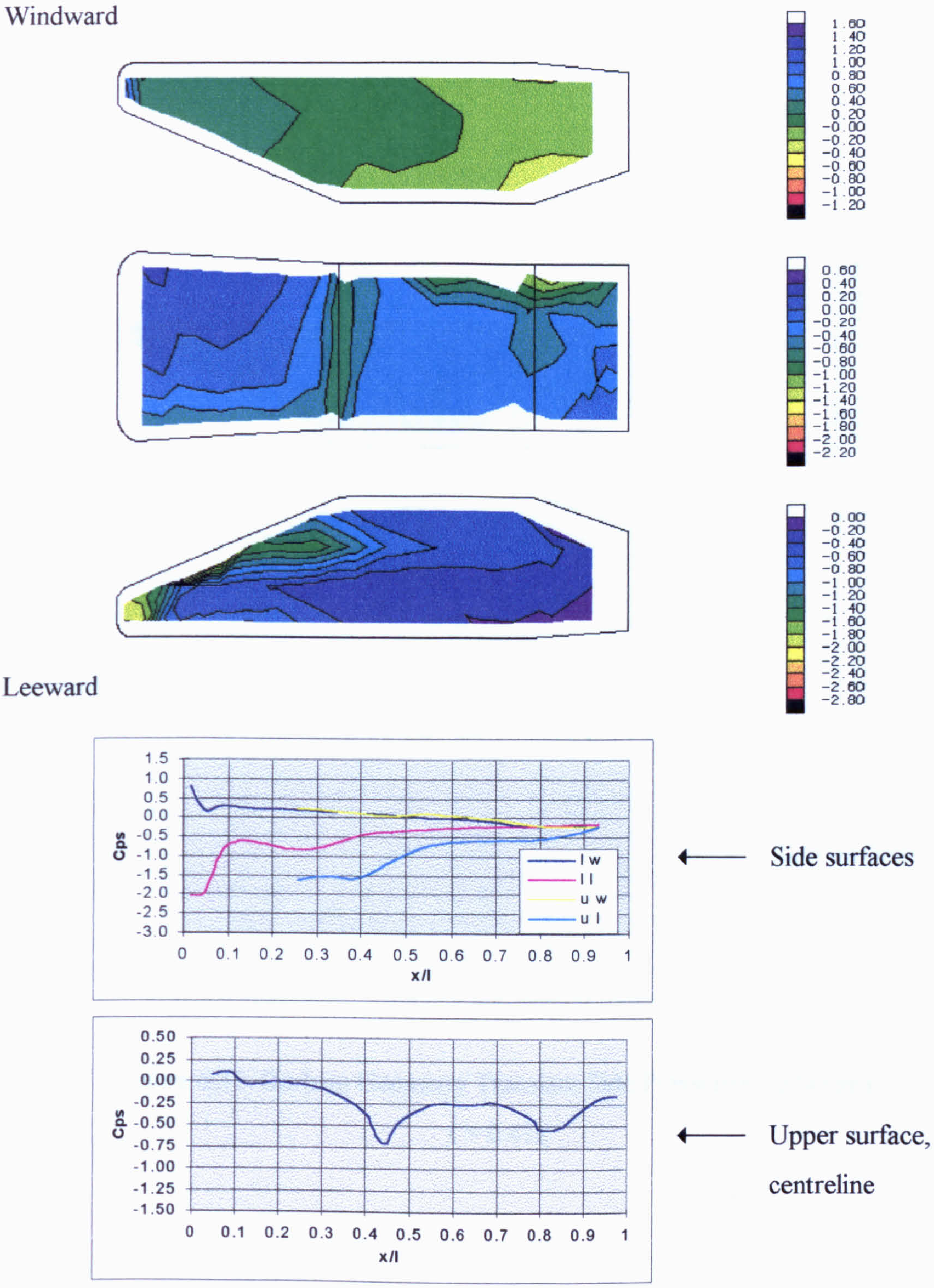

Figure 6.30 Durham Geometry Transient Surface Pressure Coefficients

t = 0.34s

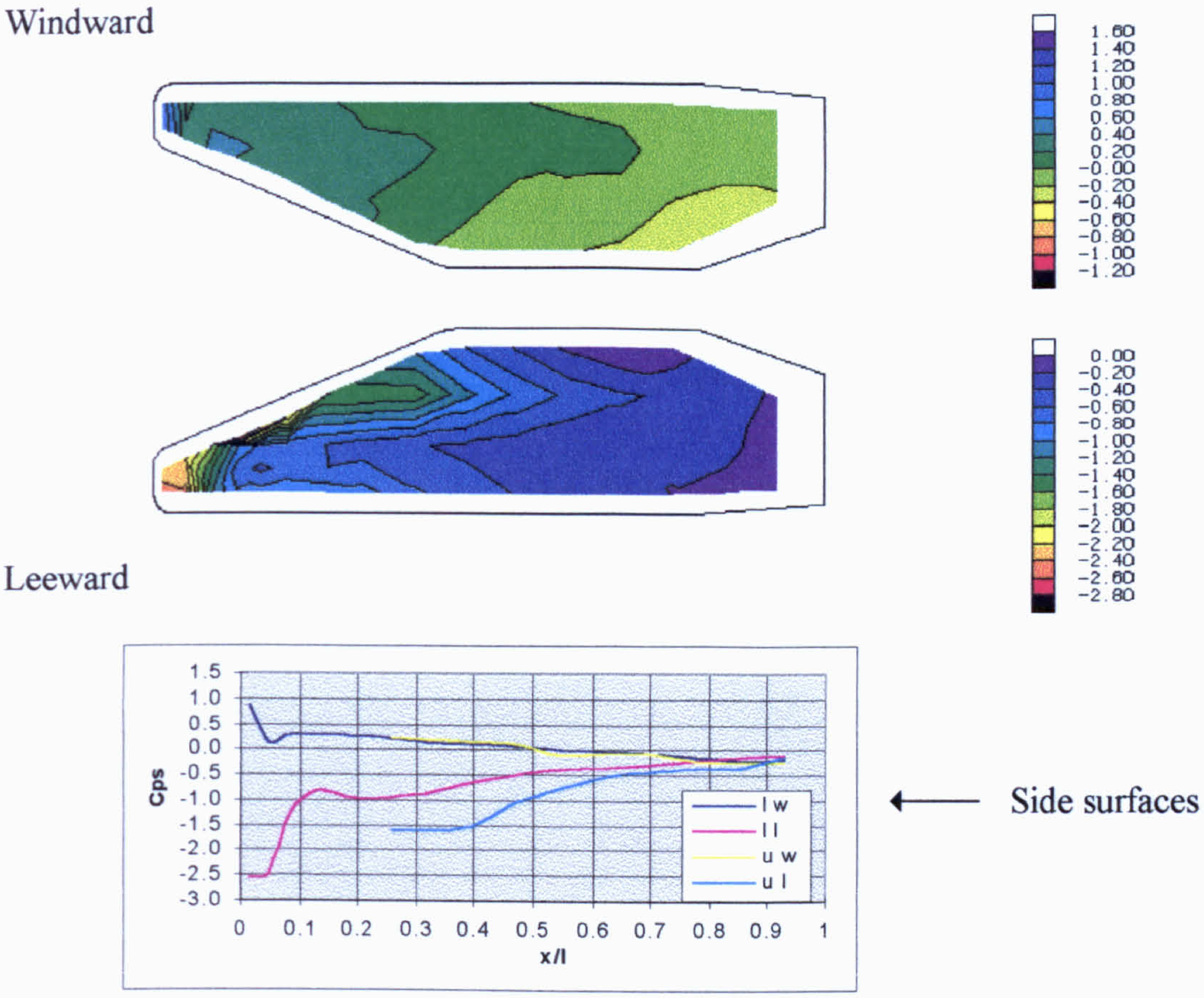

Figure 6.31 Durham Geometry Transient Side Pressure Coefficients

t = 0.47s

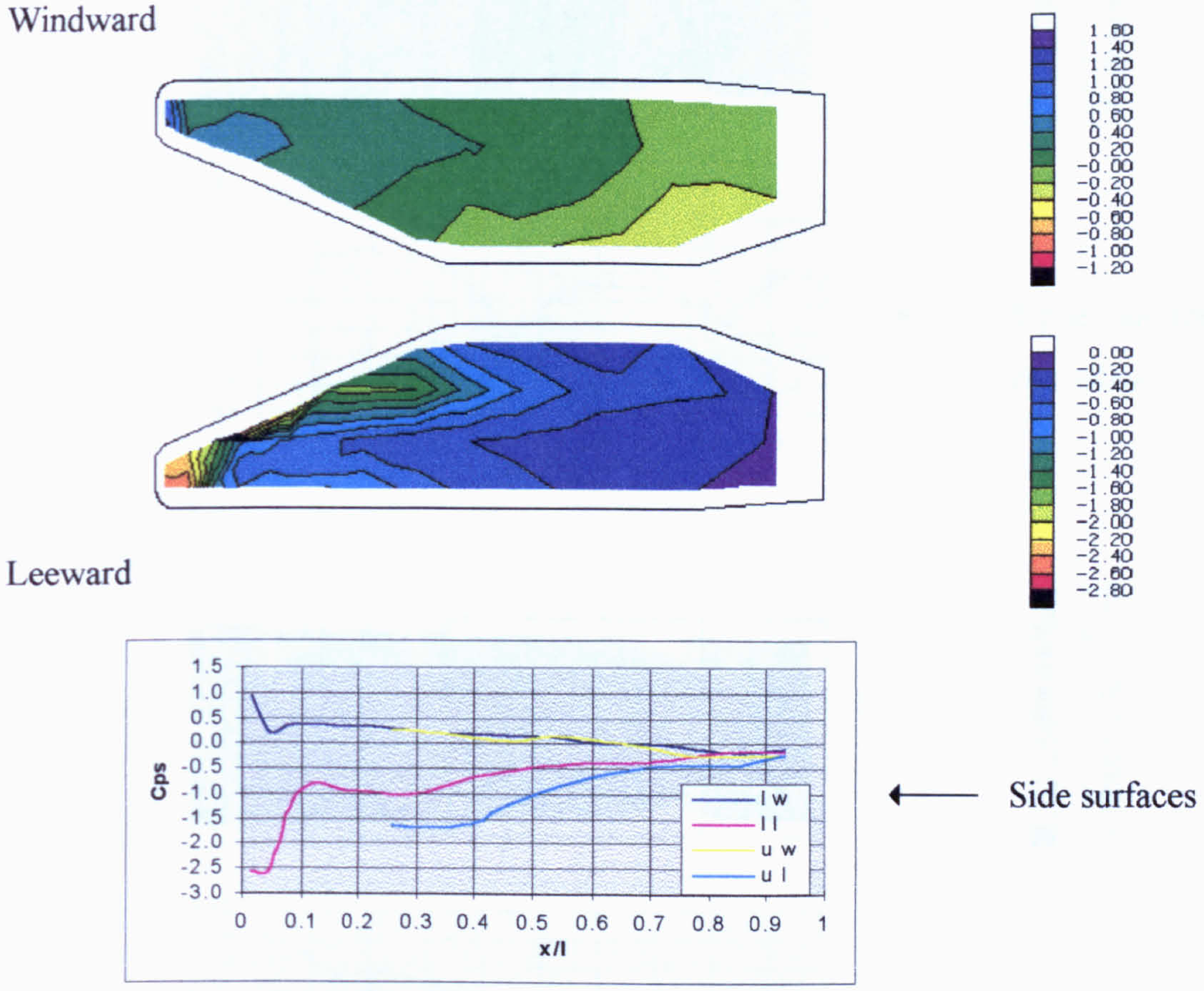

Figure 6.32 Durham Geometry Transient Side Pressure Coefficients

t = 0.52s

t = 0.45s

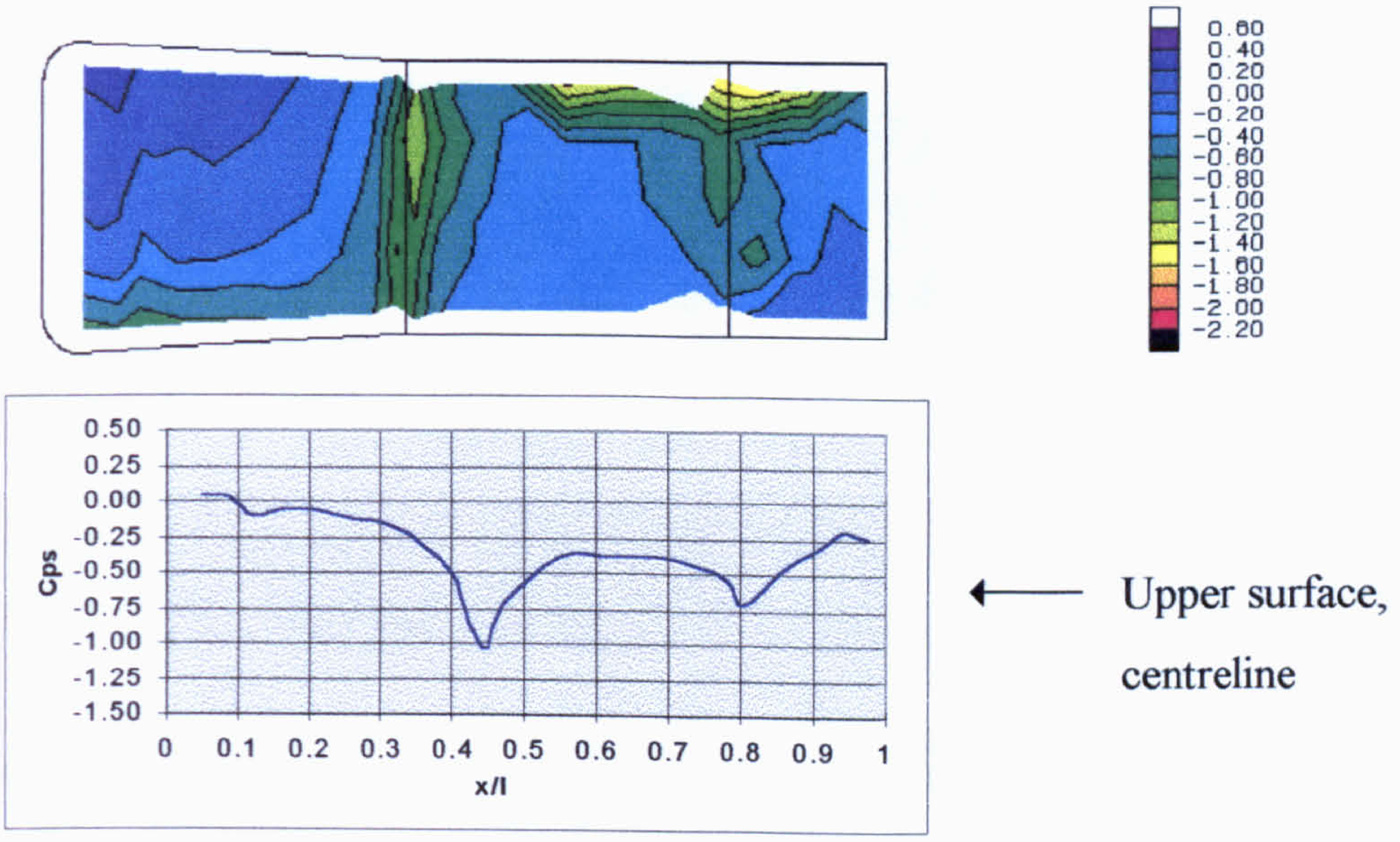

t = 0.55s

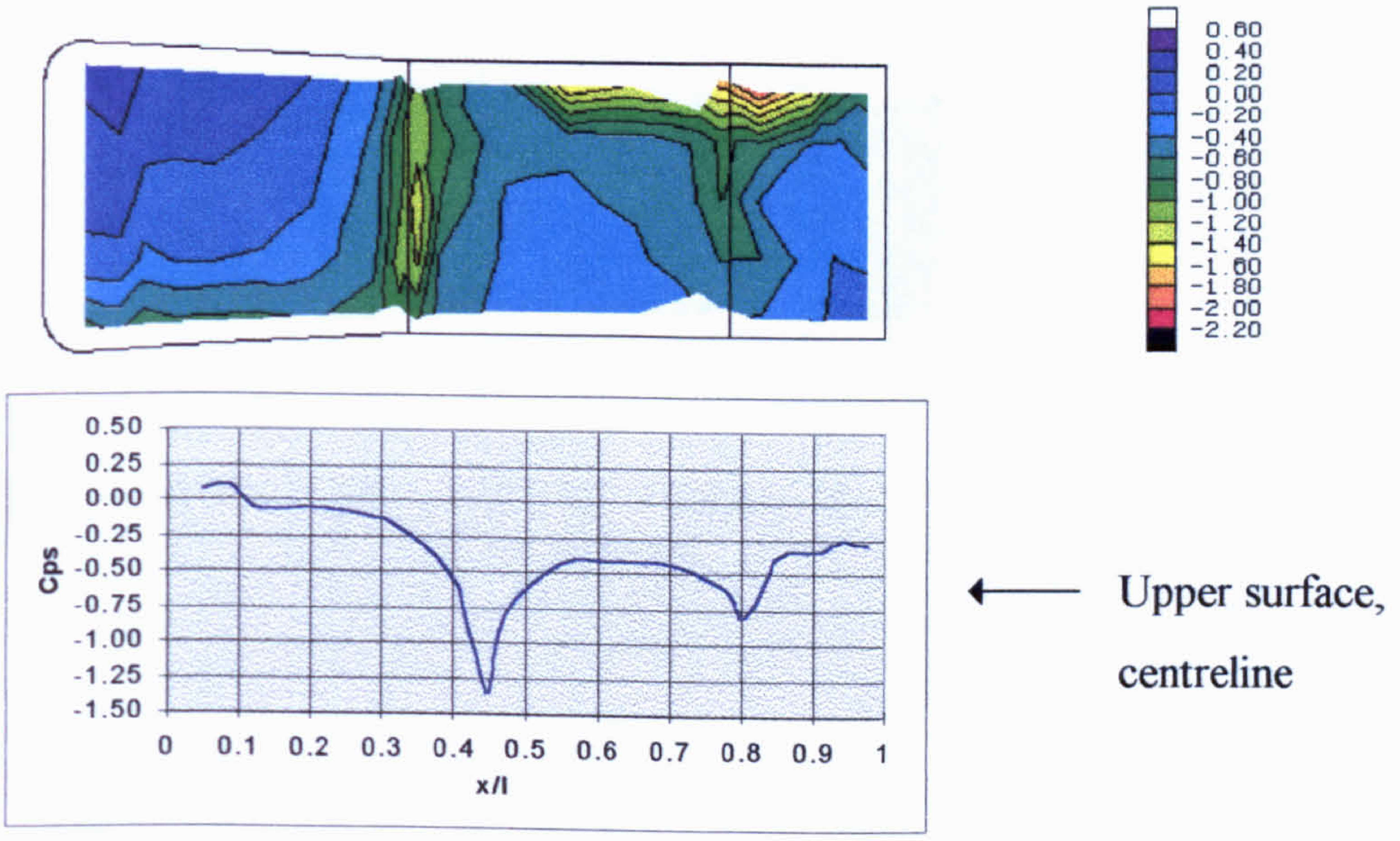

Figure 6.33 Durham Geometry Transient Upper Surface Pressure Coefficients

t = 0.74s

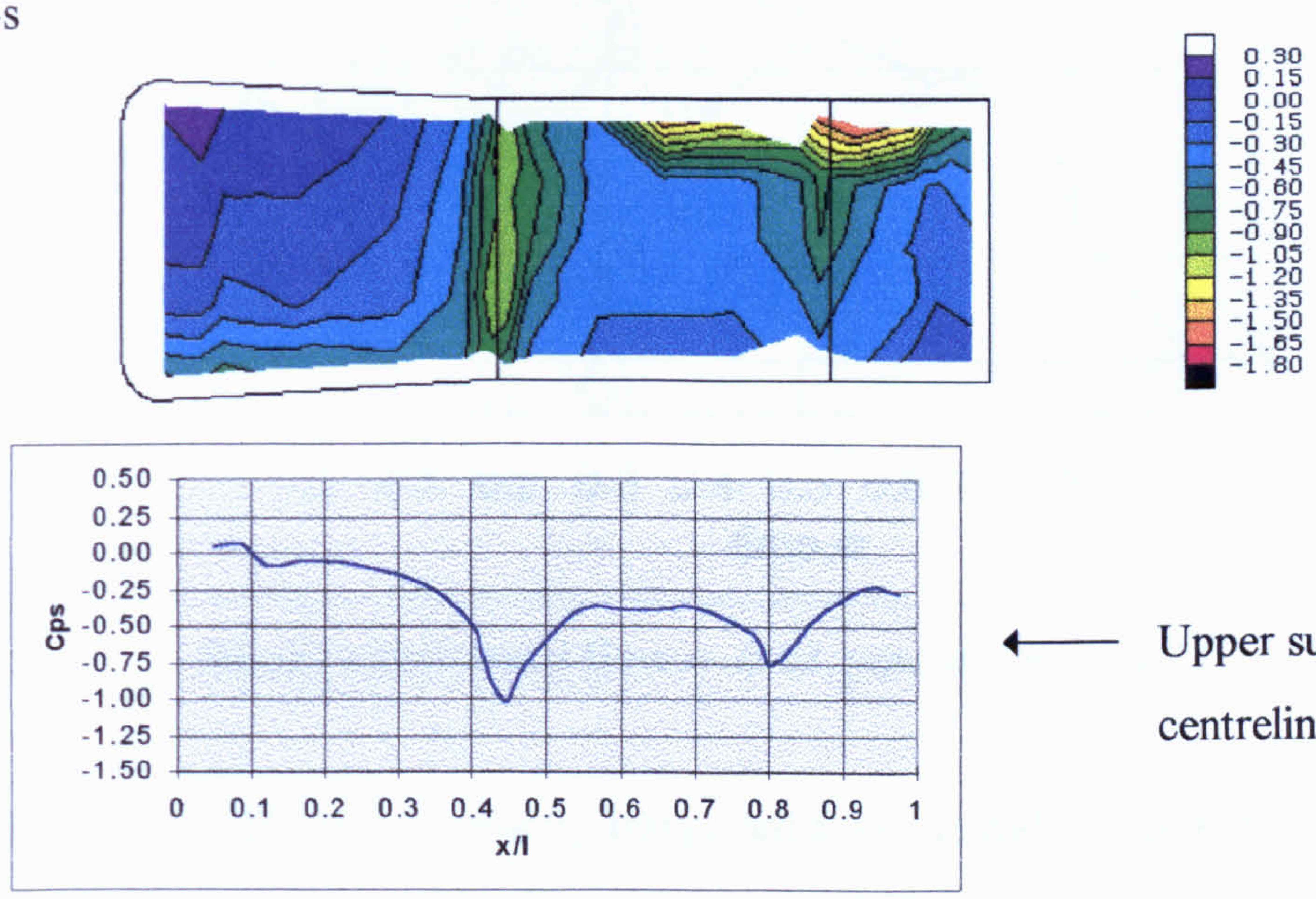

← Upper surface, centreline

t = 0.76s

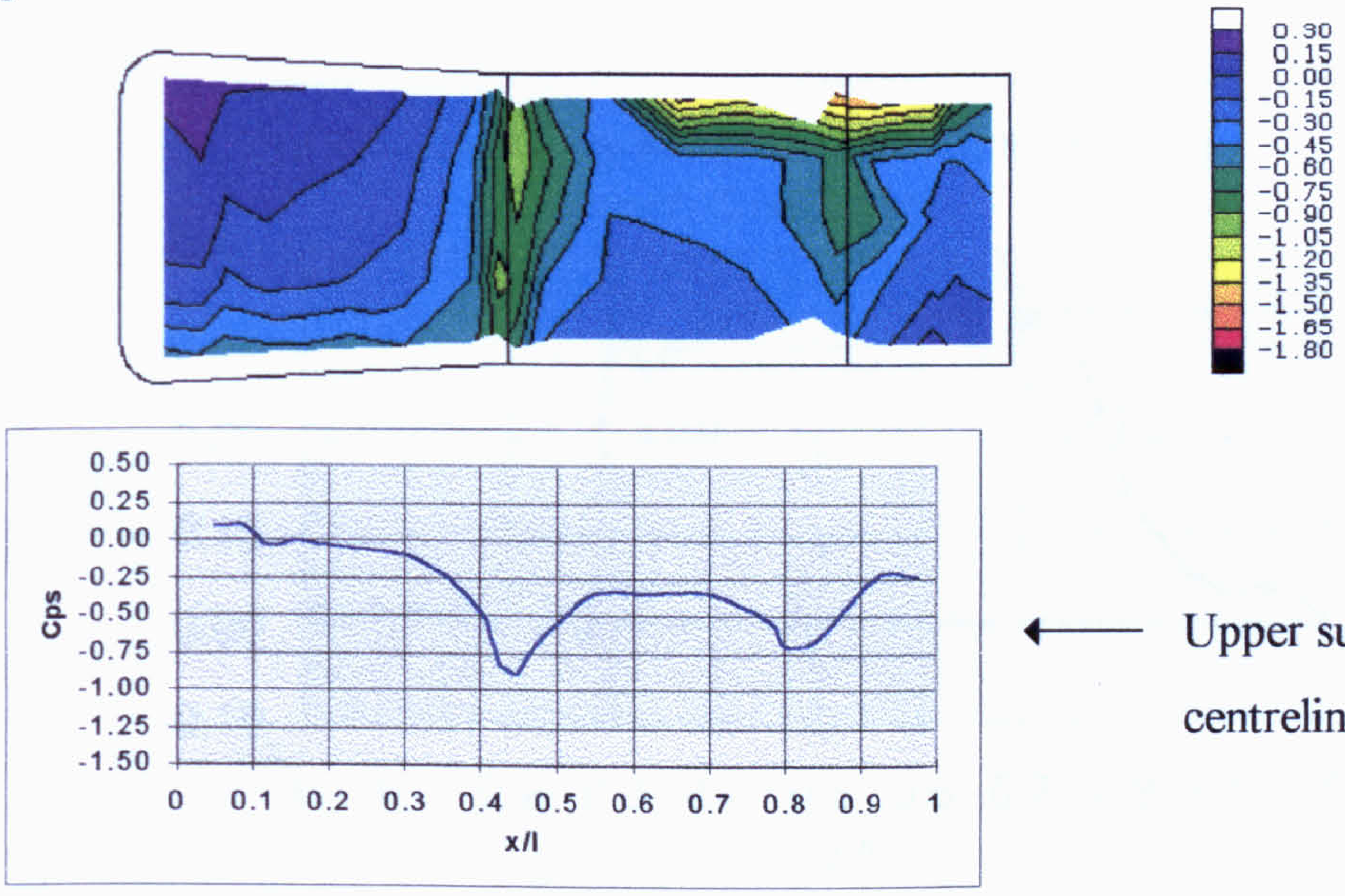

← Upper surface, centreline

Figure 6.34 Durham Geometry Transient Upper Surface Pressure Coefficients

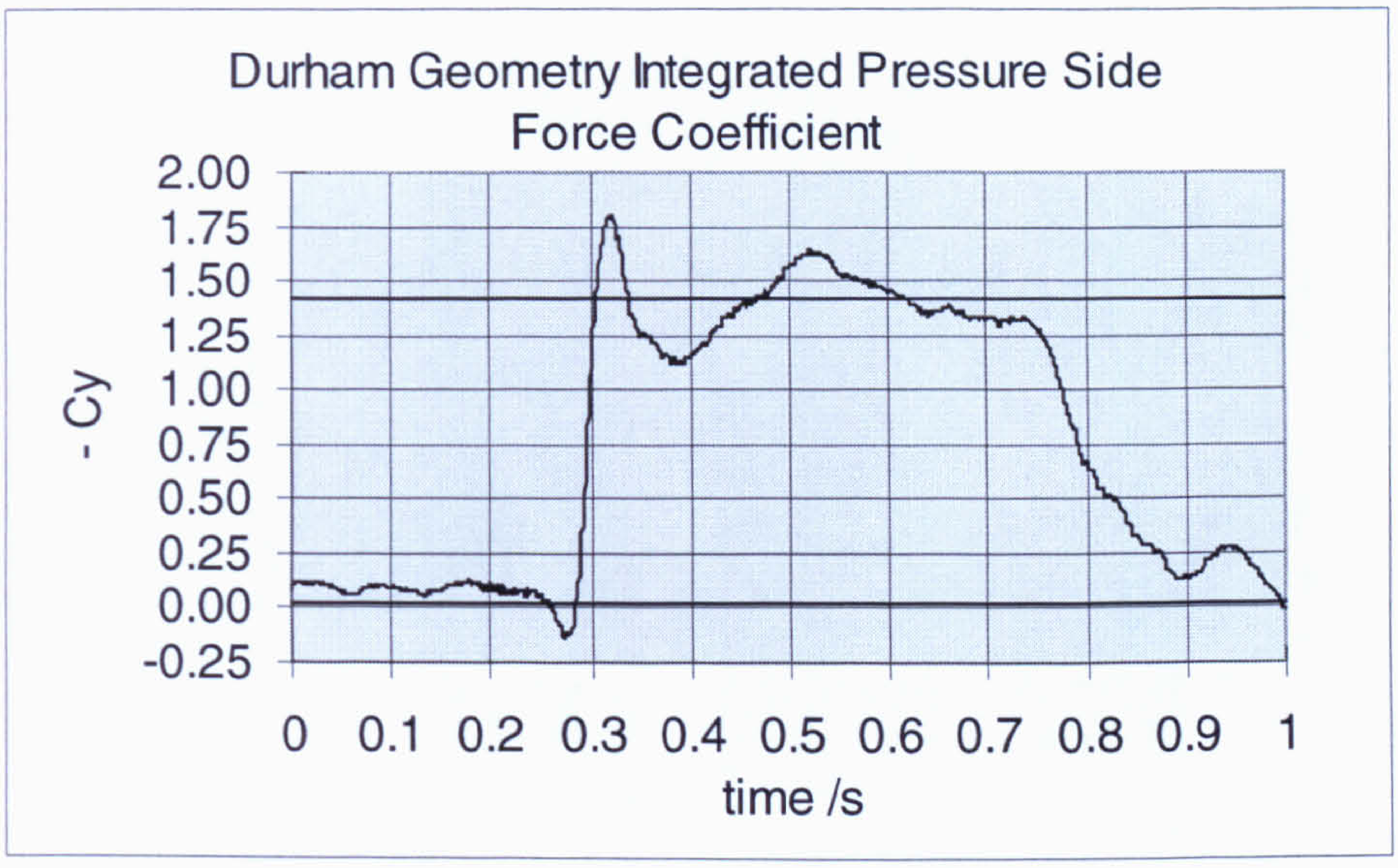

Steady values: axial flow = -0.02, yawed flow = -1.41.

Figure 6.35 Durham Geometry Integrated Pressure Side Force Coefficients

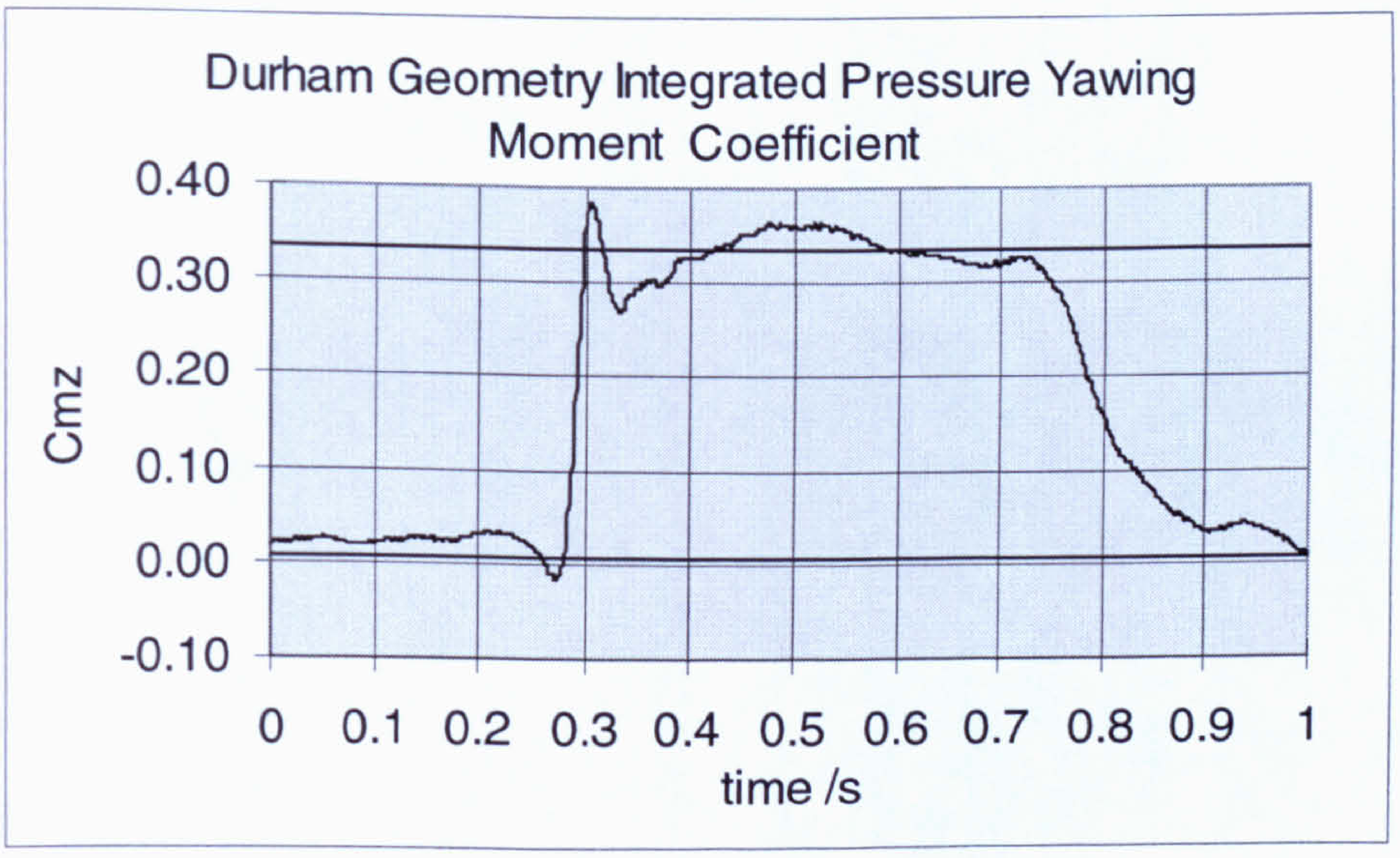

Steady values: axial flow = 0.01, yawed flow = 0.34.

Figure 6.36 Durham Geometry Integrated Pressure Yawing Moment Coefficients

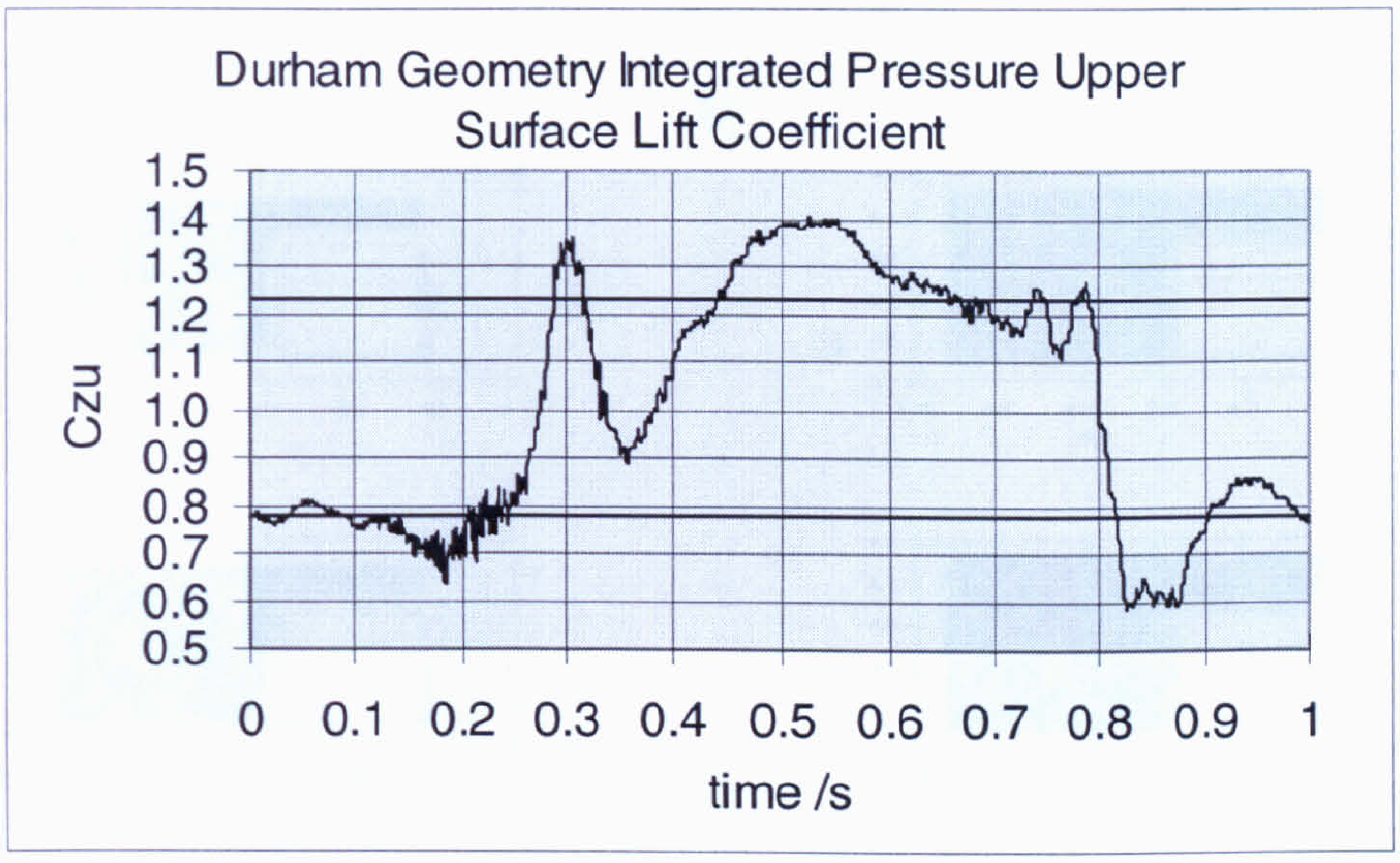

Steady values: axial flow = 0.78, yawed flow = 1.23.

Figure 6.37 Durham Geometry Integrated Pressure Upper Surface Lift Coefficients

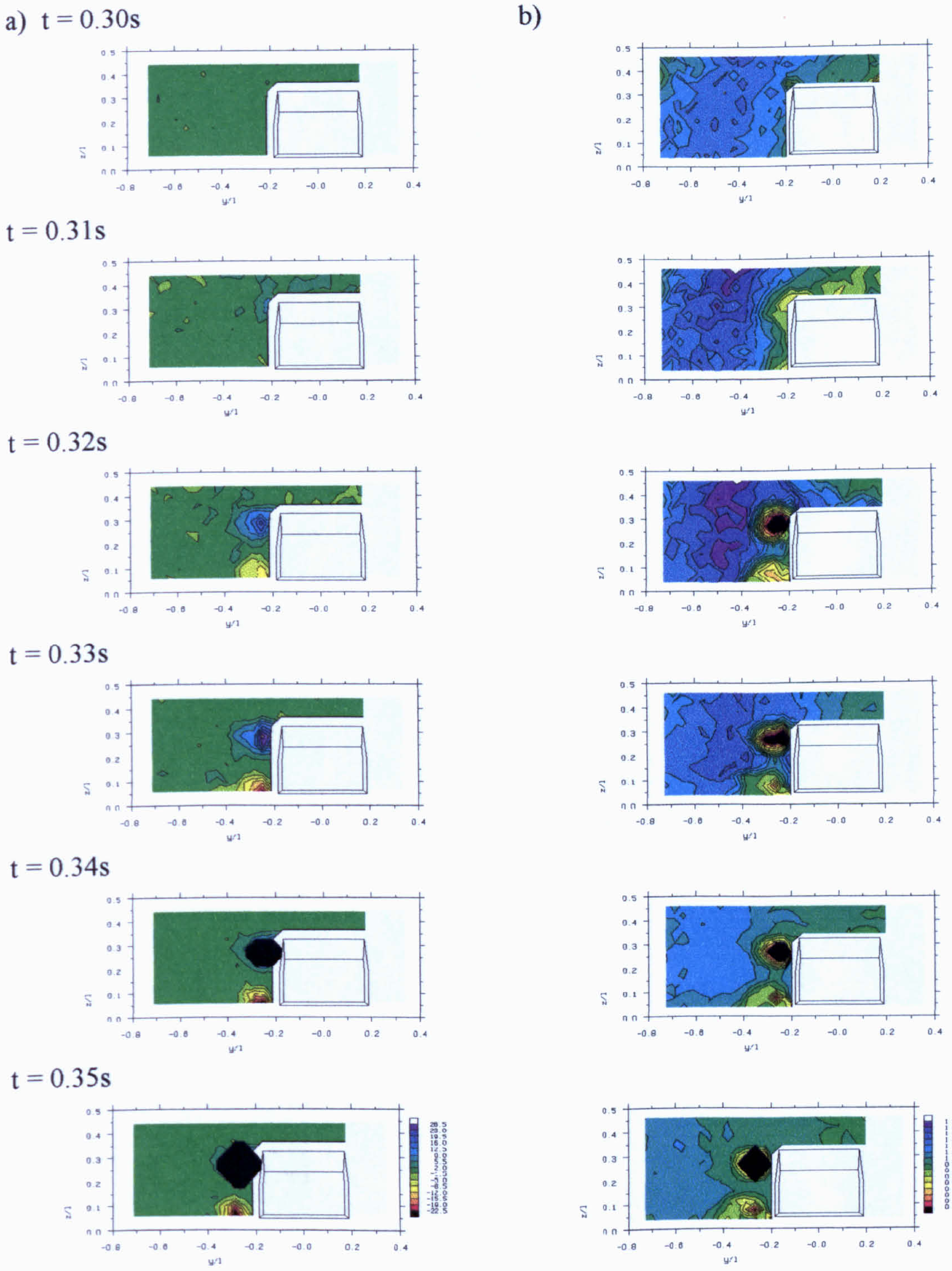
a) t = 0.30s

b)

t = 0.31s

t = 0.32s

t = 0.33s

t = 0.34s

t = 0.35s

Figure 6.38 Durham Geometry a) Vorticity and b) Total Pressure Coefficient Contours x/l = 0.75

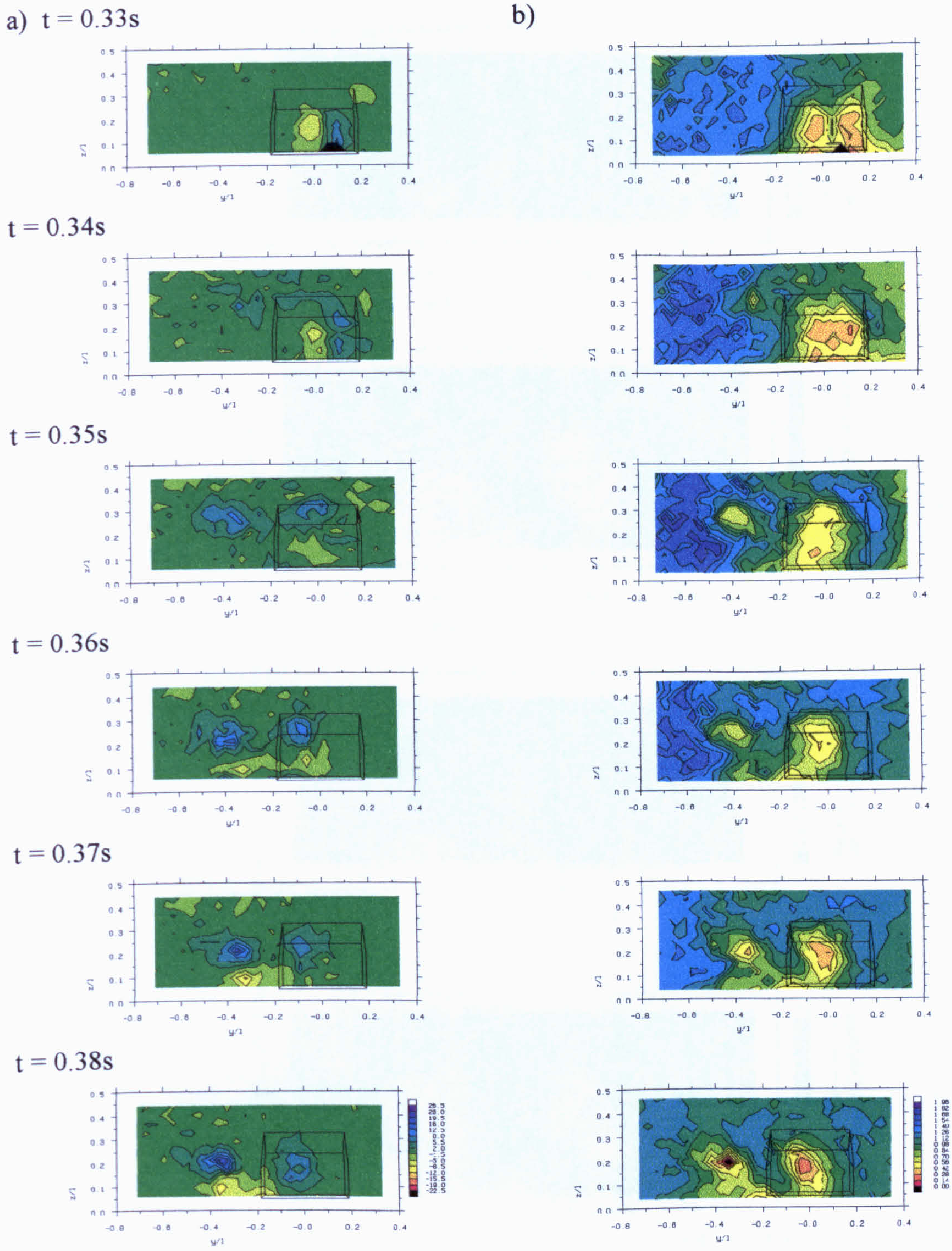

a) t = 0.33s

b)

t = 0.34s

t = 0.35s

t = 0.36s

t = 0.37s

t = 0.38s

Figure 6.39 Durham Geometry a) Vorticity and b) Total Pressure Coefficient Contours

x/l = 1.5

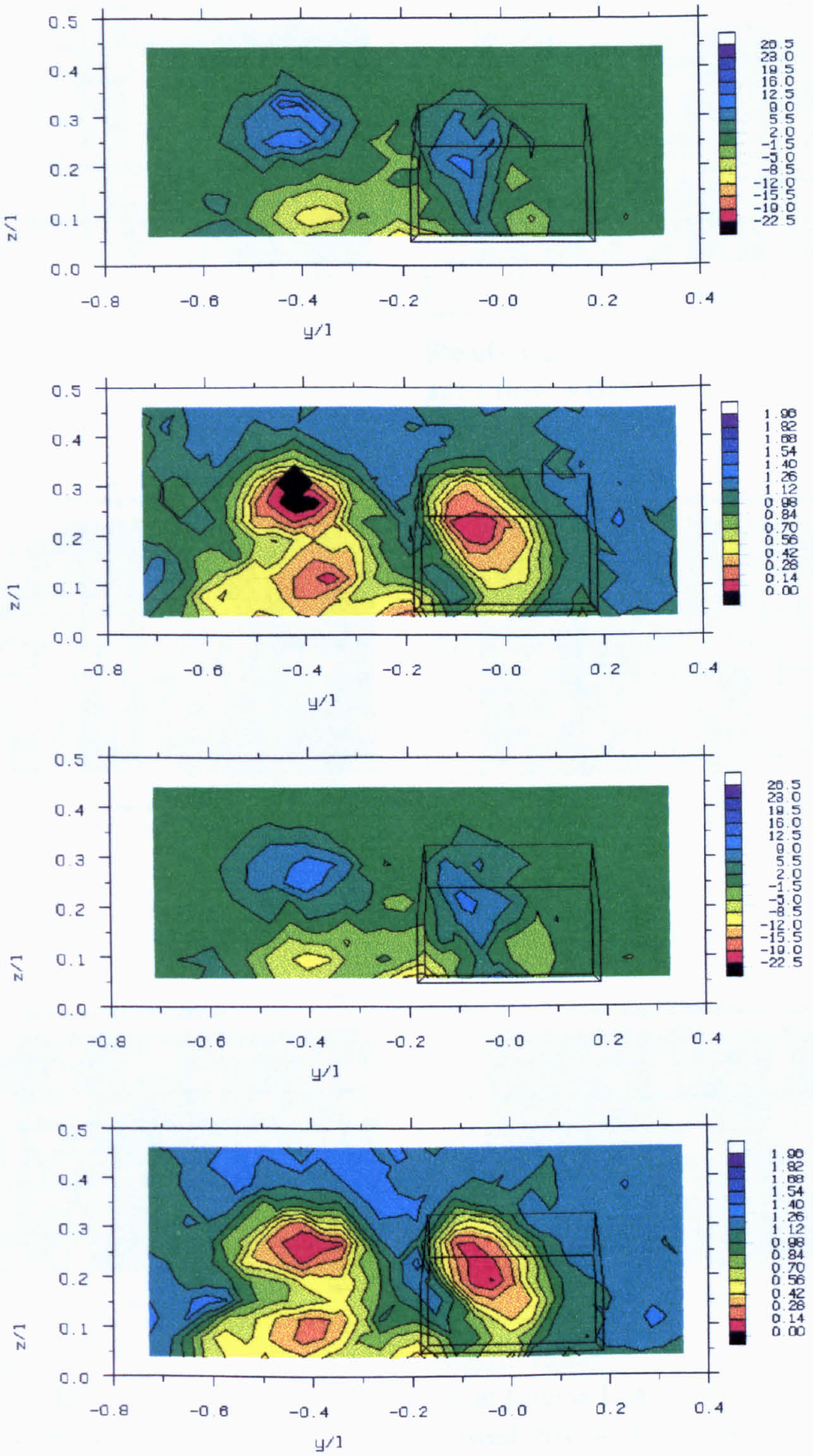

a) t = 0.52s

b) t = 0.52s

a) t = 0.57s

b) t = 0.57s

Figure 6.40 Durham Geometry a) Vorticity and b) Total Pressure Coefficient Contours

x/l = 1.5

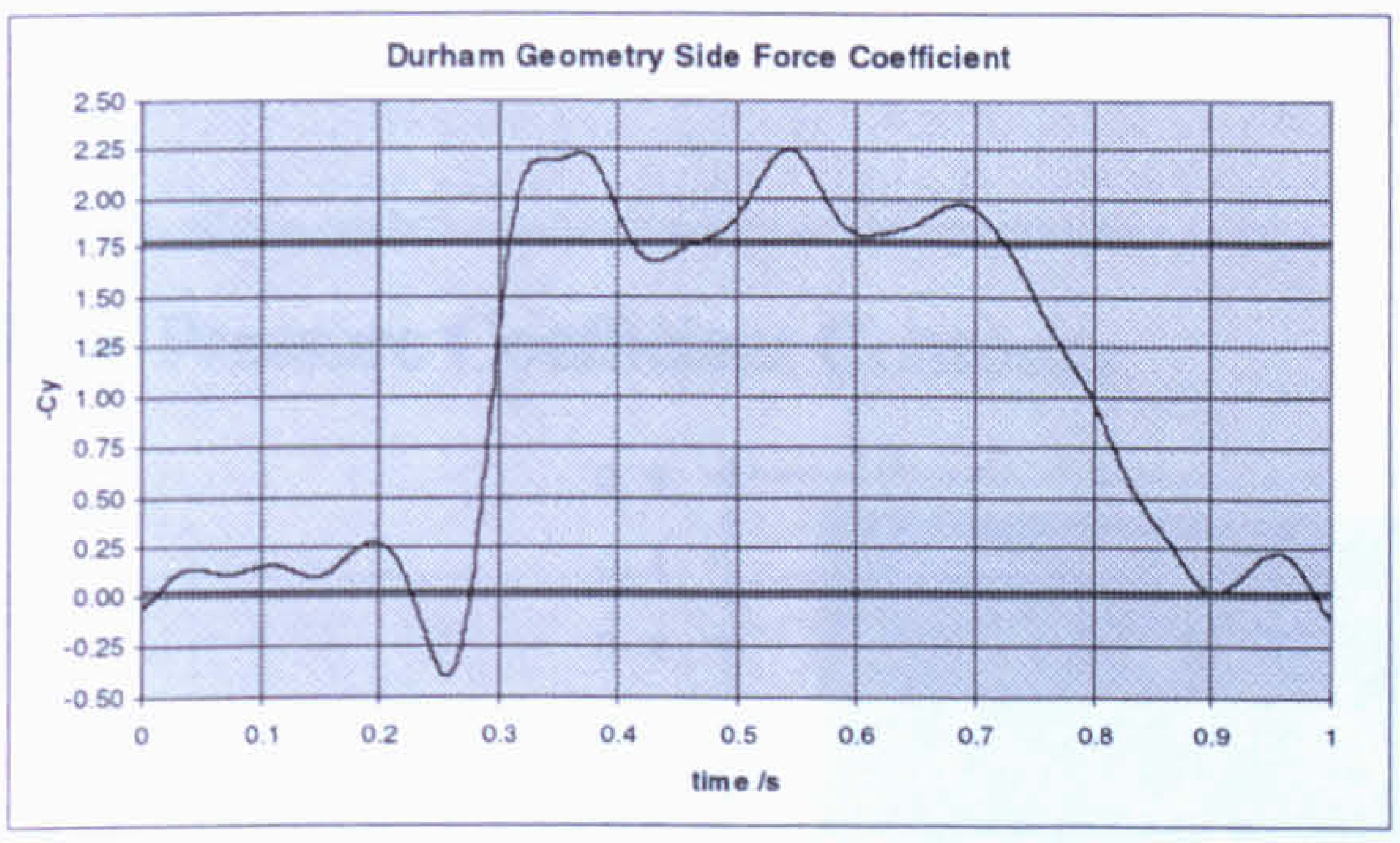

Steady values:
axial flow = -0.02
yawed flow = -1.78

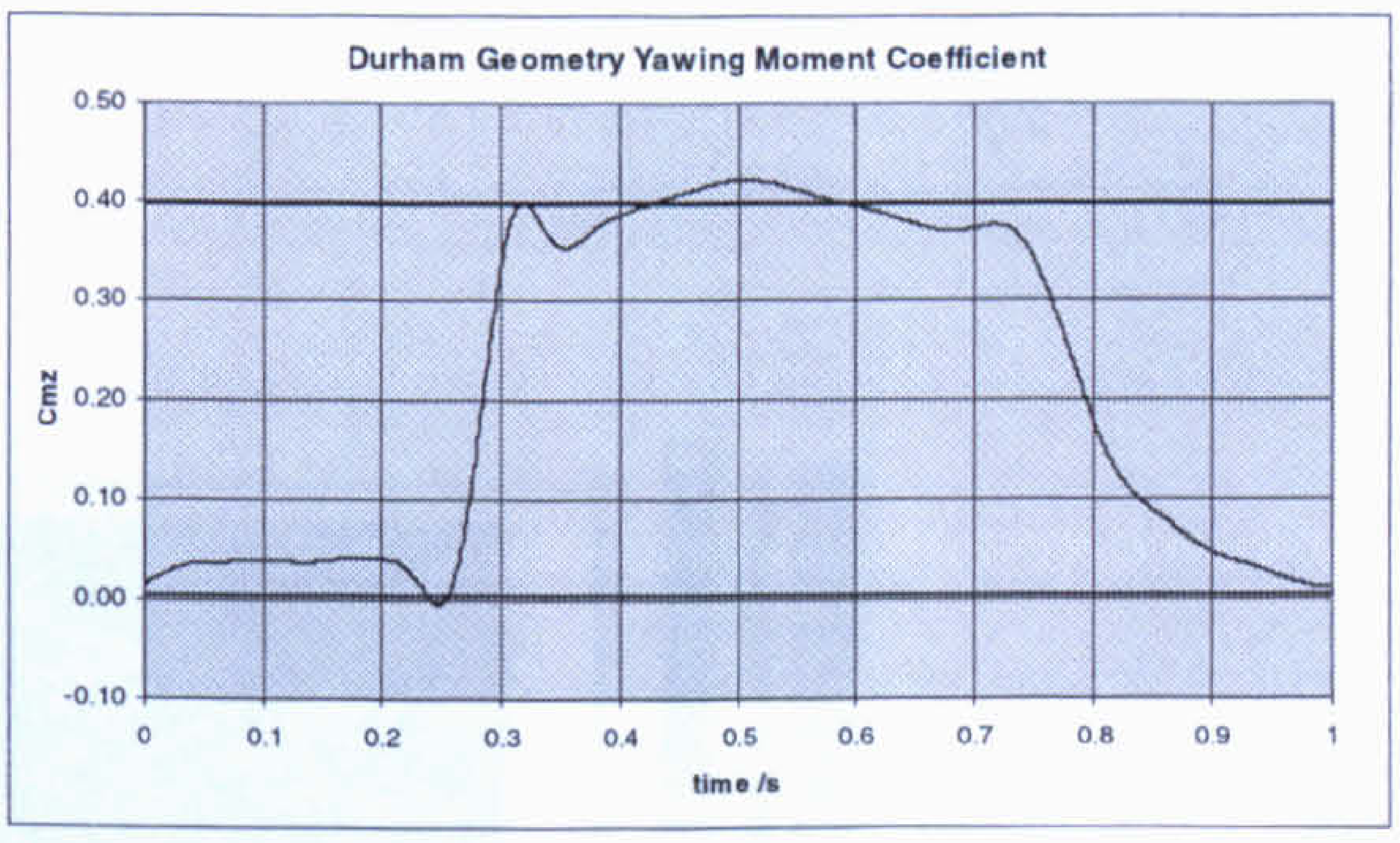

Steady values:
axial flow = 0.00
yawed flow = 0.40

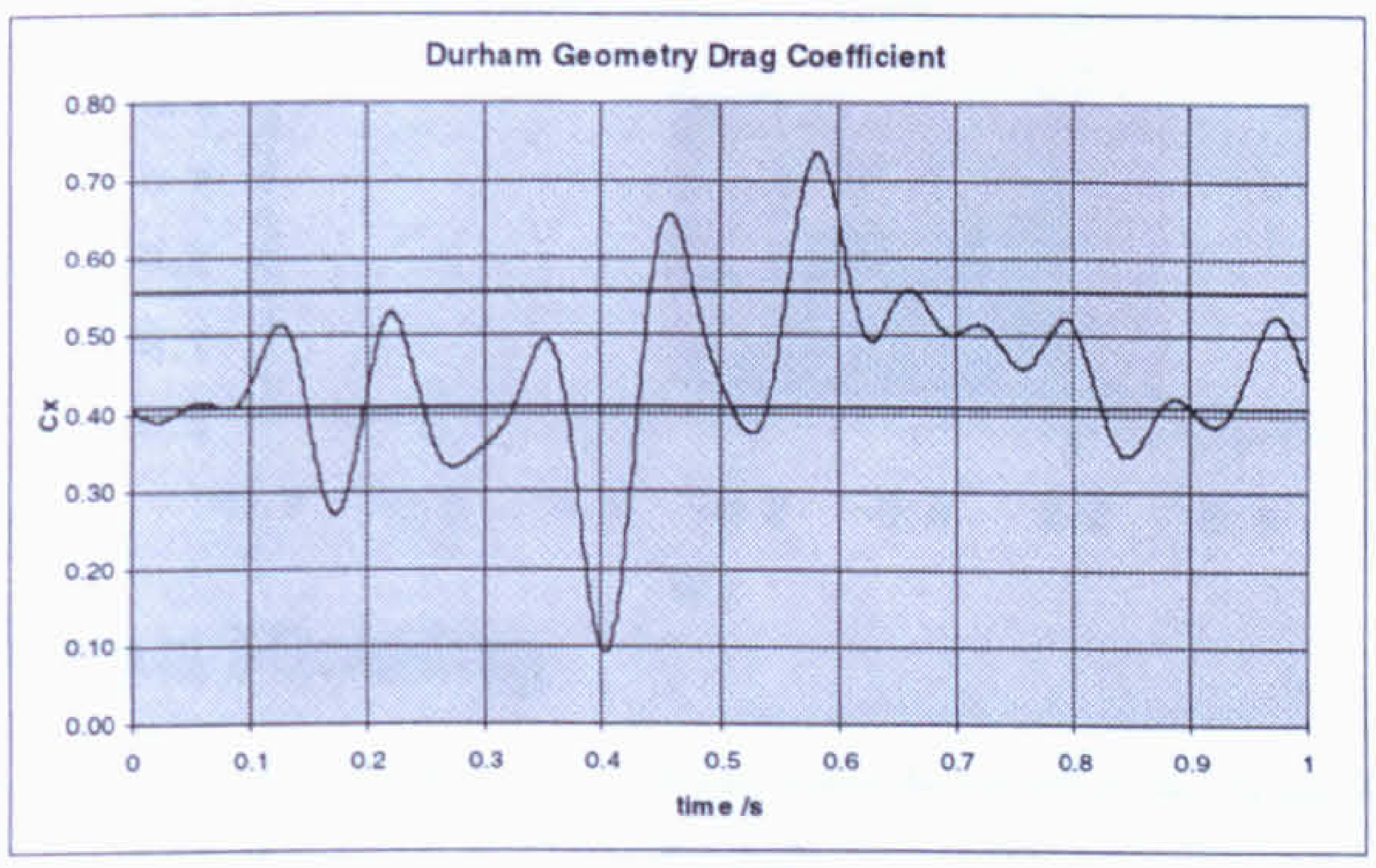

Steady values:
axial flow = 0.41
yawed flow = 0.56

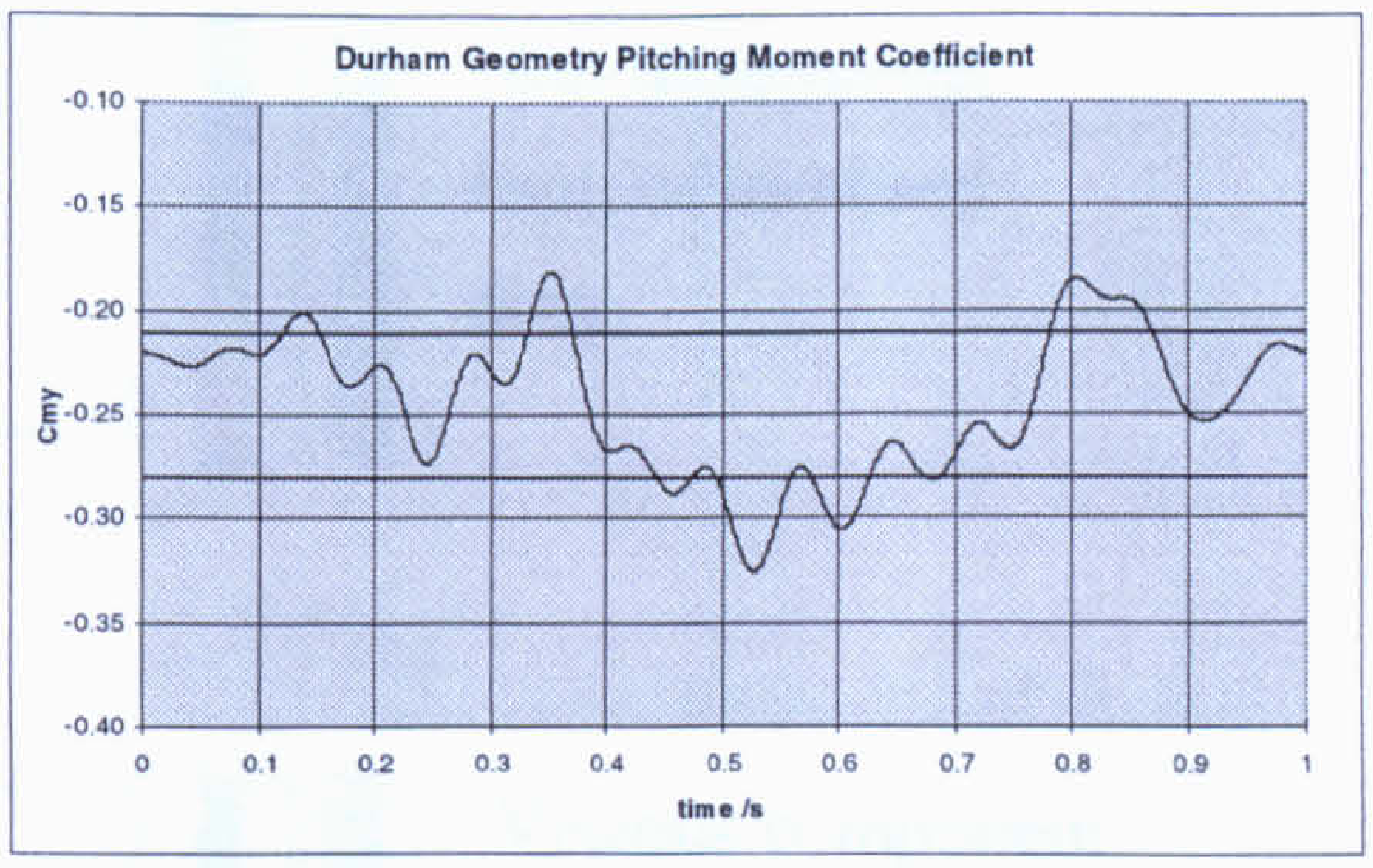

Steady values:
axial flow = -0.21
yawed flow = -0.28

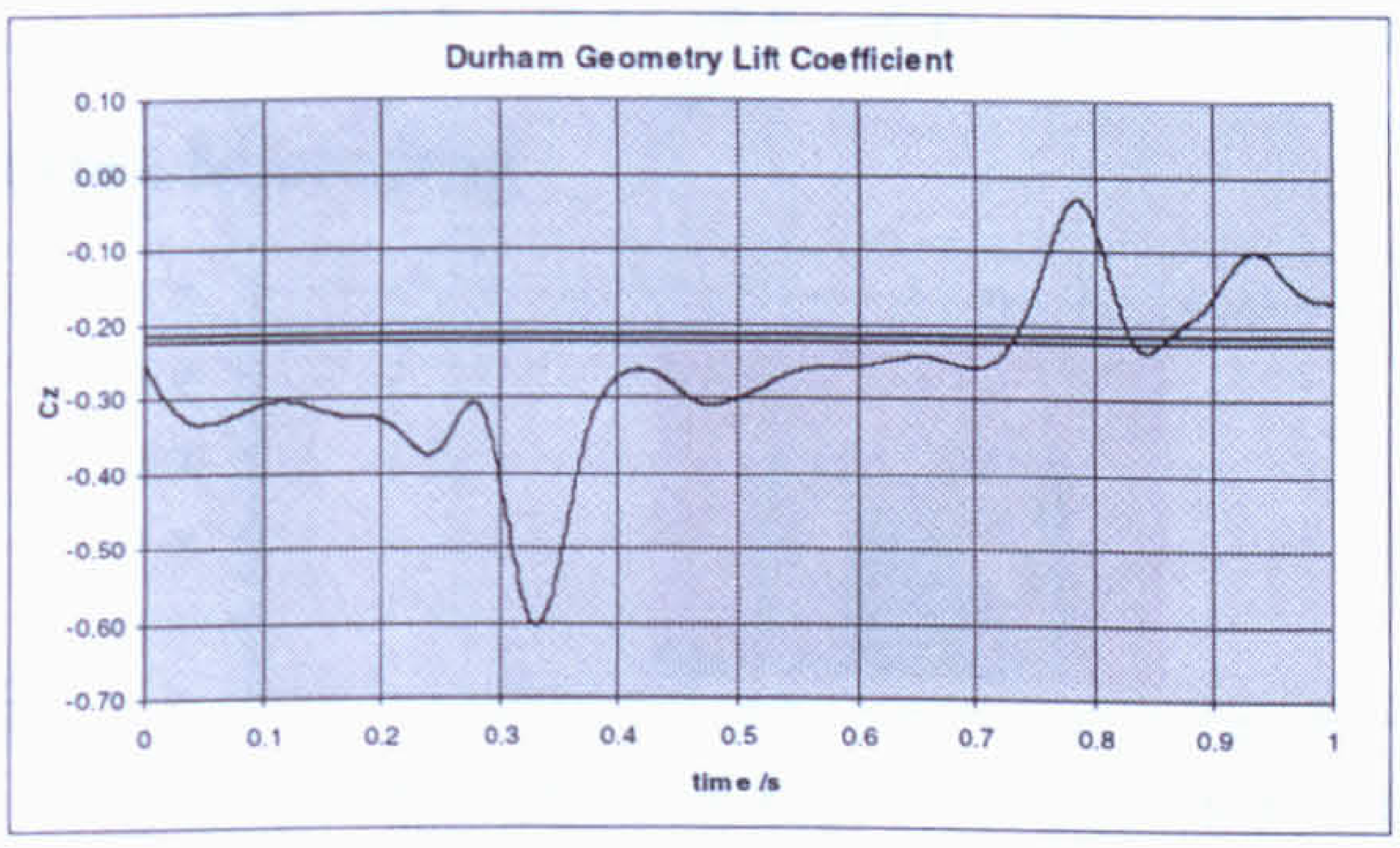

Steady values:
axial flow = -0.22
yawed flow = -0.28

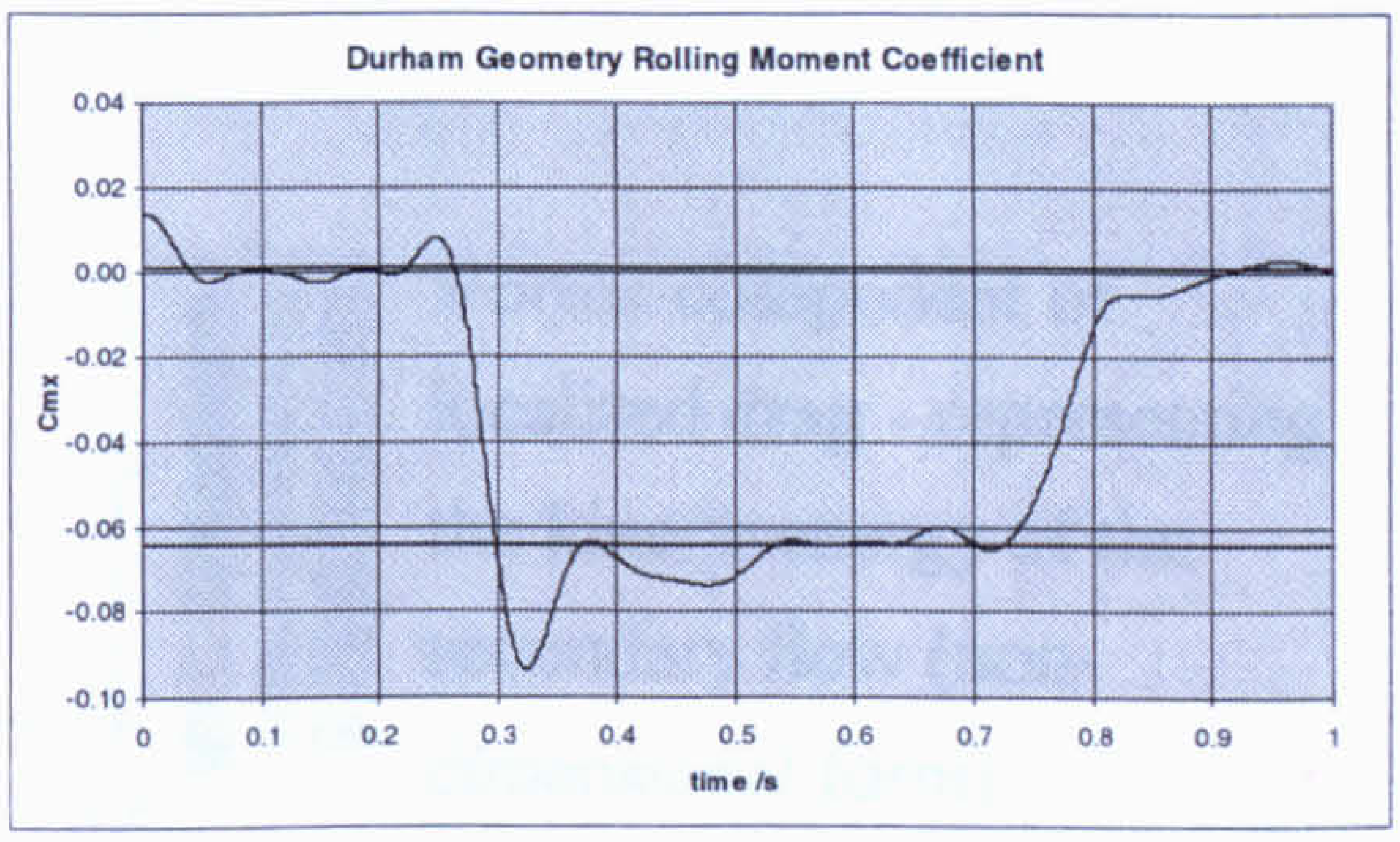

Steady values:
axial flow = 1.36×10^{-3}
yawed flow = -6.41×10^{-2}

Figure 6.41 Durham Geometry Force and Moment Coefficients

Total Pressure Coefficient Contours

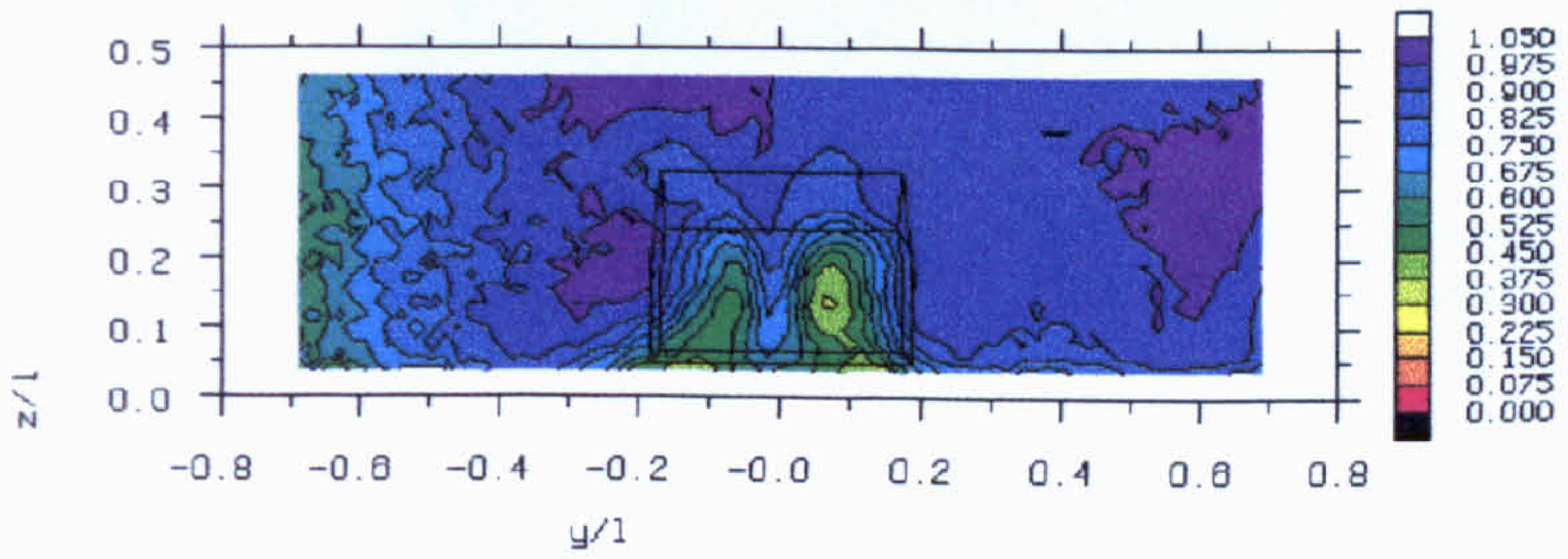

Total Microdrag

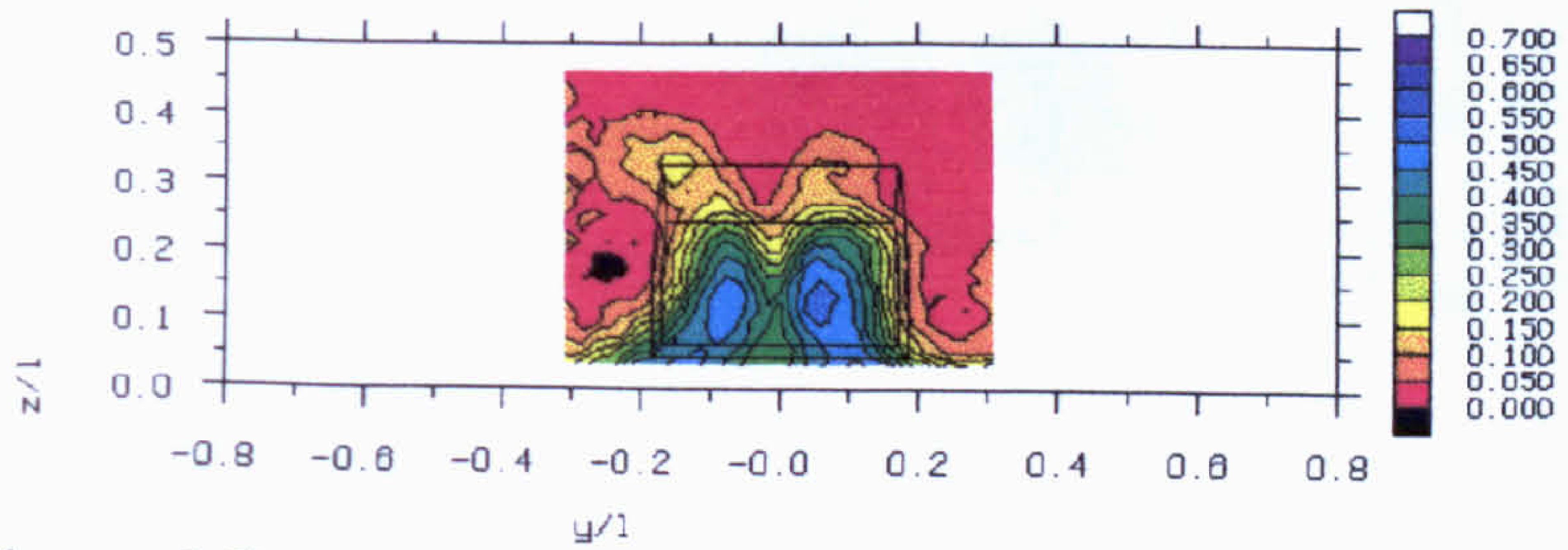

Non-dimensional form of localised drag

Viscous Microdrag

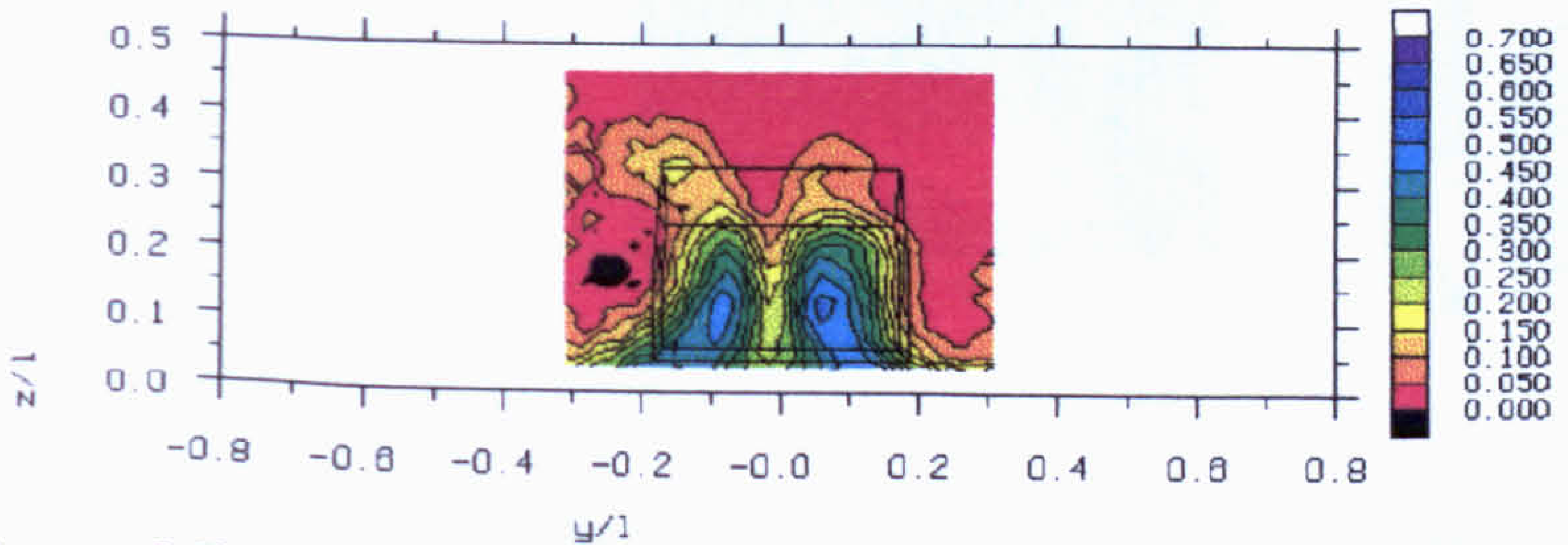

Viscous component of localised drag (non-dimensional form)

Vortex Microdrag

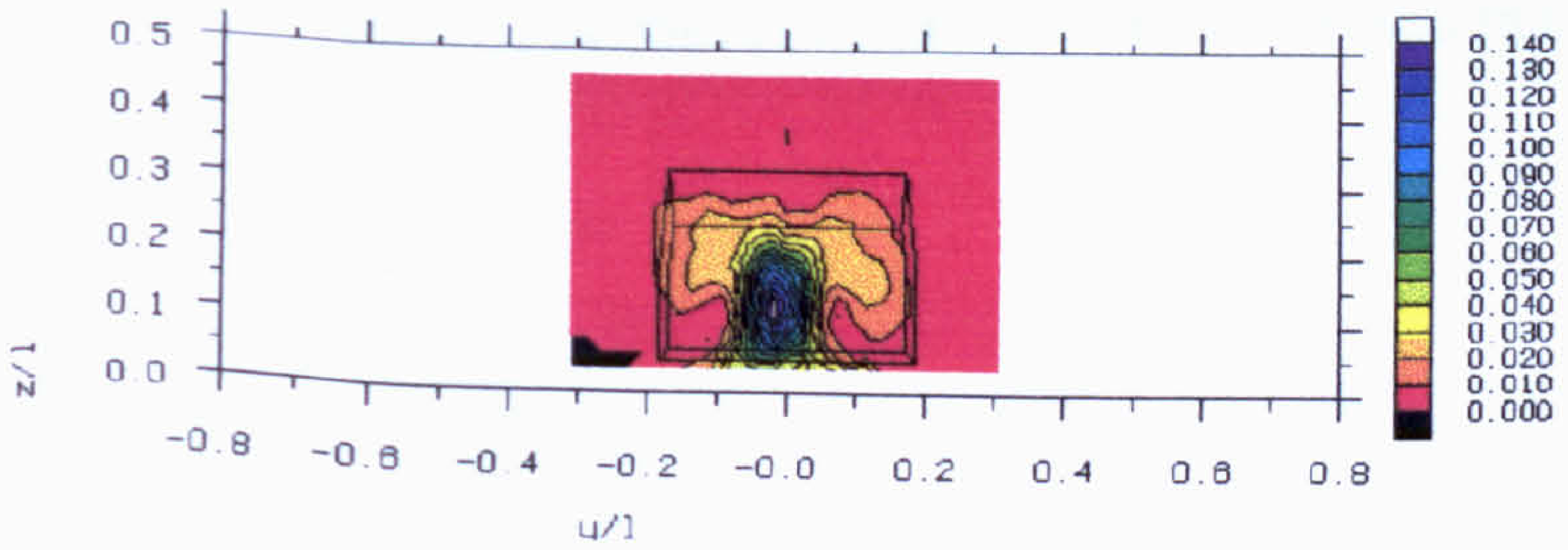

Vortex component of localised drag - representing the kinetic energy of the secondary flow (non-dimensional form)

Figure 6.42 Durham Geometry Axial Flow Wake Integral Results

(see Appendix B for wake integration and microdrag definitions)

Total Pressure Coefficient Contours

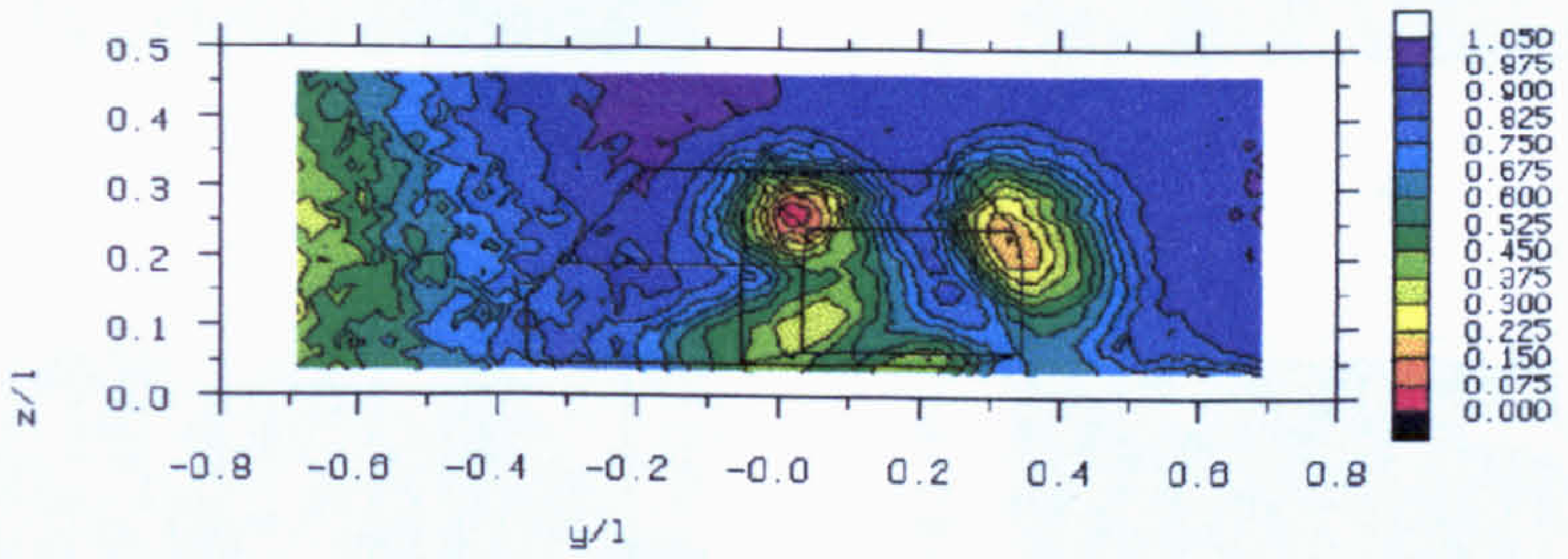

Total Microdrag

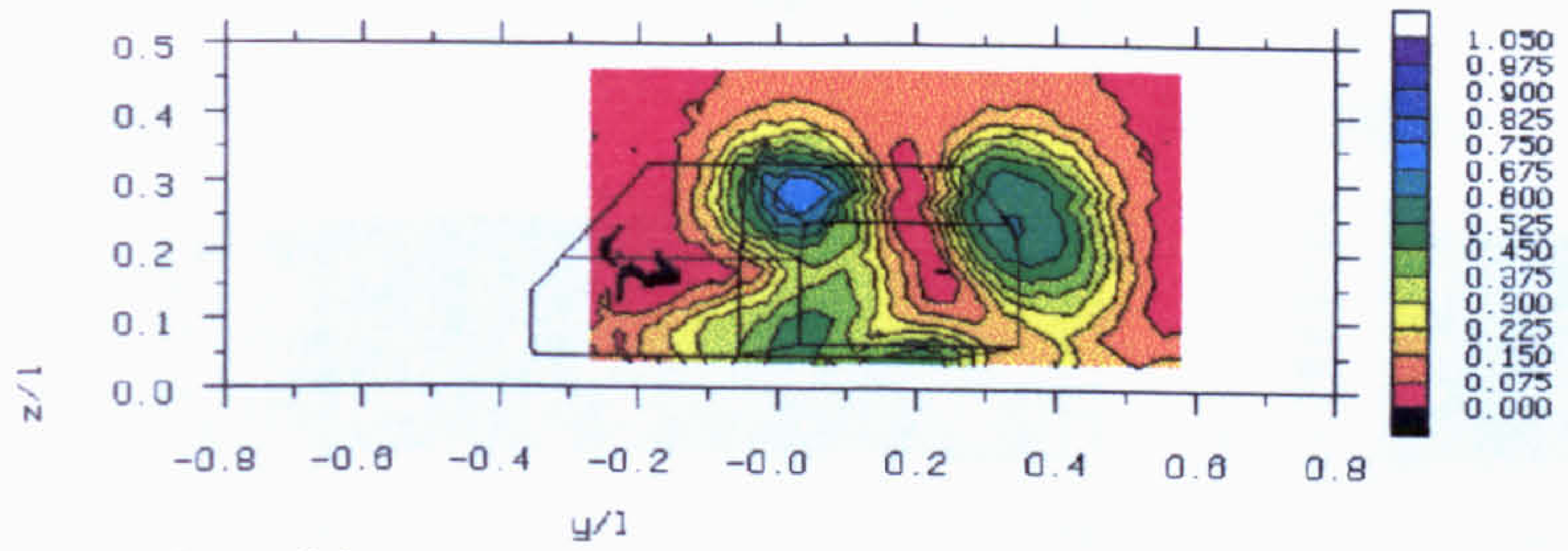

Non-dimensional form of localised drag

Total Microside

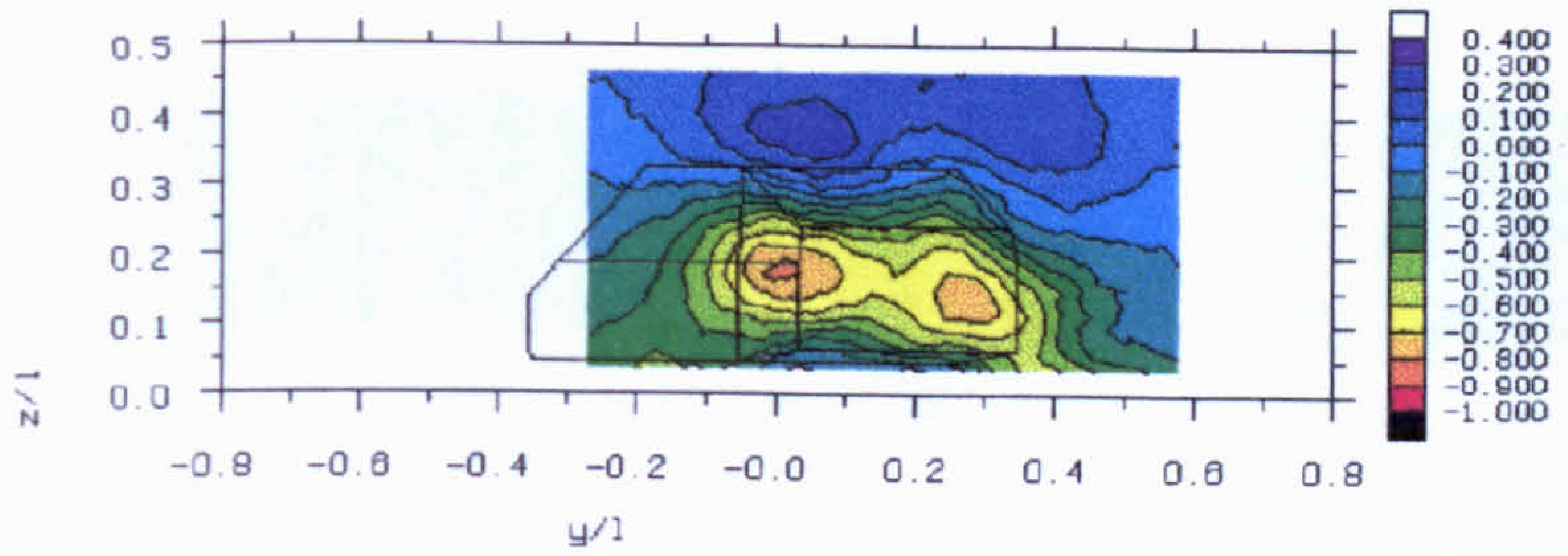

Non-dimensional form of localised side force

Figure 6.43 Durham Geometry Yawed Flow Wake Integral Results (see Appendix B for wake integration and microdrag definitions) t = 0.1098

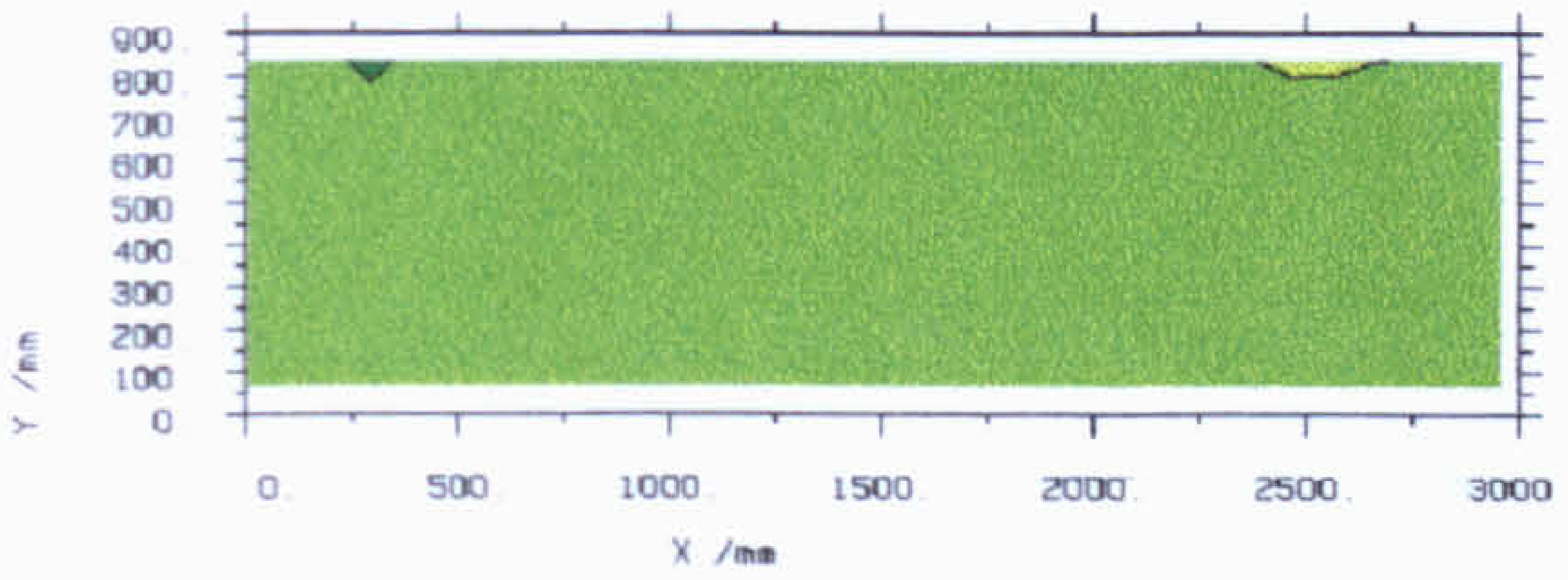

t = 0.1498

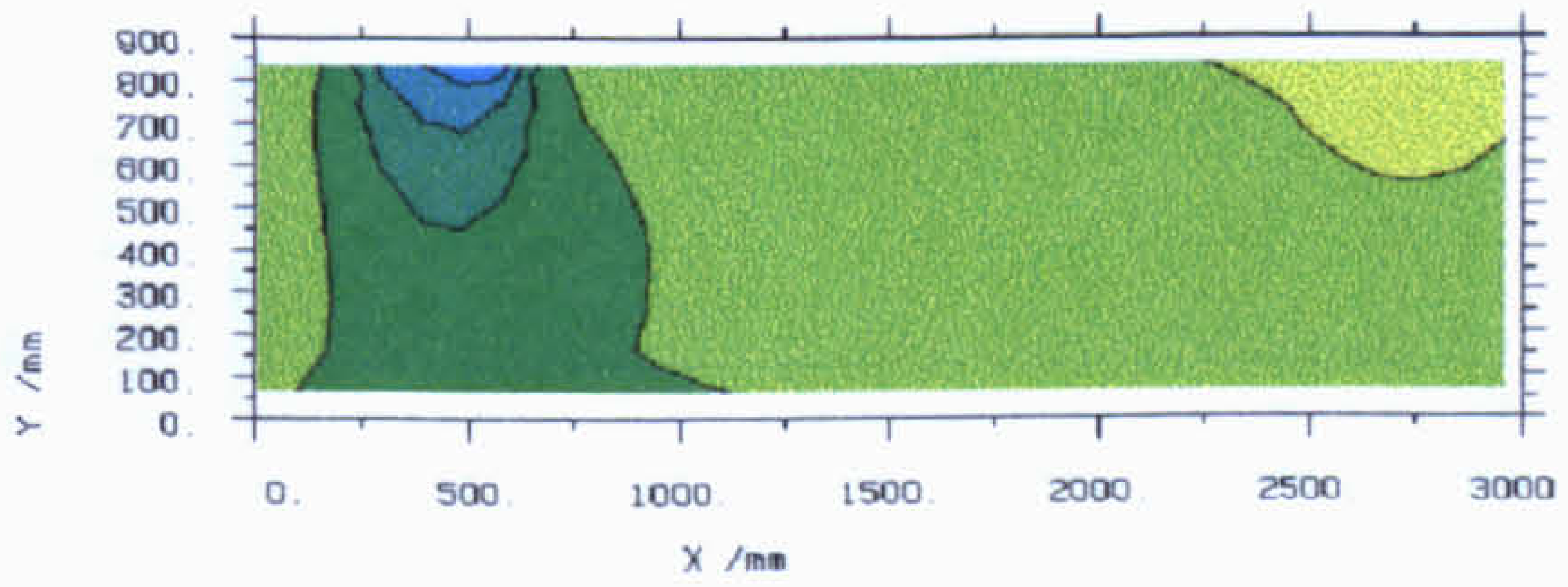

t = 0.1898

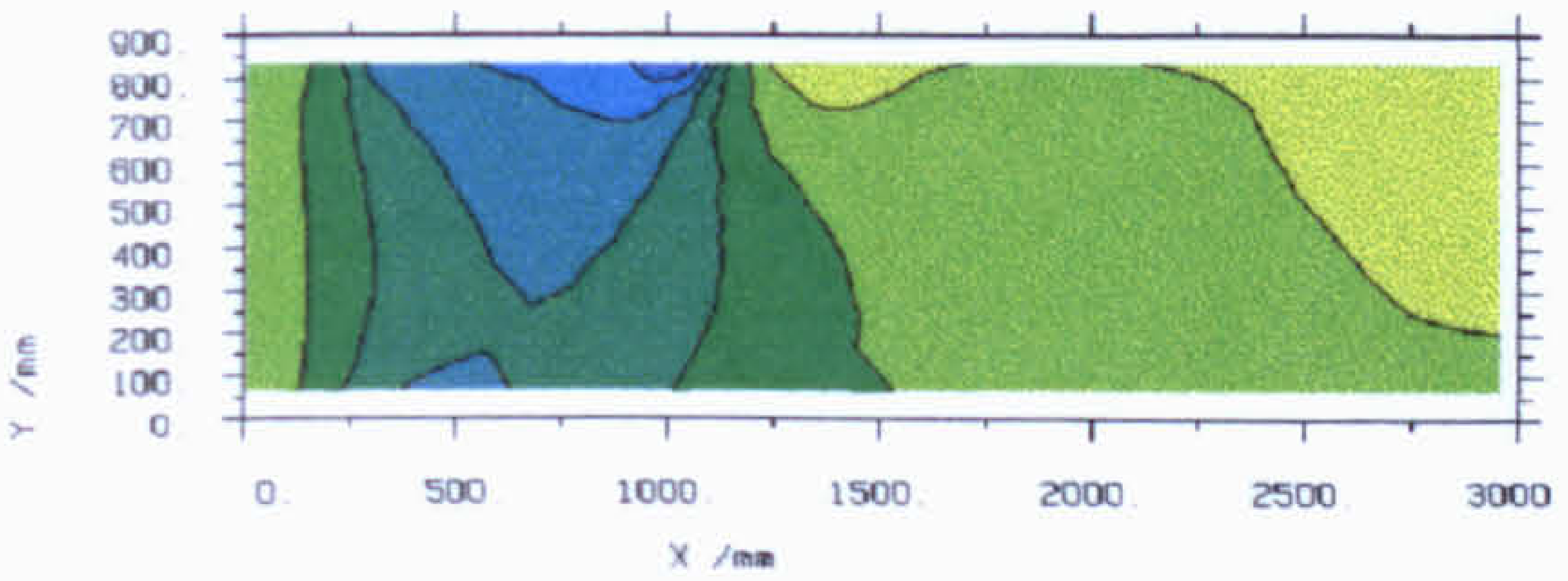

t = 0.2297

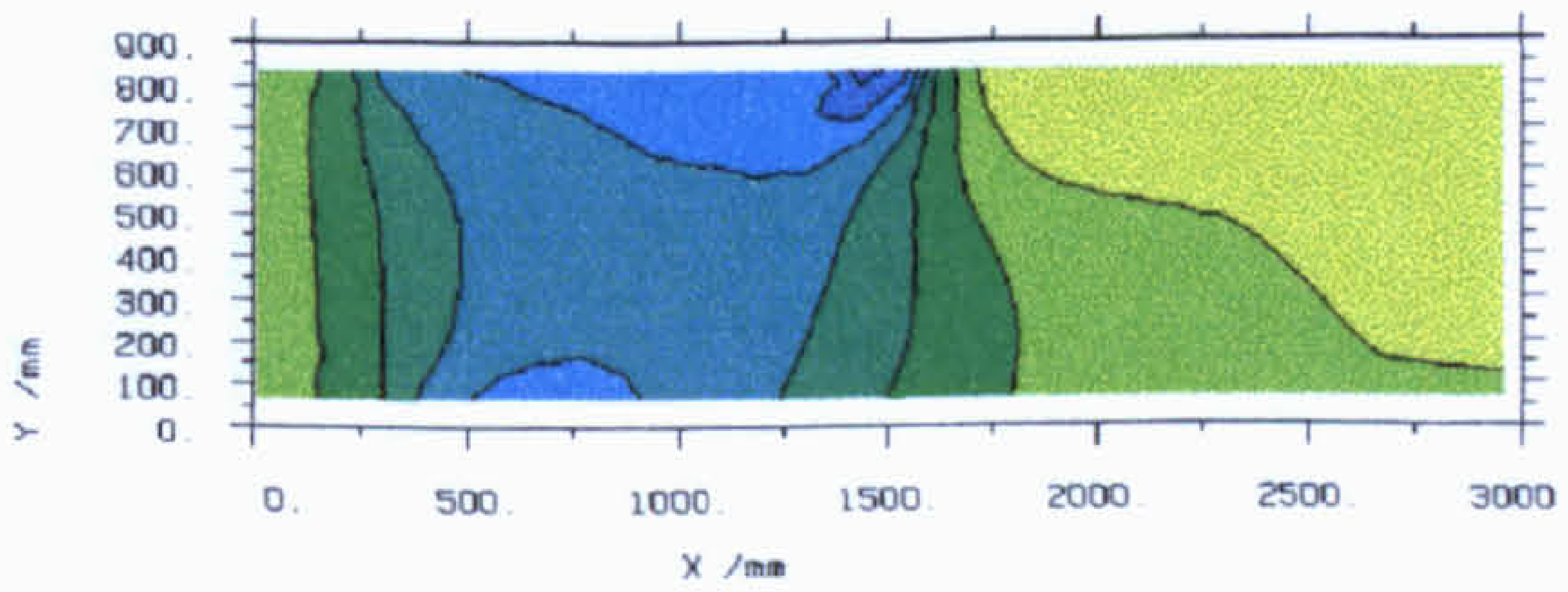

t = 0.2697

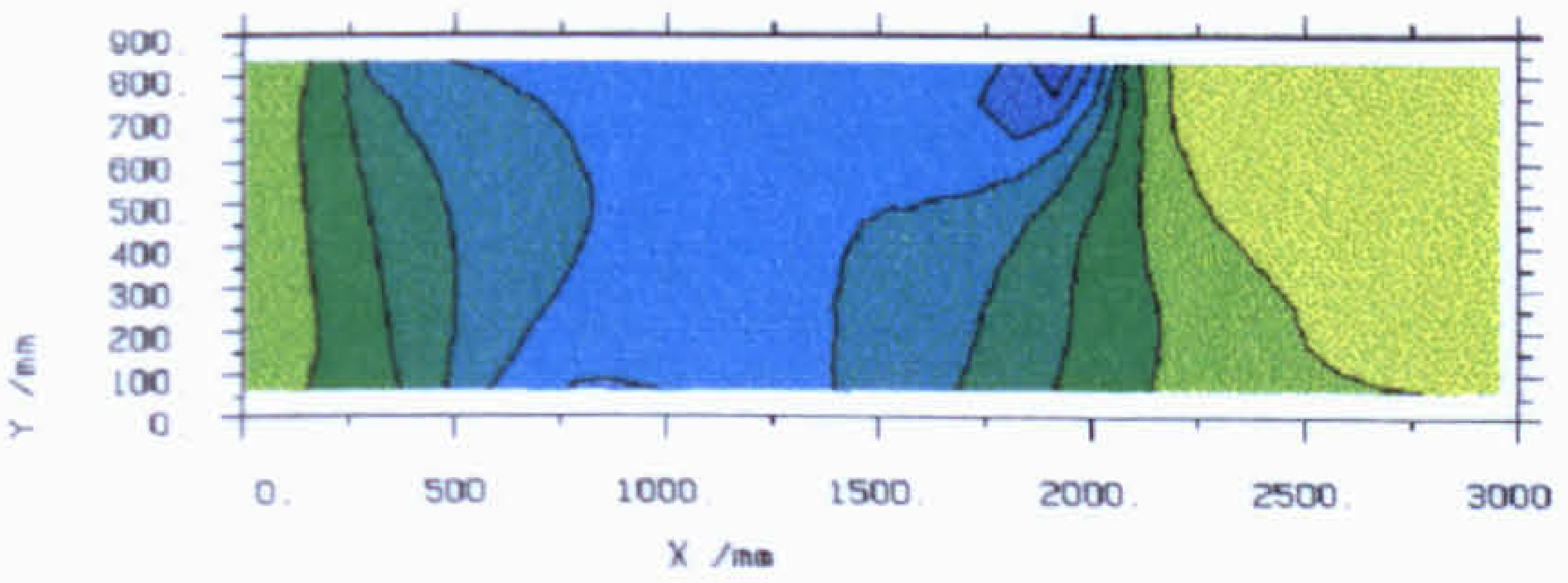

t = 0.3096

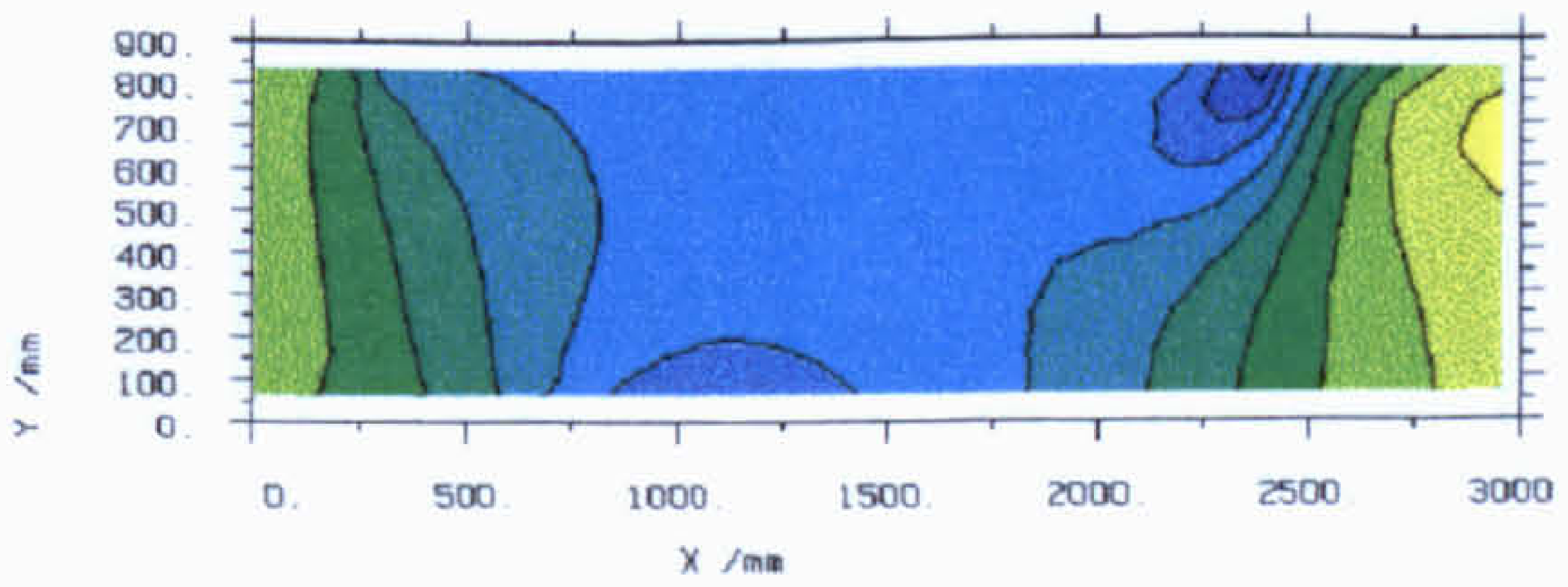

t = 0.3496

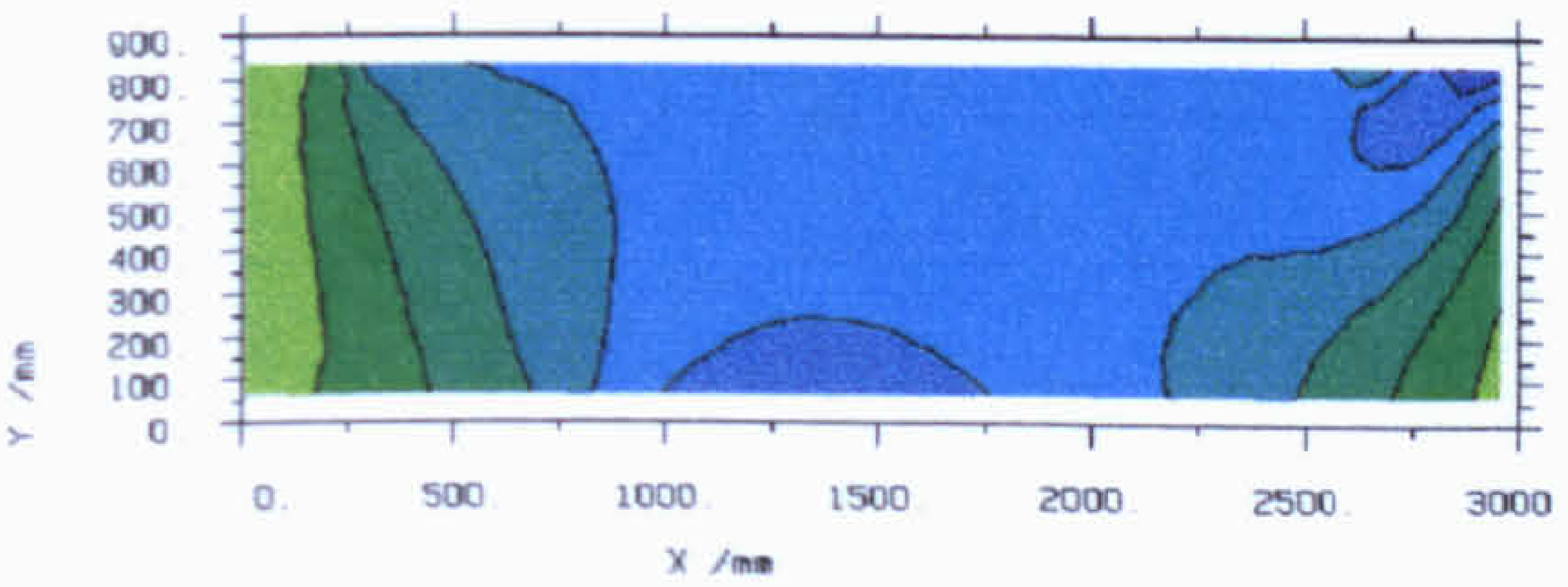

t = 0.3896

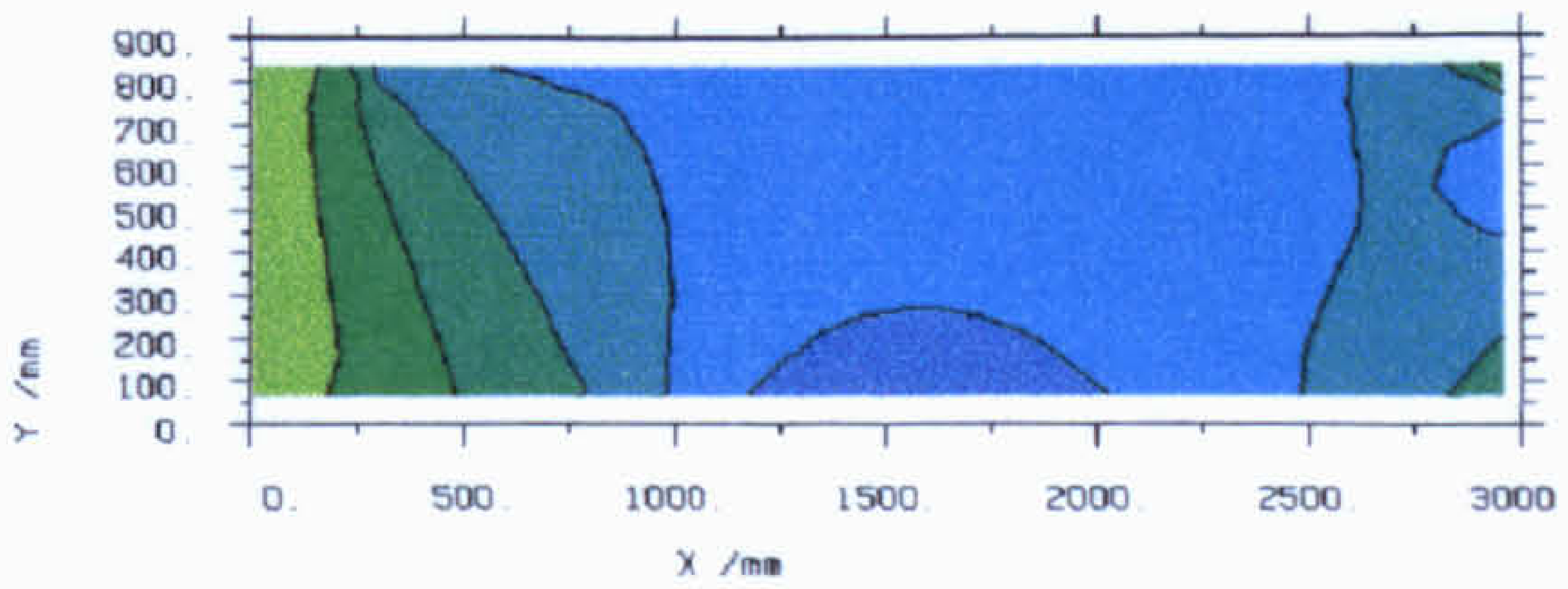

t = 0.4295

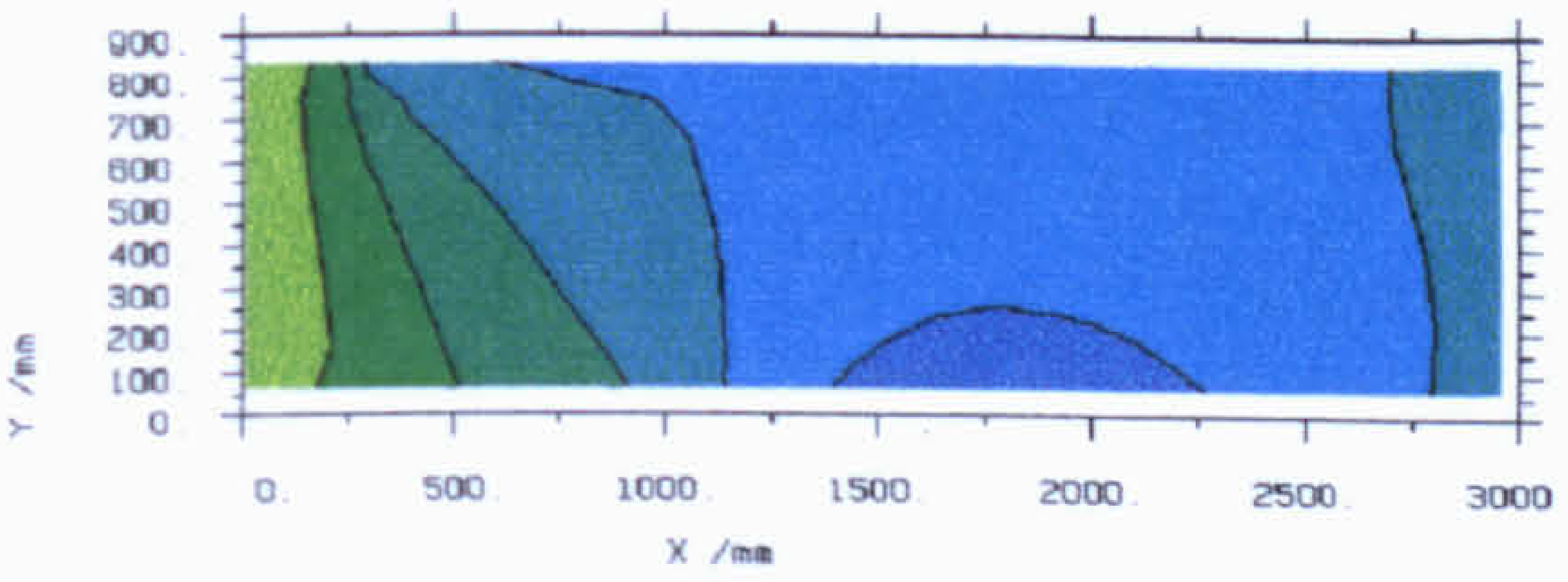

t = 0.4695

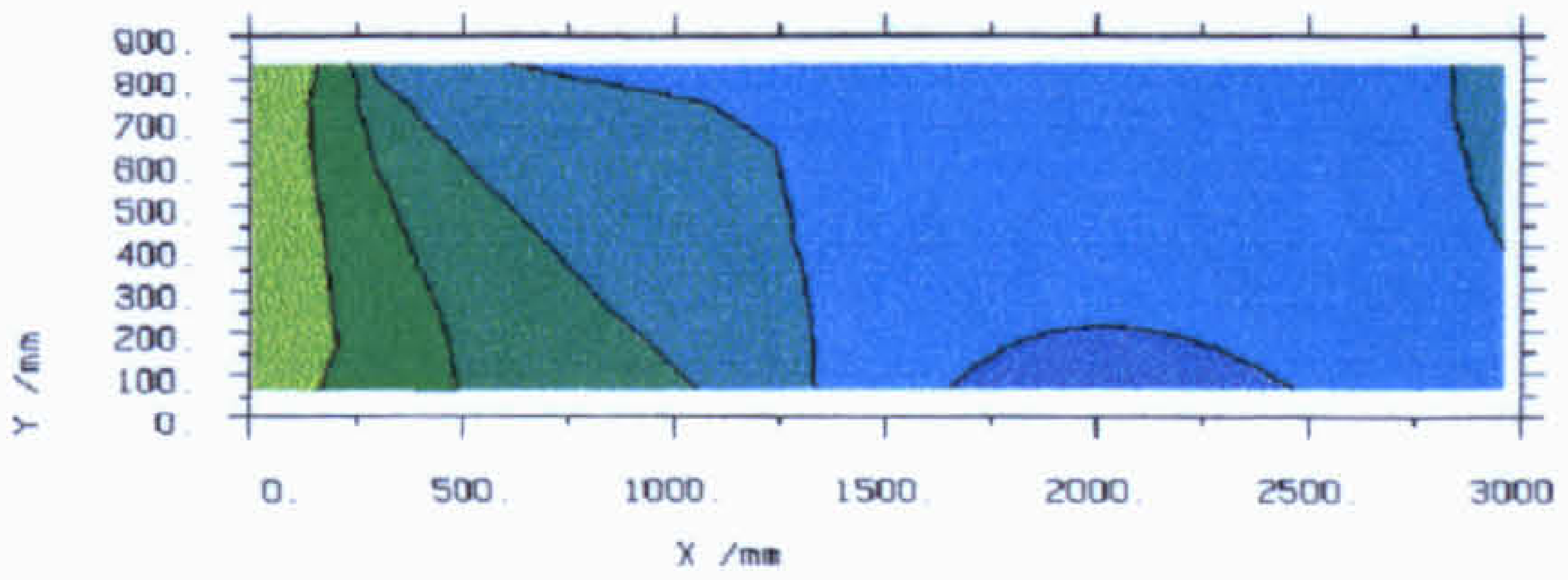

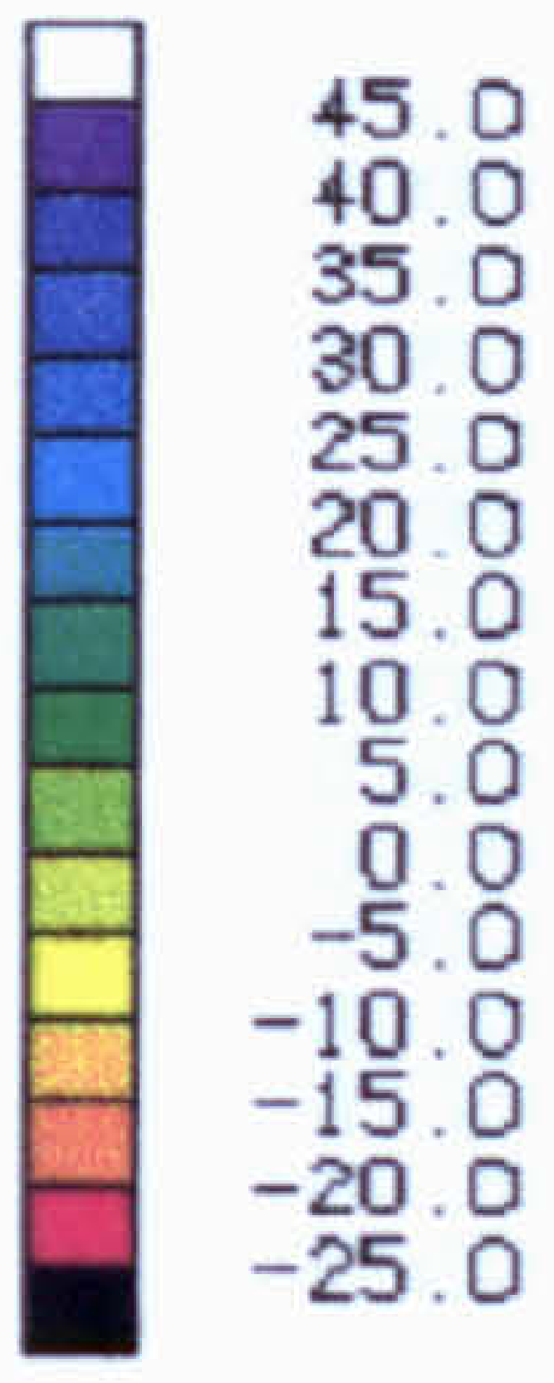

Figure 6.44 CFD Empty Working Section Transient Yaw Angle

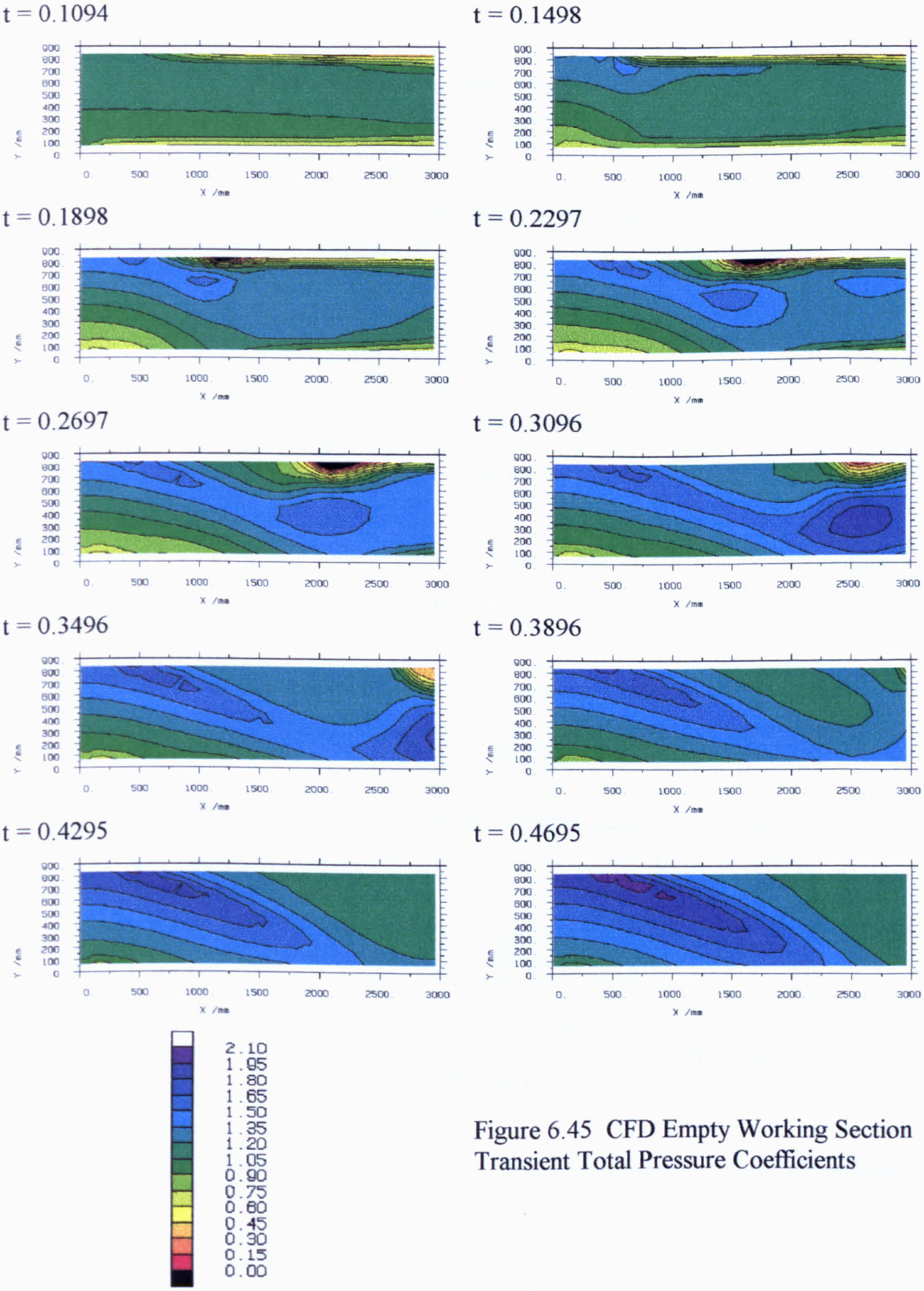

Figure 6.45 CFD Empty Working Section Transient Total Pressure Coefficients

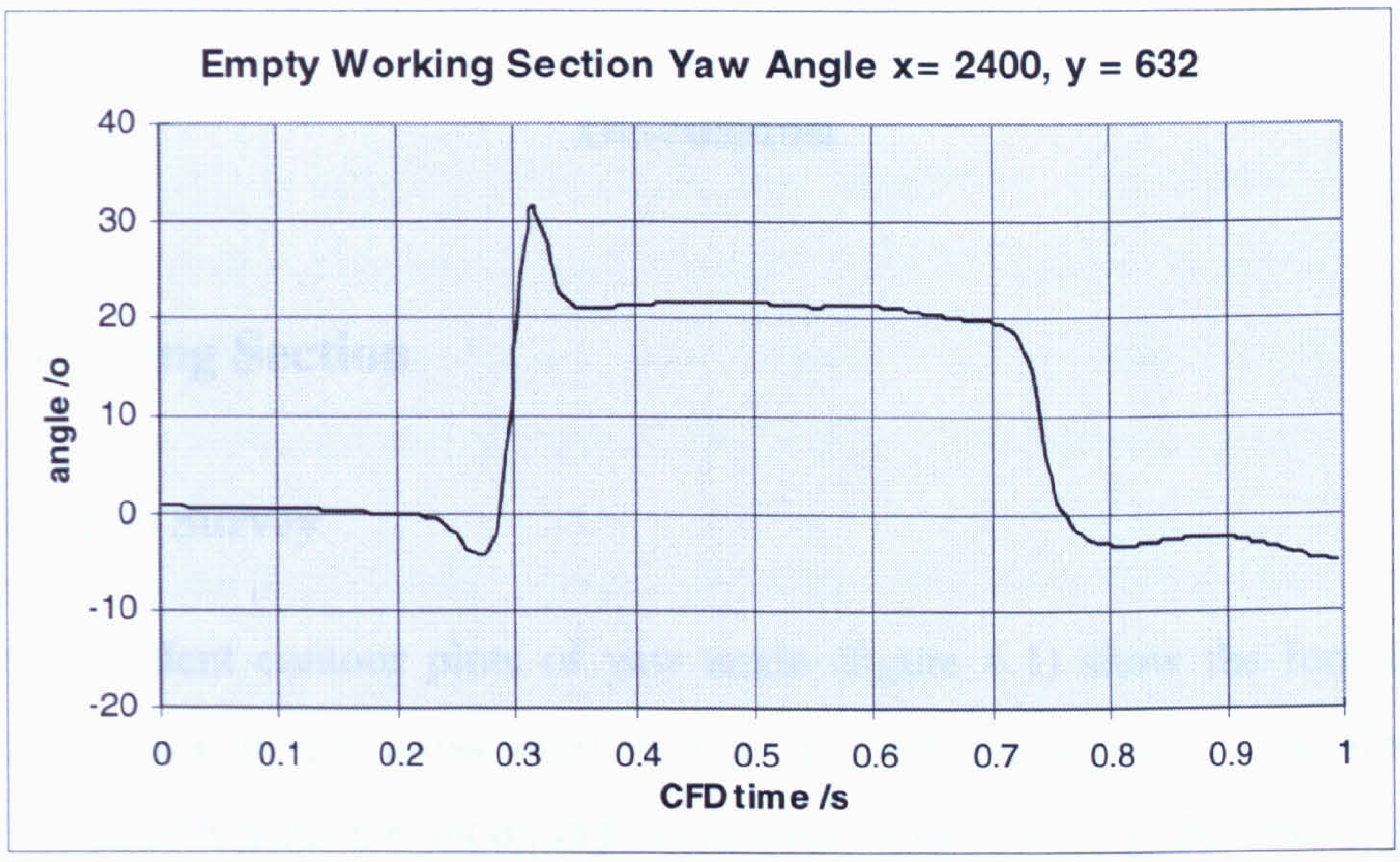

Figure 6.46 CFD Empty Working Secton Yaw Angle with Honeycomb Roughness Modelled

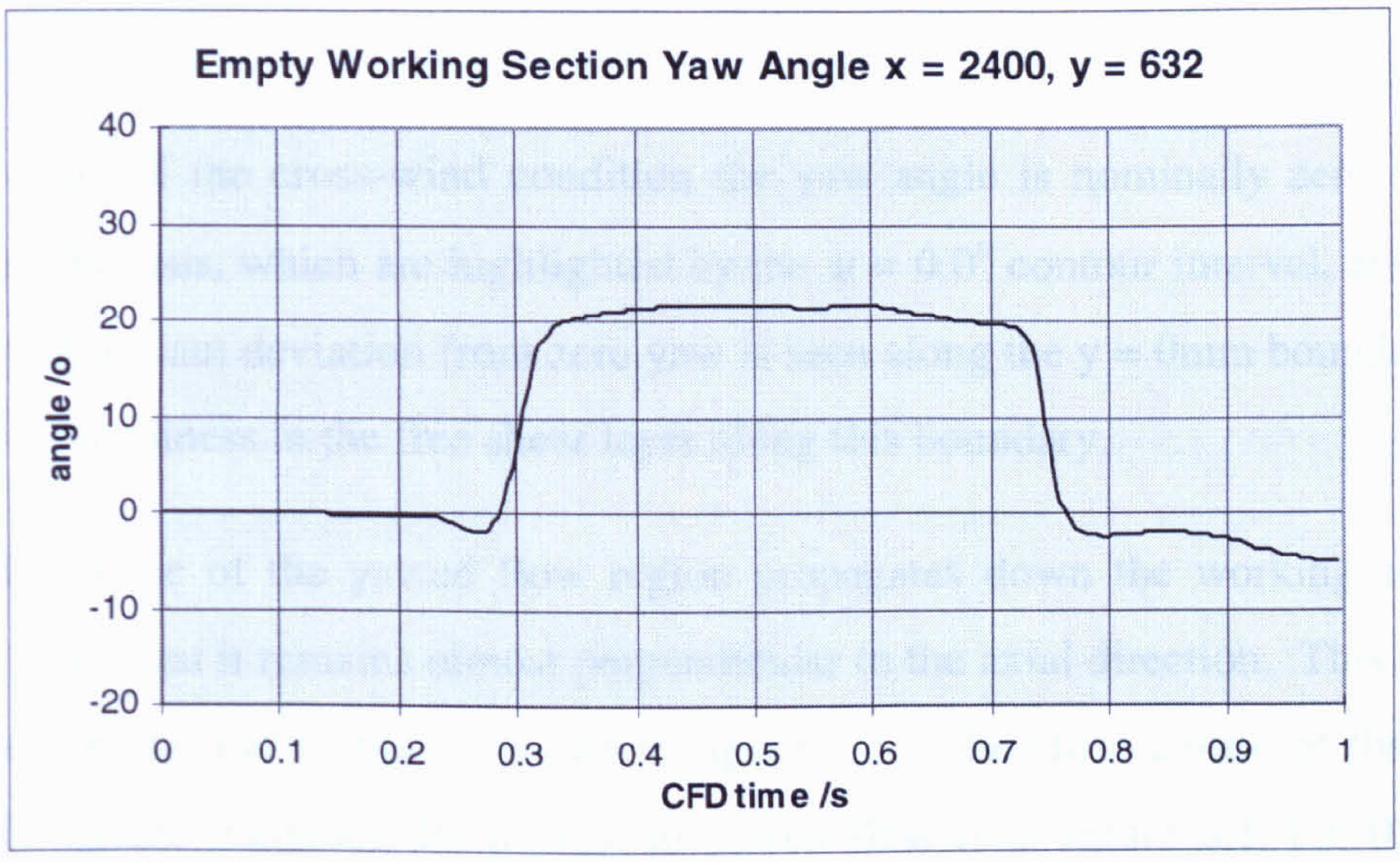

Figure 6.47 CFD Empty Working Secton Yaw Angle Honeycomb Roughness not Modelled

Chapter Seven

Discussion

7.1 Empty Working Section

7.1.1 Working Section Survey

The time-dependent contour plots of yaw angle (figure 6.1) show the formation of a sharp edged, finite length cross-wind gust in the working section. The first shutter opens at t = 0.089s with the incoming cross-wind flow affecting the yaw angle in the survey area of the working section from t = 0.14s (x = 500mm, y = 800mm, figure 6.1). The delay between shutter opening and the cross-wind flow entering the working section is from the finite time required for the fluid to move from the shutter exit plane into the working section.

Prior to onset of the cross-wind condition the yaw angle is nominally zero, although small perturbations, which are highlighted by the $\psi = 0.0^\circ$ contour interval, are present. The only significant deviation from zero yaw is seen along the y = 0mm boundary. This is due to unsteadiness in the free shear layer along this boundary.

The leading edge of the yawed flow region propagates down the working section as intended, such that it remains almost perpendicular to the axial direction. This occurs in a manner very similar to that depicted in figure 3.2. The close nature of the contour lines defining the transition from axial to yawed flow (e.g. figure 6.1, t = 0.30s, x = 2350mm) indicate the rapid nature of the transition. By t = 0.36s, the leading edge has moved sufficiently far downstream such that the entire working section is subjected to nominally steady yawed flow at constant yaw angle of 22°. This is significantly less than the intended 30°, the shortfall being a consequence of manufacturing difficulties with the honeycomb flow straightener. The cross-wind inlet only extends to x = 2500mm, and hence the flow in the region x > 2500mm is not all at 22° yaw. The closure of the shutters at the trailing edge of the cross-wind gust subsequently returns the working section to an nominally axial flow condition. The slower nature of the spring actuated shutter closure causes the return to axial flow to be significantly more blurred than the transition to yawed flow (figure 6.1, t = 0.62s - 0.94s). This is relatively easy to solve and not of importance for this investigation.

The cross-wind gust profile differs from what would be considered an ideal square wave profile in several ways:

1) Ahead of the leading edge of the gust is a region of yaw angle undershoot, where the actual yaw angle is less than that expected (e.g. figure 6.1, t = 0.30s, x = 2500mm, y = 350mm).

2) A region of yaw angle overshoot, where the yaw angle is greater than that expected, occurs at the beginning of the cross-wind gust (e.g. figure 6.1 t = 0.28s, x = 2200mm, y = 400mm).

3) A region of transient high total (and dynamic) pressure forms at the outside leading edge of the gust and is convected downstream in this relative position (e.g. figure 6.4, t = 0.28s, x = 2100mm, y = 300mm).

4) The total (and dynamic) pressure behind the leading edge of the gust reduces as the leading edge moves downstream.

The cross-stream velocity contour plots (figure 6.2) show the yaw angle overshoot to be almost uniquely coincident with an excess of cross-stream velocity. The CFD investigation of the empty working section provided significant insight into the mechanism responsible for this. Figure 6.46 shows the empty working section yaw angle at x = 2400mm, y = 632mm for the CFD calculation with the rough honeycomb simulated. This shows a small yaw angle undershoot immediately upstream of the gust front (t = 0.28s), followed by a rapid rise to the yawed flow regime, including a 10° yaw angle overshoot at the leading edge of the gust (t = 0.32s). The yaw angle then remains almost constant until an equally rapid return to axial flow conditions (t = 0.74s). This can be compared with figure 6.47, the empty working section yaw angle for the CFD calculation with the inlet modelled as a smooth wall prior to inflow. Here there is again a small yaw angle undershoot upstream of the leading edge of the gust (t = 0.28s), but no overshoot during the transition to yawed flow (0.28s < t < 0.35s). Thus it is concluded that the overshoot is connected with the thickness of the boundary layer along the cross-wind inlet, prior to cross-wind conditions being established.

The CFD data is supplied for a slightly different model centre to the experimental data as the locations of the maximum yaw angle overshoots are not coincident (CFD: x = 2400mm, y = 632mm cf. exp: x = 2400mm, y = 400mm). Comparison of the CFD and experimental transient yaw angle plots indicate that the region of maximum yaw angle overshoot is located nearer the cross-wind inlet for the CFD. For example, figure 6.44 (CFD data), t = 0.3096s, maximum yaw angle overshoot at x = 2350mm, y = 800mm cf. figure 6.1 (experimental data), t = 0.30s, maximum yaw angle overshoot at x = 2200mm, y = 500mm. Thus the CFD data is taken from a location nearer the cross-wind inlet, as this is more representative of the worst case.

The thick boundary layer that exists along the honeycomb of the experimental facility for axial flow conditions can be seen in both the total pressure and streamwise velocity coefficient contours (figure 6.4 and 6.5, t = 0.0s). Although the boundary layer grows over the entire length of the honeycomb it is only apparent for x > 1500mm due to the limitations of the traverse mechanism travel. When the first shutter opens the incoming high momentum cross-wind fluid easily convects the low momentum boundary layer fluid onto the leading edge of the cross-wind gust. As subsequent shutters open further down the working section the incoming cross-wind fluid experiences an increasingly thick boundary layer. This increase in thickness has two affects. Firstly it acts as a blockage, turning the incoming flow such that its cross-stream velocity component is increased and axial velocity component decreased, and hence the yaw angle is increased. Secondly, as the boundary layer fluid is continuously convected onto the leading edge of the cross-wind gust, a large area of high loss fluid forms.

The turning of the cross-wind fluid is highlighted in the modified velocity vectors (figure 6.3). The incoming flow at the leading edge of the cross-wind gust adjacent to the honeycomb flow straightener ($y = 800$mm) exhibits an increased cross-stream component, with the streamwise component being significantly less than the freestream velocity (e.g. $t = 0.20$s, $x = 1000$mm, $y = 800$mm). Both total pressure coefficient contours (figure 6.4) and streamwise velocity coefficient contours (figure 6.5) show the area of high loss (low total pressure and low momentum) adjacent to the honeycomb at the leading edge of the cross-wind gust (e.g. figure 6.4, $t = 0.28$s, $x = 2125$mm, 400mm $< y < 800$mm). The size of this area grows as the leading edge of the cross-wind gust moves downstream, as high loss, low momentum fluid from the boundary layer is continuously added. It should be noted that although the streamwise velocity coefficient is significantly lower than that of the freestream this area is convected downstream at freestream velocity.

Elimination of the yaw angle overshoot in the CFD calculation using the smooth wall boundary condition suggests that it may also be eliminated from the experimental facility by further facility development. Importantly, a significant reduction in the boundary layer thickness, as opposed to its elimination, is sufficient to produce a much better gust profile.

The mechanism responsible for the yaw angle undershoot immediately upstream of the cross-wind gust (e.g. figure 6.1, $t = 0.30$s, $x = 2500$mm, $y = 350$mm) is related to the relative cross-stream velocity between the fluid in the cross-wind gust and the fluid ahead of it. This relative motion forms a shear layer at the leading edge of the gust which entrains fluid from the nominally axial flow ahead of the gust. Fluid flows back across the working section (+ve y direction) to replace this entrained fluid, with this forming a region of yawed flow that corresponds to a yaw angle undershoot. The combination of fluid with a positive cross-stream velocity ahead of the leading edge of the cross-wind gust, and fluid with a negative cross-stream velocity immediately behind the leading edge of the gust leads to a flow regime typical of a vortex at the leading edge of the gust. This vortical motion can be seen in the modified velocity vectors (e.g. figure 6.3, t = 0.28s, x = 2200mm, y = 450mm). Consideration of a real world transient cross-wind situation, as depicted in figure 1.2, suggests that this is not necessarily physically unrealistic. Here entrainment of fluid from in front of the building into the shear layer will occur, with this leading to cross-flow in the opposite direction to that of the cross-wind fluid and hence the vehicle will experience a yaw angle undershoot just prior to entry into the cross-wind region. The vortex at the leading edge of the simulated cross-wind gust has an associated viscous loss at its centre. This is not clear in the total pressure coefficient contours as the total pressure field is subject to other more significant effects, however is seen in the static pressure coefficient contours (figure 6.6). The loss is apparent from t = 0.20s onwards (e.g. figure 6.6, t = 0.20s, x = 1200mm, y = 650mm), from where it moves downstream maintaining its position relative to the front of the gust. From this mechanism, it follows that for the CFD calculation with the honeycomb roughness modelled, where the magnitude of cross-stream velocity immediately behind the leading edge of the cross-wind gust and hence entrainment of fluid from ahead of the cross-wind gust is increased, will exhibit an increased yaw angle undershoot. This can be seen from comparison of the empty working section yaw angle from the two CFD calculations (figures 6.46 and 6.47, t ≅ 0.27s).

Prior to onset of the cross-wind gust the total pressure coefficient contours (figure 6.4) remain at $Cp_o \cong 1.0$ for the core of the axial jet. The pressure loss corresponding to the boundary layer along the honeycomb section (x > 1500mm, y = 800mm) and the shear layer between the leeward side of the axial jet and the stationary bulk air (x > 500mm, y = 0 - 100mm) are also apparent. The incoming fluid from the cross-wind tunnel has an identical axial velocity component to the axial jet, with an additional cross-stream component and hence greater resultant velocity. For a yaw angle of 22° consideration of the resultant velocity of the cross-wind fluid and assuming constant static pressure and density yields a maximum theoretical total pressure coefficient of $Cp_o = 1.16$. Total pressure coefficients approaching $Cp_o = 1.7$ are seen in the working section, with the area of high total pressure located at the front outer edge of the cross-wind gust. This area of high total pressure is visible as early as $t = 0.15$s, ($x = 600$mm, $y = 700$mm), from where it is convected down the working section at freestream velocity. The magnitude of the maximum total pressure increases slightly at more downstream positions. The high total pressure manifests itself as a region of increased axial velocity (e.g. figure 6.5, $t = 0.28$s, $x = 2125$mm, $y = 300$mm), however it is convected downstream at a velocity equal to the free-stream velocity.

Three possible mechanisms for the generation of this region of high total pressure have been considered, firstly a transient change in cross-wind fan operating point, secondly a transient effect caused by shutter opening, and thirdly a transient effect caused by the interaction of the two wind tunnel jets.

Although the shutters always present a constant open exit area, the exit conditions of the cross-wind tunnel change during the formation of a cross-wind gust in that the flow through the upper row of shutters exits via a section of loss inducing honeycomb into a working section of greater than ambient static pressure, whereas flow through the lower row of shutters exits directly into nominally stationary air. These differences may cause a transient change in the cross-wind fan operating point as the shutters begin to open. Figure 6.7 shows the total pressure in the cross-wind tunnel against time for the duration of a cross-wind gust. This was measured in the cross-wind tunnel, just upstream of the top row of shutters, at a position that corresponds to fluid that will subsequently exit through the shutters at the upstream end of the working section. As can be seen from figure 6.7 the total pressure remains relatively steady and certainly does not exhibit characteristics consistent with a large transient total pressure rise in the working section.

An increase in working section total pressure could also result from reduced loss through the honeycomb flow straightener. Upon a shutter opening the previously stagnating fluid behind the shutter accelerates through the shutter aperture. Thus the velocity of the fluid that initially travels through the honeycomb is low and hence the loss is low. This could lead to fluid entering the working section with a total pressure approaching that seen within the cross-wind tunnel upstream of the honeycomb, approximately 155Pa (figure 6.7). This total pressure is high enough to account for the transient overshoot in the working section (maximum observed total pressure 145Pa), however if this were the case fluid with a high total pressure would be expected to enter the working section along the entire length of the cross-wind inlet. Figure 6.8 shows total pressure coefficient against time for two positions in the working section. The first position is at the upstream end of the working section, adjacent to the honeycomb section, ($x = 200$mm, $y = 800$mm). The transient total pressure overshoot visible between $t = 0.10$s and 0.20s. The full magnitude of the overshoot is not captured at this position, with the highest pressure recorded $Cp_o \cong 1.35$. The second graph is from further down the working section, again adjacent to the honeycomb section, ($x = 700$mm, $y = 800$m). Here a total pressure coefficient spike is seen for $0.10\text{s} < t < 0.15\text{s}$, however this corresponds to high total pressure fluid that has been convected downstream. At this position cross-wind fluid enters the working section from $t = 0.16$s, with no transient total pressure overshoot apparent. Admittedly this incoming fluid is affected by the region of low total pressure boundary layer fluid along the honeycomb, thus making any overshoot difficult to observe, however some mixing would be expected between the incoming fluid and the boundary layer fluid, thus producing a region of fluid with a total pressure higher than that seen in the remainder of the boundary layer, which is not the case.

The third and most likely mechanism thought to be causing the transient high total pressure is a transient effect associated with the initial formation of the cross-wind gust. Consider the pressure forces acting on an small element of invicid, incompressible fluid within a streamtube in a horizontal plane. The element of fluid is shown in figure 7.1.

The resultant force, F, acting on the fluid:

$$F = pA - (p + \delta p)(A + \delta A) + (p + k\delta p)\delta A \tag{7.1}$$

Neglecting second order terms, this reduces to:

$$F = -A\delta p \tag{7.2}$$

Applying Newton's Second Law:

$$-A\delta p = \rho A\delta s \,.\, \frac{du}{dt} \tag{7.3}$$

Dividing by $\rho A\delta s$ and rearranging:

$$\frac{1}{\rho}\frac{dp}{ds} + \frac{du}{dt} = 0 \tag{7.4}$$

Taking the substantive derivative of $\frac{du}{dt}$:

$$\frac{1}{\rho}\frac{dp}{ds} + u\frac{\partial u}{\partial s} + \frac{\partial u}{\partial t} = 0 \tag{7.5}$$

Integrating along the streamtube:

$$\int \frac{dp}{ds}\,ds + \rho\int u\frac{\partial u}{\partial s}\,ds + \rho\int \frac{\partial u}{\partial t}\,ds = \text{constant} \tag{7.6}$$

Which yields:

$$\Delta(p + \rho u^2 / 2) + \rho \int \frac{\partial u}{\partial t} ds = \text{constant} \qquad (7.7)$$

Equation 7.7 is Bernoulli's equation with an extra time derivative term. This time derivative term is zero for steady flow conditions, however may be non-zero for transient flow conditions. This extra term can be physically interpreted as thus: if the flow is slowing down in time (i.e. decelerating) along the streamtube this term will become a non-zero negative and hence the total pressure term will rise above the steady theoretical maximum.

It is quite conceivable that as the cross-wind gust formation process begins the incoming cross-wind fluid that impinges on the main jet in the working section decelerates, thus forming the area of transient high total pressure. It is for this reason that this is thought to be the correct mechanism.

This hypothesis was further augmented by the CFD analysis of the empty working section. The CFD did not model either the cross-wind tunnel fan system or the honeycomb section, however as can be seen from transient total pressure coefficient contours (figure 6.45, t = 0.1498s - 0.3496s) a very similar region of high total pressure is formed at the leading edge of the cross-wind gust. The size of the region of high total pressure is larger than that seen for the experimental facility, however so is the shear layer that corresponds to the transition region from axial to yawed flow at the leading edge of the gust, suggesting greater mixing at the gust leading edge for the CFD. As for the experimental facility (figure 6.4) the total pressure in this region increases as it is convected downstream, with the final magnitude being slightly above that of the experimental data.

The subsequent development of the predicted transient flow (CFD) was tarnished by the imperfect boundary conditions. As can be seen from figure 6.45 (t = 0.2297s - 0.4695s) a jet of high total pressure fluid forms in the working section where the main and cross-wind jets impinge. This is not present for the experimental facility and thus limits the usefulness of the current CFD. A more physically realistic boundary condition for both axial jet and cross-wind inlets would have been a fixed total pressure boundary. A calculation with these boundary conditions was attempted, however for an unknown reason soon after the first cross-wind inlet boundary opened outflow occurred from the working section through the cross-wind inlet. This caused the calculation to become unstable and a solution was never reached.

Two further total pressure anomalies occur behind the cross-wind gust leading edge of the experimental facility. Comparing total pressure coefficient contours for $0.24s \leq t \leq 0.32s$ (figure 6.4) shows that the total pressure in the area immediately behind the leading edge of the cross-wind gust is reducing across the entire width of the working section. For $t = 0.24s$, the total pressure coefficient is almost entirely in the contour range $1.10 < Cp_o < 1.20$ (e.g. $x = 1000mm$, $y = 400mm$), however by $t = 0.28s$ a significant proportion of this fluid now lies in the contour interval $1.00 < Cp_o < 1.10$ (e.g. $x = 1300mm$, $y = 300mm$) and a further reduction occurs by $t = 0.32s$ (e.g. $x = 2000mm$, $y = 400mm$). This reduction is not caused by low pressure fluid entering the working section, but is a genuine reduction in total pressure of the fluid within the working section. It would be easy to attribute this to viscous losses, but this should not be the case as the majority of fluid is not in an area of high shear. There is a similar reduction in total pressure ahead of the trailing edge of the cross-wind gust, again this appears to be a fall in total pressure of fluid within the working section as opposed to low total pressure fluid entering the working section. It is thought that the loss of total pressure at the leading edge of the cross-wind gust maybe linked to the previous total pressure overshoot, but this is not the case at the trailing edge of the cross-wind gust, and additional work is required before the underling mechanisms are understood.

The transient total pressure coefficient contours for the period of fully developed yawed flow (figure 6.4, t = 0.54s) shows some spatial non-uniformities in total pressure. The area of influence of the cross-wind fluid should exhibit a constant total pressure of $Cp_o = 1.16$, however contours in the range $1.0 \leq Cp_o \leq 1.3$ are seen. These spatial variations are a consequence of the uneven total pressure loss through the honeycomb flow straightener along it length (section 3.3.3).

The impinging of the axial and cross-wind jets has two further consequences for the flow in the working section. Firstly, as the cross-wind fluid enters the working section it displaces the main jet fluid. The region of high static pressure located in the top left corner of the working section (figure 6.6, t = 0.20s, x = 300mm, y = 700mm) provides the necessary force for this streamline curvature. Secondly, a change in operating point of the main jet fan occurs, such that main jet fluid now enters the working section at the same (increased) total pressure as the cross-wind fluid.

From these data the most appropriate location for the model in the working section was chosen. The most fundamental criteria for this facility is that the model is far downstream in the working section, such that the cross-wind gust has sufficient time to develop before reaching the model. Practical limitations are placed on this distance by the length of the cross-wind inlet (the limit of the yawed flow region) and the free shear layer growth on the leeward side of the main jet under axial flow conditions. It was clear that wherever the model was placed, it would be subjected to total pressure anomalies, and therefore the emphasis was placed on the yaw angle characteristic. Again, no ideal location existed, with the chosen position being one that had both a yaw angle under and overshoot. The location chosen was x = 2400mm, y = 400mm.

7.1.2 Gust Characteristics at the Model Centre

Figure 6.9 shows the cross-wind gust characteristics at the model centre. Prior to onset of the transient cross-wind gust the yaw angle at the model centre has a very small negative offset. Later aerodynamic model axial flow force and moment data is consistent with a small positive yaw angle offset in the working section. This difference is a likely result of a blockage effect created by placing the model in the working section. In the empty working section the boundary layer growth along the honeycomb flow straightener would be expected to induce a small positive flow angle incidence in the vicinity of the honeycomb, however shear layer growth on the leeward side of the jet would induce a small negative flow angle incidence in its area of influence. Thus, it is suggested that for the empty working section the model centre position (x = 2400mm, y = 400mm) is one where the yaw angle is influenced by the free shear layer growth, and hence the small negative yaw angle offset under axial flow conditions.

When the model is in the working section, the flow displacement around the model is asymmetric, in that the windward side has an essentially solid boundary in close proximity, whereas the leeward side does not. The consequence of this asymmetry being a circulation around the model and small positive flow angle incidence onto the model. It should be noted that although these effects exist they are insignificant in comparison to the flow field changes that occur during the passing of a cross-wind gust.

The yaw angle undershoot ($\psi = -12.3^{\circ}$ at $t = 0.29s$) and overshoot ($\psi = 33.9^{\circ}$ at $t = 0.32s$) are visible before the steady condition of $\psi = 22^{\circ}$ is attained. The transition to yawed flow is rapid, with a steady yaw angle achieved within a time corresponding to fluid that is moving at freestream velocity covering half a model length. The yaw angle under and overshoot has a significant effect on the initial development of yawed flow around the aerodynamic models, making the calculation of yaw rate, an important vehicle stability parameter (section 1.2), inappropriate for this facility.

The streamwise velocity coefficient indicates that matching of the axial velocity of the main jet and axial velocity component of the cross-wind jet has been successfully achieved, albeit with the constraints of the slightly varying streamwise velocity component that occurs for the duration of the yawed flow ($0.30s < t < 0.76s$).

With the exception of the loss caused by the vortex at the leading edge of the gust ($t = 0.30s$), the total and dynamic pressure coefficients are almost identical. During the passing of a cross-wind gust, the maximum values for both total and dynamic pressure exceed the theoretical maximums because the position of model centre lies downstream of a region of lower loss through the honeycomb flow straightener.

The effect of the reduction in total (and dynamic) pressure immediately behind the gust leading edge ($0.30s < t < 0.45s$) and in front of the gust trailing edge ($0.60s < t < 0.75s$) is obvious, with the transient dynamic pressure only comparable to the steady yawed dynamic pressure for $0.45s < t < 0.60s$. The reduction in dynamic pressure in front of the gust trailing edge is approximately 5% of the dynamic head. The consequences of the uneven nature of the dynamic pressure on surface pressures and force and moment coefficients of an aerodynamic model is obvious, however importantly the transient dynamic pressure never exceeds the steady yawed dynamic pressure, making comparisons between the peak transient and steady yawed forces and moments valid.

The working section Reynolds number based on model length and standard atmospheric conditions of $Re_l = 3.9 \times 10^5$ is approximately an order of magnitude below that found for real vehicles (section 2.5.2), thus Reynolds number effects would be important if extrapolation to full scale Reynolds number was to be attempted. Currently the achievable Reynolds number is dictated by the available cross-wind fan mass flowrate, however there is no reason why this type of facility should not operate at a much higher Reynolds number. This could be achieved either by increasing the nominal axial velocity or the scale of the facility.

The small discrepancy in turbulence intensity between axial ($Tu = 3.4\%$) and yawed ($Tu = 2.6\%$) flow is unlikely to have any significant effects on the flow around the aerodynamic models.

7.2 The Docton Geometry

7.2.1 Steady Axial Flow

The slight asymmetry of the steady axial pressure distribution (figure 6.10) is the result of the previously discussed wind tunnel flow asymmetry. Pressure coefficients consistent with closed separation bubbles are seen on both windward and leeward sides around s/S = 0.18. A rapid pressure recovery occurs along the beginning of the sides, with the small pressure minima at s/S = 0.82 indicating early separation from the rear corners. Both integrated pressure side force and yawing moment coefficients have small offsets under axial flow conditions, these being the consequence of the asymmetric pressure distribution.

7.2.2 Steady Yawed Flow

The dominant feature of the yawed pressure distribution is the region of separated flow on the leeward side. Separation occurs just after the suction peak at s/S = 0.1, with reattachment not occurring until s/S ≅ 0.4 (figure 6.10). Separated shear layers are very unstable and hence the reattaching flow will be highly turbulent. This flow subsequently separates a second time at the leeward rear corner, with its high level of turbulence causing increased entrainment of fluid from the wake region, and hence a smaller, lower pressure wake is formed. Consequently the pressures on the rear face of the model (s/S > 0.81) are also lower than those of the axial flow condition.

The yawed flow condition, as compared to the axial flow condition, exhibits significantly increased side and drag force magnitudes (Cy = -2.62 cf. Cy = -0.10, Cx = 0.93 cf. Cx = 0.51) and yawing moment coefficient (Cmz = 0.48 cf. Cmz = 0.04).

7.2.3 Transient Flow

Prior to any development of the yawed flow regime the transient axial flow pressure distribution (figure 6.11, t = 0.0) is in good agreement with the steady axial flow pressure distribution (figure 6.10). The pressure in the stagnation region shows Cp_s = 1.0, with suction peaks, indicating flow acceleration, around the front corners and a closed separation bubble at s/S = 0.18. There are two small suction peaks at the rear corners (s/S = 0.82) prior to flow separation. The wake survey (figure 6.18, t = 0.0), shows an axially aligned wake behind the model. Although the wake survey plots are instantaneous, they are obtained from ensemble averaged data that is phase synchronised with respect to the cross-wind gust, thus any unsteady phenomena, for example vortex shedding, will not be captured unless they are forced by the gust (currently there is no evidence to suggest that vortex shedding is forced by the gust, however it is likely there would be some interaction).

At t = 0.20s the model is still subjected to nominally axial flow (cross-wind gust leading edge at x = 1750mm, figure 6.1), however the pressure distribution around the model is affected by the impending region of transient high total pressure, as observed for the empty working section. The wake survey of figure 6.18 (t = 0.20s) shows the area of influence of this high total pressure to be mainly down the windward side and around the leeward front corner of the model, although the magnitude of the increase is small at this stage. An increase in stagnation region pressure and an increase in the peak suction around the front corners, relative to t = 0.0s, are observed in the surface pressure distributions of figure 6.11 (t = 0.20s). These changes cause a slight rise in integrated pressure yawing moment coefficient (figure 6.13) and drag coefficient (figure 6.14), but have little effect on the side force coefficient (figure 6.12).

By t = 0.28s, just prior to the cross-wind gust leading edge reaching the model, the region of maximum total pressure overshoot moves down the leeward side of the model (figure 6.18, t = 0.28s). At this time the model is also subjected to the yaw angle undershoot ahead of the cross-wind gust. The combination of these two effects causes an increase in leeward side front corner pressure for $s/S < 0.12$ and an increase in suction for $0.12 < s/S < 0.2$ (relative to $t = 0.20s$). The windward side front corner, which is affected mainly by the yaw angle undershoot, exhibits decreased pressure for the region $0.0 < s/S < 0.08$ and increased suction for the region $0.08 < s/S < 0.2$ (relative to $t = 0.20s$). Little change in surface pressure profile is observed around the remainder of the model. These pressure changes result in an increased side force coefficient magnitude, and change of direction, (figure 6.12), a decreased yawing moment coefficient (figure 6.13) and a significant decrease in drag coefficient (figure 6.14) between $t = 0.20s$ and $t = 0.28s$.

Docton [61] noted similar surface pressure changes as the cross-wind gust approached the model during his experiments, astutely concluding without direct evidence that these observations were consistent with a localised region of higher axial velocity.

Development of the yawed pressure regime occurs for $t > 0.28s$. The cross-wind gust yaw angle overshoot and transient high total pressure continue to affect the pressure distribution around the model until $t = 0.34s$, thus surface static pressure and wake data for the period $0.28s < t < 0.34s$ are not shown. The effect on side force and yawing moment coefficients is evident in figures 6.12 and 6.13 respectively.

By $t = 0.34s$ rapid pressure development has occurred around the entire model, but only the front windward side pressure distribution resembles that of the steady yawed flow (figure 6.10). The windward side rear corner suction peak is significantly stronger than that observed under steady yawed flow conditions. The leeward side pressure characteristics are similar to those under axial flow conditions, however the leeward front corner suction peak is much stronger, with no evidence of flow separation. These two transient suction peaks have a significant effect on the yawing moment coefficient (figure 6.13). A peak of $Cmz = 0.74$ occurs at $t = 0.34s$, this being a 55% overshoot of the steady yawed value and occurring approximately one model length into the cross-wind gust. The magnitude of the transient side force coefficient at t = 0.34s (figure 6.12) is slightly lower than the steady yawed value (Cy = -2.25 cf. Cy = -2.62), and the transient drag coefficient (figure 6.14) is significantly lower (Cx = 0.20 cf. Cx = 0.51). These differences are a result of increased suction around the front leeward corner, decreased suction around the rear leeward corner and increased suction around the rear windward corner, when compared to the steady yawed pressure profile. The wake survey for t = 0.34s (figure 6.18) shows that the region of high total pressure is no longer influencing the pressure distribution around the model. The effect of the yaw angle undershoot on the model far wake is still apparent, with the wake meandering towards the windward side of the model (top of the picture).

The leeward front corner separation, as observed for the steady yawed flow, is only apparent from t = 0.38s onwards (figure 6.11, t = 0.38s, s/S = 0.15) and continues to increase in size until t = 0.60s, by which time reattachment is occurring at s/S ≅ 0.4, which is a comparable position to that of the steady yawed flow (figure 6.10). The leeward rear corner suction peak develops simultaneously with the leeward front corner separation (figure 6.11, 0.38 ≤ t ≤ 0.60, s/S = 0.84) suggesting the two processes may be linked by the propagation of information down the leeward side of the model. The windward rear corner suction peak significantly weakens between t = 0.34s and t = 0.38s (figure 6.11, s/S = 0.82) and is comparable to the steady yawed value by t = 0.38s (figure 6.10, s/S = 0.82). This change in windward rear corner pressure distribution is also mainly responsible for the sharp decrease in drag observed at t = 0.36s (figure 6.14).

Continued surface pressure profile development causes a peak in the transient side force magnitude at t = 0.50s, with Cy = -2.9 (figure 6.12) This corresponds to 4.5 model lengths of cross-wind flow and represents an 11% overshoot of the steady yawed value (Cy = -2.62). Part of this pressure development can be attributed to the increasing dynamic (and total) pressure within the cross-wind gust up to t = 0.50s (section 7.1.2), however this cannot account for the overshoot of the steady yawed side force coefficient. The increase in working section total pressure is visible around the windward side of the model in the wake survey of figure 6.18 ($y/l = 0.2$, $0.0 \leq x/l \leq 1.0$). At $t = 0.38$s, much of this region lies in the contour interval $0.98 \leq Cp_o \leq 1.26$, however by $t = 0.50$s it is in the interval $1.26 \leq Cp_o \leq 1.40$.

The yawed wake flow, with its much larger area of out of range data (black), is seen in figure 6.18 for $0.38\text{s} \leq t \leq 0.70\text{s}$. Interestingly, the amount of out of range data along the leeward side of the model ($y/l = -0.2$, $0.0 \leq x/l \leq 1.0$), increases significantly between $t =$ 0.38s and $t = 0.45$s. This corresponds to the formation of the leeward side front corner separation, with the out of range data associated with the region of recirculating flow.

Surface pressure profile development (figure 6.11) continues until $t = 0.60$s, by which time the transient pressure distribution and the transient force and moment coefficients (figures 6.12 - 6.14) are comparable to their steady yawed values. This development time corresponds to 7 model lengths of cross-wind flow. For an infinitely long cross-wind gust the final pressure distribution and force and moment coefficients should be equal to the steady yawed values, however this is not exactly achieved in this facility where a reduction the cross-wind dynamic (and total) pressure of approximately 5% occurs after $t = 0.60$s (section 7.1.2). This reduction in total pressure can be seen in the wake survey of figure 6.18. Comparison of $t = 0.60$s and $t = 0.70$s clearly show a general reduction in total pressure coefficient for the majority of the freestream fluid shown in the working section. Both side force (figure 6.12) and yawing moment (figure 6.13) coefficients have distinct plateaux between $0.65\text{s} < t < 0.75\text{s}$. For the side force this is approximately 6% below the steady yawed value, however the yawing moment is only approximately 2% below the steady yawed value. The drag coefficient (figure 6.14) also exhibits a reduction, but no plateau is reached and the reduction corresponds to more than 6% of the steady yawed value. Thus a degree of error is present for both yawing moment and drag coefficients, with the likely source of this being the pressure distributions on the front and rear faces of the model, as these are common to both but do not contribute to the side force coefficient.

The return to the axial flow pressure distribution occurs from t = 0.75s onwards, with the pressure distribution and force and moment coefficients in good agreement with the steady axial flow values from t = 0.90s. The return to axial flow is also seen in the wake survey of figure 6.18, although traces of yawed flow can still be seen at t = 0.90s for x/l > 1.25.

Thus it can be seen that as the transient flow conditions develop the flow remains attached around the front leeward and rear windward corners beyond the yaw angle at which it would separate under steady flow conditions, which is evidence of significant transient flow effects. Although the flow later separates, the transient side force, yawing moment and potential yaw rate that are recorded exceed comparable values obtained from steady tests, with transient testing being the only method of determining these values.

Delayed flow separation has also been observed on the suction surface of aerofoils undergoing transient pitching motions, with this having a similar effect on the transient forces and moments. For example McCroskey *et al* [112], stated that the aerodynamic forces and moments produced under transient flow conditions are considerably larger than their steady counterparts, although not quantification of their overshoots was given.

7.2.4 Force Balance Data

The qualitative agreement between the integrated pressure (figure 6.12) and directly measured side forces (figure 6.15) is good. The steady axial flow side force shows a discrepancy of ΔCy = -0.02, and the steady yawed side force a discrepancy of ΔCy = 0.10 (4%). This lies within the previously mentioned balance repeatability of approximately 5% (section 4.6). The low pass filtering has truncated part of the high frequency component associated with the transition from axial to yawed flow for the transient condition, leading to an increased rise time (figure 6.15, t ≅ 0.30s, cf. figure 6.12, t ≅ 0.30s). Filter ringing has obscured any potential transient overshoot (figure 6.15, 0.30s < t < 0.70s). The general agreement between the final transient and steady yawed values is good.

The agreement between directly measured and integrated pressure steady yawing moment is fairly good. The steady axial yawing moment exhibits a difference of ΔCmz = 0.02, and the steady yawed yawing moment a difference of ΔCmz = 0.03 (6.25%). The directly measured transient yawing moment (figure 6.16) however differs substantially from the integrated pressure transient yawing moment (figure 6.13). Firstly, the low pass filtering has truncated part of the higher frequency component associated with the rapid increase in yawing moment at the leading edge of the gust, hence the rise time to the yawed flow condition is longer (figure 6.16, t ≅ 0.30s cf. figure 6.13, t ≅ 0.30s). Secondly the balance has not resolved the double peak of the integrated pressure yawing moment, as seen at the beginning of the yawed flow (figure 6.13, 0.30s < t < 0.35s). Thirdly the magnitude of the maximum yawing moment is substantially less than that of the integrated pressure yawing moment (Cmz = 0.55 cf. Cmz = 0.79), and finally the fall to a steady yawing moment after the initial peak is much faster for the directly measured moment. The final transient value is however in good agreement with the steady yawed value (Cmz = 0.44 cf. Cmz = 0.45), and is within ΔCmz = 0.04 (6.25%) of the transient integrated pressure final value.

The discrepancies between directly measured and integrated pressure transient yawing moment are mainly associated with the rapid change in yawing moment at the beginning of the gust. This suggests they are a consequence of the limited capabilities of the balance and the inherent difficulty of measuring unsteady forces and moments (section 4.6).

The transient drag coefficient (figure 6.17) bears little resemblance to the integrated pressure drag coefficient (figure 6.14), showing little difference between the axial and yawed drag coefficients, and with a significant amount of oscillation. The magnitude of the transient drag coefficient for the axial part of the cross-wind flow (0.0s < t < 0.30s and 0.76s < t < 1.0s) is however in rough agreement with the steady axial flow drag coefficient. The steady axial drag coefficient is reasonable (Cx = 0.44), but is 14% below the steady axial integrated pressure drag (Cx = 0.51). The steady yawed drag is substantially lower than the steady yawed integrated pressure drag (Cx = 0.53 cf. Cx = 0.93). The error in yawed drag coefficient (both steady and transient) is a likely consequence of balance cross-coupling. The largest magnitude of components measured is the yawed (either steady or transient) side force and yawing moment, thus with the balance in the side force and yawing moment orientation, the cross-coupling from other components is relatively insignificant. The converse is true however when measuring the remaining four components, such that in those balance orientations the errors due to cross-coupling, and hence overall errors are at a maximum.

7.3 The Durham Geometry

7.3.1 Steady Axial Flow

The surface oil flow visualisation shows that under axial flow conditions closed separation bubbles are present at the front corners of the model on both the sides and upper surface (figure 6.20). This is usual where discontinuities of curvature occur, in this case at the interface of the corners and either the side or windshield and is advantageous in that rapid turbulent reattachment means that downstream the flow development should be relatively insensitive to Reynolds number.

After an initial acceleration around the front corners, as indicated by the suction peak in the pressure distribution, the flow down the sides of the model undergoes a rapid pressure recovery. Strong vortices are formed along the long and relatively sharp (2mm radii) A-pillars, as seen in both the surface pressure contours (figure 6.19) and the flow visualisation (figure 6.20). The leeward side A-pillar vortex is also visible in the x/l = 0.75 wakeplane, which is located just ahead of the backlight, and shown in figure 6.21. As can be seen from figure 6.21, the A-pillar vortices are drawn towards the roof by the low pressure in this region. The A-pillar vortices are not present in the x/l = 1.5 wakeplane survey (figure 6.22), suggesting they are weakened by the opposite sense C-pillar vortices. A region of low pressure, indicating accelerated flow, exists below the C-pillars on both windward and leeward sides (figure 6.19). This is caused by two effects; firstly, the boat-tailing at the rear of the model causes an acceleration at the beginning of the taper, and secondly the C-pillar vortices draw fluid onto the backlight, causing further flow acceleration in this region.

The flow over the upper surface of the model, as seen in figure 6.19, accelerates up the windshield, with a closed separation bubble at the windshield/roof intersection (figure 6.20). Pressure recovery occurs on the roof with a second separation at the roof/backlight intersection. Detailed inspection of the backlight flow visualisation, (figure 6.20), shows than on the centreline reattachment occurs two-thirds of the way down the backlight, with the region of separated flow almost triangular in shape, as seen for the Ahmed geometry in figure 2.4. Strong C-pillar vortices are apparent from the backlight flow visualisation (figure 6.20), and are seen in the x/l = 1.5 wakeplane vorticity contours (figure 6.22a), with the total pressure loss caused by viscous loss at the vortex cores apparent in the x/l = 1.5 wakeplane total pressure coefficient contours (figure 6.22b). The wind tunnel shear layer is also seen on the left side of figure 6.22b, where it has a weak interaction with the leeward (left hand) C-pillar vortex.

Careful comparison of the flow visualisation (figure 6.20) and the upper surface pressure tapping distribution (figure 4.5) shows the C-pillar vortices to be located outboard of the backlight pressure tapping distribution, and hence the low pressure vortex cores are not visible in the backlight pressure contours (figure 6.19). The pressure discontinuity between the sides and the upper surface of the model is made possible by the sharp (2mm) radii along the intersections. The small offsets of the steady axial flow integrated pressure side force and yawing moment coefficients (figure 6.35 and 6.36 respectively) are, as with the Docton geometry, the result of tunnel flow asymmetry.

7.3.2 Steady Yawed Flow

The yawed flow regime surface pressure distribution, as seen in figure 6.23, is dominated by the now very strong leeward side A-pillar vortex. This is seen in both the leeward side pressure contours, and the wake surveys (figures 6.25 and 6.26). As can be seen from figure 6.26b, the high loss (drag) region is much larger than for the axial flow regime. The far wake horizontal total pressure gradients of figure 6.26b are a consequence of the non-uniform loss through the honeycomb section. The windward side A-pillar vortex has been replaced by a vortex forming at the front of the windward side roof. This vortex draws in fluid from the side of the model, thus lowering the pressure here, and hence reducing the side force. The windward side C-pillar vortex has significantly increased in strength, thus drawing in more fluid from the windward side C-pillar region of the model. The corresponding decrease in windward side C-pillar side pressure (figure 6.23) acts to reduce the side force and increase the yawing moment coefficient. The low pressure vortex cores of the windward side roof vortex and the C-pillar vortex are seen in the upper surface pressure contour plots of figure 6.23 and the flow visualisation of figure 6.24. Apart from the vortex cores, the yawed flow visualisation was unable to shed light on the nature of the flow on the backlight. Downstream of the geometry mutual entrainment of the two windward side vortices occurs, with a single vortex core centred at $y/l = -0.05$, $z/l = 0.2$ in the $x/l = 1.5$ wakeplane (figure 6.26).

A second leeward side vortex is formed by flow under the model, although this is not nearly as strong as the leeward side A-pillar vortex. The corresponding low surface static pressure coefficients are seen near the front at the bottom of the leeward side (figure 6.23), with the vortex apparent at y/l = -0.35, z/l = 0.1 in the x/l = 1.5 wakeplane (figure 6.26).

Three other areas of vorticity are present in the x/l = 1.5 wakeplane (figure 6.26). A second vortex formed by flow under the model is centred at y/l = -0.15, z/l = 0.5. The origin of this vortex cannot be determined from the available data, although possibilities include the model windward side lower edge, the model supports or underside flow exiting from the leeward (left) side of the rear diffuser. It seems unlikely that the model supports would cause such a large vortex to form, being thin circular cylinders of a short length (25mm). It is also unlikely to be caused by flow exiting the diffuser, as in figure 6.25 this vortex is located inboard of the edge of the diffuser, in a flow regime that is nominally yawed to the left. Thus it s thought that the vortex is formed by flow around the windward side lower edge of the model. The area of weak vorticity at y/l = 0.05, z/l = 0.1 is not a vortex, but a region where flow is turned as it is entrained into the main windward roof/C-pillar vortex, and hence has non-zero vorticity. The third area of vorticity, located at y/l = -0.55, z/l = 0.075, is as a result of an effect noted by Harvey and Perry [114]. The leeward side underfloor vortex (y/l = -0.35, z/l = 0.1) induces a cross-flow on the groundboard that is in addition to the component of cross-wind in this direction. A pressure minima occurs under the core of the vortex, and consequently the boundary layer caused by this cross-flow has to negotiate an adverse pressure gradient once it has passed under this core. When a vortex is near enough to the floor, as is the case here, the adverse pressure gradient is enough to cause separation of the boundary layer. Further downstream, the separation bubble grows to the point at which it detaches from the floor as a second vortex, with opposite sense vorticity to the main vortex.

The remainder of the upper surface static pressure contours, (figure 6.23), show flow acceleration up the windshield of the model, with the yawed flow regime clearly visible. The contours are significantly less skewed at the windshield/roof intersection, suggesting the flow in this region is dominated by the axial component of the flow around this relatively sharp corner, although the windshield/roof separation bubble does exhibit a higher peak suction than that observed under axial flow conditions ($-1.2 < Cp_{s\ min} < -1.0$ for yawed flow cf. $-1.0 < Cp_{s\ min} < -0.8$ for axial flow).

7.3.3 Quasi-Steady Wake Surveys

These data (figure 6.27) provide more information about the wake structure changes as the model is subjected to incident flow of increasing yaw angle, but under steady flow conditions. The leeward side A-pillar vortex, which is dominant under yawed flow conditions is visible from $\psi = 7^\circ$. As the yaw angle increases, the size and strength of this vortex increases, with the core moving further from the model as the nominal flow angle in the wake increases. The influence of the low pressure on the roof of the model decreases with increasing yaw angle, as indicated by the reduction in height of the centre of the vortex.

No increase in windward side vortex peak vorticity is recorded at $\psi = 7^\circ$, (although this may be due, in part, to the coarse nature of the survey grid). An increase in strength is however seen by $\psi = 14^\circ$. This could be due to either a simple increase in vortex strength with yaw, or the formation of the windward side roof vortex, which subsequently entrains the windward side C-pillar vortex resulting in an increase in vorticity. The original leeward side C-pillar vortex decreases in strength and by $\psi = 22^\circ$ ceases to exist. The leeward side underfloor vortex is apparent form $\psi = 14^\circ$ onwards, although the final location is subtly different from that described in 7.3.2. This difference, and the other slight differences, can be attributed to the two different techniques used to place the model in yawed flow (section 5.2.4). The other areas of weak vorticity, as seen in the previous steady yawed wakeplane (figure 6.26) are also apparent.

Davis [33] presented wake traverses for a similar geometry under steady yawed flow conditions for yaw angles of $0^\circ \leq \psi \leq 10^\circ$ in 2° increments. He also found a strengthening of the leeward side A-pillar vortex with yaw, with a second leeward side vortex formed at the front of the model from flow under the model. His windward side C-pillar vortex exhibited almost constant vorticity up to 10° yaw, while the leeward side C-pillar vortex remained up to the maximum yaw angle with no decrease in peak vorticity. For comparison he also tested a model with well rounded A-pillars and one with an obvious angle change between the bonnet and windshield. Both these exhibited much weaker A-pillar vortices and had significantly lower yawed side force coefficients, from which he concluded that the A-pillar vortices make a significant contribution to the yawed side force.

Davis [45] later studied a high performance road car at yaw. For this geometry a total separation of the leeward side flow between $\psi = 10^\circ$ and 11° changed the trailing vortex structure over the top rear deck of the car; giving rise to a much larger windward side vortex. This is in contrast to the Durham geometry, which exhibits a significant change in the windward side vortex structure without the total leeward side separation.

7.3.4 Transient Flow

Many of the features observed in the transient development of the yawed flow regime around the Docton geometry are also present for the Durham geometry. Further information about the flow development is available from the wake surveys, however it should be noted that because elements of fluid from different parts of the model travel different distances, and hence take different times, to reach a particular wake plane, it is not possible to correlate a transient wake plane at a particular time to a transient surface pressure distribution at a previous time. Thus, a transient wake plane integral is meaningless, but transient wake planes can add significantly to the understanding of the structure of a vehicle wake

Transient yawed flow development again commences around t = 0.28s. Prior to this both surface static pressures (figure 6.28) and wake surveys (figure 6.38) are in good agreement with the steady axial flow data. At t = 0.30s the effects of the cross-wind gust anomalies (high total pressure and yaw angle overshoot) again result in spurious surface static pressure data (figure 6.29). The effect on the side pressures, forces and moments are as for the Docton geometry, with the roof experiencing a brief reduction in pressure coefficient, and the model a corresponding increase in upper surface lift coefficient (figure 6.37).

The transient axial flow (0.0s < t < 0.25s) integrated pressure side force (figure 6.35) and yawing moment (figure 6.36) coefficient offsets are more significant than those of the steady flow conditions. A likely cause of this is a slight leakage of cross-wind fluid flow through the closed shutters, augmenting the already asymmetrical wind tunnel flow.

The subsequent side pressure data indicates rapid surface pressure development on both windward and leeward sides, with the pressure distributions comparable to those of the steady yawed flow from t = 0.34s onwards (figure 6.30). The transient side force coefficient (figure 6.35) exhibits the characteristic under and overshoot created by this cross-wind facility before rising to the steady yawed value by t = 0.47s. The rise between t = 0.34s and t = 0.47s is partially accounted for by the increase in cross-wind tunnel dynamic pressure, however the subsequent overshoot of the steady yawed value and then reduction indicates that flow development must continue up to t = 0.60s (7 model lengths of cross-wind flow). The maximum side force coefficient of Cy = -1.63 at t = 0.52s represents a 16% overshoot of the steady yawed value. As seen with the Docton geometry, development of a region of separated flow can take up to 7 model lengths of cross-wind flow. Thus it is suggested that this increase in side force is a result of delayed leeward side A-pillar and underfloor flow vortex development. Comparison of the leeward side surface pressures at t = 0.47s (figure 6.31) and t = 0.52s (figure 6.32) shows small differences in pressure coefficient for the A-pillar region, with the latter time exhibiting lower pressures (this however could be due to the inherently unsteady A-pillar vortex moving such that the pressure tappings were subjected to a lower pressure part of the core).

A reduction in side force from the maximum occurs as the transient flow subsequently tends towards the steady yawed flow. As for the Docton geometry, with an infinitely long gust, the final side force coefficient would be expected to match that of the steady yawed flow. Again, this is not the case, with the approximately 6% discrepancy accounted for by the reduction in cross-wind dynamic pressure after t = 0.60s (figure 6.9).

The transient yawing moment coefficient (figure 6.36) is similar in shape to the side force coefficient, with the transient value exceeding the steady yawed value for the period 0.42s < t < 0.6s. The maximum yawing moment of Cmz = 0.36 at t = 0.52s corresponds to a 7% overshoot of the steady yawed value. It is suggested, that as with the transient side force overshoot, the transient yawing moment overshoot is a result of the delayed leeward side A-pillar and underfloor vortex flow development. As the surface static pressure distribution subsequently tends towards the steady yawed distribution, so does the integrated pressure yawing moment, with the final approximate 6% discrepancy again accounted for by the wind tunnel dynamic pressure shortfall.

The pressure coefficients over the majority of the upper surface also exhibit rapid development, with a yawed flow pressure regime apparent from t = 0.34s. The integrated pressure upper surface lift coefficient (figure 6.37) however does not reach a maximum until t = 0.55s, thus pressure development must continue until this time. The increase in upper surface lift between t = 0.36s and t = 0.45s can again partially be accounted for by the increase in wind tunnel dynamic pressure, but the subsequent increase must be caused by delayed flow development, and it is this phenomena that is of greater interest. Comparison of the upper surface pressure contours at t = 0.45s and t = 0.55s (figure 6.33) shows that this delayed flow development is occurring in the regions of separated flow. In this case, the windshield/roof closed separation bubble and the windward side roof/C-pillar vortex, where significant decreases in pressure coefficient are seen. This also causes a reduction in pressure coefficient over a larger section of the roof. The reduction in pressure coefficients observed for the windward side roof/C-pillar vortex are much more apparent than those of the A-pillar vortex, seemingly confirming that delayed pressure development in areas of separated flow of this nature is a true effect. The delayed development of the windward side roof/C-pillar vortex may also affect the side force and yawing moment coefficients through increased entrainment of fluid from the windward side of the model, although any contribution from this mechanism is likely to be small.

The maximum transient upper surface lift coefficient recorded is Czu = 1.38 at t = 0.50s, corresponding to a 12% overshoot of the steady yawed value and occurring after 5 model lengths of cross-wind gust. The upper surface lift coefficient subsequently decays and undershoots the steady yawed value. Unlike the other coefficients, it does not reaches a plateau, with two spurious spikes occurring prior to the end of the cross-wind gust. The cause of these spikes is predominately, although not uniquely, small pressure changes on the windshield surface of the model. It is not, as might be expected, associated with an unsteady region of separated flow. Figure 6.34 shows the upper surface pressure distributions for t = 0.74s (high lift) and t = 0.76s (low lift), with no significant changes is surface static pressure magnitudes apparent. This effect may be aerodynamic, but is potentially the result of a yet unknown gust characteristic.

Development of the leeward side A-pillar and underfloor vortex occurs in the x/l = 0.75 wakeplane (figure 6.38) from t = 0.31s, with both being fully developed by t = 0.34s. The total pressure coefficient contours show the wind tunnel high total pressure region passing down the leeward side of the model. The cores of both vortices exhibit high loss (drag), with the loss of the A-pillar vortex being significantly higher. Unfortunately, much of the data for the fully developed A-pillar vortex is out of range of the probe calibration. Much more information is provided about the development of the yawed trailing vortex structure by the x/l = 1.5 wakeplane (figure 6.39). The increase in strength of the windward side A-pillar vortex at t = 0.33s is a result of the cross-wind yaw angle undershoot. Development of the C-pillar and windward side roof vortices is seen from t = 0.34s onwards. The leeward side C-pillar vortex moves to the right, with the windward side C-pillar vortex moving to the left. At t = 0.35s, the windward side C-pillar/roof vortex has moved far enough to the right that it 'leap-frogs' over the leeward side vortex. The leeward side A-pillar vortex also becomes apparent at this time (y/l = -0.4, z/l = 0.25). Momentarily both C-pillar vortices exist, with the windward vortex located above the leeward vortex, which is still in a position similar to that it occupies under axial flow conditions. The leeward side C-pillar vortex then disappears completely and the windward side vortex centre reduces in height such that by t = 0.38s the flow structure is comparable with that of the steady yawed flow. The cross-wind gust high total pressure region is again seen passing the leeward side of the model in the total pressure coefficient contours. As the yawed wake develops, the original two discrete areas of loss, corresponding to the two C-pillar vortices, amalgamate to form a single area of loss corresponding to the windward side C-pillar/roof vortex (y/l = 0.0, z/l = 0.15). The second main area of loss for the yawed flow corresponds to the leeward side A-pillar vortex (y/l = -0.3, z/l = 0.2), with the loss here significantly higher that that of the windward side vortex.

The delayed flow development of the leeward side vortices, as seen on the side surface static pressures, should be apparent at a later time in the wake. Comparison of x/l = 1.5 wakeplane data for t = 0.52s and t = 0.57s (figure 6.40) (these roughly correspond to surface pressure data at t = 0.47s and t = 0.52s respectively) show no significant differences in either vorticity or total pressure. Thus it is assumed that the downstream diffusion of the vortices obscures the apparent increase in vortex strength at the model surface.

7.3.5 Force Balance Data

As with the Docton geometry, the Durham geometry transient side force and yawing moment coefficients (figure 6.41) mirror the trends seen in the transient integrated pressure coefficients. The side force again exhibits balance oscillations, with these not apparent in the yawing moment. The yawing moment is particularly similar to the integrated pressure yawing moment, exhibiting both the transient overshoot and final value undershoot. The magnitudes of the steady yawed and transient yawed side force and yawing moment coefficients are significantly higher that those of the integrated surface pressure coefficients (integrated pressure steady yawed: Cy = -1.41, Cmz = 0.34, force balance steady yawed: Cy = -1.78, Cmz = 0.40). It is likely that the coarse pressure tapping distribution on the side surfaces of the Durham geometry was unable to entirely resolve the low pressure cores of the leeward side vortices, and if so the integrated pressure forces will underpredict the magnitude of both yawed side force and yawing moment coefficients. The transient yawing moment coefficient exhibits a maximum 5% overshoot of the steady yawed value, which compares well with the 7% transient overshoot of the integrated surface pressure yawing moment coefficient (figure 6.36).

The transient drag coefficient is again dominated by balance oscillations, although some agreement can be seen between the steady axial flow and axial part of the transient flow ($0.0s < t < 0.30s$ and $0.76s < t < 1.0s$). The steady axial flow drag coefficient (Cx = 0.41) can be considered accurate, but as with the Docton geometry, the yawed value (Cx = 0.56) is probably underpredicted due cross-coupling.

The transient pitching moment exhibits the oscillations generally seen in the force measurements, although agreement between the steady and transient conditions for axial and yawed flow is relatively good. The pitching moment remains negative (nose down) for all conditions; this being a consequence of low pressure on the backlight of the model, caused by the attached flow regime.

Little agreement is apparent for the lift coefficients. The steady axial and yawed values are very similar, which is unlikely given the significant changes in flow structure seen on the upper surface of the model. The steady axial flow and the axial part of the transient flow are also significantly different, giving little confidence in these results. The low absolute magnitude of the lift coefficient (when compared to side force) makes accurate measurement of lift much more difficult, with the error contribution from cross-coupling under yawed flow conditions also at a maximum. One characteristic of interest is that the transient lift, as with the integrated pressure upper surface lift of figure 6.37, shows a marked increase just prior to the end of the cross-wind gust ($t = 0.78s$), although this agreement should be treated with caution. This single peak, as opposed to the two seen for the integrated pressure upper surface lift, is a likely consequence of the inability of the balance to resolve high frequency force oscillations. The oscillations of the integrated pressure lift occur at a frequency of ≅ 20Hz, which is higher than the balance filter stop frequency of 18Hz.

The rolling moment coefficients appear reasonable, with good agreement between steady and transient axial and yawed conditions. This is especially surprising as the magnitude of the coefficient is small. Under axial flow conditions the coefficient is nominally zero, with a significant decrease occurring as the yawed flow develops. The effect of cross-wind tunnel yaw angle under and overshoots are visible ($t = 0.25s$ and $t = 0.32s$ respectively), with the steady yawed value not reached until $t = 0.53s$. The negative value of the coefficient under yawed flow conditions indicates the centre of pressure is below the mid-height of the model. Although the magnitude of rolling moment is small, it would be significant if the overall vehicle dynamic response were to be evaluated.

As with the Docton geometry side force and yawing moment coefficients, a correlation exists between the spectral distribution of the force and moment components and the time-domain oscillations, with the components that have a significant amount of energy around 18Hz exhibiting the most pronounced ringing. Appendix C shows the autospectral density functions of the six components of force and moment for the Durham geometry.

This balance system presents an improvement in the force and moment measurements, compared to the work of Docton [61], however is still in need of significant development. Raising the balance natural frequency yields twofold improvements. Firstly, the higher the resonant frequency, the less the aerodynamic exciting force will be at that frequency, and therefore the smaller the effect of resonance. Secondly, a higher filter cut-off frequency would allow developments to the filter geometry to minimise the effects of ringing. That said, an increase in balance natural frequency is not easy to achieve without compromising measurement accuracy.

7.3.6 Wake Integration

The wake integral derived drag coefficient for the axial flow condition (Cx = 0.40) is in good agreement with the force balance data (Cx = 0.41). Viscous drag accounts for 90% of the total drag, the remaining 10% being from the transfer of energy into the trailing vortices (vortex drag). The largest local contribution to drag, both viscous and vortex, comes from the trailing vortices, as seen in the microdrag of figure 6.42.

The wake integral derived axial flow side force coefficient (Cy = 0.02) is not in agreement with the integrated pressure and force balance side force coefficients of Cy = -0.02. The wake plane contains negative cross-stream momentum that is a consequence of the flow asymmetry in the working section. The wake integration is unable to differentiate between this and cross-stream momentum that is a consequence of forces on the fluid within the control volume, and hence returns an erroneous value. This problem could be eliminated by surveying a plane upstream of the model and integrating the differences in momentum between the two planes, as opposed to assuming uniform axial flow upstream of the model.

The extra blockage of the yawed model in the working section clearly requires a larger integration area for the yawed flow wake integral, however the available area is limited by the proximity of the shear layer to the leeward side of the model. Thus the area used for the yawed model integration violates the requirement of the integration that the boundaries of the control volume parallel to the streamwise direction are sufficiently far from the model that no changes in flow occur (Appendix B). The subsequent resolution of forces from the working section axes to yawed model axes causes any error to affect both drag and side force coefficients.

The yawed model side force coefficient (Cy = -0.84) is substantially lower than the integrated pressure side force (Cy = -1.41) or the force balance data (Cy = -1.78), this discrepancy undoubtedly being a consequence of the small size of the integration area. The drag coefficient (Cx = 0.98) is higher than expected, however an increase in magnitude of the side force would reduce this on resolution of the forces, thus this result is not unexpected. Neglecting the inaccuracy in magnitude, inspection of the microdrag (figure 6.43) shows that the leeward side A-pillar vortex makes the highest local contribution to drag, this being followed by the windward side roof/C-pillar vortex. The yawed flow microside plot also shows it is the leeward side A-pillar vortex that is providing the highest local contribution to side force, with this followed by the windward side roof/C-pillar vortex.

7.4 Comparison of Docton Geometry and Durham Geometry Results

The Docton and Durham models are geometrically very different, however the most significant result applies to both geometries. This is that the transient flow development can take up to 7 model lengths of cross-wind flow before the model surface pressure distributions become comparable to the steady, yawed pressure distributions. These long development times are associated with regions of separated flow. During pressure development, transient pressure overshoots are observed in the regions of separated flow, resulting in transient force and moment overshoots. Mullarkey [101] also commented that the most important flow phenomenon responsible for differences between steady and transient flow is separation.

The most striking of these overshoots is the 55% integrated pressure yawing moment overshoot of the Docton geometry. This is particularly large and as comparison with the Durham geometry results show (table 7.1), this overshoot is much smaller for a more realistic passenger car geometry. The significantly higher yawing moment overshoot of the Docton geometry is a consequence of its peculiar geometry. The overshoots result from transient suction pressure peaks. On the Docton geometry two such transient suction peaks occur, one on the front leeward corner and one on the rear windward corner. Both these act to increase yawing moment, with the suction peaks acting over the full height of the model (hence large area) and at a position where the moment arm is near maximum. This can be contrasted to the Durham geometry, where the yawing moment overshoot is mainly a consequence of suction peaks within the cores of the leeward side A-pillar and underfloor vortices. These suction peaks act over a relatively small area, and at a position where the moment arm is relatively small, and hence the yawing moment overshoot is not as significant.

The majority of passenger cars would be expected to have a response similar to that of the Durham geometry, however the magnitude of overshoot experienced by vans or people carrier vehicles, that are characterised by their one-box shape, may well be of concern. The transient force and moment overshoots, as obtained from the integrated pressure forces and moments, are summarised in table 7.1.

	Docton Geometry	Durham Geometry
Side Force	• 11% - after 4.5 model lengths of cross-wind	• 16% - after 5 model lengths of cross-wind
Yawing Moment	• 55% - after 1 model length of cross-wind	• 7% - after 5 model lengths of cross-wind flow
Drag	• No transient overshoot	
Upper Surface Lift		• 12% - after 5 model lengths of cross-wind flow

Table 7.1 A Summary of the Transient Force and Moment Overshoots

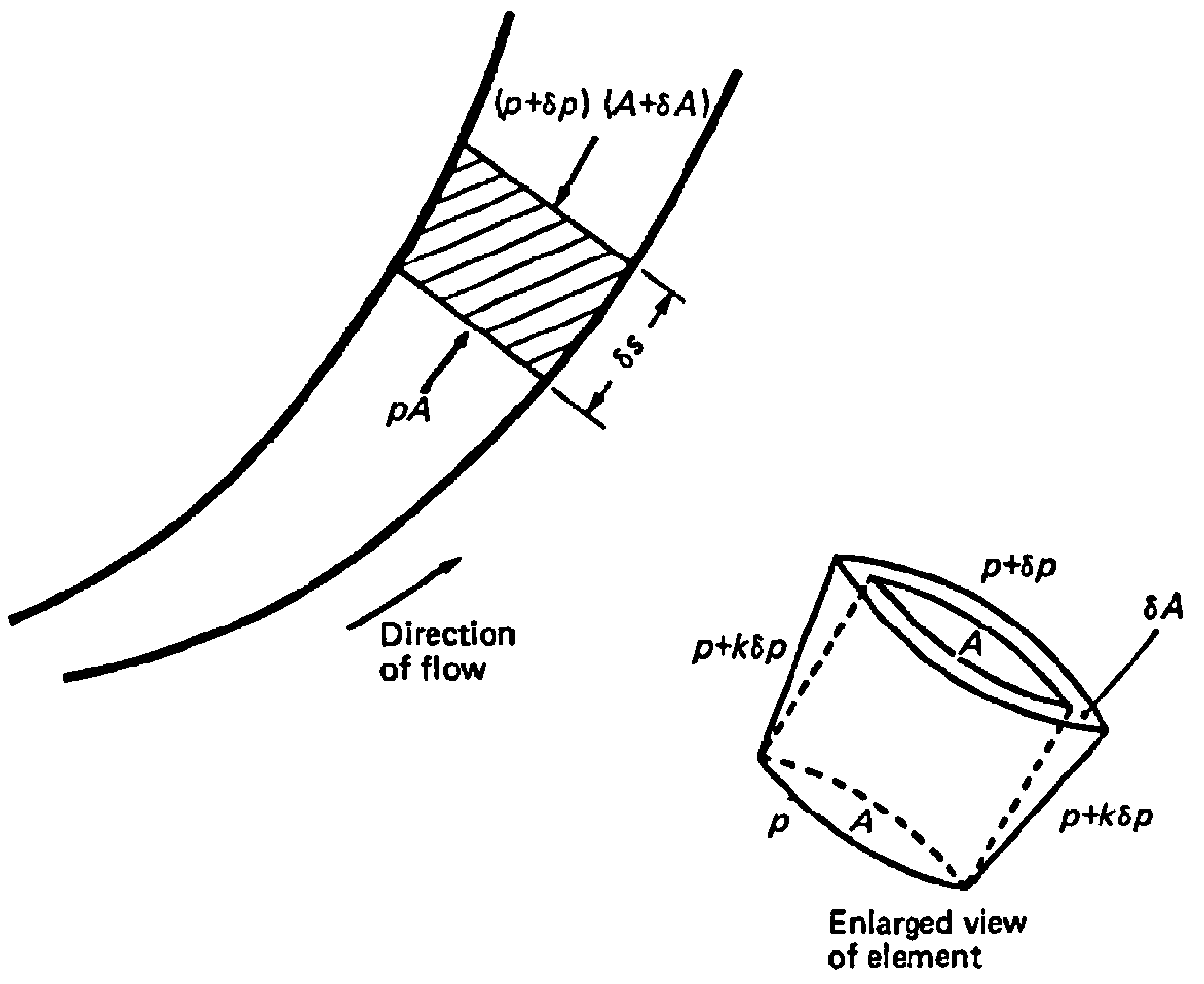

Figure 7.1 Forces on an Element of Fluid in a Streamtube (from Massey [112])

Chapter Eight

Conclusions

8.1 Empty Working Section

The unique University of Durham transient cross-wind facility has been developed such that repeatable, finite length, sharp edged cross-wind gusts can be generated at the rate of 1000/hr. Currently these cross-wind gusts have two inherent problems. Firstly there is a transient yaw angle undershoot ($\psi = -12.3^{\circ}$) and then overshoot ($\psi = 33.9^{\circ}$) at the leading edge of the gust, prior to the final yaw angle of $\psi = 22.0^{\circ}$ being attained. Secondly, there are total pressure anomalies. These anomalies take two forms; a concentrated region of transient overshoot at the leading edge of the gust where $Cp_o \leq 1.7$ (maximum theoretical $Cp_o = 1.16$), and an uneven total pressure distribution within the gust, whereby the total pressure at the leading edge of the gust rises slowly from the axial flow value ($Cp_o = 1.0$) to the yawed flow value ($Cp_o = 1.16$), with a further approximately 6% reduction in total pressure occurring near the trailing edge of the gust.

CFD analysis of the working section has shown the yaw angle overshoot to be a consequence of the thick boundary layer along the cross-wind inlet. Reducing the thickness of the boundary layer was shown to eliminate the yaw angle overshoot for a CFD calculation. Future development of the experimental facility should be able to replicate this result. Reducing the yaw angle overshoot also has the desirable effect of reducing the yaw angle undershoot. The effect of the current yaw angle under and overshoots on aerodynamic data is however clearly apparent, allowing erroneous data to be identified.

Evidence from the experimental facility and the CFD suggests that the total pressure overshoot is linked to a transient interaction between the two jets as the cross-wind gust is formed. Although this is undesirable its effect on the transient forces and moments is limited. Further work is required to establish the cause of the uneven total pressure within the gust. Importantly, the total and dynamic pressures of the transient gust do not rise above their steady counterparts, making the comparison of steady and transient aerodynamic data valid.

8.2 Aerodynamic Models

Two substantially different aerodynamic models have been tested under steady axial, yawed and transient flow conditions. The first model, the so called 'Docton geometry', was a two-dimensional geometry of the one-box type with large radii corners and end plates fitted to promote two-dimensional flow. The second model, the 'Durham geometry' was a generic three-dimensional vehicle shape. Time accurate measurements of surface static pressures and forces and moments were taken. Wake traverses were also conduced behind the Durham geometry.

Initial aerodynamic investigations showed that ensemble averaging provided a dramatic increase in the signal to noise ratio of surface static pressure and five hole probe data, and in fact is essential for the acquisition of meaningful data. The rapid gust production rate and time synchronised logging procedures of this facility allowed all data to be averaged over 20 cross-wind gusts, with the volume of averaged data produced within the time frame still significantly higher than that possible from alternative transient cross-wind testing procedures.

Difficulties were experienced with force balance resonance and cross-coupling during direct measurement of the forces and moments, however integration of the surface pressures yielded relatively accurate limited forces and moments.

The integrated pressure forces and moments from the Docton geometry showed a significant transient yawing moment overshoot of 55% of the steady yawed value immediately on entry into the cross-wind gust. A transient side force overshoot was also observed, although the magnitude was significantly smaller (11%). The cause of these overshoots was found to be the delayed formation of regions of separated flow, and in particular the separation around the front leeward corner. No transient overshoot was observed for the drag, although the yawed drag coefficient (Cx = 0.93) was significantly higher that its axial flow counterpart (Cx = 0.51). Full flow development was not observed until after 7 model lengths of cross-wind flow.

Similar transient overshoots were observed for the Durham geometry. The yawing moment experienced a 7% overshoot, while the side force overshoot was 16%. The upper surface lift also experienced a 12% overshoot. The cause of these overshoots was again delayed flow development in regions of separated flow, which for this model were the trailing vortices. Again, full flow development required 7 model lengths of cross-wind flow. The wake surveys indicated a significant increase in the strength of the leeward side A-pillar vortex under yawed flow conditions. The windward side A-pillar vortex was replaced by a vortex forming at the leading edge of the windward side roof. This subsequently entrained the stronger windward side C-pillar vortex, such that they appear as a single vortex core in the wake. No evidence of the leeward side C-pillar vortex was seen in the yawed wake.

As discussed in section 1.2, from a perspective of the required driver input, sharp edged finite length cross-wind gusts are considered a worst case scenario. These investigations have highlighted significant transient aerodynamic effects under those precise conditions, with these aerodynamic effects acting to decrease vehicle stability in all cases. This vindicates the need for transient testing procedures, and clearly facilities are required that allow rapid and repeatable generation of sharp edged cross-wind gusts in excess of seven model lengths in length.

Chapter Nine

Recommendations for Further Work

9.1 Facility Development

The CFD investigations have shown that the cross-wind yaw angle overshoot can be eliminated by a significant reduction in the boundary layer along the cross-wind inlet plane. Thus a possible solution would be to bleed high momentum fluid from the cross-wind tunnel into the boundary layer. This may well cause a change in the nominally axial flow yaw angle in the working section, although any change may be offset by angling the plane of the shutters away from the working section in the downstream direction, or by rotating the model in the working section.

The yaw angle undershoot would be more difficult to remove, although as discussed in section 7.1.1, it is not necessarily physically unrealistic. The CFD shows a reduction in yaw angle undershoot when the yaw angle overshoot is eliminated, thus on elimination of the overshoot, it would become less of a concern.

The honeycomb flow straightener along the cross-wind inlet plane causes spatial total pressure gradients in the yawed flow working section, and clearly this needs rectifying. Ideally, it would be replaced by a honeycomb section that has a relatively smooth outer surface, thus also helping to reduce the axial flow boundary layer growth.

The elimination of the total pressure overshoot may be more problematic. If, as concluded, it is caused by an interaction between the two jets as the cross-wind forms, one possible solution would be to deflect the axial jet away from the cross-wind fluid entering the working section. This could be achieved using a series of turning veins mounted along the axial jet exit plane. These would be rotated about their vertical axis, in a similar manner to the opening of the shutters, such that fluid from the main jet was directed out of the side of the working section as cross-wind fluid entered it, thus minimising the interaction with the incoming fluid. The potential of this solution could be easily be assessed using CFD, although it would probably be much more difficult to implement in practice.

Development of the CFD simulations may yield more important information about the flow development. For this the correct boundary conditions (of fixed stagnation pressure) need to be implemented. Thus far, this has proved to be very problematic. Modelling of all, or part of, the cross-wind tunnel may yield a solution, although the current author found it impossible to implement the time-dependent boundary conditions of the shutter mechanism when this was attempted. The CFD may then become an accurate predictive tool for the transient flow around the aerodynamic models.

Other developments for the facility include the solenoid closure of shutters to produce a sharp transition from yawed to axial flow. A rolling road, which is now available, could be implemented to provide the correct floor boundary condition. This may also go some way to providing the correct skew velocity profile. Finally an increase in working section Reynolds number can be achieved by replacing the cross-wind tunnel fans.

In the longer term, once the problems associated with the facility have been overcome, a larger scale, higher speed facility could be manufactured that would allow the testing of more detailed models at more realistic Reynolds numbers.

9.2 Instrumentation

For accurate measurement of the six components of transient force and moment the balance needs developing. Currently two problems exist, the cross-coupling between components and the natural frequency of the balance.

The successful manufacture of load cells provides opportunity in that any future balance design will not be constrained by the available commercial load cells. Thus, a six component balance that was suitable for internal mounting could be manufactured. This would eliminate the problems of cross-coupling.

Increasing the natural frequency of the balance is more difficult. If deflection is to be measured by load cells this can only be done by using higher capacity cells, but this approach has an associated loss in accuracy. Reduction in mass of the balance/model system would also increase the natural frequency, however this places restrictions on any aerodynamic model that is to be used.

Implementation of an advanced flowfield measurement technique, for example PIV, would significantly aid the investigation of flowfield structures in both the empty working section and around the aerodynamic models, however this does have the limitation of not providing pressure data.

9.3 Aerodynamic Investigations

The basic principles of the aerodynamic mechanisms causing the transient force and moment overshoots have been identified. Parametric studies of simplified bodies would provide valuable information regarding the relative importance of geometrical parameters, for example corner radii, A-pillar sharpness and backlight angle.

Thus far, the forces and moments induced on a scale vehicle have not be investigated, this would provide significant insight into the 'real world' importance of transient testing.

References

1. Barnard R.H.
Road Vehicle Aerodynamic Design
Longmann, ISBN 0-582-24522-2, 1996.

2. Ahmed S.R., Ramm G., Faltin G.
Some Salient Features of the Time-Averaged Ground Vehicle Wake
SAE 840300, 1984.

3. Bearman P.W.
Near Wake Flows Behind Two- and Three- Dimensional Bluff Bodies
J. Wind Eng. and Ind. Aerodyn. Vol 69-71, pp. 33-54, 1997.

4. Dominy R.G.
Flow Unsteadiness over Passenger Vehicle Rear Surfaces
Autotech 95, paper no. C498/36/181, 1995.

5. Ishihara Y., Takagi M.
Unsteady Pressure Analysis of the Wake Flow Behind a Passenger Car Model
SAE 1999-01-0810, SP 1441, pp. 185-195, 1999.

6. Hucho W.H. (Ed.)
Aerodynamics of Road Vehicles
Butterworths, ISBN 0-0408-014229-9, 1987.

7. Freymann R., Kerschbaum H., Pracher W.
The Influence of the Heat Control Airflow on the Drag of a Road Vehicle
Autotech 95, paper no. C498/36/232, 1995.

8. Her J.Y., Wallis S., Chen R.H., Lee W. T.
Vehicle Flow Measurement and CFD Analysis for Wind Noise Assessment
SAE 970403, SP 1232, pp. 241-246, 1997.

9. Lida N.
Measurement and Evaluation of Aerodynamic Noise
SAE 1999-01-1124, SP 1441, pp. 227-235, 1999.

10. Carr G.W.
Potential for Aerodynamic Drag Reduction in Car Design
Int. J. of Vehicle Design, Technological Advances in Vehicle Design Series, SP3, Impact of Aerodynamics on Vehicle Design, pp. 44-56, 1983.

11. Coleman S. A., Baker C. J.
The Reduction of Accident Risk for High Sided Road Vehicles in Cross-Winds
J. Wind Eng. and Ind. Aerodyn. Vol 41-44, pp. 2685-2695, 1992.

12. Narita N., Katsuragi M.
Gusty Wind Effects on Driving Safety of Road Vehicles
J. Wind Eng. and Ind. Aerodyn. Vol 9, pp. 181-191, 1981.

13. Buchheim R., Maretzke J., Piatek R.
The Control of Aerodynamic Parameters Influencing Vehicle Dynamics
SAE 850279, 1985.

14. Howell J.
The Influence of Aerodynamic Lift on Lane Change Manoeuvrability
MIRA Int. Conf. on Vehicle Aerodynamics, Coventry, U.K., 1998.

15. Barlow J., Guterres R., Ranzenbach R., Williams J.
Wake Structures of Rectangular Bodies with Radiused Edges Near a Plane Surface
SAE 1999-01-0648, SP 1441, pp. 13-36, 1999.

16. Ahmed S.R.
Wake Structures of Typical Automobile Shapes
J. of Fluids Eng. Vol 103, pp. 162-169, March 1981.

17. Lajos T.
Drag Reduction by the Production of a Separation Bubble on the Front of a Bluff Body
J. Wind Eng. and Ind. Aerodyn. Vol 22, pp. 331-338, 1986.

18. Williams J., Barlow J., Ranzenbach R.
Experimental Study of Cd Variation with Aspect Ratio
SAE 1999-01-0649, SP 1441, pp. 37-49, 1999.

19. Howell J., LeGood G.
The Influence of Aerodynamic Lift on High Speed Stability
SAE 1999-01-0651, SP 1441, pp. 59-67, 1999.

20. LeGood G.M., Howell J.P., Passmore M.A., Garry K.P.
On-Road Aerodynamic Drag Measurements Compared with Wind Tunnel Test Data
SAE 950627, SP 1078, pp. 63-84, 1995.

21. Sims-Williams D.B.
Passenger Car Aerodynamic Unsteadiness
University of Durham internal report, 1998.

22. Morel T.
The Effect of Base Slant Angle on the Flow Pattern and Drag of Three-Dimensional Bodies
Symposium on Aerodynamic Drag Mechanisms of Bluff Bodies and Road Vehicles, Warren, Michigan, pp. 191-216, 1978.

23. Sedney R.
A Flow Model for the Effect of a Slanted Base on Drag
Aerodynamics of Transportation ASME - CSME Conference, Niagara Falls, pp. 53-59, 1979.

24. Ahmed S.R., Baumert W.
The Structure of Wake Flow Behind Road Vehicles
Aerodynamics of Transportation ASME - CSME Conference, Niagara Falls, pp. 93-103, 1979.

25. Bearman P.W.
Some Observations on Road Vehicle Wakes
SAE 840301, 1984.

26. Nouzawa T., Haruna S., Hiasa K., Nakamura T., Sate H.
Analysis of the Wake Pattern for Reducing Aerodynamic Drag of a Notchback Model
SAE 900318, 1990.

27. Cogotti A.
Flow-Field Surveys Behind Three Squareback Car Models Using a New Fourteen Hole Probe
SAE 870243, SP 706, pp. 1-20, 1987.

28. Onorato M., Costelli A.F., Garrone A.
Drag Measurement Through Wake Analysis
SAE 840302, 1984.

29. Cogotti A.
A Strategy for Optimum Surveys of Passenger-Car Flow Fields
SAE 890374, 1989.

30. Hackett J.E., Sugavanam A.
Evaluation of a Complete Wake Integral for the Drag of a Car-Like Shape
SAE 940577, 1984.

31. Hackett J.E., Williams J.E., Patrick J.
Wake Traverses Behind Production Cars and Their Interpretation
SAE 850280, 1985.

32. Maskell E.C.
Progress Towards a Method for the Measurement of the Components of the Drag of a Wing of Finite Span
Royal Aircraft Establishment Technical Report no. 72232, 1973.

33. Davis J.P.
Wind Tunnel Investigation of Road Vehicle Wakes
PhD Thesis, University of London, 1982.

34. Docton M.K.R.
The Side Load Distribution on a Range Rover under Simulated Crosswind Conditions
University of Durham internal report, October 1998.

35. Macklin A.R., Garry K.P., Howell J.P.
Comparing Static and Dynamic Testing Techniques for the Crosswind Sensitivity of Road Vehicles
SAE 960674, 1996.

36. MacAdam C.C., Sayers M.W., Pointer J.D., Gleason M.
Crosswind Sensitivity of Passenger Cars and the Influence of Chassis and Aerodynamic Properties on Driver Preferences
Vehicle System Dynamics, pp. 281-316, 1990.

37. Kobayashi N., Yamada M.
Stability of a One-Box Type Vehicle in a Cross-Wind - An Analysis of Transient Aerodynamic Forces and Moments
SAE 881878, 1988.

38. Kramer C., Grundmann R., Gerhardt H.J.
Testing of Road Vehicles Under Cross Wind Conditions
J. Wind Eng. and Ind. Aerodyn. Vol 38, pp. 59-69, 1991.

39. Yoshida Y., Muto S., Imaizumi T.
Transient Aerodynamic Forces and Moments on Models of Vehicles Passing Through Cross-Wind
SAE 770391, 1977.

40. Ryan A., Dominy R.G.
The Transient Aerodynamic Characteristics of a Passenger Vehicles Passing Through A Cross-Wind Jet
Autotech 97, paper no. C524/117/97, 1997.

41. Ryan A., Dominy R.G.
The Transient Aerodynamic Forces Induced on a Passenger Vehicle in Response to a Transient Cross-Wind Gust at a Relative Incidence of 30°
SAE 980392, SP 1318, pp. 181-189, 1998.

42. Dominy R.G., Ryan A.
An Improved Wind Tunnel Configuration for the Investigation of Aerodynamic Cross-Wind Gust Response
SAE 1999-01-0808, SP 1441, pp. 169-175, 1999.

43. Cooper K.R.
The Effect of Front-Edge Rounding and Rear-Edge Shaping on the Aerodynamic Drag of Bluff Vehicles in Ground Proximity
SAE 850288, 1985.

44. Davis J.P.
Cross-Wind Stability of High Performance Road Cars
SAE 870724, 1987.

45. Gilhaus A.M., Renn V.
Drag and Driving Stability Related Aerodynamic Forces and Their Interdependence - Results of Measurements on 3/8 Scale Basic Car Shapes
SAE 860211, 1986.

46. Howell J.P.
Shape Features Which Influence Crosswind Sensitivity
IMechE paper no. C466/036/93, 1993.

47. Kohir I., Kataoka T.
Research on Improvements of Cross-Wind Properties of Passenger Vehicles
JSAE review, Vol 10, No. 3, pp. 46-51, 1989.

48. Bearman P.W., Davis J.P., Harvey J.K.
Measurement of the Structure of Road Vehicle Wakes
Int. J. of Vehicle Design, SP3, pp. 493-499, 1983.

49. Howell J.P.
Wake Properties of Typical Road Vehicles
Procs. 2nd. AIAA Symposium on Aerodynamics of Sports and Competition Vehicles, pp. 99-109, 1974.

50. Baker C.J.
Ground Vehicles in High Cross Winds Part I: Steady Aerodynamic Forces
J. of Fluids and Structures Vol 5, pp. 69-90, 1991.

51. Baker C.J.
Ground Vehicles in High Cross Winds Part II: Unsteady Aerodynamic Forces
J. of Fluids and Structures Vol 5, pp. 91-111, 1991.

52. Baker C.J.
Ground Vehicles in High Cross Winds Part III: The Interaction of Aerodynamic Forces and the Vehicle System
J. of Fluids and Structures Vol 5, pp. 221-241, 1991.

53. Humphreys N.D., Baker C.J.
The Application of Wind Engineering Techniques to Moving Ground Vehicles
R.Ae.S. Vehicle Aerodynamics Conference, Loughborough, ISBN 1-85768-006-5, pp. 5.1-5.12, 1994.

54. Beauvais F. N.
Transient Nature of Wind Gust Effects on an Automobile
SAE 670608, 1967.

55. Stewart M.J.
Transient Aerodynamic Forces on Simple Road Vehicle Shapes in Simulated Cross-Wind Gusts
MIRA Research report 1977/5, 1977.

56. Chadwick A., Garry K., Howell J.P.
Determination of the Transient Flow Field Characteristics by the Measurement of Surface Pressures
SAE 2000-01-0876, SP 1506, pp. 317-323, 2000.

57. Garry K.P., Cooper K.R.
Comparison of Quasi-Static and Dynamic Wind Tunnel Measurements of Simplified Tractor-Trailer Models
J. Wind Eng. Ind. Aerodyn. Vol 22, pp. 185-194, 1986.

58. Bearman P.W., Mullarkey S.P.
Aerodynamic Forces on Road Vehicles due to Steady Side Winds and Gusts
R.Ae.S. Vehicle Aerodynamics Conference, Loughborough, ISBN 1-85768-006-5, pp. 4.1-4.12, 1994.

59. Scott A.L.
A New Technique to Investigate the Stability of Cars in Cross-Winds
University of Durham internal report, 1991.

60. Docton M.K.R.
Unsteady Vehicle Aerodynamics
University of Durham internal report, 1991.

61. Docton M.K.R.

The Simulation of Transient Cross-Winds on Passenger Vehicles
PhD Thesis, University of Durham, 1996.

62. Docton M.K.R., Dominy R.G.
The Simulation of Transient Cross-Winds on Passenger Vehicles
MIRA International Vehicle Aerodynamics Conference, Birmingham, October 1996.

63. Docton M.K.R., Dominy R.G.
Passenger Vehicles in Unsteady Cross-Winds
R.Ae.S. Vehicle Aerodynamics Conference, Loughborough, ISBN 1-85768-006-5, pp. 7.1-7.6, 1994.

64. White R.G.S.
A Rating Method for Assessing Vehicle Aerodynamic Side Force and Yawing Moment Coefficients
MIRA report no. 1970/1, 1970.

65. Tran V.T.
Determining the Wind Forces and Moments Acting on Vehicles by Means of Pressure Sensors
SAE 900313, 1990.

66. Tran V.T.
A Calculation Method for Estimating the Transient Wind Forces and Moments Acting on A Vehicle
SAE 910315, SP 855, pp. 111-122, 1991.

67. Carr G.W., Atkins P.D., Somerville J.
An Empirically Based Prediction Method for Car Aerodynamic Lift and Side Force
R.Ae.S. Vehicle Aerodynamics Conference, Loughborough, ISBN 1-85768-006-5, pp. 33.1-33.16, 1994.

68. Hucho W.H., Emmelmann H.J.
Theoretical Prediction of the Aerodynamic Derivatives of a Vehicle in Cross-Wind Gusts
SAE 730232, 1973.

69. Perzon S., Janson J., Hoglin L.
On Comparison Between CFD Methods and Wind Tunnel Tests on a Bluff Body
SAE 1999-01-0805, SP 1441, pp. 133-148, 1999.

70. Axelsson N., Ramnefors M., Gustafsson R.
Accuracy in Computational Aerodynamics Part I: Stagnation Pressure
SAE 980037, SP 1318, pp. 107-118, 1998.

71. Gaylard A.P., Baxendale A.J., Howell J.P.
The Use of CFD to Predict the Aerodynamic Characteristics of Simple Automotive Shapes
SAE 980036, SP 1318, pp. 97-106, 1998.

72. Okumura K., Kuriyama T.
Practical Aerodynamic Simulations (Cd, Cl, Cym) Using a Turbulence Model and 3rd Order Upwind Scheme
SAE 950629, 1995.

73. Okumura K., Kuriyama T.
Transient Aerodynamic Simulation in Crosswind and Passing an Automobile
SAE 970404, 1997.

74. Baxendale A.J., Graysmith J.L., Howell J.
Comparisons Between CFD and Experimental Results for the Ahmed Reference Model
R.Ae.S. Vehicle Aerodynamics Conference, Loughborough, ISBN 1-85768-006-5, pp. 30.1-30.11, 1994.

75. Baker C.J., Brockie N.J.
Wind Tunnel Tests to Obtain Train Aerodynamic Drag Coefficients: Reynolds Number and Ground Simulation Effects
J. Wind Eng. and Ind. Aerodyn. Vol 38, pp. 23-28, 1991.

76. Fago B., Linder H., Mahrenholtz O.
The Effect of Ground Simulation on the Flow Around Vehicles in Wind Tunnel Testing
J. Wind Eng. and Ind. Aerodyn. Vol 38, pp. 47-57, 1991.

77. Lajos T., Hegel I.
Some Experiences of Ground Simulation with Moving Belt
R.Ae.S. Vehicle Aerodynamics Conference, Loughborough, ISBN 1-85768-006-5, pp. 34.1-34.11, 1994.

78. Hackett J.E., Baker J.B., Williams J.E., Wallis S.B.
On the Influence of Ground Movement and Wheel Rotation in Tests on Modern Car Shapes
SAE 870245, SP 706, pp. 37-65, 1987.

79. Howell J.P.
The Influence of Ground Simulation on the Aerodynamics of Simple Car Shapes with an Underfloor Diffuser
R.Ae.S. Vehicle Aerodynamics Conference, Loughborough, ISBN 1-85768-006-5, pp. 36.1-36.11, 1994.

80. Howell J.P., Goodwin J.C.
The Influence of Ground Simulation on the Aerodynamics of Simple Car-Like Shapes with Underbody Roughness
Autotech 95 paper no. C498/36/158, 1995.

81. Papenfuss H.D., Kronast M.
Moving Model Technique used in Automobile Aerodynamics for Measurement of Ground Effects

Experiments in Fluids, Vol 11, pp. 161-166, 1991.

82. Barth R.
Effect of Unsymmetrical Wind Incidence on Aerodynamic Forces Acting on Vehicle Models and Similar Bodies
SAE 650136, 1965.

83. Baker C.J., Humphreys N.D.
Assessment of the Adequacy of Various Wind Tunnel Techniques to Obtain Aerodynamic Data for Ground Vehicles in Cross Winds
J. Wind Eng. and Ind. Aerodyn. Vol 60, pp. 49-68, 1996.

84. Panton R.L.
Incompressible Flow -2nd Edition
John Wiley & Sons Inc., ISBN 0-471-59358-3, 1995.

85. Bearman P.W., Morel T.
Effect of Free Stream Turbulence on the Flow Around Bluff Bodies
Prog. Aerospace Sci. Vol 20, pp. 97-123, 1983.

86. Hegel I., Bearman P.W.
Effect of Ground Motion and Wind Turbulence on the Aerodynamic Force Coefficients of a Basic Bluff Body
R.Ae.S. Vehicle Aerodynamics Conference, Loughborough, ISBN 1-85768-006-5, pp. 8.1-8.9, 1994.

87. Macklin R., Garry K., Howell J.
Assessing the Effects of Shear and Turbulence During the Dynamic Testing of the Crosswind Sensitivity of Road Vehicles
SAE 970135 SP 1233, pp. 29-40, 1997.

88. Wiedemann J., Ewald B.
Turbulence Manipulation to Increase Effective Reynolds Numbers in Vehicle Aerodynamics

AIAA Journal, Vol 27, No. 6, pp. 763-769, 1989.

89. Bearman P.W.
Some Effects of Free-Stream Turbulence and the Presence of the Ground on the Flow Around Bluff Bodies
Symposium on Aerodynamic Drag Mechanisms of Bluff Bodies and Road Vehicles, Warren, Michigan, 1978.

90. Bearman P.W.
An Investigation of the Forces on Flat Plates Normal to a Turbulent Flow
J. Fluid Mech. Vol 46, Part 1, pp. 177-198, 1971.

91. Garry K.P., Wallis S.B., Cooper K.R., Fediw A., Wilsden D.J.
The Effect on Aerodynamic Drag of the Longitudinal Position of a Road Vehicle Model in a Wind Tunnel Test Section
SAE 940114, 1994.

92. Sims-Williams D.B., Dominy R.G.
Experimental Investigation into Unsteadiness and Instability in Passenger Car Aerodynamics
SAE 980391, SP-1318, pp. 169-189, 1998.

93. Sims-Williams D.B., Dominy R.G.
The Validation and Application of a 5-Hole Pressure Probe with Tubing Transfer Function Correction for Time-Accurate Measurements in Unsteady Flows
2nd. MIRA International Conference on Vehicle Aerodynamics, Coventry, UK, 1998.

94. Bruun H.H.
Hot wire Anemometry, Principles and Signal Analysis
Oxford University Press, Oxford, 1995.

95. Dominy R.G., Hodson H.P.

An Investigation of Factors Influencing the Calibration of 5-Hole Probes for 3-D Flow Measurements
ASME International Gas Turbine and Aeroengine Congress and Exposition, Cologne, Germany, 1992.

96. SensorTechnics
Pressure Transducers and Transmitters 94/95
SensorTechnics Manual, 1994.

97. Duell E.G., George A.R.
Experimental Study of a Ground Vehicle Body Unsteady Near Wake
SAE 1999-010-0812, SP 1441, pp. 197-208, 1999.

98. Rediniotis O.K., Pathak M.M.
Simple Technique for Frequency Response Enhancement of Miniature Pressure Probes
Technical note, AIAA Journal, Vol 37, no. 7, pp. 897-899, 1999.

99. Irwin H.P.A.H., Cooper K.R., Girard R.
Correction of Distortion Effects Caused by Tubing Systems in Measurements of Fluctuating Pressures
J. of Ind. Aerodynamics 5, pp. 93-107, 1979.

100. Sims-Williams D.B.
Self-Excited Aerodynamic Unsteadiness Associated with Passenger Cars
PhD Thesis, University of Durham, to be published 2000.

101. Mullarkey S.P.
Aerodynamic Stability of Road Vehicles in Side Winds and Gusts
PhD Thesis, University of London, 1990.

102. Press W.H., Teukolsky S.A., Vetterling W.T., Flannery B.P.
Numerical Recipes in Fortran - Second Edition
Cambridge University Press, 1992.

103. Williams C.S
Designing Digital Filters
Prentice-Hall, ISBN 0-13-201856-X, 1986.

104. Gossweiler C.R., Kupferschmied P., Gyarmathy G.
On Fast Response Probes: Part I - Technology, Calibration, and Application to Turbomachinery
J. of Turbomachinery, Vol 117, pp. 611-617, 1995.

105. Amplicon
User Manual for PC-30PGL and PC-30PGH Cards

106. Treaster A.L., Yocum A.M.
The Calibration and Application of Five-hole Probes
Instrument Society of America Transactions, Vol 18, no. 3, pp. 23-34, 1979.

107. McCroskey W.J.
Some Current Research in Unsteady Fluid Mechanics
J. of Fluids Eng. Vol 99, pp. 8-38, 1977.

108. Graysmith J.J., Baxendale A.J.,
Further CFD Analysis of Flow Around the Ahmed Body
Autotech 95, paper no. C498/36/160, 1995.

109. Ichinose K., Ito S.
Accuracy of Drag Prediction on Bluff Bodies Using CFD
JSAE Review 19, pp. 151-160, 1998.

110. Angelis W., Drikakis D., Durst F., Khier W.
Numerical and Experimental Study of the Flow Over a Two-Dimensional Car Model
J. Wind Eng. and Ind. Aerodyn. Vol 62, pp. 57-79, 1996.

111. Computation Dynamics
StarCD Methodology
StarCD Manual, Version 3.05, 1998.

112. Massey B.S.
Mechanics of Fluids -6th Edition
Chapman & Hall, ISBN 0-412-34280-4, 1991.

113. McCroskey W.J., Carr L.W., McAlister K.W.
Dynamic Stall Experiments on Oscillating Airfoils
AIAA Journal, Vol 14, No. 1, pp. 57-63, 1976.

114. Harvey J.K., Perry F.J.
Flowfield Produced by Trailing Vortices in the Vicinity of the Ground
Technical Note, AIAA Journal, Vol 9, No. 8, 1971.

Appendix A

A.1 Five Hole Probe Calibration Coefficients

Listed in equations (A.1-5) are the calibration coefficients used to formulate the five hole probe calibration maps.

Pitch angle coefficient:

$$\mathrm{Cp} = \frac{p_4 - p_5}{p_1 - p_{av}} \tag{A.1}$$

Yaw angle Coefficient:

$$\mathrm{Cy} = \frac{p_2 - p_3}{p_1 - p_{av}} \tag{A.2}$$

Stagnation pressure coefficient:

$$\mathrm{Ct} = \frac{p_1 - p_o}{p_1 - p_{av}} \tag{A.3}$$

Static pressure Coefficient:

$$\mathrm{Cs} = \frac{p_{av} - p_s}{p_1 - p_{av}} \tag{A.3}$$

where:

$$\mathrm{p_{av}} = \frac{(p_2 + p_3 + p_4 + p_5)}{4} \tag{A.5}$$

and $p_{1\text{-}5}$ are the individual pressures of the five holes.

A.2 Five Hole Probe Calibration Maps

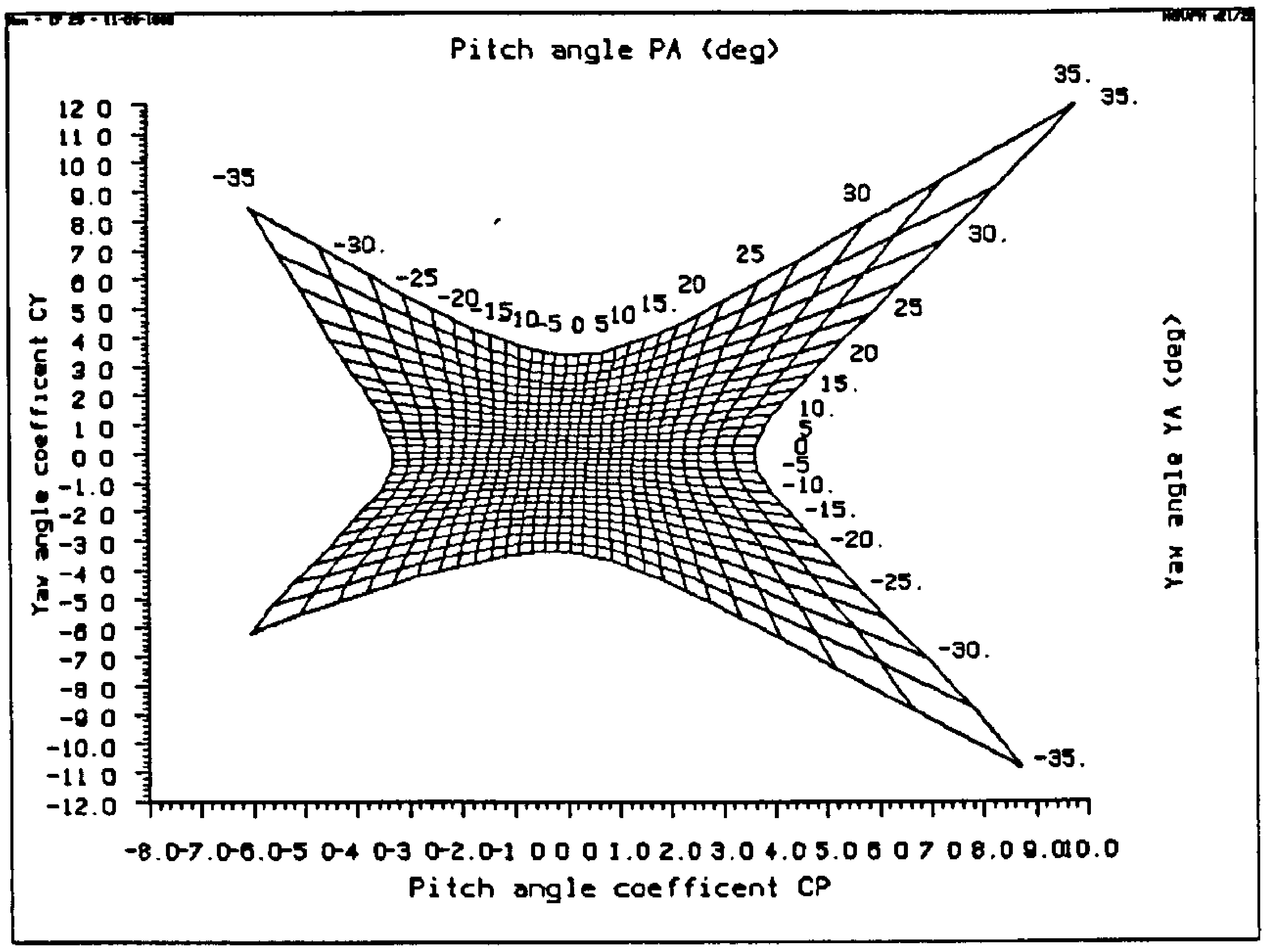

Figure A.1 Pitch/Yaw Coefficient Calibration Map

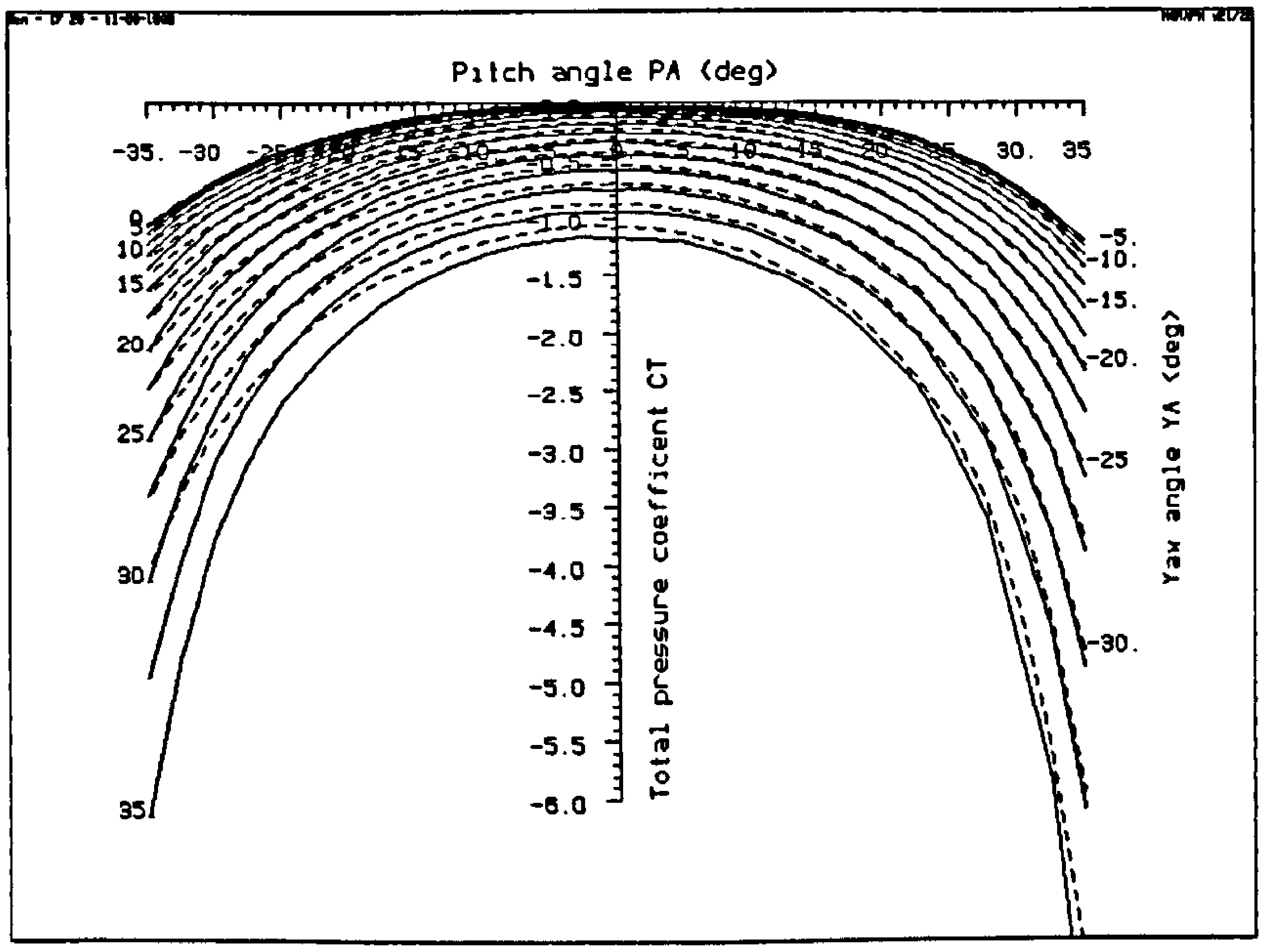

Figure A.2 Total Pressure Coefficient Calibration Map

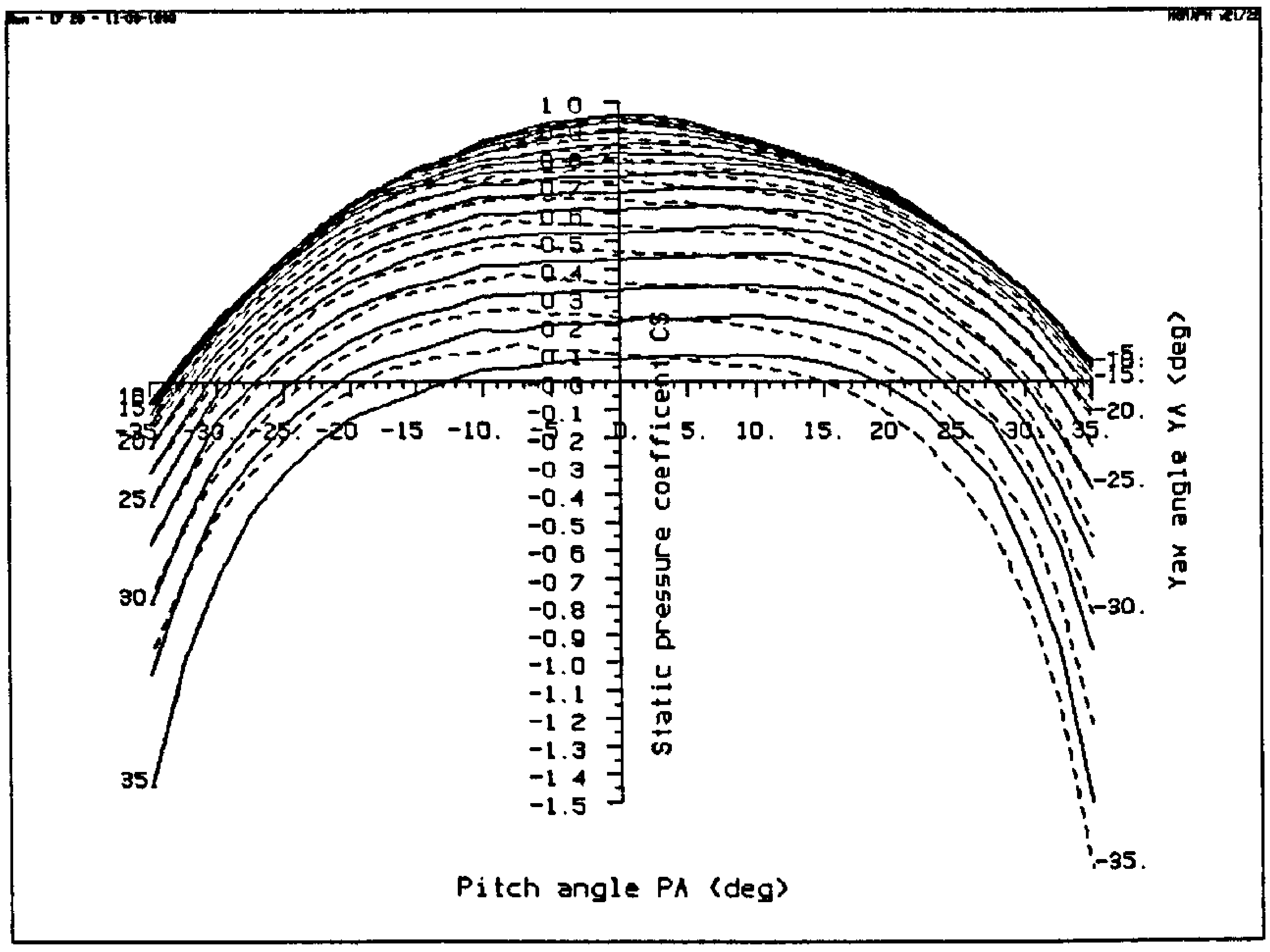

Figure A.3 Static Pressure Coefficient Calibration Map

Appendix B

B.1 The Momentum Equation to Wake Integration

The hydrodynamic force exerted on a body from the fluid flowing past it may be calculated from the momentum equation.

B.1.1 One-Dimensional Flow

Consider the one-dimensional flow situation shown in figure B.1. Here a body lies within a control volume, such that uniform flow with velocity u_{ref} and static pressure p_{s_ref}, with $p_{s\_ref} = 0.0$, occurs at the upstream boundary, AB. Boundaries AD and BC are parallel to the flow, and sufficiently far from the body that the flow at these planes is unaffected by the presence of the body. Boundary CD lies behind the body, such that local changes in velocity and static pressure are experienced along its length. The local velocity at CD in the direction of u_{ref} is u, and the static pressure p_s.

The mass flow rate through an element of boundary CD of thickness δy and unit breadth is $\rho u \delta y$, where ρ is the density of the fluid. The rate of increase of momentum of this fluid is therefore $\rho u \delta y(u - u_{ref})$. Integrating along the length of CD yields the total rate of increase of momentum for the control volume, as seen in equation (B.1).

Total rate of increase in momentum:

$$\int_C^D \rho u(u - u_{ref})\,dy \tag{B.1}$$

The rate of increase of x-momentum is equal to the sum of the forces on the fluid in the x-direction. These forces are F_x, the x component of the force exerted by the body on the fluid and any force resulting from the pressure in the plane CD differing from that at AB. The net pressure force acting downstream is as shown in equation (B.2).

Net downstream pressure force:

$$\int_B^A p_{s\_ref}\,dy - \int_C^D p_s\,dy = \int_C^D (p_{s\_ref} - p_s)\,dy \tag{B.2}$$

The momentum equation then becomes:

$$F_x + \int_C^D (p_{s\_ref} - p_s)\,dy = \int_C^D \rho u(u - u_{ref})\,dy \tag{B.3}$$

Thus the axial force on the body, F_x is given by:

$$F_x = \int_C^D \left\{(p_{s\_ref} - p_s) - \rho u(u - u_{ref})\right\} dy \tag{B.4}$$

Similarly, the perpendicular force on the body in the +ve y direction, F_y is:

$$F_y = \int_C^D -\rho uv\,dy \tag{B.5}$$

B1.2 Three-Dimensional Flow

Equation (B.4) can be extrapolated for three dimensional flow.

From total pressure definition:

$$p_{s\_ref} = p_{o\_ref} - \tfrac{1}{2}\rho(u_{ref}^2 + v_{ref}^2 + w_{ref}^2) \tag{B.6}$$

where p_{o_ref} is the upstream total pressure and u_{ref}, v_{ref} and w_{ref} are the three upstream velocity components. The flow at the upstream boundary (AB) is assumed axial and uniform, thus $v_{ref} = w_{ref} = 0.0$. Similarly:

$$p_s = p_o - \tfrac{1}{2}\rho(u^2 + v^2 + w^2) \qquad \text{(B.7)}$$

where p_o is the local total pressure in plane CD and v and w are the local secondary flow velocity components.

The axial force on the body, F_x then becomes:

$$F_x = \int_C^D \left\{(p_{o\_ref} - p_o) - \tfrac{1}{2}\rho(u_{ref}{}^2 + u^2) + \rho u u_{ref}\right\} dy \; +$$

$$\int_C^D \left\{\tfrac{1}{2}\rho(v^2 + w^2)\right\} dy \qquad \text{(B.8)}$$

The first line of equation (B.8) represents energy loss through fluid entrainment into the boundary layer and wake of the body, and is commonly termed ‘viscous drag’. The second line represents energy required to maintain the secondary flow - so called ‘vortex drag’.

Assuming the assumptions of B.1 are held, no such extrapolation is required for the perpendicular force on the body.

B1.3 Microdrag and Microside

The numerical evaluation of the wake integral from experimental data at discrete points in a wakeplane allows the local contribution (i.e. the contribution from a single point) to either drag or side force to be evaluated. These are commonly referred to as ‘microdrag’ and ‘microside’ respectively, and are defined in equations (B9) and (B10).

$$m_d = \frac{F_x}{p_{dyn\_ref} \times dA} \qquad \text{(B.9)}$$

$$m_s = \frac{F_y}{p_{dyn\_ref} \times dA} \qquad \text{(B.10)}$$

where m_d and m_s are the microdrag and microside respectively, F_x and F_y the drag and side force respectively, as evaluated at a single point in the wake, p_{dyn_ref} the reference dynamic pressure and dA the area associated with a single point in the wake. The inclusion of dA for the reference area makes the two quantities independent of the wake traverse resolution, thus permitting a wider comparison of results.

B1.4 Resolution of Forces

For the yawed flow wake integral traverse where the Durham geometry was yawed in the working section, the axial and perpendicular forces (as shown in figure B.2) required resolving into body axis axial (drag - F_a) and perpendicular (side - F_p) forces. This is outlined in equations (B.11) and (B.12).

$$F_a = F_x \cos\psi + F_y \sin\psi \qquad \text{(B.11)}$$

$$F_p = F_y \sin\psi - F_x \cos\psi \qquad \text{(B.12)}$$

where ψ is the yaw angle of the model.

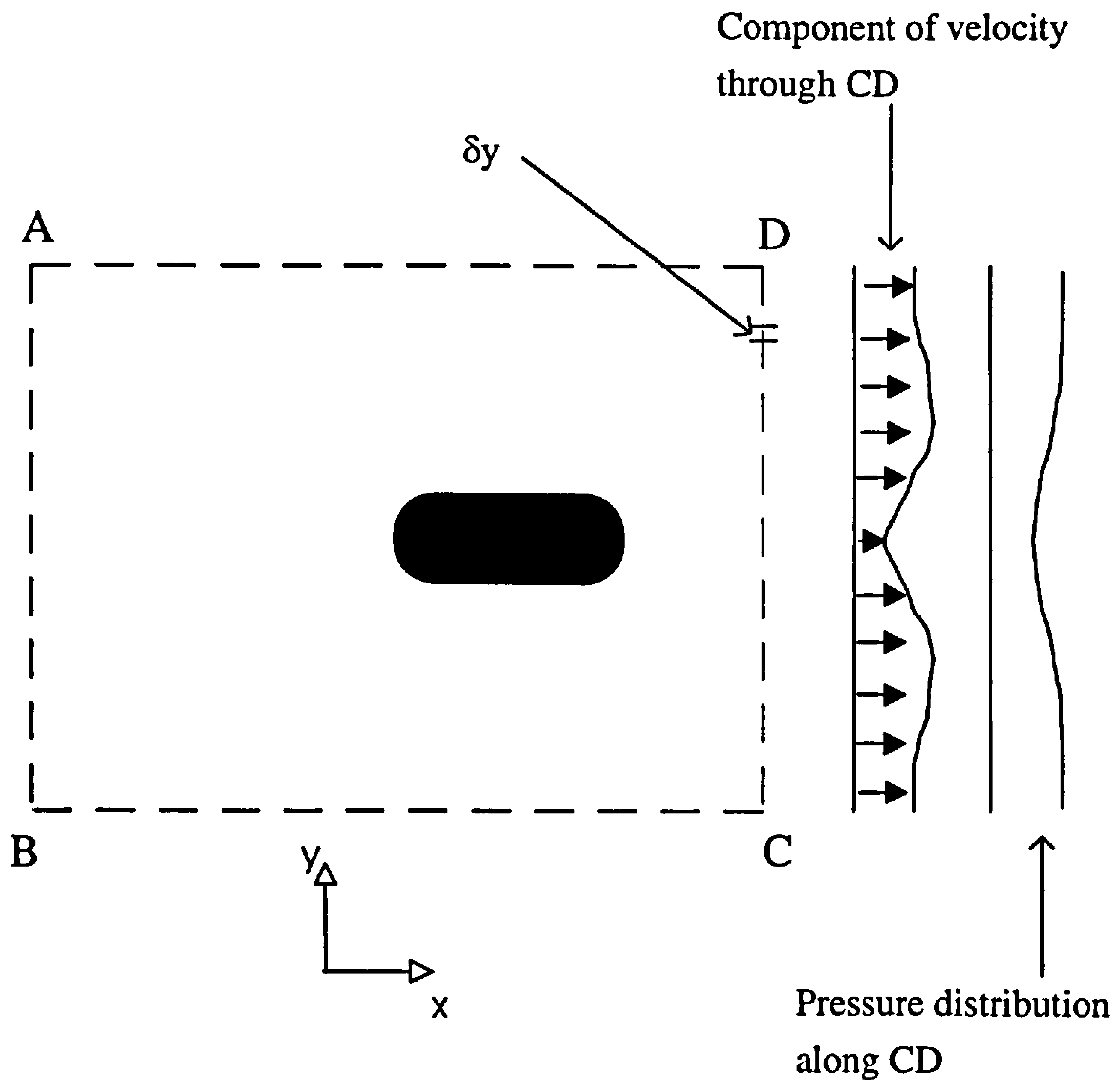

Figure B.1 One Dimensional Flow in A Control Volume

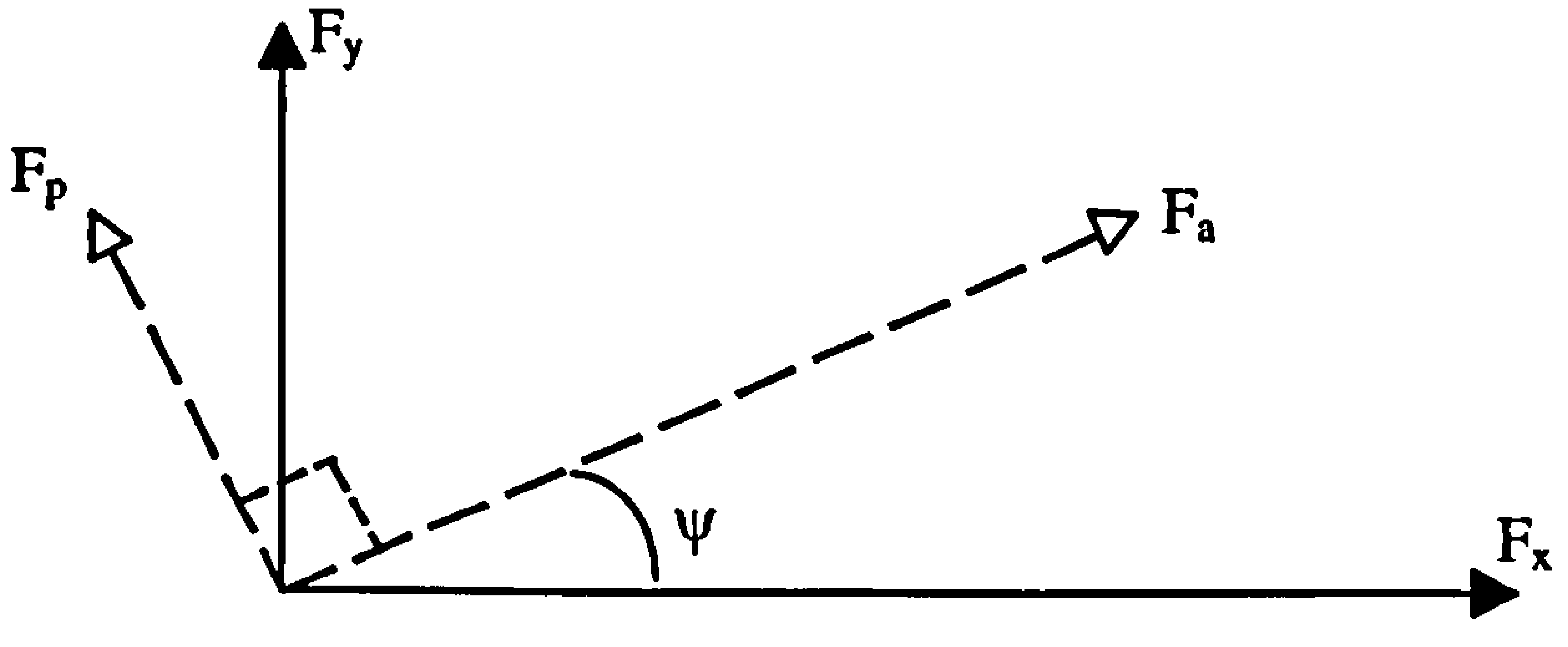

Figure B.2 Resolution of Yawed Body Forces

Appendix C

C.1 Durham Geometry Autospectral Density Functions

Figure C.1 shows autospectral density of all six components of force and moment, as measured by the two component balance, for the Durham geometry.

Side Force Yawing Moment

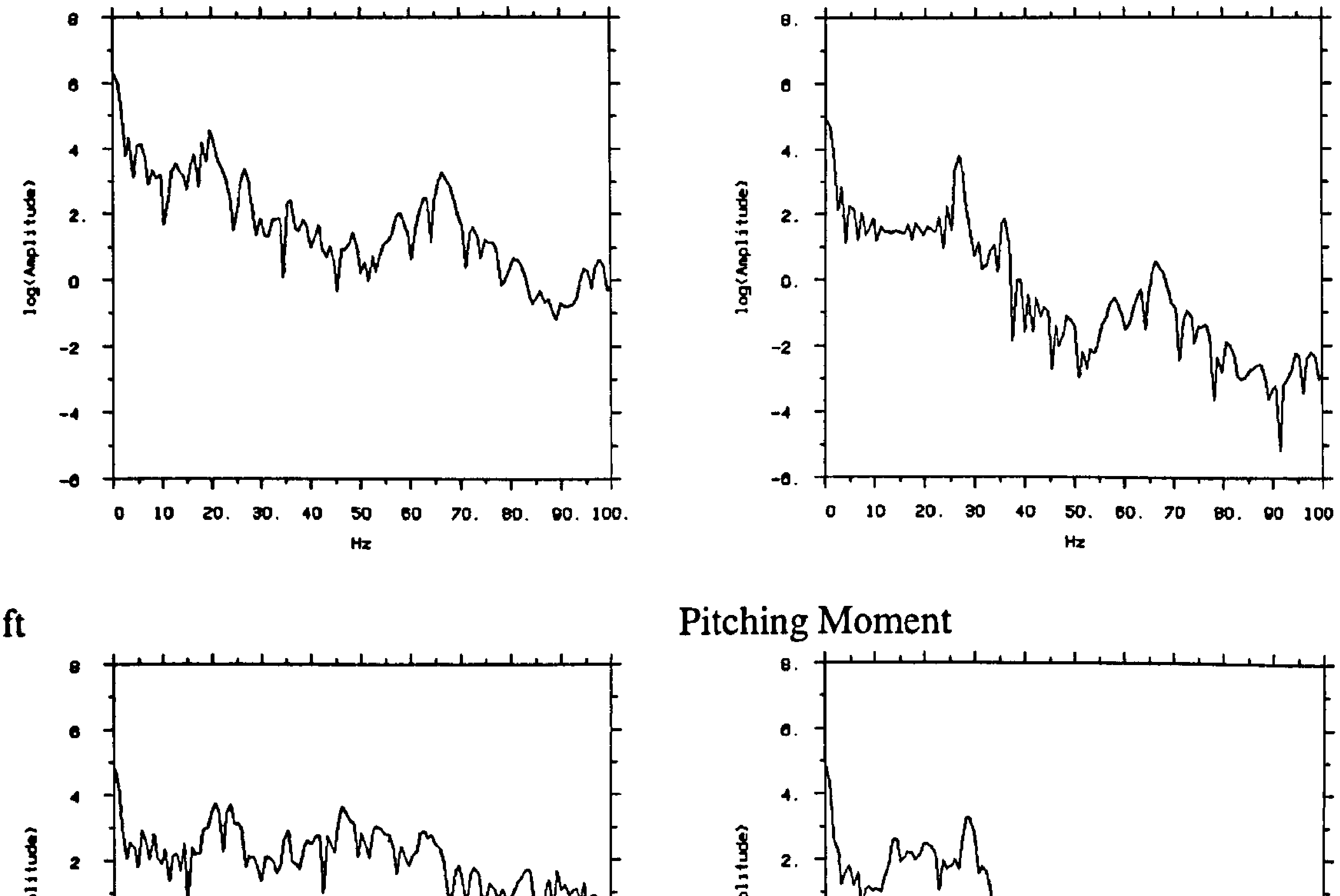

Lift Pitching Moment

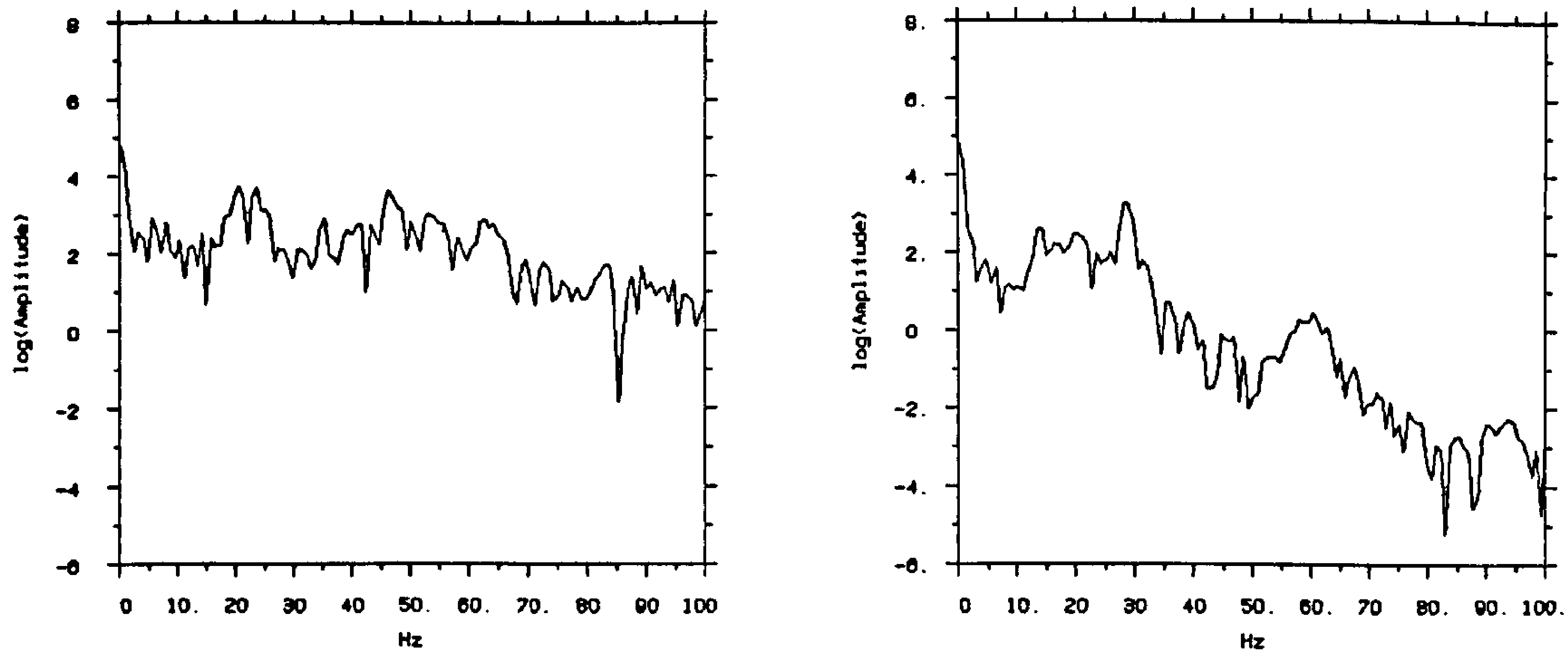

Figure C.1 (page 1 of 2)

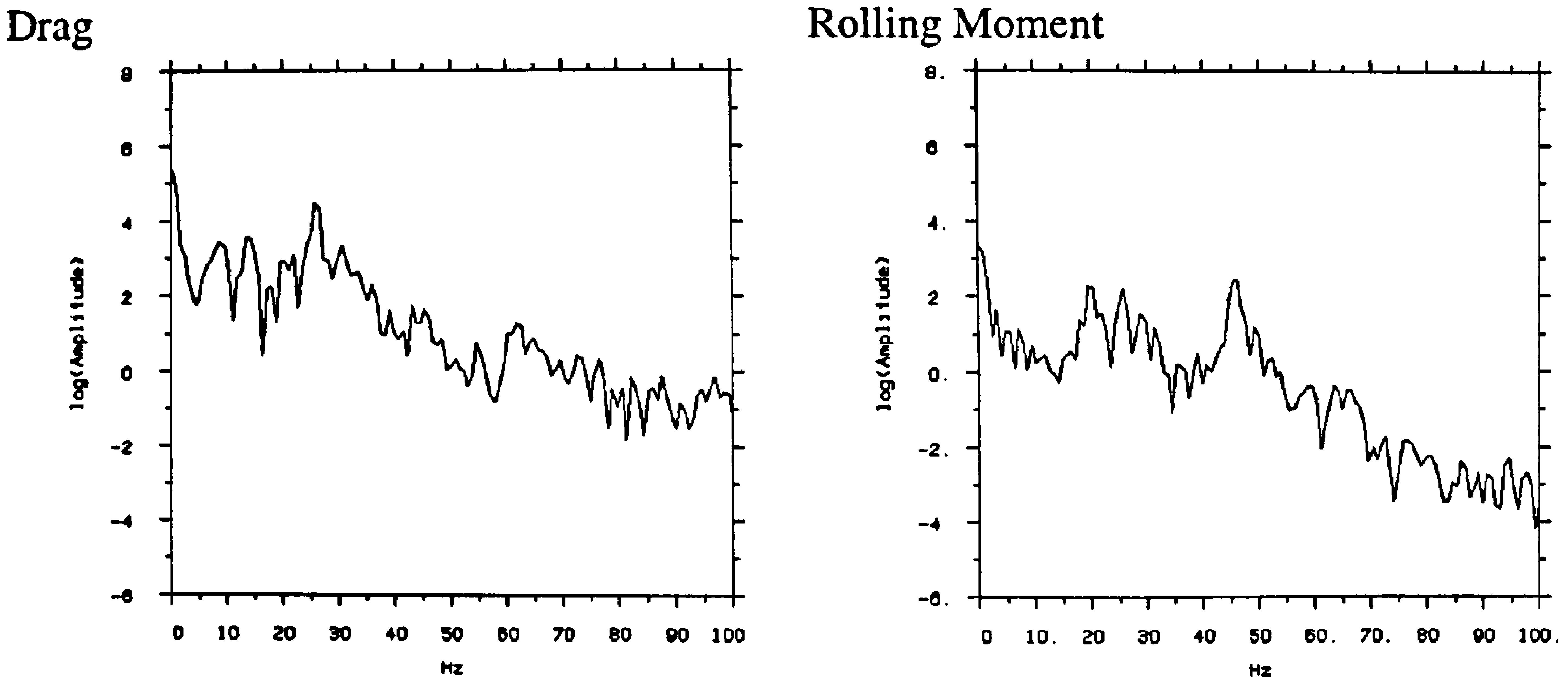

Figure C.1 (page 2 of 2) Autospectral Density Functions for the Durham Geometry Forces and Moments